Blind and Pointed Sunyaev-Zel'dovich Observations with the Arcminute Microkelvin Imager

Timothy William Shimwell

Cavendish Astrophysics and Churchill College

University of Cambridge

A dissertation submitted to the University of Cambridge for the degree of Doctor of Philosophy

September, 2011

To my family.

Declaration

This dissertation is the result of work carried out in the Astrophysics Group of the Cavendish Laboratory, Cambridge, between October 2007 and September 2011. Except where explicit reference is made to the work of others, the work contained in this dissertation is my own and is not the outcome of work done in collaboration. No part of this dissertation has been submitted for a degree, diploma or other qualification at this or any other university. The total length of this dissertation does not exceed 60,000 words.

Timothy William Shimwell
September 2011

Acknowledgements

I have thoroughly enjoyed the four years that I have spent living in Cambridge and working at the Cavendish. There are many people that I need to thank for this.

My supervisors Keith Grainge and Richard Saunders have been exceptionally supportive throughout my PhD, they have offered me endless encouragement and countless helpful suggestions. I would have found many of the problems I have faced, far more difficult, had not been for the excellent help that I received from Dave Green, Mike Hobson, Guy Pooley, Paul Scott, Dave Titterington and Liz Waldram. Additionally, I was lucky enough to receie advice from other students working with AMI, including Matthew Davies, Farhan Feroz, Tom Franzen, Natasha Hurley-Walker, Malak Olamaie, Yvette Perrott, Carmen Rodríguez Gonzálvez, Michel Schammel and John Zwart. I also would like to thank all other members of the AMI Consortium and the Astrophysics group. I feel privileged to have been welcomed by such a kind, enthusiastic and encouraging community.

I started my PhD along with Luke Butcher, Douglas O'Rourke, John Pober, Carmen Rodríguez Gonzálvez and Chris Thomas – all of whom have become good friends. Carmen Rodríguez Gonzálvez has patiently tried to teach me Spanish and has been a fantastic office mate. With Luke Butcher and Douglas O'Rourke I have enjoyed many evenings out and about in Cambridge. Chris Thomas has taught me all about military history and John Pober has been missed since he left for America after the first year. I am grateful to have met all the other PhD (and postdoc) students from the Cavendish (and Kavli). I will miss you all. I also would like to thank all of my friends who

are not based at the Cavendish or Kavli, including those I met whilst living in Wilbarston, Rutland, Sheffield and at Churchill College. I am especially indebted to my friends from Sheffield who supported my application and undergraduate studies, without your help I would never have been here.

My family have provided me with so much help over the years and I am sure that without their tireless encouragement my life would have been very different. Without all of this support I would never have achieved this PhD. The help that each of you has provided is far too much to even begin describing here but I hope that you all know just how much I appreciate everything that you have done for me over the years.

I am grateful for the financial support provided by STFC, the computer services and expertise provided by Stuart Rankin and Andrey Kaliazin, who respectively ran the Darwin and COSMOS supercomputers. I would also like to extend my thanks to my examiners Michael Brown and Richard Davis. Finally, I would like to thank Cambridge University and Churchill College for the opportunity to study in such a wonderful environment.

Abstract

In this thesis I discuss my work on the Arcminute Microkelvin Imager (AMI). I focus on the detection of Sunyaev-Zel'dovich (SZ) signatures at 14-18 GHz.

Once the background science and operation of the instrument are described I proceed to present my contribution to the calibration of AMI, including: primary beam measurements; refinements to the known antenna geometry and flagging geostationary satellite interference. This is followed by an outline of the software that I have developed to subtract sources from visibilities, concatenate data from multiple observations, simulate data, and perform jack-knife tests to evaluate the magnitude of systematic errors.

The Bayesian analysis that I use to obtain parameter estimates and to quantify the significance of putative SZ detections is described. I perform realistic simulations of clusters and use these to characterise the analysis. I then, for the first time, apply the analysis to data from the AMI blind cluster survey. I identify several previously unknown SZ decrements.

Finally, I conduct pointed observations towards a high luminosity subsample of eight clusters from the Local Cluster Substructure Survey (LoCuSS). For each of these I provide probability distributions of parameters such as mass, radius, β and temperature. I compare my results to those in the literature and find an overall agreement.

Contents

Chapter 1

Introduction

An unbiased study of the evolution of clusters of galaxies can be used to tie-down the growth of large-scale structure and measure the rms mass fluctuation amplitude as a function of redshift. This chapter is largely introductory; much of the material presented here can be found, in one form or other, in e.g. Peebles (1993), Carlstrom *et al.* (1996), Longair (1996), Birkinshaw (1999), Peacock (1999) and Thompson *et al.* (2001).

The largest cluster catalogues currently available are built up from clusters discovered either in the X-ray or optical wavebands. These catalogues are unfortunately strongly biased because the radiation that X-ray and optical telescopes detect from clusters falls off rapidly with redshift, is particularly sensitive to mass concentrations and suffers from confusion from foreground and background objects. The surface brightness of the Sunyaev-Zel'dovich (SZ; Sunyaev & Zeldovich 1970) effect of a particular cluster is wholly independent of the redshift at which it lies: this redshift-independence is unique in cosmology and is of fundamental importance. The SZ signal is also much less affected by confusion and is a direct measure of cluster thermal energy and hence a clear proxy of the key quantity, mass. Several blind surveys for galaxy clusters via SZ are underway but none is yet finished.

The Arcminute Microkelvin Imager (AMI) is a radio interferometer optimised to observe the SZ effect from galaxy clusters. AMI has been conducting a blind cluster survey over a 12 deg^2 region, searching for galaxy clusters with total masses greater than $\approx 3 \times 10^{14} M_\odot h_{70}^{-1}$ (with $h_{70} = 1$ if $H_0 = 70 \mathrm{km\,s^{-1}Mpc^{-1}}$).

AMI has also accumulated a large collection of high quality, low noise, pointed observations towards galaxy clusters that appear in X-ray, optical, or other SZ catalogues. In this thesis I present results from survey and pointed observations and I explain the reduction, commissioning, observing and analysis tasks that I have been involved with.

This first chapter provides a brief introduction to basic cosmology, the SZ effect and the operation of AMI.

1.1 Cosmological Background

The Einstein field equation is vital to our understanding of how the evolution of the Universe is affected by its energy and matter content. It is a cornerstone of modern cosmological theories. The Einstein field equation is

$$G_{uv} = \frac{8\pi G}{c^4} T_{uv}, \tag{1.1}$$

where the Einstein tensor (G_{uv}) relates the geometry of space-time to the energy-momentum tensor (T_{uv}).

The curvature of space can be described by a metric. The Euclidean metric is used to define a classical, flat and static space with three dimensions (x, y, z), and takes the form

$$g_{uv} = \begin{pmatrix} 1 & 0 & 0 \\ 0 & 1 & 0 \\ 0 & 0 & 1 \end{pmatrix}. \tag{1.2}$$

It is used to determine the separation (ds) between two points in Euclidean space:

$$ds^2 = g_{\alpha\beta} dx^\alpha dx^\beta = dx^2 + dy^2 + dz^2. \tag{1.3}$$

This line element describes the distance between points on a three dimensional static gird that has no time dimension.

To account for four-dimensional space-time the Euclidean metric is modified to the Minkowski metric – this also describes a flat and static space.

$$g_{uv} = \begin{pmatrix} -1 & 0 & 0 & 0 \\ 0 & 1 & 0 & 0 \\ 0 & 0 & 1 & 0 \\ 0 & 0 & 0 & 1 \end{pmatrix}. \tag{1.4}$$

The separation between two points in Minkowski space-time is

$$ds^2 = dx^2 + dy^2 + dz^2 - c^2dt^2, \tag{1.5}$$

However, the Universe is expanding and a modification to the static Minkowski metric is required. The Universe expands at a rate that can be described by a comoving coordinate system, such as that depicted in Figure 1.1.

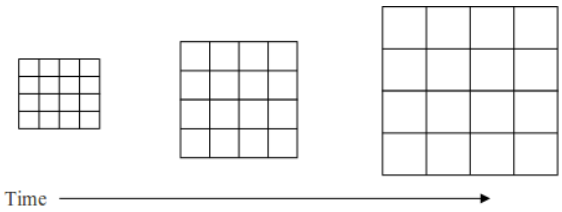

Figure 1.1: Comoving coordinate system. The scale factor, a(t), of the coordinate system is defined to be proportional to the distance between coordinates.

In a comoving coordinate system objects retain the same coordinates throughout the expansion of the space, even though the separation between the objects is changing. Consider two objects of separation $\bar{r}(t)$ which are not moving with respect to the Hubble flow; their comoving separation is

$$\bar{x} = \bar{r}(t)/a(t), \tag{1.6}$$

where a is the scale factor.

In a four-dimensional expanding Universe the three spatial dimensions evolve according to Equation 1.6, but the time dimension is not affected by the expansion. This alteration, together with the addition of curvature to the static Minkowski metric gives the Friedmann-Robertson-Walker (FRW) metric:

$$g_{uv} = \begin{pmatrix} -1 & 0 & 0 & 0 \\ 0 & a^2(t) & 0 & 0 \\ 0 & 0 & a^2(t) & 0 \\ 0 & 0 & 0 & a^2(t) \end{pmatrix}. \tag{1.7}$$

This metric is an accurate description of the geometry of an expanding (or contracting) Universe. The separation between two points in the FRW metric is

given, in spherical coordinates, by

$$ds^2 = c^2dt^2 - a(t)^2\left(\frac{dr^2}{1+kr^2} + r^2(d\theta^2 + sin^2\theta d\phi^2)\right). \tag{1.8}$$

Here, t is the cosmic time, r, θ and ϕ are comoving spherical coordinates and k is a constant that describes the geometry of the Universe. k-values of +1, 0, and -1 correspond to a closed, flat and an open Universe respectively (see Figure 1.2). The geodesics described by the FRW metric follow the curvature of space.

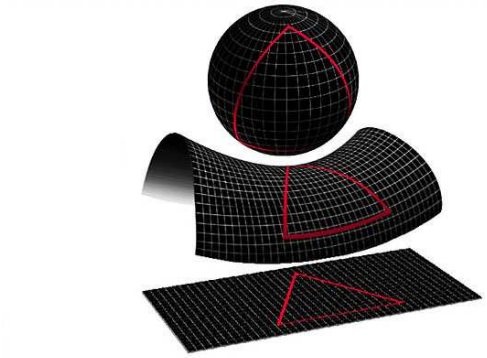

Figure 1.2: A two-dimensional analogy of the three-dimensional curvature in the Universe, with white lines showing geodesics and red lines showing the shortest distance between two points. At the top is a closed Universe ($k = -1$), in the middle is a open Universe ($k = -1$) and at the bottom is a flat Universe ($k = 0$).

The FRW metric is used to derive the Einstein tensor in the Einstein field equation (Equation A.1). This describes how energy density affects the curvature of the Universe:

$$G_{uv} = R_{uv} - \frac{1}{2}g_{uv}R, \tag{1.9}$$

where R_{uv} is known as the Ricci tensor, R the Ricci scalar and g_{uv} is the FRW metric.

The stress energy tensor T_{uv} for an observer in an homogeneous and isotropic Universe is

$$T_{uv} = \begin{pmatrix} \rho & 0 & 0 & 0 \\ 0 & p & 0 & 0 \\ 0 & 0 & p & 0 \\ 0 & 0 & 0 & p \end{pmatrix}, \tag{1.10}$$

where p is the mean pressure and ρ is the mean energy density ($\rho = \rho_R + \rho_M$).

Using the FRW metric and the stress energy tensor we can find a solution to the Einstein field equation, the Friedmann equation (see Appendix A for derivation):

$$H^2 = \left(\frac{\dot{a}}{a}\right)^2 = \frac{8\pi G\rho}{3} - const, \tag{1.11}$$

where H is the Hubble parameter and the constant arises from integration and represents the curvature of the Universe. The constant is given by $\frac{kc^2}{a^2}$.

The original field equations were revised by Einstein in 1917 to include the cosmological constant (ρ_Λ).

$$G_{uv} = \frac{8\pi G}{c^4} T_{uv} + \rho_\Lambda g_{uv} \tag{1.12}$$

This in turn has an effect on the Friedmann equation, which now has the form

$$H^2 = \left(\frac{\dot{a}}{a}\right)^2 = \frac{8\pi G\rho}{3} - \frac{kc^2}{a^2} + \frac{\Lambda c^2}{3}. \tag{1.13}$$

By defining $\frac{\rho_\Lambda}{c^2} = \frac{\Lambda}{8\pi G}$ and $\frac{-\rho_k}{3c^3} = \frac{k}{8\pi G a^2}$ the Friedmann equation is frequently written as

$$\left(\frac{\dot{a}}{a}\right)^2 = H_0^2 \left(\Omega_M a^{-3} + \Omega_R a^{-4} + \Omega_\Lambda + \Omega_k a^{-2}\right), \tag{1.14}$$

where $\rho_{tot} = \sum_i \rho_i = \rho_M + \rho_R + \rho_\lambda + \rho_k$ and $\Omega_{tot} = \sum_i \Omega_i = \Omega_M + \Omega_R + \Omega_\lambda + \Omega_k$

$$\Omega_i = \frac{\rho_i}{\rho_c} = \frac{8\pi G\rho_i}{3H_0^2} \tag{1.15}$$

and Ω_M is the density parameter of non relativistic matter, Ω_R is the density parameter of relativistic matter, Ω_Λ the density parameter of the cosmological constant, Ω_k is the curvature of the Universe and ρ_c is the critical energy density of the Universe. For a flat Universe

$$\rho_c = \frac{3H_0^2}{8\pi G}. \tag{1.16}$$

The orders of the scale-factor terms in Equation 1.14 are explained later in this section.

By taking the trace of the Einstein field equation one can derive another important equation called the acceleration equation:

$$\frac{\ddot{a}}{a} = \frac{-4\pi G}{3}\left(\rho_{tot} + \frac{3p_{tot}}{c^2}\right). \tag{1.17}$$

This equation shows how the expansion of the Universe depends upon the mean energy density ρ_{tot} and the mean pressure density p_{tot}. If the Universe is matter or radiation dominated where $(\rho_{tot}+3p_{tot}) > 0$ then the expansion of the Universe will decelerate. It is also possible for the expansion of the Universe to accelerate if $(\rho_{tot} + 3p_{tot}) < 0$, however, this requires a substance that has negative energy density or negative pressure density.

By relating the time derivative of Equation 1.13 to Equation 1.17 and assuming a flat Universe one can derive

$$\dot{\rho} = -3H(\rho_{tot} + \frac{p_{tot}}{c^2}), \tag{1.18}$$

for which a solution is

$$\rho_{tot} \propto a^{-3(1+\omega)}, \tag{1.19}$$

where ω is the equation of state parameter ($\omega = \frac{p_{tot}}{\rho_{tot}}$). Note that this equation can also be derived by assuming an adiabatic and homogeneous expanding Universe and applying the first law of thermodynamics. From Equation 1.19 the a dependencies of the density parameters in Equation 1.14 can be obtained. For radiation ω=1/3, for matter ω=0, for Λ $\omega = -1$ and for k $\omega = -1/3$. Therefore the density components vary with the scale factor as:

$$\text{radiation} : \rho_{\mathrm{R}} \propto \mathrm{a}^{-4}, \tag{1.20}$$

$$\text{matter} : \rho_{\mathrm{M}} \propto \mathrm{a}^{-3}, \tag{1.21}$$

$$\text{dark energy} : \rho_{\Lambda} \propto \mathrm{a}^{0}, \tag{1.22}$$

$$\text{curvature} : \rho_{\mathrm{k}} \propto \mathrm{a}^{-2}. \tag{1.23}$$

The cosmological constant was originally introduced to explain a static Universe, although it is unable to do so. It is now used to explain the observed acceleration in the expansion of the Universe. This acceleration was originally discovered by comparing the measured redshifts of type Ia supernovae to their

measured luminosity distances. The supernovae have a consistent peak luminosity and such observations reveal the variation in the scale factor as a function of redshift. The redshift is determined from supernovae emission/absorption lines from

$$1 + z = \frac{\lambda_{obs}}{\lambda_{em}} = \frac{a(t_{obs})}{a(t_{em})}, \tag{1.24}$$

where λ_{em} is the wavelength of emitted light, λ_{obs} is the wavelength of observed light, $a(t_{em})$ and $a(t_{obs})$ are the scale factors at the redshift of the emitting object and the observer respectively. For a flat Universe luminosity distance, d_L, is given by

$$d_L = \frac{c(1+z)}{H_0} \int_0^z \frac{dz}{\sqrt{\Omega_M (1+z)^3 + \Omega_\Lambda}}, \tag{1.25}$$

and plotted in Figure 1.8. Because the type Ia supernovae are standard candles their d_L can also be determined from their apparent magnitude. If both d_L and z are known then the values of Ω_M and Ω_Λ can be constrained. The first measurements of Ω_Λ were presented in Riess *et al.* (1998).

The latest Cosmic Microwave Background (CMB) observations have shown that the Universe is flat ($k = 0$) to within 1% (Larson *et al.* 2011) with contributions from Ω_M, Ω_R and Ω_Λ. The Ω_M component can be split into weakly interacting cold dark matter (Ω_c) of which the exact form is presently unknown, and baryonic matter (Ω_b). Estimated density parameters for the current epoch are given in Table 1.1 and an image showing the evolution of these density parameters is presented in Figure 1.3. This description of the Universe is known as the flat ΛCDM Universe.

Table 1.1: Cosmological density parameters taken from Larson *et al.* (2011).

Parameter	Value
Ω_b	0.0449±0.0028
Ω_c	0.222±0.026
Ω_M	0.266±0.029 ($\Omega_b + \Omega_c$)
Ω_Λ	0.734±0.029
Ω_R	6×10^{-5}

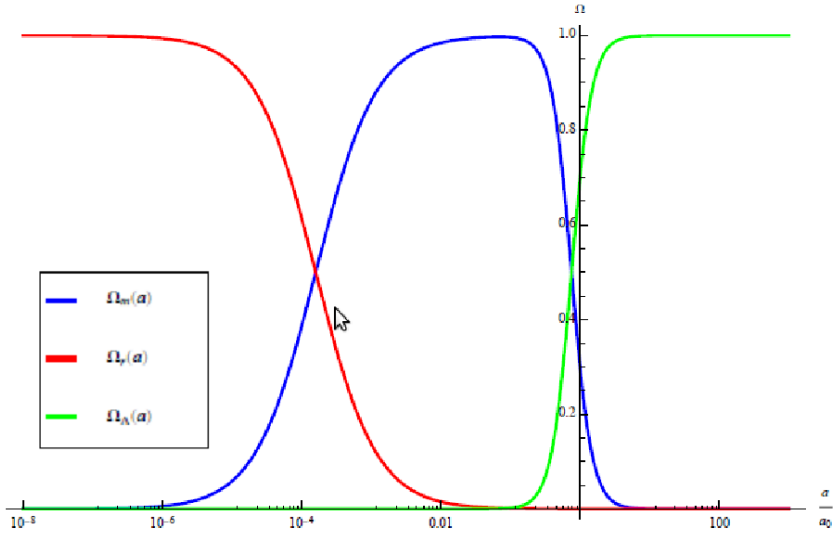

Figure 1.3: The evolution of the density parameters with scale factor for a flat Universe. The present values $\left(\frac{a}{a_0} = 1\right)$ are given in Table 1.1.

1.1.1 The Cosmic Microwave Background

An almost uniform background of radiation in all directions was discovered by Penzias & Wilson (1965). This background is now known as the CMB and is well explained in the Big Bang theory of the Universe.

As the Universe expanded after the Big Bang, its content cooled sufficiently so that the formation of hydrogen and helium atoms was no longer prohibited. At this point the Universe became transparent rather than opaque because the Thomson scattering of the huge excess of photons by ions ceased. This phase transition, known as recombination or the surface of last scattering, occurred at $z = 1,100$ with a thickness of $\Delta z \approx 80$ and at a temperature of $\approx 3,000$K. Before recombination the baryon-photon coupling kept the plasma in thermal equilibrium and as a result the CMB photons have a characteristic blackbody spectrum. Once recombination was complete the photons have since travelled through the Universe almost undisturbed. As they have travelled they have cooled and redshifted as a result of the expansion of the Universe; the temperature of the CMB is now $T_{CMB} = 2.71$K and the CMB spectrum peaks at 160 GHz.

We know from the existence of planets, stars, galaxies and clusters that the Universe cannot have been completely uniform at the time of recombination (or indeed far earlier). Hence, after the discovery of the CMB many experiments have focused on detecting and characterising the predicted anisotropies. Temperature fluctuations in the CMB were first discovered by the Cosmic Background Explorer (COBE) satellite (Smoot *et al.* 1992); the maximum amplitude of these spatial fluctuations is $\Delta T/T \approx 10^{-5}$. Since COBE, many ground-based and balloon-borne instruments have studied the temperature fluctuations in greater detail. Notably, a second generation satellite, the Wilkinson Microwave Anisotropy Probe (WMAP), was launched in 2001 and a third generation satellite, Planck, was launched in 2009.

Presently the most detailed all-sky CMB map has been produced from the WMAP 7-year data (Larson *et al.* 2011). However, the Planck satellite is currently performing an all-sky scan with improved resolution and $10\times$ higher sensitivity; Planck will continue to gather data until at least the end of 2011. The WMAP resolution is low and the satellite only obtains excellent constraints on the large angular features in the CMB. The ground-based South Pole Telescope (SPT) has made measurements of the anisotropies with a much higher angular resolution (Keisler *et al.* 2011). The WMAP image of the CMB and the combined WMAP and SPT power spectrum are shown in Figure 1.4.

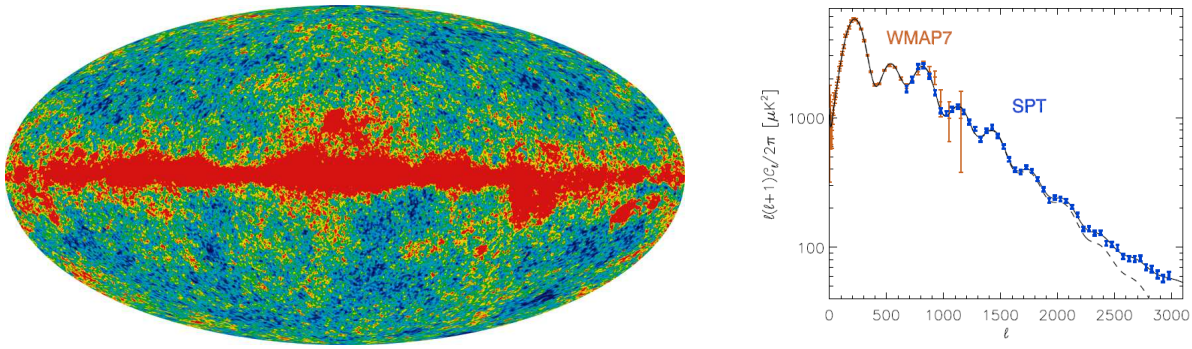

Figure 1.4: Left: The WMAP 7-year data release q-band (41 GHz) all-sky map before galaxy subtraction. The colour scale is from blue (-200μK) to red (200μK) (WMAP Science Team). Right: The corresponding WMAP 7-year power spectrum (Larson *et al.* 2011) together with the higher resolution SPT power spectrum (Keisler *et al.* 2011). l of 1000 corresponds to an angular scale of ≈ 0.2 deg. The best fit ΛCDM model is shown with the dashed line; the solid line shows the best fit ΛCDM+foregrounds.

The anisotropies that are observed in the CMB can be split into two types: primary anisotropies that occur either before or at the surface of last scattering, and secondary anisotropies that have developed since the surface of last scattering. Main causes of primary anisotropies are: gravitational redshifting of the photons as they climb out of potential wells (the non-integrated Sachs-Wolfe effect); temperature fluctuations caused by the interplay between pressure and gravity in the photon-baryon plasma (acoustic perturbations), and the Doppler shift of photons due to the photons' peculiar bulk velocities. Secondary anisotropies can be induced by: gravitational redshifting of the photons as they climb out of evolving potential wells after the surface of last scattering (the integrated Sachs-Wolfe effect and the Rees-Sciama effect); gravitational lensing of the CMB and the scattering of CMB photons off hot plasma in galaxy clusters (the kinetic Sunyaev-Zel'dovich effect and the thermal Sunyaev-Zel'dovich effect).

The peaks in the CMB power spectrum (Figure 1.4) are due to acoustic perturbations. The amplitude of the CMB begins to fall off at about l of 1000 due to a combination of silk dampening and incoherent addition. Silk damping (Silk 1968) is caused by photon diffusion during recombination and dramatically reduces the

amplitude of small scale photon perturbations. Incoherent addition arises due to the finite thickness ($\Delta z \approx 80$) of recombination; for small scale peaks we would expect cancellation effects due the existence of many such oscillations along the line of sight.

1.1.2 Structure Formation

The full relativistic derivation for the evolution of structure formation is presented in detail in e.g. Liddle (2003). A perturbation is added to the FRW metric and to the energy-momentum tensor, and the evolution of this perturbation is calculated. The evolution of the density perturbations with conformal time η (where $ad\eta = dt$) produces simple solutions when the Universe is matter-dominated, radiation-dominated or Λ-dominated (see Figure 1.3). The solutions are found to depend upon the size of the perturbation – in the radiation era the sub-horizon perturbations evolve differently to super-horizon perturbations. The sound horizon is the speed of sound multiplied by the age of the Universe, the sound horizon is used here because the sound speed is the rate at which pressure can be transmitted. Sub-horizon perturbations are entirely enclosed within a horizon, super-horizon fluctuations are not. The equations describing the evolution of the density perturbations are given in Table 1.2.

Table 1.2: Evolution of density perturbations with conformal time in the matter, radiation and Λ dominated eras.

	Super-horizon	Sub-horizon
Radiation era	$\delta_m \propto \eta^2$	$\delta_m \propto 1$
Matter era	$\delta_m \propto \eta^2$	$\delta_m \propto \eta^2$
Λ era	1	1

As the Universe evolves the size of the horizon increases and larger length-scale perturbations enter the horizon. In Figure 1.5 the evolution of two different sized perturbations through the matter, radiation and Λ dominated eras is shown.

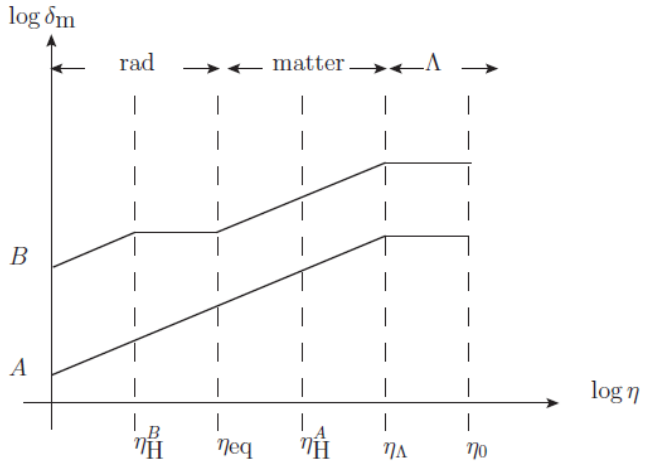

Figure 1.5: The evolution of density perturbations A and B. Perturbation B is smaller in length-scale and enters the horizon at η_H^B. Perturbation A is larger in length-scale and enters the horizon at η_H^A. η_{eq} is the η of matter and radiation equality and η_Λ is the η when the Λ density begins to dominate.

Although the general evolution of a perturbation is described in Figure 1.5 it must also be considered that before the surface of last scattering the photons and baryons were tightly coupled. After perturbations enter the horizon the opposing gravitational and pressure forces cause an oscillation with a frequency that depends upon their length-scale size. At the time of recombination (when oscillation ceases) the phase of the perturbation depends upon the time since that perturbation entered the horizon (this is the cause of the acoustic peaks in Figure 1.4). It should be noted that even before the surface of last scattering the dark matter was not tightly coupled to photons. As a consequence the dark matter density perturbations did not oscillate but evolved as would be expected from matter (Figure 1.5).

The gravitational potentials of the overdense regions continue to grow until Λ domination. This hierarchical growth implies that the largest structures (clusters of galaxies) form last.

1.1.3 The Thermal Sunyaev-Zel'dovich Effect

The Sunyaev-Zel'dovich (SZ; Sunyaev & Zeldovich 1970, Sunyaev & Zeldovich 1972) effect is a secondary CMB anisotropy and occurs when CMB radiation interacts with the plasma in the potential well of clusters of galaxies (see Birkinshaw (1999) and Carlstrom *et al.* (2002) for reviews). There are two types of SZ effect, these are: the thermal SZ effect which is caused by the scattering of CMB photons in the hot plasma contained by the cluster's gravitational well, and the kinetic SZ effect caused by the bulk motion of the cluster plasma with respect to the Hubble flow. Here I focus on the thermal SZ effect which for typical clusters causes significantly larger secondary anisotropies in the CMB than the kinetic SZ effect (for ν not close to 220 GHz).

Observations of clusters indicate that they typically have a virial radius of 1-2 Mpc (within which the average density is greater than ≈200 times the critical density at the cluster redshift) and within this radius the total mass can occasionally exceed $10^{15} M_{\odot}$. The intracluster "gas" is a plasma with temperature typically 4-8 keV. The SZ effect is caused when a CMB photon passing through a cluster of galaxies interacts with an energetic intracluster electron and undergoes inverse Compton scattering. The isotropic CMB photons that scatter off intracluster electrons have altered directions and on average an increase in energy. Although the net direction change cancel out, the increase in energy is observable. Kompaneets (1957) demonstrated that first order scattering effects cancels, but to second order the energy gain of an electron is $\propto \frac{v^2}{c^2} \propto \frac{k_B T_e}{m_e c^2}$, where v is the electron velocity, k_B is the Boltzmann constant, T_e is the electron temperature and $m_e c^2$ is the electron rest mass energy. The fractional temperature change of the CMB due to the thermal SZ effect is

$$\frac{\Delta T_{SZ}}{T_{CMB}} = f(x) y = f(x) \int \frac{n_e k_B T_e}{m_e c^2} \sigma_T dl, \tag{1.26}$$

where y is the Compton y-parameter, n_e is the electron number density, σ_T is the Thomson cross section and the integral is over the line of sight through the cluster. The frequency dependence is contained within the f(x) term:

$$f(x) = \left(x \frac{e^x + 1}{e^x - 1} - 4 \right) (1 + \delta(x, T_e)) \,. \tag{1.27}$$

Here $x = \frac{h\nu}{K_B T_{CMB}}$ and $\delta(x, T_e)$ is a relativistic correction (see e.g. Challinor *et al.* 1997 and Itoh *et al.* 1998). In the Rayleigh-Jeans regime $f(x) = -2$ and Equation 1.26 reduces to

$$\frac{\Delta T_{SZ}}{T_{CMB}} \approx -2 \int \frac{n_e k_B T_e}{m_e c^2} \sigma_T dl. \tag{1.28}$$

This temperature change in the CMB blackbody radiation causes a shift in the CMB frequency spectrum. At frequencies less than 218GHz an intensity drop is observed while for higher frequencies an increment is observed. Figure 1.6 shows an exaggerated shift in the CMB intensity.

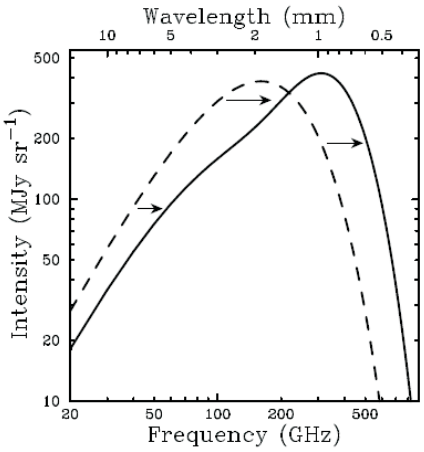

Figure 1.6: The dashed line shows the CMB thermal spectrum before any secondary distortions and the solid line shows the CMB spectrum after thermal SZ distortion, note the effect is exaggerated by a factor of 1000 for clarity. At frequencies less than 218 GHz the SZ effect decreases the CMB intensity. Figure taken from Carlstrom et al., (2002).

To determine the total SZ flux density from a cluster we integrate over its solid angle, Ω, on the sky:

$$\Delta S_{SZ} \approx -\frac{2T_{CMB}}{d_A^2} \int \frac{n_e k_B T_e}{m_e c^2} \sigma_T dl d\Omega. \tag{1.29}$$

The integrated SZ signal is thus dependent upon the integral along the line of sight of the density of electrons multiplied by their temperature,

$$\Delta S_{SZ} \propto -\frac{1}{d_A^2} \int n_e T_e dV, \tag{1.30}$$

i.e. the plasma thermal energy (e.g. Bartlett & Silk 1994). With the assumption that the cluster is virialized, isothermal, spherical and that all its kinetic energy is in plasma microscopic internal energy, $T_e \propto M^{2/3}$, where M is the cluster mass, and the integrated SZ effect is

$$\Delta S_{SZ} \propto -\frac{M^{5/3}}{d_A^2}. \tag{1.31}$$

Equation 1.31 implies that the SZ signal is an excellent measure of cluster mass. This relationship has support from galaxy cluster observations: in Figure 1.7 I show the Planck observed relationship between $d_A^2 Y_{SZ}$ and $M_{gas,500}$, where Y_{SZ} is the y-parameter integrated out to r_{500}.

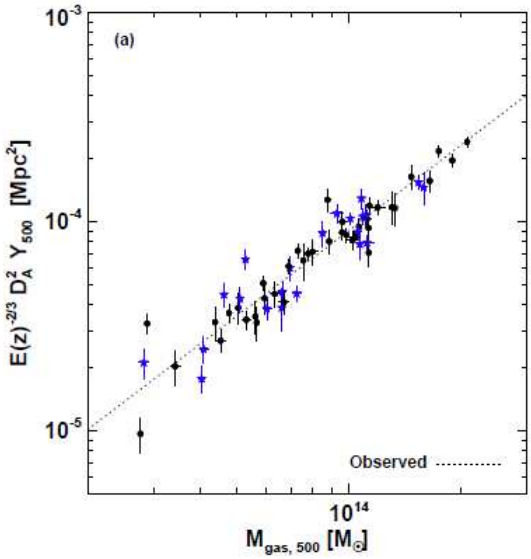

Figure 1.7: The $d_A^2 Y_{SZ}$ (within r_{500}) and $M_{g,500}$ relationship from Planck observations of 62 clusters that have been observed with XMM-Newton. The $d_A^2 Y_{SZ}$ was derived from Planck data and $M_{g,500}$ was derived from XMM measurements. Cool core systems are in blue and all other clusters are in black. The best fit relation is $E(z)^{-2/3} d_A^2 Y_{SZ} = 10^C \left(\frac{M_{g,500}}{1\times10^{14}}\right)^B$, where $C = 4.044 \pm 0.010$ and $B = 1.36 \pm 0.07$. The logarithmic intrinsic scatter is $\sigma_{log,i} = 0.092 \pm 0.011$. These results are taken from Planck Collaboration *et al.* (2011c)

Another important property of the SZ effect is the independence of its surface brightness on redshift. It may be expected that the SZ signal surface brightness

be dimmed with redshift like the CMB surface brightness ($(1+z)^4$), in fact, this dimming is exactly cancelled by the increasing temperature of the CMB with redshift, i.e. the ratio of the magnitude of the SZ to the CMB is redshift independent. However, the integrated SZ flux from a cluster does depend upon the angular size of the clusters via d_A^2. Although at high redshifts the angular diameter distance is relatively redshift independent (Figure 1.8).

A further property is that the SZ effect is not significantly affected by the dynamical history of clusters, this is demonstrated by Arnaud *et al.* (2010), whose results are presented in Figure 1.9.

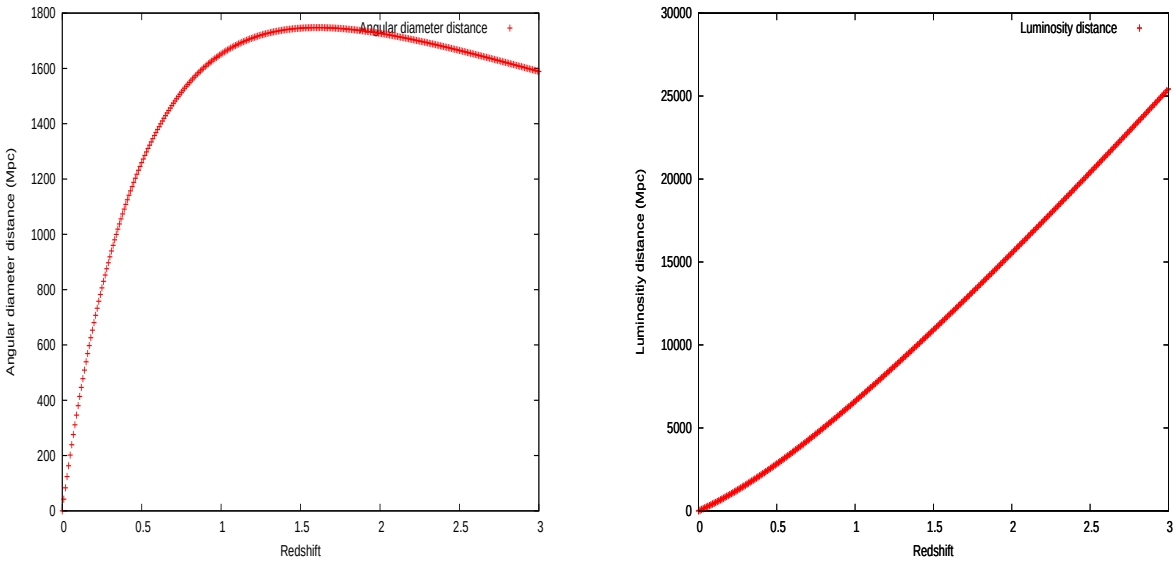

Figure 1.8: On the left is the angular diameter distance (d_A) as a function of redshift, on the right is a corresponding plot for the luminosity distance (d_L). d_A is given by $\frac{c}{H_0(1+z)}\int_0^z \frac{dz}{\sqrt{\Omega_M(1+z)^3+\Omega_\Lambda}}$ and for these plots I have used $\Omega_M = 0.3$, $\Omega_\Lambda = 0.7$ and $h_{70} = 1$. The luminosity distance is a factor of $(1+z)^2$ larger than the angular diameter distance. The angular diameter distance is the ratio of an objects physical size to its angular size, it does not increase indefinitely with redshift due to the expansion of the Universe.

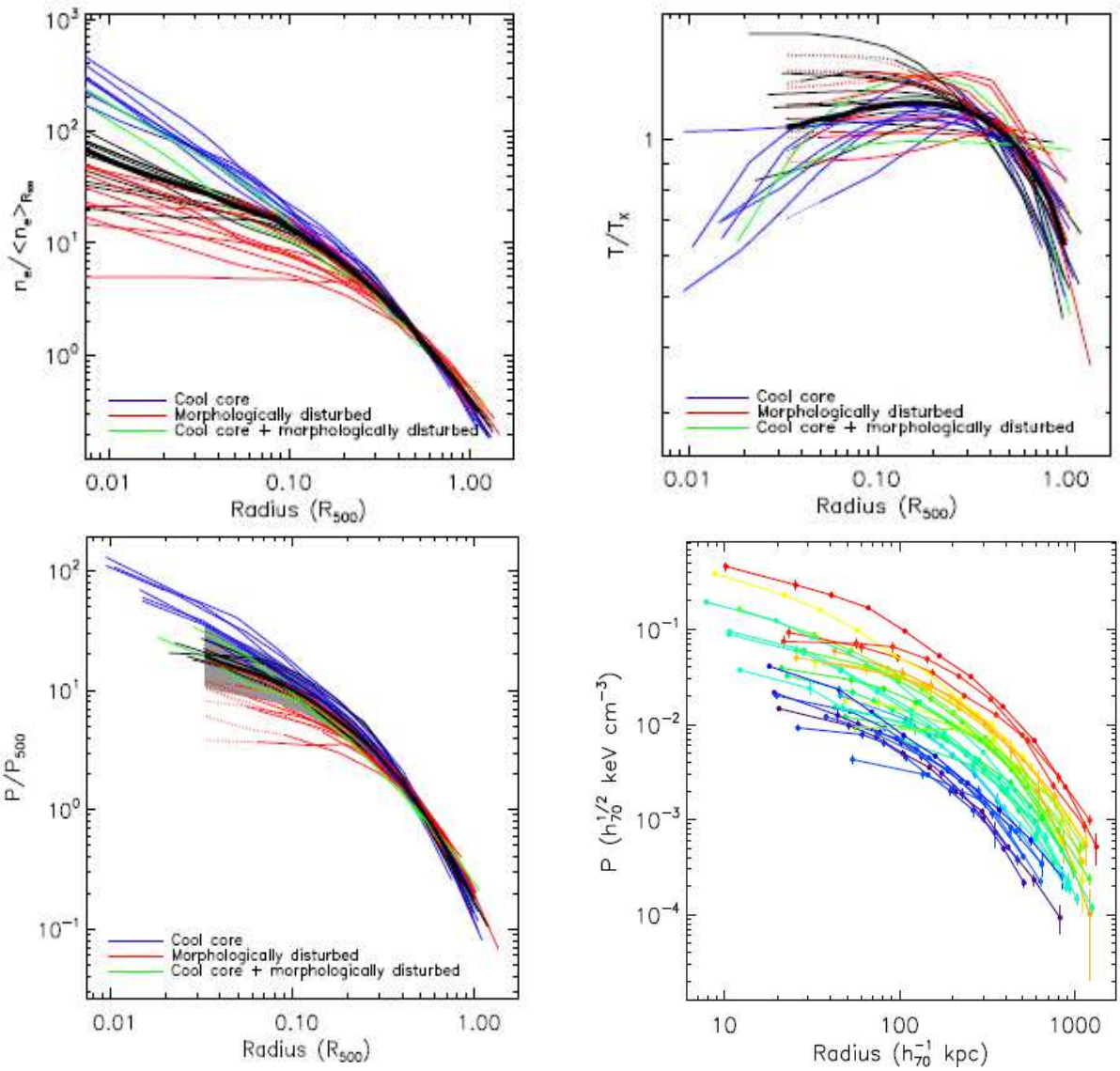

Figure 1.9: XMM Newton cluster profiles of electron density, temperature and pressure from 33 low-redshift ($z < 0.2$) clusters in the Representative XMM-Newton Cluster Structure Survey (REXCESS). The top left shows the n_e variation with radius and the top right shows T as a function of radius. There is an anti-correlation between n_e and T. On the bottom left plot the scaled pressure as a function of radius is shown (the SZ effect is the integrated pressure). The thick black line gives the average scaled profile and the grey area shows the 1σ dispersion. The bottom right plot shows the unscaled pressure profiles with error bars. Because of the anti-correlation between n_e and T the pressure profile is quite consistent between all the observed clusters. Plots are taken from Arnaud *et al.* (2010).

1.2 The Arcminute Microkelvin Imager

Sited at the Mullard Radio Astronomy Observatory, Cambridge, AMI consists of a pair of aperture synthesis interferometric arrays optimised for SZ-effect imaging over 14-18 GHz.

The Small Array (SA) has been operating since 2005, with a resolution to match the typical size of a galaxy cluster ($\sim 3'$) and is used to observe the SZ effect. The Large Array (LA) has been operating since 2008 with a high resolution ($\sim 30''$) and a sensitivity aimed at detecting radio sources that can contaminate our SZ observations.

The specifications of the arrays are summarised in Table 1.3, and AMI Consortium: Zwart *et al.* (2008) thoroughly describes the telescope. A schematic of the AMI LA hardware, which is almost identical for the two arrays, is shown in Figure 1.10. The geometric configurations of the arrays is shown in Figure 1.11.

Table 1.3: AMI technical summary. In practice on six of the eight frequency channels are used. This is due to severe interference in the two lowest frequency channels.

	SA	LA
Antenna diameter	3.7 m	12.8 m
Number of antennas	10	8
Number of baselines	45	28
Baseline length	5–20 m	18–110 m
16-GHz power primary beam FWHM	$19.6'$	$5.6'$
Synthesized beam FWHM	$\approx 3'$	$\approx 30''$
Flux-density sensitivity	$30\,\mathrm{mJy\,s^{-1/2}}$	$3\,\mathrm{mJy\,s^{-1/2}}$
Observing frequency	13.9–18.2 GHz	
Bandwidth	6.0 GHz	
Number of channels	8	
Channel bandwidth	0.72 GHz	
Polarization measured	I + Q	

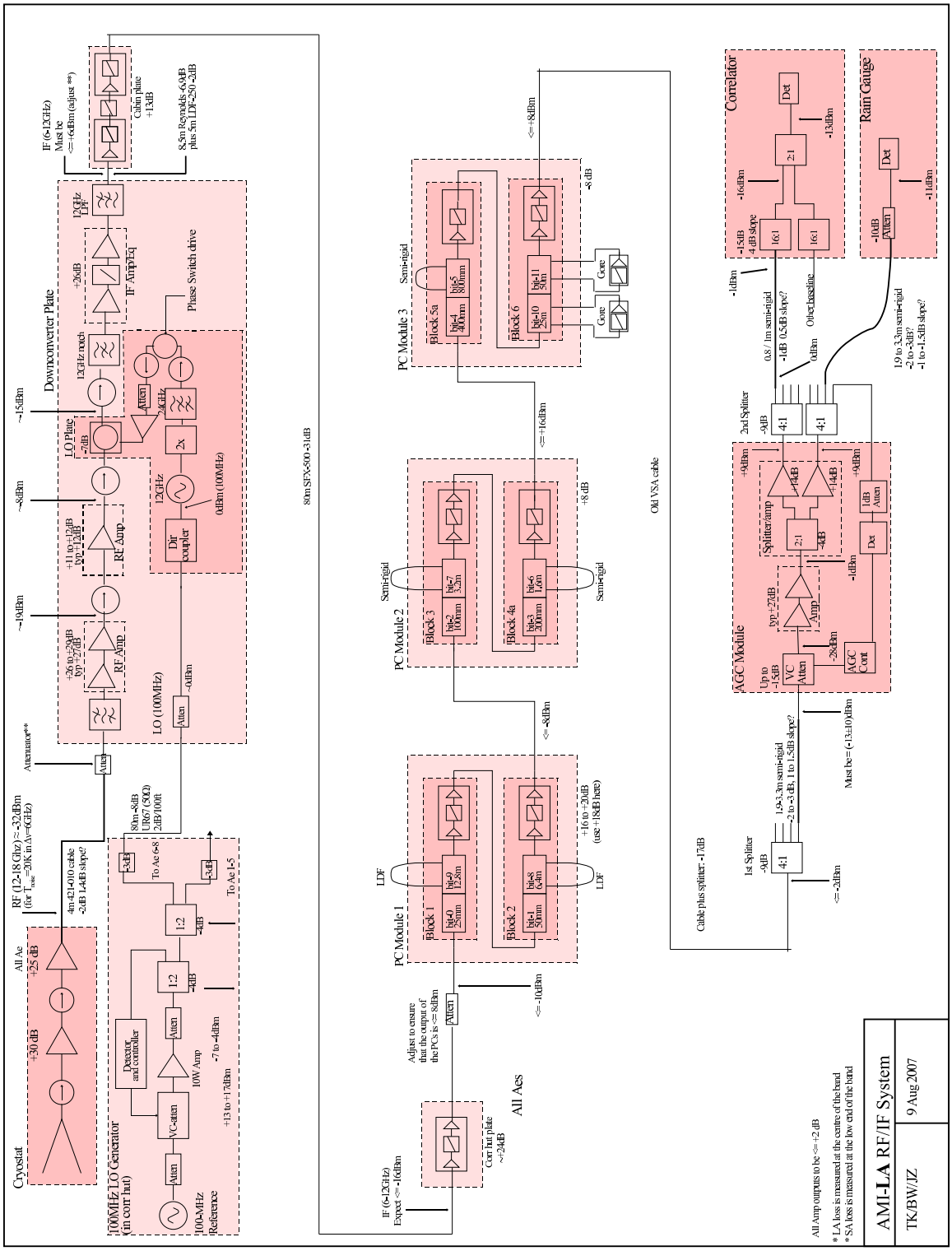

Figure 1.10: The Large Array RF-IF system. Thanks to Tak Kaneko, Brian Wood and Jonathan Zwart.

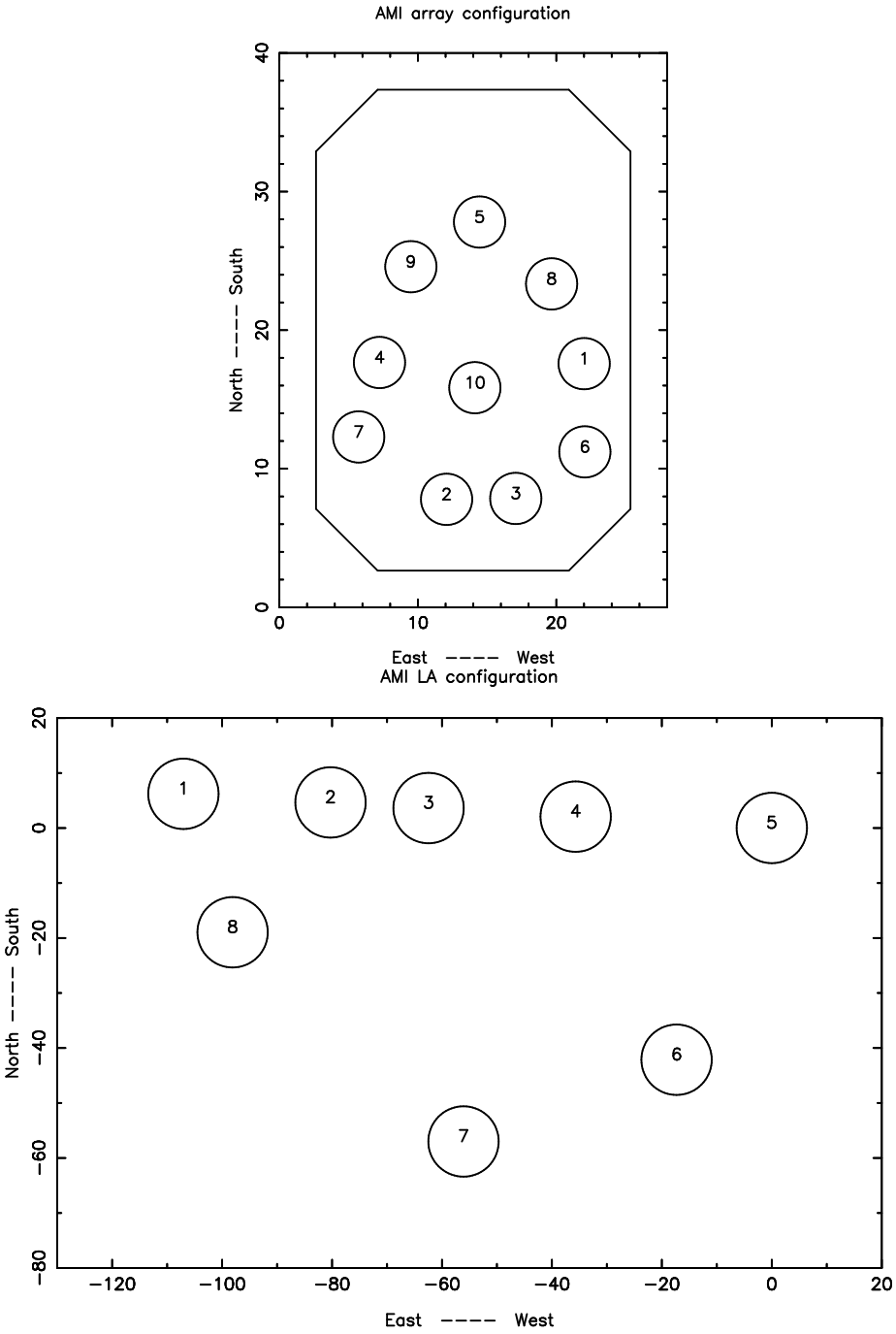

Figure 1.11: Top: The configuration of the SA antennas. Bottom: The configuration of the LA antennas.

1.2.1 Radio Interferometry with AMI

Imagine two aerials (Ae1 and Ae2), separated by a distance D and pointing towards an astronomical point source in the far field (Figure 1.12). Each aerial receives electromagnetic waves from the point source, and brings the wave front to a focus at which

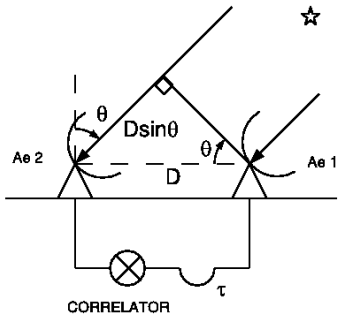

Figure 1.12: Two antennas separated by a distance D pointing towards a source in the far field; their separation in the x (east-west) direction.

$$\left(\nabla^2 - \frac{1}{c^2}\frac{\delta^2}{\delta t^2}\right) E = 0, \tag{1.32}$$

where ∇^2 is the Laplace operator in space, c is the speed of light, t is time and E is electric field and so the received wave can be described by

$$E(x,t) = E_0 e^{i(k_{RF}x - \omega_{RF}t)}, \tag{1.33}$$

where RF denotes radio (incident) frequency, $k_{RF} = \frac{2\pi}{\lambda_{RF}}$ is the wave number of the incoming radiation, E_0 is the amplitude and ω_{RF} is the angular frequency. The wave from Ae2 travels a distance $Dsin\theta$ further. The signals received by Ae1 and Ae2 are given at time t by

$$E_1(x_1,t) = E_1 e^{-i(\omega_{RF}t)} e^{i(k_{RF}x_1)}, \tag{1.34}$$

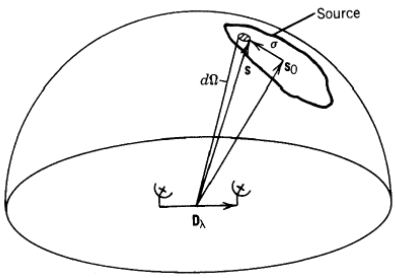

Figure 1.13: Two antennas separated by a distance D_λ both pointing towards a source in the far field.

$$E_2(x_2,t) = E_2 e^{-i(\omega_{RF}t)} e^{i(k_{RF}(x_1+Dsin\theta))}. \tag{1.35}$$

An interferometer measures the correlation between the two signals received by the antennas using a correlator. The response, r(x,t), of the correlator is

$$r(x,t) =< E_1(x_1,t)E_2^*(x_2,t) > . \tag{1.36}$$

This response is independent of the distance from the source to the antennas and instead depends upon the separation of the antennas (D) and the position of the source in the sky (θ), i.e. as

$$r(D,\theta) = E_1 E_2^* e^{-i(k_{RF}Dsin\theta)}. \tag{1.37}$$

By defining $\underline{s_0}$ as a vector that connects the baseline to the source and $\underline{D_\lambda}$ as the separation of the antennas in λ (Figure 1.13), we can derive

$$r(D_\lambda, s_0) = E_1 E_2^* e^{-i(2\pi(\underline{D_\lambda}\cdot\underline{s_0}))}. \tag{1.38}$$

This can be generalised for sources offset from $\underline{s_0}$ by $\underline{\sigma}$ to

$$r(D_\lambda, s_0) = E_1 E_2^* e^{-i(2\pi(\underline{D_\lambda})\cdot(\underline{s_0}+\underline{\sigma})))}. \tag{1.39}$$

E_1 and E_2^* are the amplitudes of the electromagnetic waves and are dependent upon both the brightness of the source, $B(\sigma)$, and the antenna response attenuation, which is also known as the power primary beam, $A_P(\sigma)$. To obtain the total

instantaneous response of the interferometer to a single frequency we integrate Equation 1.39 over the whole sky, giving

$$r(D_\lambda, s) = \int_{4\pi} B(\sigma) A_P(\sigma) e^{-i(2\pi(\underline{D_\lambda})\cdot(\underline{s_0}+\underline{\sigma}))} d\sigma. \tag{1.40}$$

Equation 1.40 describes the basic response of a single frequency interferometer. But AMI has a 6GHz passband and its response is integrated over frequency. If we assume that AMI has a perfectly rectangular passband centred on ν_{RF} with a bandwidth $\Delta\nu$, then the response of AMI is

$$r(D_\lambda, s) = \int_{4\pi} \int_{\nu_{RF}-\Delta\nu/2}^{\nu_{RF}+\Delta\nu/2} B(\sigma) A_P(\sigma) e^{-i(2\pi(\underline{D_\lambda})\cdot(\underline{s_0}+\underline{\sigma}))} d\nu d\sigma. \tag{1.41}$$

Defining the geometric delay τ_g as $\tau_g = \frac{D\cdot(s_0+\sigma)}{c}$ and recalling that $\lambda_{RF} = \frac{c}{\nu_{RF}}$, the AMI response simplifies to

$$r(D_\lambda, s_0) = \int_{4\pi} \int_{\nu_{RF}-\Delta\nu/2}^{\nu_{RF}+\Delta\nu/2} B(\sigma) A_P(\sigma) e^{-i(2\pi\tau_g\nu)} d\nu d\sigma. \tag{1.42}$$

When integrated over frequency, this gives

$$r(D_\lambda, s_0) = \int_{4\pi} \frac{B(\sigma)A_P(\sigma)}{2\pi\tau_g} e^{-i(2\pi\nu_{RF}\tau_g)} (e^{-i(2\pi\frac{\Delta\nu}{2}\tau_g)} - e^{i(2\pi\frac{\Delta\nu}{2}\tau_g)}) d\sigma. \tag{1.43}$$

Using $e^{i\theta} = cos\theta + isin\theta$ gives

$$r(D_\lambda, s_0) = \int_{4\pi} B(\sigma) A_P(\sigma) \frac{sin\pi\Delta\nu\tau_g}{\pi\Delta\nu\tau_g} e^{-i(2\pi\nu_{RF}\tau_g)} d\sigma. \tag{1.44}$$

The sinc function in Equation 1.44 has the characteristic that when $\pi\Delta\nu\tau_g$ is large the response is small. However, it is desirable that $\Delta\nu$ is large so that the telescope's sensitivity is maximised. To solve this apparent contradiction and ensure that the response does not become too small when τ_g is non zero, we insert an artificial delay, the path compensation, τ_i, into the path of the antenna with the shorter path. This delay is inserted into the telescope at an intermediate frequency ν_{IF}, which is related to the radio frequency by $\nu_{RF} = \nu_{LO} + \nu_{IF}$, where $\nu_{LO} = 24GHz$ is the frequency of the local oscillator (Figure 1.10). Note that ν_{RF} and ν_{IF} have a bandwidth whereas ν_{LO} is a single value and that ν_{IF} is negative (implying that the wave travels in the opposite direction). The delay is inserted

at an intermediate frequency because the electronics are cheaper and work better at lower frequencies. Also, if the path compensation were to be inserted into the RF then the astronomical fringe rate would be removed, this would make it harder to apply fringe rate filtering to reject interference from e.g. geostationary satellites. It is appropriate to insert this extra delay into Equation 1.42, hence the response of the telescope is

$$r(D_\lambda, s_0) = \int_{4\pi} \int_{\nu_{RF}-\Delta\nu/2}^{\nu_{RF}+\Delta\nu/2} B(\sigma) A_P(\sigma) e^{-i2\pi(\tau_g \nu - \tau_i \nu_{IF})} d\nu d\sigma, \tag{1.45}$$

which is equal to

$$r(D_\lambda, s_0) = \int_{4\pi} \int_{\nu_{RF}-\Delta\nu/2}^{\nu_{RF}+\Delta\nu/2} B(\sigma) A_P(\sigma) e^{-i2\pi\nu(\tau_g-\tau_i)} e^{-i2\pi(\tau_i \nu_{LO})} d\nu d\sigma \tag{1.46}$$

and integrates to

$$r(D_\lambda, s_0) = \int_{4\pi} B(\sigma) A_P(\sigma) \frac{sin\pi\Delta\nu(\tau_g - \tau_i)}{\pi\Delta\nu(\tau_g - \tau_i)} e^{-i(2\pi(\nu_{RF}(\tau_g-\tau_i)+\tau_i\nu_{LO})} d\sigma. \tag{1.47}$$

The AMI correlator does not measure all of this signal. It uses a "real" correlator, implying that it only measures the real part of $r(D_\lambda, s_0)$; the imaginary parts are measured later by a process that is described later in this section. Hence the actual response from the AMI correlator is

$$r(D_\lambda, s_0) = \int_{4\pi} B(\sigma) A_P(\sigma) \frac{sin\pi\Delta\nu(\tau_g - \tau_i)}{\pi\Delta\nu(\tau_g - \tau_i)} cos(2\pi(\nu_{RF}(\tau_g - \tau_i) + \tau_i \nu_{LO})) d\sigma. \tag{1.48}$$

As the Earth rotates, θ changes, as does τ_g; to compensate for the changes in τ_g we switch cables of different electronic lengths in and out of the system to alter τ_i. By altering τ_i (our smallest path compensation is 25mm) we can try to keep $\tau_g = \tau_i$ for sources at the phase centre; this ensures that the telescope's response to these sources is maximum.

AMI has a non-zero beam size and it is also important to consider the response to sources away from the pointing centre. If $\tau_g = \tau_i$ at the pointing centre, then for a source offset from the phase centre by $\tau_g - \tau_i = \Delta\tau_g$, the larger the value of $\Delta\nu\Delta\tau_g$ the lower the response, and to keep the response for these sources high it is essential that $\Delta\nu\Delta\tau_g << 1$. The maximum extra geometric delay from the source at the edge of the field is

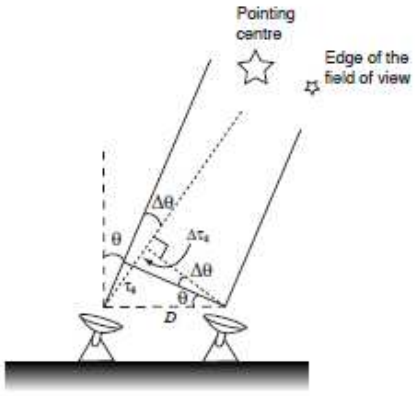

Figure 1.14: Two antennas separated by a distance D_λ pointing towards a source in the far field. There is a another source an angle $\Delta\theta$ from the pointing centre, this is at the edge of the field of view and introduces an extra geometric time delay $\Delta\tau_g$.

$$\Delta\tau_g = (D/c)cos\theta sin\Delta\theta < D\Delta\theta/c, \tag{1.49}$$

where we have used the approximation $sin\Delta\theta \approx \Delta\theta$. The field of view of the antennas in radians is $\Delta\theta \approx \lambda_{RF}/d$, where d is the antenna diameter. Hence, for a source at the edge of the field $\Delta\tau_g = \frac{\lambda_{RF}D}{cd} = \frac{D}{\nu_{RF}d}$. Both arrays operate at $\nu_{RF} \approx 15$GHz and we can calculate that for the LA (d = 13m and D = 110m) $\Delta\tau_g << 7.2 \times 10^{-10}s$ which corresponds to 216mm; we obtain a similar result for the SA (d = 3.7m and D = 20m). It must be borne in mind that this calculation has been performed for the longest baseline and it should be noted that for most AMI SA and LA baselines this value will be significantly less. However, this does indicate that for a source right at the edge of our field of view, $\tau_g \neq \tau_i$.

Recalling that we require $\Delta\nu\Delta\tau_g << 1$, we find that

$$\Delta\nu << \frac{\nu_{RF}d}{D}. \tag{1.50}$$

This implies that for the LA, $\Delta\nu << 1.8GHz$, whilst for the SA, $\Delta\nu << 2.8GHz$. Unless you have an bandwidth smaller than these limits the data will suffer from chromatic aberration. In order to have a bandwidth greater than this, whilst

also making the most of our field of view, a lag correlator measuring the response at different time delays, or lags, is used to correlate the signals on AMI. The correlator on both the AMI SA and LA has 16 lags from -200mm to +175mm with a nominal step of 25mm – this additional path will be referred to as τ_{ic}. A lag correlator can be used to calculate the frequency spectrum (S(ν)) from a response recorded at lags (R(τ_{ic})) by

$$S(\nu) = \int_{-\infty}^{\infty} R(\tau_{ic}) e^{-i2\pi\nu\tau} d\tau. \tag{1.51}$$

If we consider the simple case of a bright source in the phase centre of the telescope with $\tau_g = 0$ or $\tau_g - \tau_i = 0$, then τ_{ic} varies as the signal is correlated with different instrumental lags in the correlator. If the bright point source is the only significant signal in the telescope's field of view then we can disregard the integral over the whole sky and substitute Equation 1.48 into Equation 1.51 to find

$$S(\nu) = \int_{-\infty}^{\infty} B(\sigma) A_P(\sigma) \frac{sin\pi\Delta\nu\tau_{ic}}{\pi\Delta\nu\tau_{ic}} cos(2\pi\tau_{ic}\nu_{IF}) e^{-i2\pi\nu\tau_{ic}} d\tau_{ic}. \tag{1.52}$$

This Fourier transform can be solved using the modulation theorem (see e.g. Bracewell 2000). This states that if $f(\tau)$ has the Fourier transform $F(\nu)$, then $f(\tau)cos(\omega\tau)$ has the Fourier transform $\frac{1}{2}F(\nu - \frac{\omega}{2\pi}) + \frac{1}{2}F(\nu + \frac{\omega}{2\pi})$. The function that we have in Equation 1.52 is a cosine modulated by a sinc. Therefore, as the Fourier transform of a sinc is a top-hat function, the resulting Fourier transform of Equation 1.52 has a real component of two top-hat functions and the imaginary component is zero. Hence, all the spectral information is contained within the sinc and not the cosine. It is important that the sinc function is Nyquist-sampled, so the minimum lag spacing is given by $\delta\tau_{ic} = \frac{1}{2\Delta\nu}$. AMI has $\Delta\nu = 6\,\mathrm{GHz}$ and a corresponding $\delta\tau_{ic} = 25$mm. In Figure 1.15 the AMI response is plotted along with its Fourier transform.

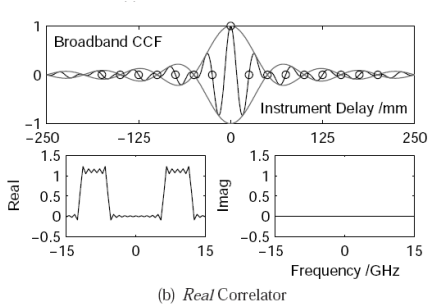

Figure 1.15: The response of a lag correlator to a point source at the phase centre (where $\tau_g = 0$) is a cosine modulated by a sinc function. This response is sampled by the 16 lags of the AMI correlator; lag 8 is the central lag and samples at delay space 0, lags are separated by 25mm, and so the outer lags sample at 200mm. The top Figure shows the response across the lags, whilst the bottom Figure illustrates the Fourier transform of this response in the frequency domain. Figure taken from Holler *et al.* (2007b).

Numerical integration of Equation 1.52 is in practice challenging because AMI has non-equally spaced lags and we have to deal with unknown lag errors. Note that the Discreet Fourier Transform (DFT) allows for non equally spaced lags, although, in the present version of our data reduction software, REDUCE, we assume all lags are equally spaced and apply a Fast Fourier Transform (FFT) which we find produces the same result as a DFT but is faster. For a DFT the frequency response of channel $S(\nu_k)$ (for channels k=0, ..., N-1) is

$$S(\nu_k) = \frac{1}{N} \sum_{\tau_{ic}=0}^{N-1} R(\tau_{ic}) e^{-\frac{i2\pi\nu_k\tau_{ic}}{N}}, \tag{1.53}$$

where

$$R(\tau_{ic}) = \frac{1}{T} \int_0^T A(t)B(t+\tau_{ic})dt. \tag{1.54}$$

A(t) and B(t) are the signals received by the antennas at a time t, T is the integration time and N is the number of lags. Defining τ_0 as the time taken for

light to travel 25mm ($\frac{1}{12*10^9}$ seconds). The DFT can be expanded to give

$$\begin{aligned} S(\nu_k) &= \frac{1}{16}(R(\tau_0) + R(\tau_1)e^{-\frac{i2\pi\nu_k\tau_0}{16}} + R(\tau_2)e^{-\frac{i4\pi\nu_k\tau_0}{16}} + ... \\ &\quad +R(\tau_{14})e^{-\frac{i28\pi\nu_k\tau_0}{16}} + R(\tau_{15})e^{-\frac{i30\pi\nu_k\tau_0}{16}}) \end{aligned}$$

Because $R(\tau_{ic})$ is real, this DFT is symmetric according to $S(\nu_k) = S(\nu_{N-k})^*$. From the 16 independent measurements of the cross-correlation function we therefore obtain 8 complex frequency channels.

When the signals $A(t)$ and $B(t)$ enter Ae1 and Ae2, we obtain $A(t)B(t)$ by multiplying the signal from Ae1 and Ae2 with the Walsh functions $f(t)$ and $g(t)$ respectively. Walsh functions have the following properties: they are either +1 or -1; over some period they integrate to zero; the multiple of two different Walsh functions is a new Walsh function and the square of a Walsh function is equal to 1. The output from the AMI add and square correlator is multiplied by fg and integrated to give

$$\int fg(fA + gB)^2 dt = \int fg(fA)^2 + 2(fg)^2 AB + fg(gB)^2 dt \propto AB. \qquad (1.55)$$

In the AMI system we have + and - correlator boards for each baseline. Whilst one of these correlators is measuring the $(A + B)^2$ signal the other measures the $(A - B)^2$ signal. Having two independent measures of the signal increases the sensitivity by $\sqrt{2}$. Walsh functions are also very useful as they allow us to reject signals which occur within the phase-switch loop but on just a single antenna, such as cross talk (see e.g. Kaneko 2005).

A final essential component of interferometry is the spatial frequency to which the interferometric arrays are sensitive to. The coordinate transform between (u, v, w) and the fixed position of the AMI antennas (X, Y, Z) is

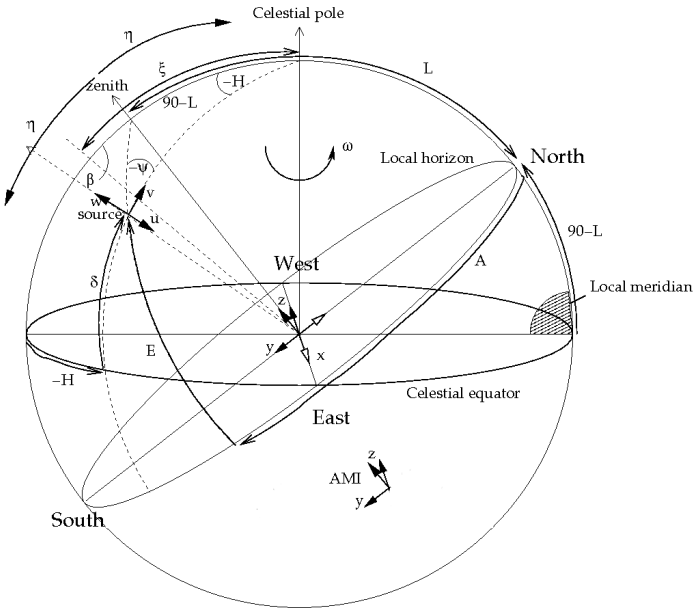

Figure 1.16: The relationship between different coordinate systems of AMI, courtesy of John Zwart.

$$\begin{pmatrix} u \\ v \\ w \end{pmatrix} = \begin{pmatrix} -\cos H & \sin H \sin L & \sin H \cos L \\ -\sin\delta \sin H & -\sin\delta \cos H \sin L - \cos\delta \cos L & -\sin\delta \cos H \cos L + \cos\delta \sin L \\ \cos\delta \sin H & \cos\delta \cos H \sin L - \sin\delta \cos L & \cos\delta \cos H \cos L + \sin\delta \sin L \end{pmatrix} \begin{pmatrix} X_\lambda \\ Y_\lambda \\ Z_\lambda \end{pmatrix} \tag{1.56}$$

where L is the latitude of the telescope, H is the hour angle of the source and δ is the source declination. A visual representation the (u, v, w) and (X, Y, Z) coordinate systems is shown in Figure 1.16.

When we observe an object we only sample specific angular spatial frequencies; these are set by the u and v coordinates of our antennas which describe the projected baseline vector perpendicular to the source. An example of the SA and LA u, v coverage is shown in Figure 1.17.

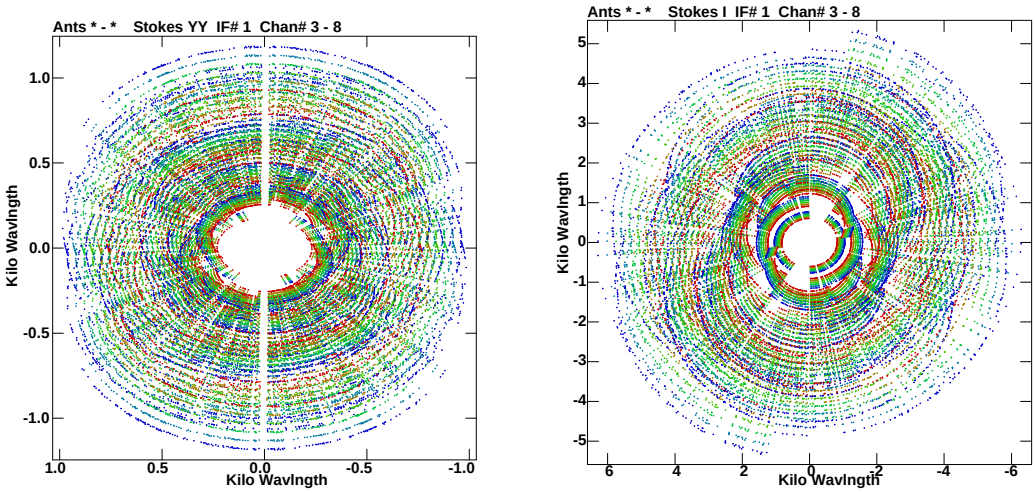

Figure 1.17: On the left is the typical SA uv coverage whilst on the right is the typical LA uv coverage. Both observations are at declination +34, the duration of the SA observation is 40 hours and the LA observation consists of 17 hours of data.

To form an image of the sky we first consider the frequency response of AMI. Given that the time sample function is described by $C(u,v)$ (the LA samples every 1/2 second and the SA samples every second) then the frequency response of a uv baseline is derived from Equation 1.52 to give:

$$S(u,v) = \int_{4\pi}\int_{-\infty}^{\infty} B(\sigma)A_P(\sigma)C(u,v)\frac{sin\pi\Delta\nu\Delta\tau_g}{\pi\Delta\nu\Delta\tau_g}cos(2\pi(\nu_0\Delta\tau_g+(\tau_i+\tau_{ic})\nu_{LO}))e^{-i2\pi\nu\tau_{ic}}d\sigma d\tau_{ic}, \tag{1.57}$$

where $\Delta\tau_g = \tau_g - (\tau_i + \tau_{ic})$. This can be inverse Fourier transformed to find the sky brightness:

$$B(\sigma)A_P(\sigma) = \int_{4\pi}\int_{-\infty}^{\infty} S(u,v)C(u,v)\frac{sin\pi\Delta\nu\Delta\tau_g}{\pi\Delta\nu\Delta\tau_g}cos(2\pi(\nu_0\Delta\tau_g+(\tau_i+\tau_{ic})\nu_{LO}))e^{i2\pi\nu\tau_{ic}}d\sigma d\tau_{ic}. \tag{1.58}$$

Note that this sky brightness is known as the dirty image. To find the true image we must remove the sampling function, $C(u,v,)$; this operation can be done with deconvolution because 1.58 is the convolution of the true sky brightness with

$$\int_{-\infty}^{\infty} C(u,v)e^{i2\pi\nu\tau_{ic}}d\sigma d\tau_{ic}. \tag{1.59}$$

This Fourier transform of the sampling function is known as the synthesized beam.

1.3 Blind SZ Effect Surveys

1.3.1 AMI

AMI is conducting a blind cluster survey at 16GHz in 12 regions, each typically a deg^2. The AMI cluster survey focuses on depth, aiming to detect weak SZ effect signals from clusters of galaxies with a mass above $M_{200} = 3 \times 10^{14} M_{\odot} h_{70}^{-1}$, where $M_{200} h_{70}^{-1}$ corresponds to the cluster mass within a spherical volume such that the mean interior density is 200 times the mean density of the Universe at the cluster epoch, the radius of this volume is r_{200}. The first blind cluster detected in the AMI survey is presented in AMI Consortium: Shimwell *et al.* (2010) and discussed further in Section 5.

The AMI SA is designed to have a typical *uv* coverage to maximise the arrays sensitivity to arc minute angular scales, as this matches the angular size of typical galaxy clusters. With this resolution the SA resolves out the majority of the larger scale primordial CMB signal and atmospheric effects. The main contaminant of the SZ-effect at the range of frequencies which AMI operates within is the signal from radio point sources. To remove this contamination we make use of the higher resolution and flux-density sensitivity of the AMI LA. The LA resolution is high enough to resolve out almost all of the SZ signal but is of course just as suitable for observing radio point sources whose signal is independent of the angular scale sampled. By observing the same area with both arrays we use our knowledge of radio sources from the LA observations to help model the contamination they cause to our SA data. Once we have modelled the radio source contamination we can statistically account for the CMB and thermal noise contributions to our data and search for any SZ contribution.

1.3.2 South Pole Telescope

The South Pole Telescope (SPT) is a 10-metre telescope operating with a deg^2 field of view at an altitude of 2800m in the South Pole (Carlstrom *et al.* 2009).

The array operates at 95 GHz, 150 GHz and 220 GHz with beam full-widths at half-maxima (FWHM) of 1.6′, 1.1′ and 1.0′ respectively. The SZ signal is a decrement at 95 GHz and 150 GHz and close to the null at 220 GHz.

The SPT blind SZ survey plans to cover an area of 2500 deg^2 to a depth of 18μK-arcmin^2 at 150 GHz. The first 4 galaxy clusters detected (3 previously unknown) in the survey are detailed in Staniszewski *et al.* (2009) who report results from a preliminary study of 40 deg^2; these detections represented the first clusters discovered by an SZ survey. In Vanderlinde *et al.* (2010) 178 deg^2 were analysed and within this region 21 clusters were detected, 12 of which were new discoveries. In the latest results, Williamson *et al.* (2011) have analysed the entire 2500 deg^2, 1500 deg^2 of which have been surveyed to the final depth and the remaining 1000 deg^2 to a depth of 54μK-arcmin^2 at 150 GHz. The high signal-to-noise (> 7) SZ detections within this area consists of 26 clusters with masses in the range $9.8 \times 10^{14} M_{\odot} h_{70}^{-1} \leq M_{200} \leq 3.1 \times 10^{15} M_{\odot} h_{70}^{-1}$. In Williamson *et al.* (2011) they emphasise that the upcoming publications will significantly expand the SPT catalog and include lower signal-to-noise detections. By extrapolating from their current yields they expect to detect ≈ 750 clusters with S/N > 4.5.

1.3.3 Atacama Cosmology Telescope

The Atacama Cosmology Telescope (ACT) is a 6-metre telescope operating with a deg^2 field of view at an altitude of 5200m in the Atacama Desert (Fowler 2004). The telescope operates at 148 GHz, 218 GHz and 277 GHz with beam FWHM of 1.37′, 1.01′ and 0.91′. The SZ signal will be a decrement at 148 GHz, at its null at 218 GHz and an increment at 277 GHz.

In Hincks *et al.* (2010), the first SZ maps of 8 previously known clusters that have been detected in the ACT survey were presented. In Marriage *et al.* (2010) 23 clusters were blindly detected in the 148 GHz, 455 deg^2 2008 survey data, 10 of these were new discoveries. The ACT cluster sample is 80% complete at $M_{500} > 6.0 \times 10^{14} M_{\odot} h_{70}^{-1}$, where M_{500} is the mass of the cluster within a radius corresponding to an average density of 500 times the critical density of the Universe at the cluster redshift. The ACT SZ survey is not finished – there

is data from other observing seasons and a new survey area has been chosen, for future publications all three frequency bands will be used.

1.3.4 Planck

The Planck satellite (Planck Collaboration *et al.* 2011a) is in the unique position of being sensitive to the SZ effect and having full sky coverage. The satellite will produce the first all-sky cluster survey since the ROSAT all-sky survey which was conducted at X-ray frequencies. The capabilities of Planck are demonstrated by the 189 clusters which have been detected with high signal-to-noise ratios ($> 6\sigma$) in data obtained from only 10 months of observations (Planck Collaboration *et al.* 2011b). Included in this 189 clusters are 20 previously unknown cluster candidates, many of which have now been confirmed (Planck Collaboration *et al.* 2011e and AMI Consortium *et al.* 2011). Planck was launched in May 2009 and will continue collecting data until at least the end of 2011. Once complete the Planck SZ catalogue will contain substantially more than the 189 clusters already detected.

The Planck High Frequency Instrument (HFI) that is used to search for galaxy clusters has a beam size of 4-10 arcmin depending on frequency (Planck HFI Core Team *et al.* 2011). This is sufficient resolution to find typical clusters of galaxies anywhere from nearby to redshifts of 0.3-0.7, these limits are highly dependent on the cluster mass and size. At larger redshifts beam dilution becomes significant and cluster detection is hindered. However, recently Planck discovered a massive cluster at redshift 1.0 (Planck Collaboration *et al.* 2011d).

1.3.5 Sunyaev-Zel'dovich Array

The Sunyaev-Zel'dovich Array (SZA) is a radio interferometer situated in Owens Valley Radio Observatory. It consists of eight 3.5m antennas and operates from 27-35GHz. Six of the antennas are in a close-packed configuration with spacings from 4.5-11.5m, the other two antennas provide longer baselines of up to 65m. The close-packed array is sensitive to arcminute scales and the longer baselines provide higher-resolution data that is suitable for point source detection. The

detected sources are subtracted from the short baseline data to remove the point source contamination from SZ observations.

The SZA has completed a blind SZ survey covering an area of 6.1 square degrees. Simulations have shown that the survey is 50% complete at $6 \times 10^{14} M_{\odot} h_{70}^{-1}$. The final results from the survey are described in Muchovej *et al.* (2011): within the survey area no SZ decrements were detected.

1.3.6 The Latest Results from Blind SZ Surveys

As described in the previous sections the AMI, SPT, ACT and Planck have all blindly discovered galaxy clusters. Most of the clusters that have been discovered in these surveys are shown in Figure 1.18 which is taken from Planck Collaboration *et al.* (2011b).

Figure 1.18 highlights the very different selection functions of the SZ surveys. To understand these selection functions is challenging, not only because of the telescope properties (i.e. the beam size) and contamination but also because the detection of clusters is sensitive to the temperature and electron number, both of these are highly dependent upon the clusters dynamical state. However, to extract cosmology from a SZ survey it is essential that the selection function is thoroughly understood. Otherwise, accurate knowledge of the number of clusters as a function of mass and redshift cannot be obtained.

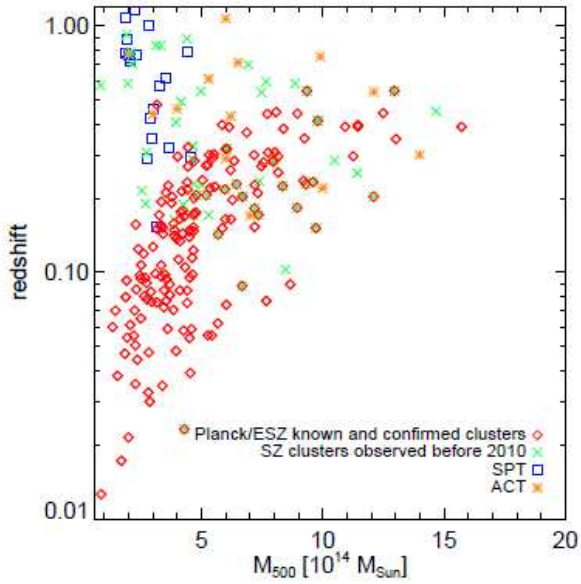

Figure 1.18: The mass versus redshift for a selection of galaxy clusters. Included on this plot are: the Planck all-sky early SZ cluster sample Planck Collaboration *et al.* (2011b); the SPT blindly detected clusters in Menanteau (2010); the ACT blindly detected clusters in Vanderlinde *et al.* (2010) and a selection of SZ effects observed prior to 2010. Each SZ experiment has a different selection function, the SPT is able to detect higher redshift and less massive clusters than Planck. A prediction of the AMI selection function is shown in Figure 4.2.

1.4 Thesis Outline

- Chapter 2 describes my contribution to the commissioning and calibration of AMI. I also outline the current AMI data reduction pipeline.
- Chapter 3 provides details of the software that I have developed to manipulate AMI data and perform tasks such as source subtraction and data concatenation.
- Chapter 4 presents the Bayesian analysis that is used to analyse our AMI observations and describes simulations that I have performed to characterise this analysis.

- Chapter 5, an analysis of the AMI SA and LA survey data. Including the identification of several previously unknown SZ decrements.
- Chapter 6 describes AMI observations of eight clusters from the Local Cluster Substructure Survey (LoCuSS).
- Chapter 7 summarises the results from preceding Chapters.

Chapter 2

Calibration

On my arrival in Cambridge much of the software required for the AMI data reduction was complete and the commissioning of the arrays was moving towards the final stages. However, several tools still needed to be developed in order to improve the telescope's performance and to streamline the data reduction pipeline.

In this chapter I discuss several of the main calibration and reduction tasks that I have undertaken, including: correlator lag calibration; time average smoothing corrections; identifying and flagging interference and measuring the primary beam. After this discussion I present the current standard AMI data reduction pipeline.

2.1 Correlator Lag Calibration

An AMI correlator board is shown in Figure 2.1; the theory behind this correlation was discussed in Section 1.2.1.

IF signals from two antennas enter the correlator board and are propagated along thin microstrip lines. Each signal is split into two at four separate occasions and are correlated at 16 different lags. The electrical path difference between the signals from the two antennas is 175mm at lag 1 and -200mm at lag 16; the design spacing between lags is 25mm. The design and testing of the AMI correlator is described in detail in Kaneko (2005), Holler (2003) and Holler *et al.* (2007a).

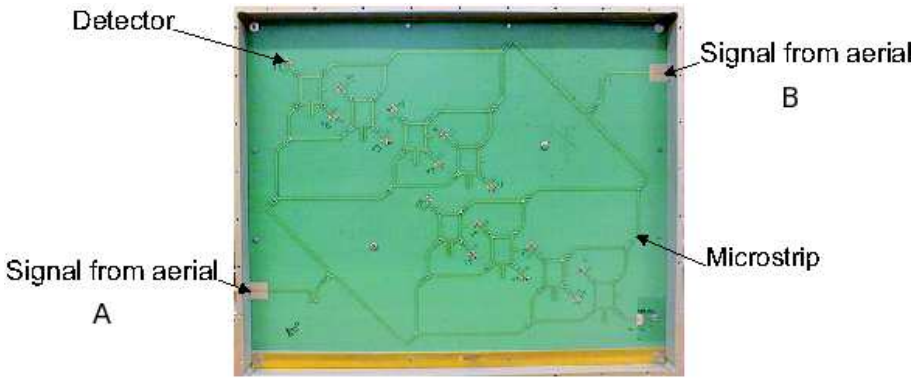

Figure 2.1: An AMI correlator board, showing the signal inputs, microstrip and the detectors.

The AMI correlator boards require careful calibration for two reasons. Firstly, the gain of the detectors (Schotty barrier diodes) varies by a factor of up to 4. Secondly, the separation in lag lengths is not exactly 25mm but are typically between 24mm and 26mm.

The correlator lag spacings and the lag gains can be extracted from the data of a `pc drift` observation. This type of observation is carried out by tracking a point source with the path compensators fixed. As the source moves in the sky the apparent path difference between the antennas changes and the signal from the source drifts through the AMI correlator lags. The time the signal takes to shift from one lag to the next depends upon the rate of change of the path length of the source and also on the distance between lags on the correlator board. The shape of the interference fringe is a cosine function modulated by a sinc curve, as is described by Equation 1.48 and the amplitude of the signal is indicative of the detector gains. If the correlator were perfect, the fringes would all have the same amplitude and the lag spacings would be equal to 25mm (Figure 2.2(a)), although as previously explained this is not the case (Figure 2.2(b)).

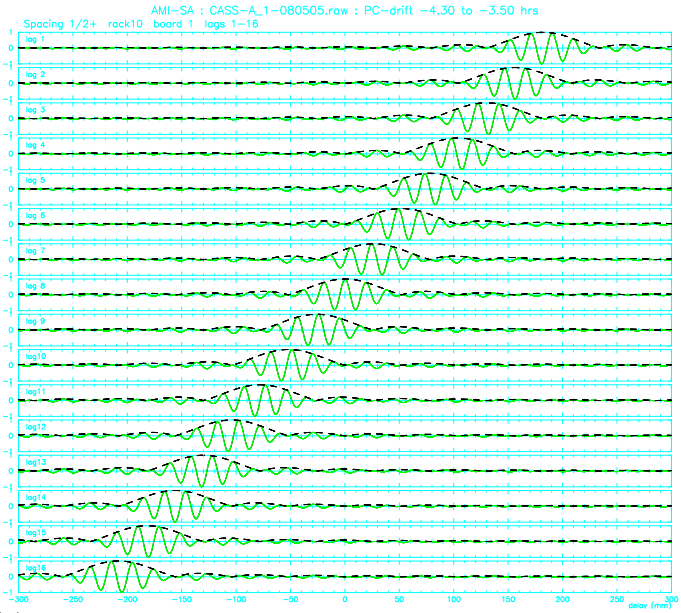

(a) Simulated `pc drift` lag data; the lag spacings and the lag amplitudes are all equal. The passband is a top hat and the shape of the lag response is clearly a cosine modulated by a sinc curve.

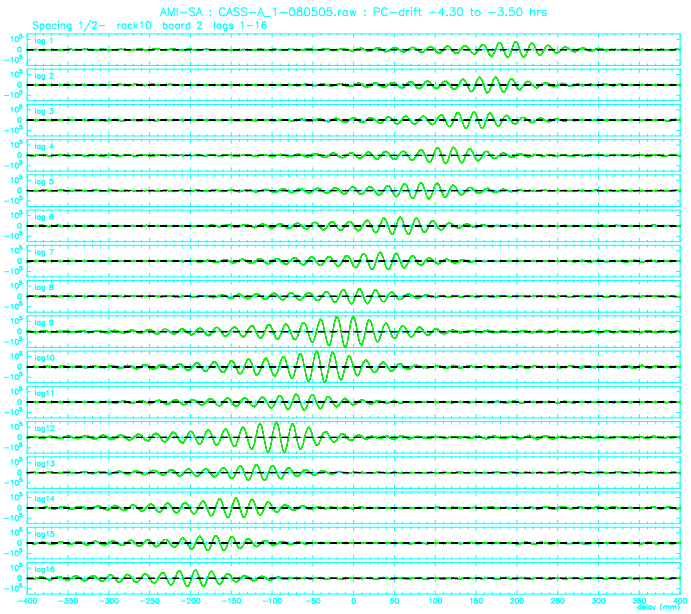

(b) Real `pc drift` data, demonstrating the variation in lag gains and spacings. The lag gains vary by a factor of 2 and none of the lag lengths are exactly 25mm. The passband is not a perfect top hat and as a consequence the lag data is not perfectly sinc-like.

Figure 2.2: A comparison between the lag data from a simulated `pc drift` observation and a real observation. Amplitude is plotted on the y-axis and delay (mm) is plotted on the x-axis.

2.1.1 Calibrating a PC Drift Observation

The REDUCE routine `cal pcdrift` is used to analyse `pc drift` observations after the data has been flagged for pointing errors, shadowing, path compensator errors and slow fringes. This routine uses the rms of the `pc drift` data within a fringe as a measure of the lag gain. For the lag spacings we align the lag fringes using the correlation between the response of each lag and a reference lag. I have made the lag calibration routine significantly more robust by implementing the following:

- Variations in atmospheric absorption affect the amplitude of the lag gains (Figure 2.3(a)). The AMI data are not amplitude corrected for system temperature variations until after they have been Fourier transformed to frequency space. Hence observations with significant variation in the system temperature must be flagged.

- Interference can cause spikes in a `pc drift` observation (Figure 2.3(b)). If the lag gains are determined by the maximum amplitude of the sinc curve then this can result in a spurious value. Instead, the rms value around the sinc curve is used because it is less susceptible to interference.

- Visibilities that have been flagged, because of e.g. pointing errors, can occur during the observation of the fringes (Figure 2.4(a)). If there are incomplete fringes then neither the cross correlation nor the amplitude of the fringe can be accurately determined. A check is now in place to ensure that data within the fringe used are not flagged.

- If the projected baseline is close to the line of sight then the path difference between the antennas varies slowly (Figure 2.4(b)). This slow fringe rate would require a long observation to observe the fringe drift between all 16 lags. Often a `pc drift` observation is an hour long and we found that unless the projected baseline is more than 30 degrees from the line of sight it is not possible for all the fringes on all the lags to be observed. Baselines with slow fringe rates are now flagged for `pc drift` analysis.

- A `pc drift` observation that is contaminated with a large amount of interference must be identified. Often such observations are recognisable because an error occurs in the cross correlation and the distance between lags is grossly overestimated.

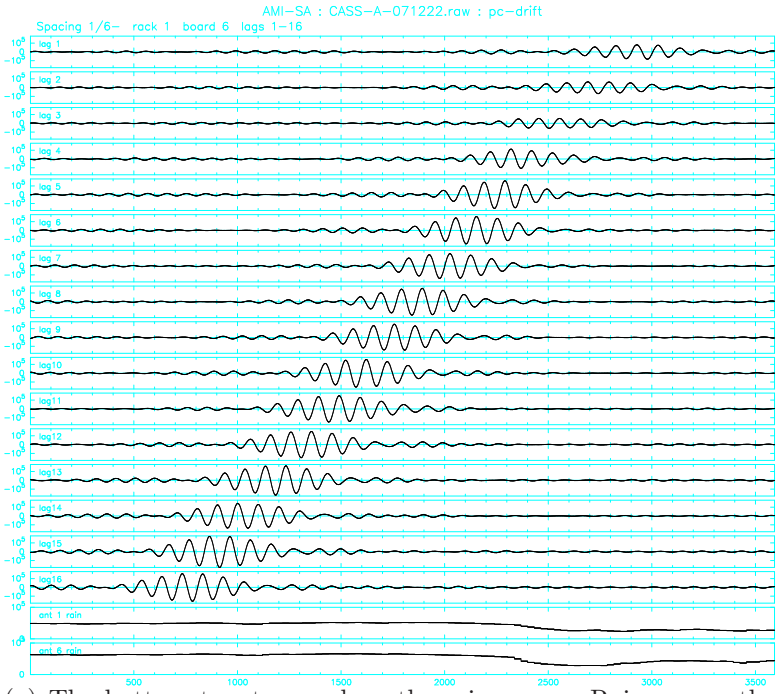

(a) The bottom two traces show the rain gauge. Rain causes the system temperature to vary dramatically during the observation. The lag gains are affected.

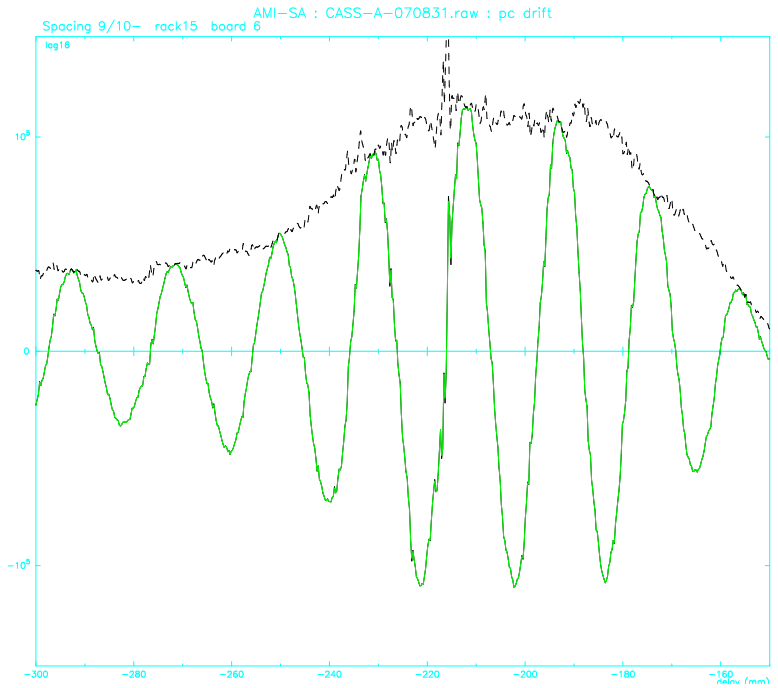

(b) A spike in the data has produced a spike in the fitted sinc curve which has provided a false maximum gain.

Figure 2.3: Pc drift calibration errors. Amplitude is plotted on the y-axis and delay (mm) is plotted on the x-axis.

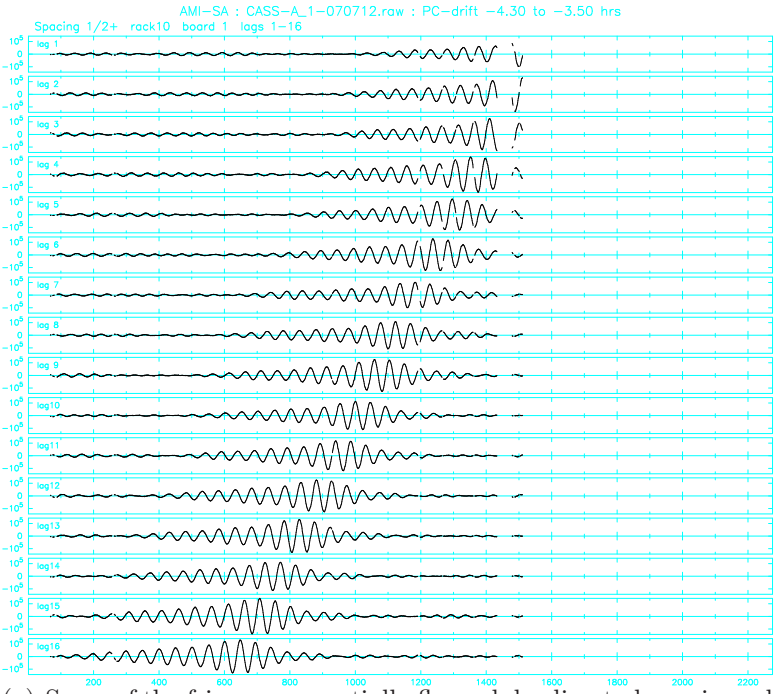

(a) Some of the fringes are partially flagged, leading to lag gain and lag spacing errors.

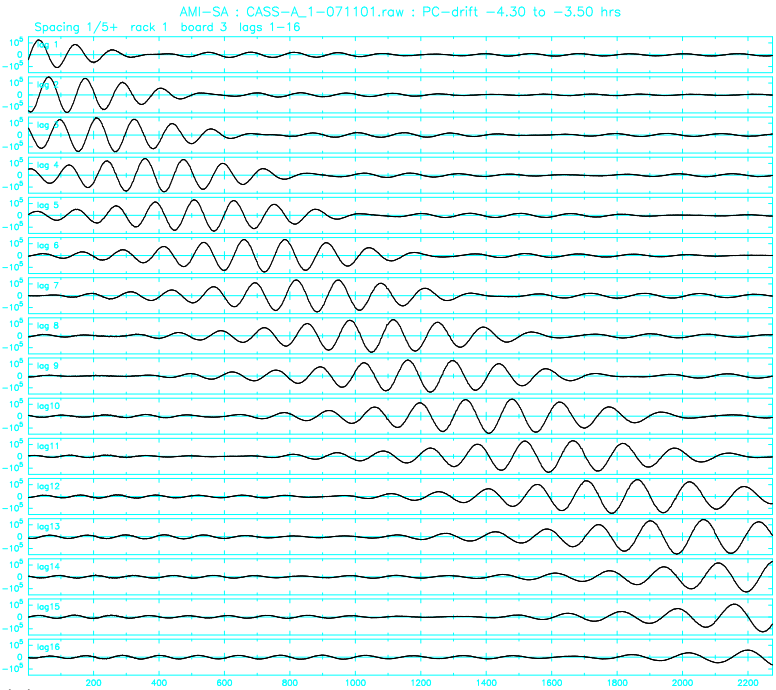

(b) The projected baseline is close to the line of sight, this leads to a low fringe rate and fringes are not observed in all lags .

Figure 2.4: Pc drift calibration errors. Amplitude is plotted on the y-axis and delay (mm) is plotted on the x-axis.

2.2 Geometry of the Large Array

The positions of the AMI antennas are specified by a right handed Cartesian coordinate system (X, Y, Z). However, in radio interferometry it is common to use the (u, v, w) orthogonal coordinate system. The relationship between these coordinate systems depends upon the latitude of the telescope (L), the hour angle of the source being observed (H) and the source declination (δ) see Figure 1.16 and Equation 1.56. When observing a point source at the phase reference position (the field centre) the geometric phase contribution is $2\pi\omega$ (see e.g Thompson *et al.* (2001)). From Equation 1.56 we can calculate that

$$\begin{aligned}\phi = 2\pi\omega &= 2\pi((X_\lambda \cos\delta)\sin H + (Y_\lambda \cos\delta \sin L + Z_\lambda \cos\delta \cos L)\cos H \\ &\quad + (-Y_\lambda \sin\delta \cos L + Z_\lambda \sin\delta \sin L)). \end{aligned} \tag{2.1}$$

In the AMI REDUCE program the `fringe rotation` routine subtracts the calculated phase (Equation 2.1) from the observed phase. For an observation which has a point source at the pointing centre and no other bright sources within the field of view, we expect that after `fringe rotation` the residual phase is approximately zero. However, if there are errors in the positions of the antennas then the phase is incorrectly calculated, the phase error is

$$\begin{aligned}\Delta\phi &= 2\pi\frac{15}{24}((\Delta X_\lambda \cos\delta)\sin H + (\Delta Y_\lambda \cos\delta \sin L + \Delta Z_\lambda \cos\delta \cos L)\cos H \\ &\quad + (-\Delta Y_\lambda \sin\delta \cos L + \Delta Z_\lambda \sin\delta \sin L)), \end{aligned} \tag{2.2}$$

where the ΔX, ΔY and ΔZ are the geometry errors that must be added to the currently applied values to obtain the true geometry. The $\frac{15}{24}$ factor is $\frac{9}{24}$ less than unity and arises because the path compensators have been applied at the IF frequency (-9 GHz) and the LO operates at 24 GHz. By observing a bright source with an interleaved calibrator that is offset in declination but at a very similar hour angle, the geometry errors can be determined. This fitting task is performed by the REDUCE routine `fit geometry`. Figure 2.5(a) shows an example of a geometry error and Figure 2.5(b) shows the phase of the same observation once the fitted geometry has been applied. It should be noted that phase errors are not always associated with incorrect geometry and can occur due to a combination of: path compensation artifacts; drifts in e.g. cable lengths and even temperature fluctuations in the correlator room. In practice it took many

observations to correct the geometry and we still perform monthly observations to ensure that the geometry errors in both arrays are minimised.

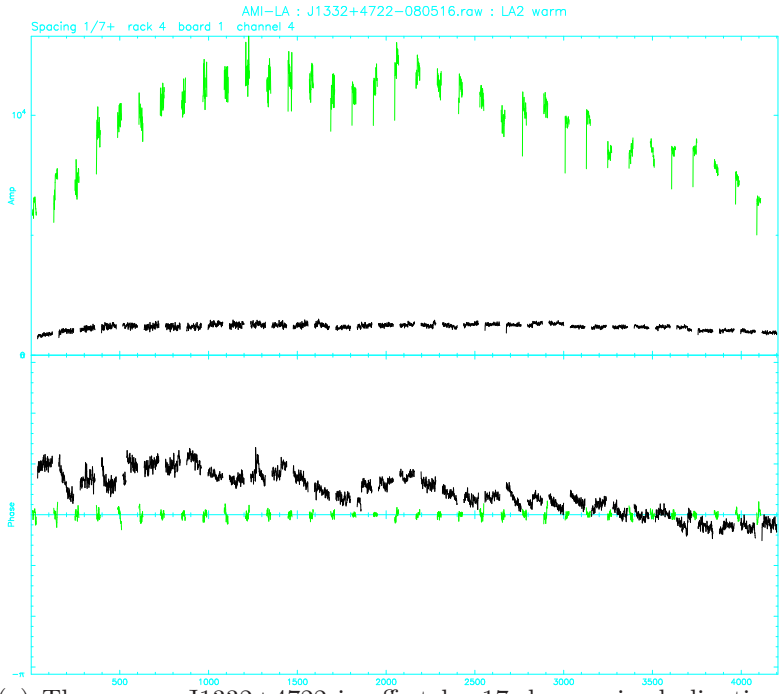

(a) The source J1332+4722 is offset by 17 degrees in declination from the interleaved calibrator (3C286); the phases do not track each other particularly well implying that the phase varies with declination, hence a geometry error.

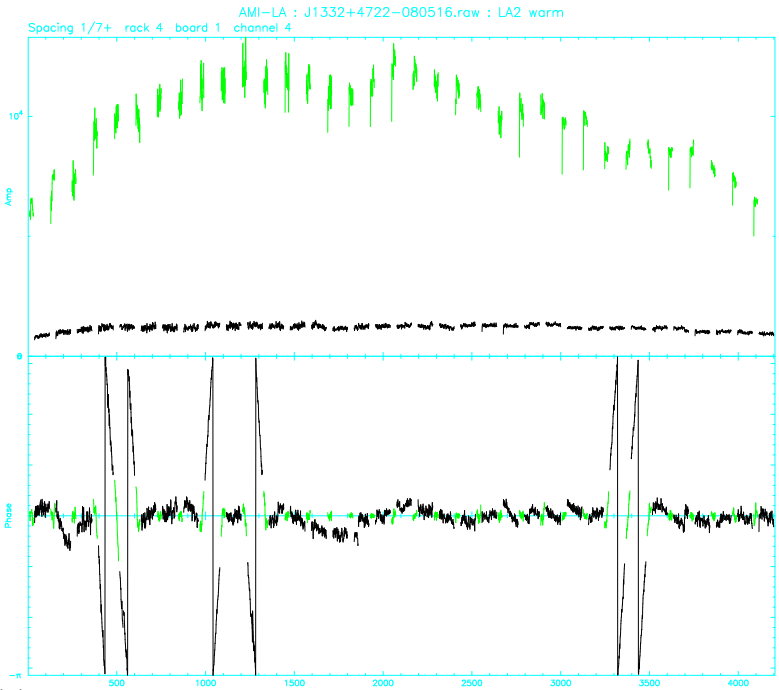

(b) Once geometry corrections are applied the phases track each other well, implying that the phase no longer varies with declination.

Figure 2.5: Manual X-Y-Z geometry corrections. Amplitude and phase are plotted on the y-axis and time is plotted on the x-axis.

2.3 Smoothing Amplitude Corrections

The AMI correlators integrate the signal for a finite period of time before the time average of the integrated signal is passed to the readout board. The minimum possible integration time is 1/8s but with this value the AMI data files will be large. Instead, we sample at 0.5s for LA data and at 1s for SA data. By sampling the signal at these lower rates the quantity of data will be significantly decreased but we must account for the effects of the averaging.

Given that a complex signal with a fringe rate ω can be described by

$$V(t) = V_0 e^{i\omega t}, \tag{2.3}$$

where V_0 is the initial amplitude, ω is the angular frequency and t is time. When this complex signal is integrated over the time period ΔT, the mean amplitude of the signal is

$$\bar{V} = \frac{1}{\Delta T} \int_{\frac{-\Delta T}{2}}^{\frac{\Delta T}{2}} V(t)dt = V_0 sinc(\omega \Delta T/2). \tag{2.4}$$

As the integration time is increased the amplitude of the signal drops but because ω is known (Equation 2.1) the drop in amplitude can be correctly calibrated out. Note that the signal-to-noise decrease can not be corrected. I have added a routine to REDUCE that automatically performs this correction which is less than 3% for all observations.

2.4 Flagging Interference

Although there are many procedures in place to flag interference in AMI data I have helped implement an additional two procedures into the REDUCE package to further improve the AMI data quality.

2.4.1 Interference Spikes

In the AMI lag data there is often significant interference. The routine `flag interference` (see Hurley-Walker 2009) scans the lag data for interference. It focuses on finding and flagging interference with a duration of at least several samples. How-

ever, individual spikes in the data and low level interference can be missed by `flag interference`.

The new routine `flag data` allows the user to flag the data either with a hard cut or a cut at a multiple of the rms of the data. This routine can be applied to both lag data and frequency data. In the lag data the amplitude has not been calibrated and due to different settings of AGC units the number of correlator units varies dramatically for different baselines. Hence a hard cut should not be used to flag lag data.

2.4.2 Geostationary Satellites

The emission from geostationary satellites contaminates the AMI observations, especially at low declinations. When AMI is tracking an astronomical object the observed phase of the object changes with time because the object moves with respect to the observing baseline (this is corrected for by the `fringe rotation` command). However, for a geostationary satellite the phase will remain constant because the satellite is always above the same point on earth and therefore its position with respect to the observing baseline is constant.

To distinguish between astronomical signals and geostationary satellites the signal from the telescope can be Fourier transformed to frequency space, phase corrected for the effects of path compensation on the phase, but not phase corrected for the path of the astronomical source (Equation 2.1). If the data are then smoothed over several samples, the amplitude of the signal from geostationary satellites will be enhanced compared to the amplitude from astronomical sources. An example of a satellite signal in the frequency domain is shown in Figure 2.6(a), here the data has been smoothed by 20 seconds.

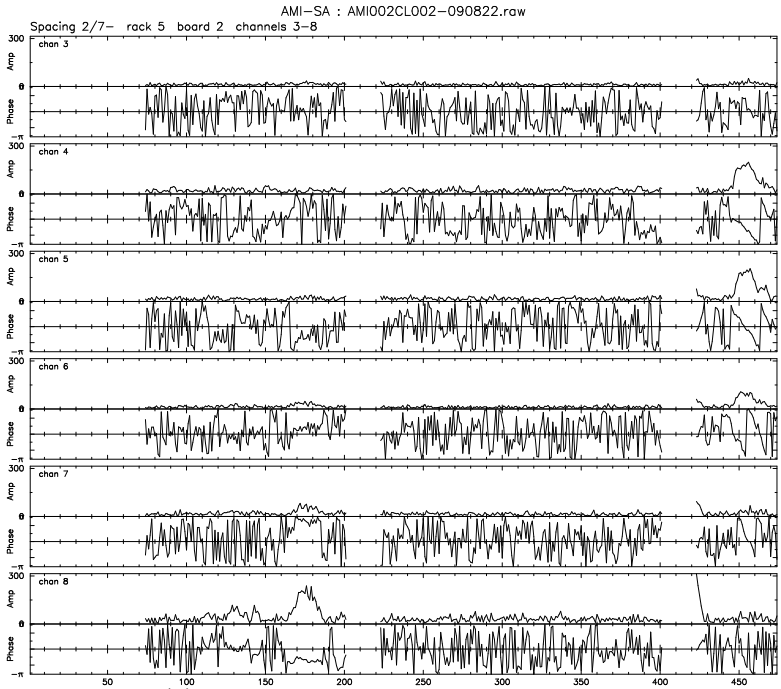

(a) Before `flag amplitude` is applied.

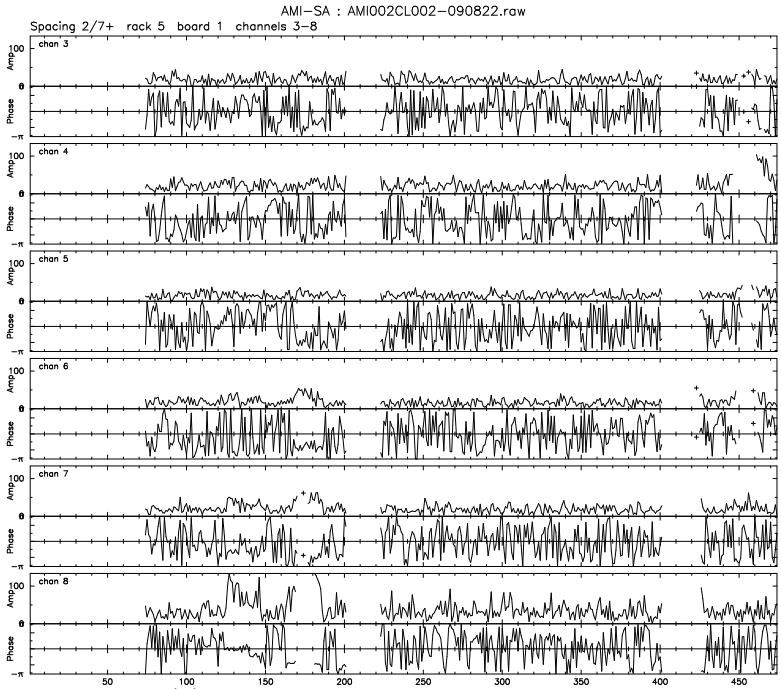

(b) After `flag amplitude` is applied.

Figure 2.6: Plot of the channel 3-8 amplitudes and phases (y-axis) versus time (x-axis) of a faint object at declination $\approx +25°$. There is significant interference towards the end of the observation. The data has been `smoothed` by 20 and phase corrected for path compensators but not for the astronomical path of the object being observed. Note that the amplitude scales for plots a) and b) are different.

The satellite interference can be identified by its amplitude and non random phase, as is very clear in Figure 2.6(a). However, this interference was not detected in the lag space at greater than three times the rms of the data (using the routine `flag data`) or by the routine `flag interference`. After applying the above procedure, using a smoothing of 20 and an amplitude cut of three times the rms, the interference from Figure 2.6(a) was flagged and the remaining data are shown in Figure 2.6(b). Dave Titterington has adapted the REDUCE routine `flag amplitude` so that it can adaptively smooth the data and implement the procedure outlined.

2.5 Power Primary Beam Measurements

Each AMI antenna has a voltage primary beam pattern ($A_V(\sigma+\phi)$) that describes its response as a function of angle (ϕ) from the pointing centre (σ). When the signals from two dishes are correlated the combined beam pattern ($A_{V,1}(\sigma + \phi)A^*_{V,2}(\sigma + \phi)$) is known as the power primary beam ($A_P(\sigma + \phi)$).

To measure the beam I have used three types of observation: the `raster offset`, the `ha offset` or declination `dec offset`, and the `drift scan`. `raster offset` observations are useful to determine the 2D primary beam. Both `ha offset` and `dec offset` observations determine a 1D slice through the primary beam. `drift scan` observations are useful because they eliminate any pointing errors that may contaminate the other observations.

Ideally each baseline on an array will have an identical $A_P(\sigma + \phi)$ to all other baselines on that array. Although this is not exactly the case due to slight dish distortions and slight feed positioning errors, we have used the observations mentioned above to determine an accurate mean power primary beam model for both the SA and the LA. I have calculated the best fit Gaussian models and derived the n^{th} order polynomial parameters (these are used in the imaging software AIPS)[1] which describe the beam according to

$$PB(x) = 1.0 + x\frac{PB_3}{10^3} + x^2\frac{PB_4}{10^7} + x^3\frac{PB_5}{10^{10}}, \tag{2.5}$$

[1] http://www.aips.nrao.edu

where x is the distance from the pointing centre in arc minutes. To derive the polynomial equations I have used Dave Green's program *pbparms*.

2.5.1 Raster Offset Observations

For a `raster offset` observation we observe a bright point source at the phase centre; the source is selected to have no significantly bright sources nearby. The frequency response of AMI to such an observation is given in Equation 1.52, and plotted in Figure 1.15. We then offset one of the antennae in the baseline by an angle $\Delta\phi(\Delta H, \Delta\delta)$, where ΔH is the hour angle offset and $\Delta\delta$ is the declination offset. The offset antenna is moved around a grid of different ΔH and $\Delta\delta$. At each position in the grid the baseline response is recorded. Hence we are measuring $A_{V,1}(\sigma + \Delta\phi) \times A_{V,2}(\sigma)$, and because $A_{V,2}(\sigma)$ is not offset we know its value is unity and by shifting one antennas pointing around a grid we map out $A_{V,1}(\sigma+\phi)$.

An example of a SA raster offset observation is shown in Figure 2.7, for this example the grid size is 25×25 and the spacing between grid points is $3.25'$.

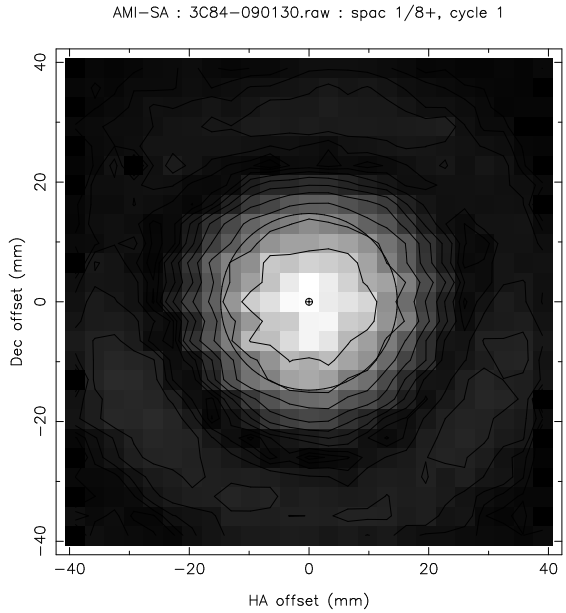

Figure 2.7: The variation of amplitude as a function of ΔH and $\Delta\delta$ from the data of a single baseline, lighter colours are higher amplitude. In this 6 hour observation taken on the 30$^{\text{th}}$ January 2009 the grid size is 25×25 (625 pointings), the separation between grid pointings is $3.25'$ and the integration time at each grid position is 15 seconds. The 6 hour observation contains two complete cycles through the 625 pointings; here I have plotted cycle 1 for antenna 8 channel 4. The lighter colour indicates higher amplitude and the amplitude ranges from 2600 to 80 correlator units. Contour levels start at 80; thereafter contours are spaced by a factor of $\sqrt{(2)}$.

To analyse a `raster offset` observation the REDUCE routine `plot raster` is used after the data have been flagged for pointing errors, shadowing, path compensator errors and slow fringes, Fourier transfered to the frequency domain, fringe rotated to the position of the source, phase corrected for the path compensation and amplitude corrected for system temperature variations (Section 2.6 describes these REDUCE procedures). `plot raster` outputs a file containing the identity of the offset antenna, the grid spacing and the mean amplitude at each position in the grid. `plot raster` was used to output a separate file for each of the AMI channels. In a typical observation half the antennas will be offset, so for the SA there will be 25 baselines each with "plus" and "minus" correlations

with one offset antenna and one on source, and for LA observations there will be 16 such baselines.

For each grid in the output files the amplitudes are fitted with a two dimensional Gaussian. The fitted Gaussian which is not centred on 0,0 is shifted and centred on 0,0 using bilinear interpolation. We centre each Gaussian because this corrects for pointing errors, assuming the pointing errors are equal for each point on the grid. After this procedure is performed for each grid, the standard deviation and mean are calculated at each grid position. The grid amplitudes are then averaged together, discarding any data that contains significantly discrepant amplitudes. Discarding such data helps to eliminate the effects of interference. We assume that the $A_{V,1}(\sigma+\phi) = A_{V,2}(\sigma+\phi)$ and square our resulting data to obtain $A_P(\sigma+\phi)$. The power primary beam was calculated for each of the six AMI channels and for the "continuum". The "continuum" is the average over channels 3-8.

2.5.2 Hour Angle and Declination Offset Observations

`ha offset` and `dec offset` offset observations are similar to a `raster offset` observation, but instead of the offset antenna moving in both hour angle and declination it moves on only one axis. This is therefore simply a 1 dimensional slice of a `raster offset` observation. An example of the frequency data from a LA `dec offset` observation is shown in Figure 2.8.

The REDUCE routine `offset scan` is used to analyse the data after the data has been reduced following the procedure outlined for `raster offset` observations. The `offset scan` routine identifies all baselines containing one offset antenna and one on source, it proceeds to calculate the average amplitude and its error for each offset. Pointing errors are included by calculating the average pointing error for each offset; the position of the offset is then set as the average pointing position rather than the desired pointing position. Figure 2.9 shows typical LA pointing errors during a `dec offset` observation; the pointing errors are largest for the first few data samples and are around $1'$ throughout the rest of the observation. Each offset cycle (Figure 2.8 contains 6 offset cycles) is fitted with a Gaussian. The fitted Gaussian which is not centred on $0'$ is normalised

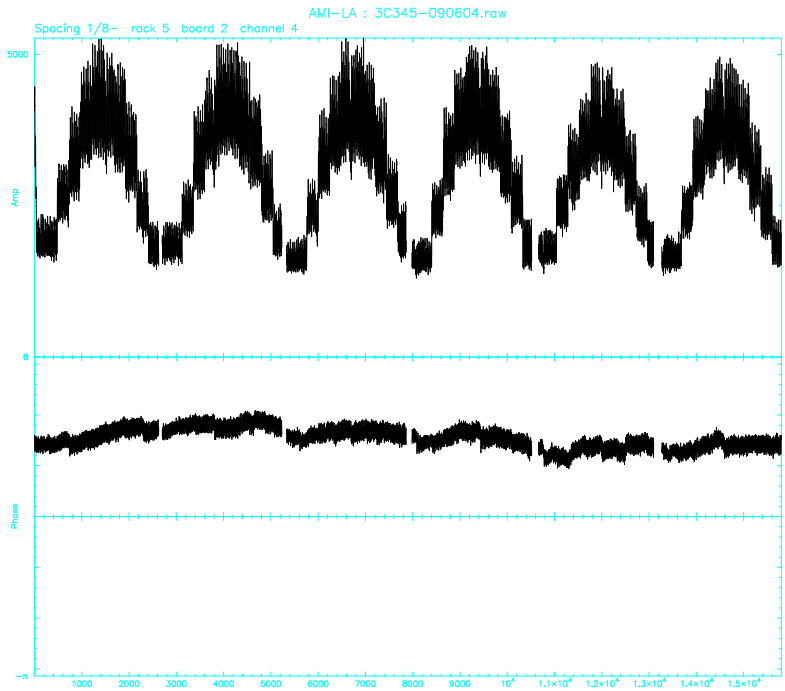

Figure 2.8: A LA `dec offset` primary beam measurement. One antenna is offset by 11 steps of $1'$. At each declination offset 120 data samples (60 seconds) are obtained, the total observation length for this run is around 2 hours. Amplitude and phase are plotted on the y-axis and time is plotted on the x-axis.

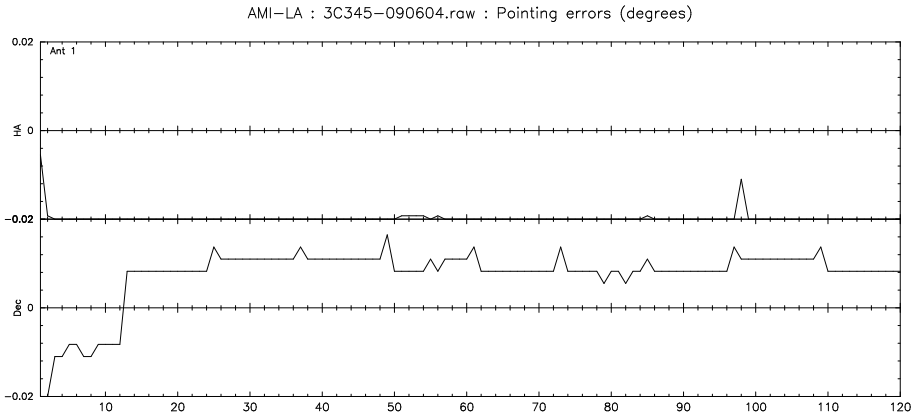

Figure 2.9: Declination pointing errors on LA antenna 1 during a `dec offset` observation. The x axis indicates time and the y axis shows the pointing error in degrees. At the beginning of the run antenna 1 is supposed to be offset by $5'$ and 12 samples later by $4'$ (moving by $1'$ or 0.017 degrees). However, for the first pointing there is a -0.01 degree pointing error and when supposedly pointing at offset 2 there is a -0.01 degree pointing error in the opposite direction. Hence the antenna is pointing half way between offsets 1 and 2 instead of moving between the two offsets. Also it is apparent that at the start of the run the offset antenna is pointing at the source and hence there is a large error in its pointing as the antenna slews to the desired position ($5'$ offset).

to have an amplitude of 1.0 and then shifted to be centred on $0'$ offset. After all Gaussians within a data set are aligned those with significantly different widths from the mean are discarded. This helps to eliminate the effects of interference. The mean fitted Gaussian is squared to give $A_P(\sigma + \phi)$ as a function of either ΔH or $\Delta\delta$. This procedure was followed for each channel and the continuum.

2.5.3 Drift Scan Observations

A `drift scan` observation can be used to determine the primary beam. In this observing mode we keep the antennas stationary while keeping the path compensators tracking a bright source. As the bright source passes through the telescope's field of view we are able to trace out the beam because we know the rate of change of the position of the source. If both antennas are offset we mea-

sure $A_P(\sigma + \phi)$ directly and if one antenna is offset we measure $A_{V,1}(\sigma + \phi)$ or $A_{V,2}(\sigma + \phi)$.

The frequency response of the `drift scan` observations are analysed by fitting a Gaussian to the response of each baseline, rejecting outliers and taking an average of the fit for each channel and the continuum.

2.5.4 Small Array Primary Beam

Using the SA I have conducted both `raster offset` and `drift scan` observations and in Hurley-Walker (2009) the SA primary beam was measured using a `ha offset` observation in which a single antenna was offset. The `drift scan` measurements were used only as a confirmation of the results from the `raster offset` observations, to ensure that they were not contaminated with pointing errors.

The `raster offset` results that I obtained for SA power primary beam measurements were calculated from two 4 hour observations made between 3$^{\text{rd}}$ December 2008 and 30$^{\text{th}}$ January 2009. The derived beams for channels 3-8 and the continuum are plotted in Figure 2.10.

The fitted parameters for SA power primary beams are shown in Table 2.1, and these values agree well with the values quoted in Hurley-Walker (2009) and those that I derived from `drift scan` observations. In Figure 2.11 I plot the σ of the best fitted Gaussians (σ_δ and σ_H) as a function of frequency (ν) and find that $\sigma \propto \frac{1}{\nu}$. The best fit values from Figure 2.11 are presented in Table 2.1.

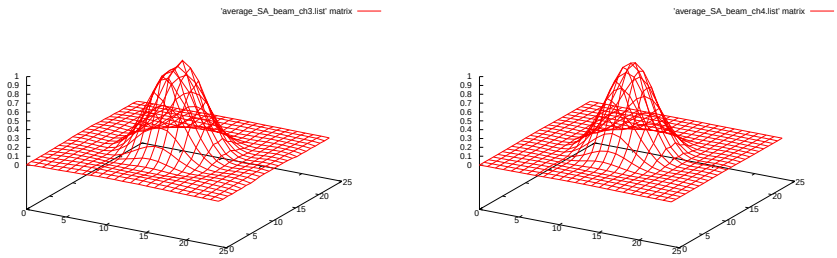

(a) SA channel 3. (b) SA channel 4.

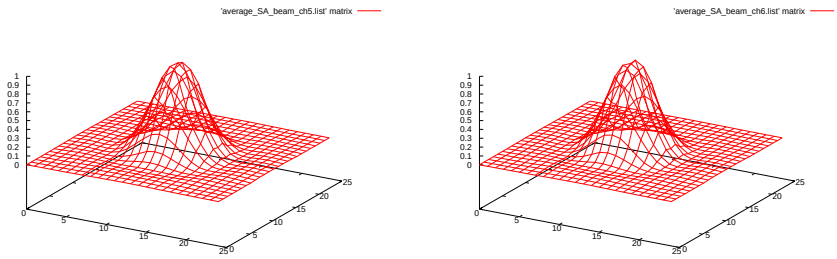

(c) SA channel 5. (d) SA channel 6.

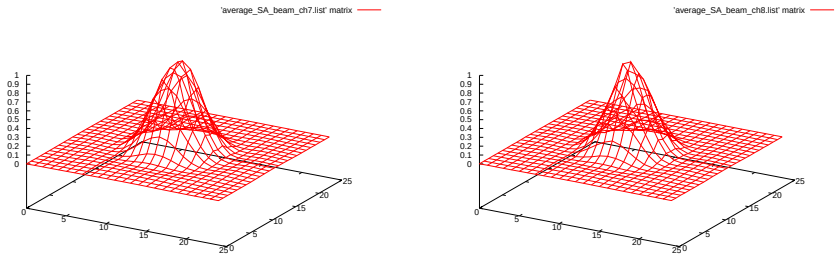

(e) SA channel 7. (f) SA channel 8.

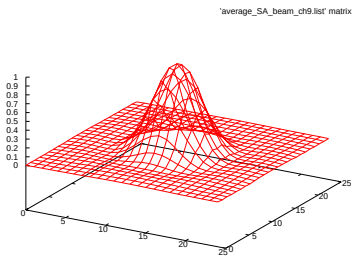

(g) SA continuum.

Figure 2.10: SA power primary beam measurements. Amplitude is plotted on the z-axis against pixel offset in RA and Dec on the x-axis and y-axis (the pixel size is 3.25').

Table 2.1: The parameters for the SA power primary beam. These have been determined from 25×25 `raster offset` observations with a spacing of 3.25′. The σ_{fit} value is derived from Figure 2.11. The polynomial parameters are derived from σ_{fit} using Dave Green's program *pbparms*.

Chan	Freq GHz	σ_δ ′	σ_H ′	σ_{fit} ′	$PB_{3,fit}$ 10^{-02}	$PB_{4,fit}$ 10^{-03}	$PB_{5,fit}$ 10^{-05}
3	13.87	9.39	9.22	9.18	-3.02	3.95	-2.11
4	14.62	8.57	8.53	8.80	-2.95	3.78	-1.98
5	15.37	8.44	8.47	8.46	-2.89	3.62	-1.85
6	16.12	8.32	8.28	8.15	-2.82	3.47	-1.74
7	16.87	8.01	7.94	7.88	-2.76	3.32	-1.63
8	17.62	7.53	7.52	7.62	-2.71	3.18	-1.53
Cont	15.75			8.31	-2.85	3.53	-1.79

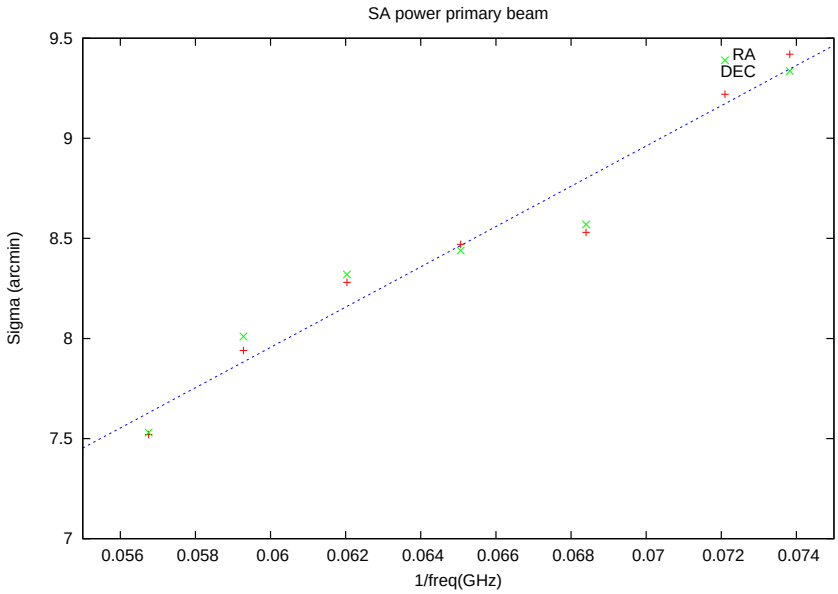

Figure 2.11: The SA power primary beam sigma vs the frequency. I have included both the σ_δ and σ_H derived parameters to give an indication of the errors. The line of best fit is $\sigma = \frac{m}{\nu} + c$, where ν is in GHz, m was found to be 101 and c was 1.89.

2.5.5 Large Array Primary Beam

The `ha offset` results that I obtained for LA power primary beam measurements were calculated from the 2 hour `ha offset` observation on the 4$^{\text{th}}$ June 2009 and the 1 hour `dec offset` observation also on the 4$^{\text{th}}$ June 2009. I found that the three 2 hour `raster offset` observations made between 11$^{\text{th}}$ March 2009 and 3$^{\text{rd}}$ April 2009 were significantly contaminated with pointing errors and therefore I did not extract primary beam parameters from these observations. I used `drift scan` measurements to check the results obtained from the `ha offset` and `dec offset` offset observations.

The `ha offset` and `dec offset` observations I have used have a $1'$ step size, 11 steps and an integration of 60 seconds at each step. Each step is revisited several times (Figure 2.8). The primary beam from each offset cycle is plotted in Figure 2.12 together with the best-fit Gaussian. The best-fit parameters are presented in Table 2.2 and the best fit Gaussians (σ_δ and σ_H) as a function of frequency (ν) are plotted in Figure 2.13. The noise on these measurements was lower than that obtained in the `drift scan` observations and the agreement between the derived parameters was good.

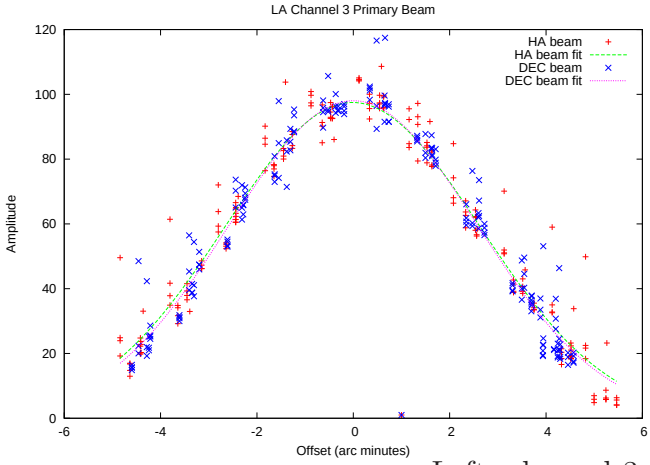

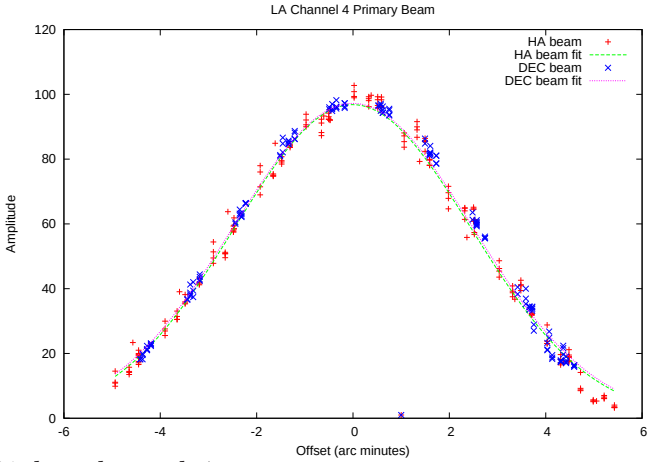

Left: channel 3. Right: channel 4.

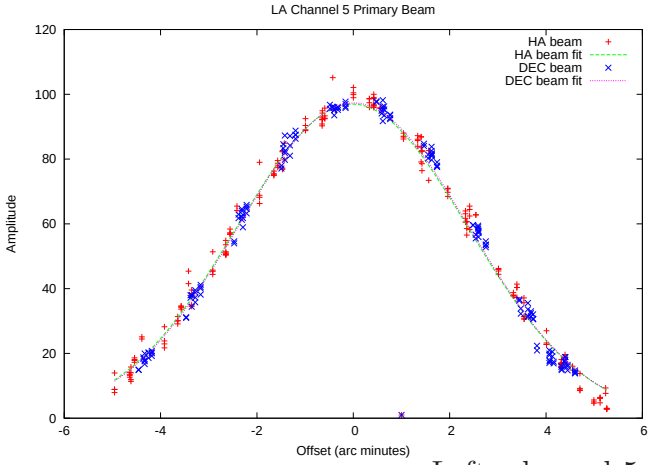

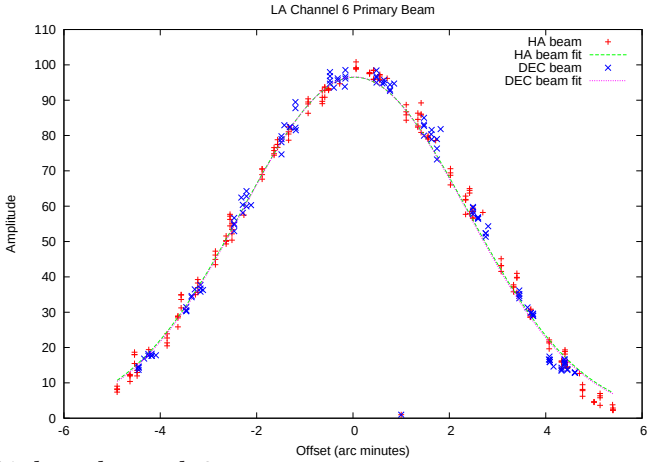

Left: channel 5. Right: channel 6.

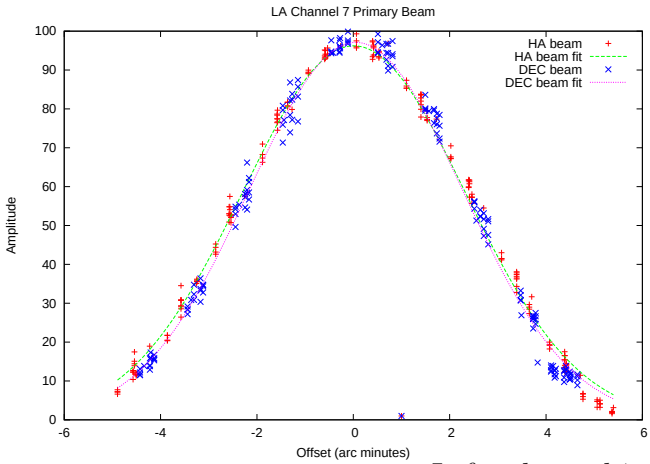

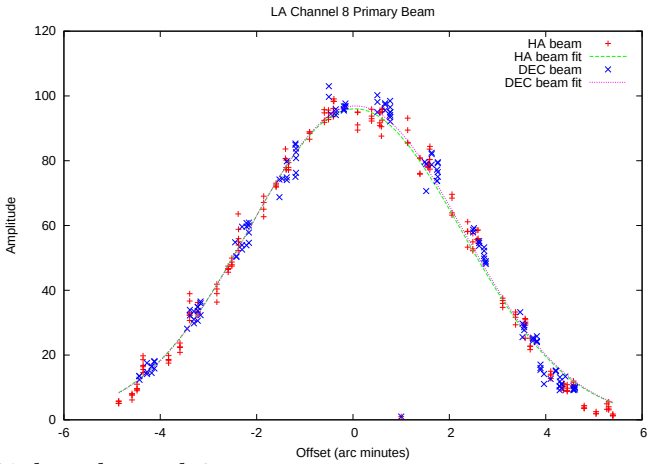

Left: channel 7. Right: channel 8.

Figure 2.12: LA power primary beam measurements.

Table 2.2: The derived parameters for the LA power primary beam. These have been determined from `ha offset` and `dec offset` observations with a spacing of 1.0′. The σ_{fit} value is derived from Figure 2.13. The polynomial parameters are derived from σ_{fit} using Dave Green's program *pbparms*.

Chan	Freq GHz	σ_δ ′	σ_H ′	σ_{fit} ′	$PB_{3,fit}$ 10^{-01}	$PB_{4,fit}$ 10^{-01}	$PB_{5,fit}$ 10^{-02}
3	13.87	2.58	2.65	2.60	-3.79	6.23	-4.19
4	14.62	2.50	2.46	2.50	-3.66	5.83	-3.79
5	15.37	2.41	2.40	2.41	-3.55	5.47	-3.44
6	16.12	2.34	2.35	2.34	-3.44	5.13	-3.13
7	16.87	2.27	2.32	2.27	-3.33	4.82	-2.85
8	17.62	2.07	2.22	2.07	-3.23	4.53	-2.60
all	15.75			2.38	-3.48	5.25	-3.24

2.6 Standard Reduction for AMI Observations

The data from the LA and SA are reduced using the same pipeline.

The raw data from all 16 lags of the correlator are loaded into REDUCE. It is then the responsibility of the user to manually check for dead or faulty antennas, large system temperature fluctuations (referred to as "rain gauge" fluctuations) and AGC errors. After the user has flagged out any obvious errors then if the field contains no bright point sources the user runs the following procedures:

- `Flag all`– Visibilities (samples from a single channel of a baseline) affected by pointing errors, correlator errors, path compensator errors, shadowing or slow fringe rates are flagged.
- `Flag interference` – The data is scanned for interference spikes which persist over several samples.
- `Flag data` – The data is scanned for $3\times\sigma_{lag}$ features which are flagged, where σ_{lag} is the rms of the data in each lag.

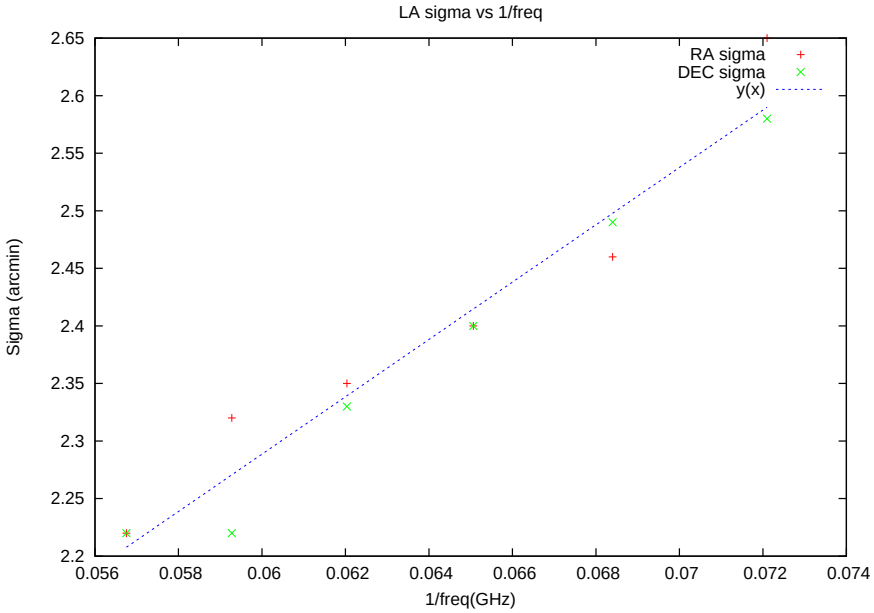

Figure 2.13: The LA power primary beam σ_δ and σ_H versus ν. The difference between the derived σ_δ and σ_H gives an indication of the errors. The line of best fit has been added as $\sigma = \frac{m}{\nu} + c$, where ν is in GHz, m was found to be 24.905 and c was 0.79

- `Update pcals`– A primary calibrator is used to update the baseline gains and nominal rain gauge values for each baseline.
- `Update lcals` – The lag amplitudes are corrected for known correlator board detector gain variations.
- `Subtract zeros` – Subtract a residual zero level from the data.
- `Subtract means` – Subtract a mean level from the data.
- `FFT` – Fast Fourier transform the data to convert from the time domain to the frequency domain. The 16 lags provide a phase and amplitude for eight frequency channels each with a bandwidth of 0.75GHz.
- `Frotate` – Correct the phase of the data for the path compensation. The primary calibrator gains (that were updated with the routine `update pcals`) are also applied, these convert the amplitude from correlator units to Jy.

- `Flag amplitude` – Perform an adaptive smoothing and flag features with an amplitude $> 3\sigma_{sm20,chan}$ from the mean, where $\sigma_{sm20,chan}$ is the rms of the channel data that have been averaged over 20 samples.
- `Frotate` – Fringe rotate the data to the phase centre by subtracting the calculated astronomical phase at the field centre from the observed phase.
- `Flag amplitude` – Flag data where the amplitude is more than 3 σ_{chan} from the mean amplitude, where σ_{chan} is the rms of the channel data on a specific baseline and channel.
- `Apply rain` – Apply an amplitude correction to the data and their weights to account for atmospheric absorption and increases in system temperature.
- `Cal inter` – Apply a phase correction and shift the phase of the data to ensure that the phase of the interleaved calibrator is 0. The phase of the field being observed is corrected by extrapolating between the interleaved calibrator observations.
- `Reweight` – Weight each visibility according to σ_{chan}. Noisier baselines are downweighted.
- `Smooth 200` – Apply a time smoothing of 200 samples by taking the mean of the real and the imaginary parts. This significantly reduces the size of the output files without causing significant time average smearing and enables deeper flagging.
- `Flag bad` – Compare the mean amplitude for the channel data on all baselines. Baselines that have channels with high or low means have those channels flagged.
- `Flag amplitude` – Flag the smoothed 200 data at an amplitude of $3\sigma_{sm200,chan}$ from the mean, where $3\sigma_{sm200,chan}$ is the rms of the smoothed 200 data.
- `Write fits/multifits` – Write the observation out as a UVFITS or a multi-source UVFITS file.

After applying the above pipeline typically 25% of the data is flagged.

2.7 Conclusions

I have contributed to the overall pipeline used to reduce the AMI data, in particular I have achieved the following:

- Added functionality to the lag calibration routine – this has created a significantly more robust algorithm.
- Improved the accuracy with which the geometry of the AMI antennas is known.
- Corrected the amplitude of AMI observations to compensate for the finite integration time of the correlator readout boards.
- Implemented several routines to remove interference from the AMI data; in particular reducing the interference from geostationary satellites.
- Primary beams of the SA and the LA are now well characterised.

Chapter 3

Post-Reduction Data Manipulation Tools

The AMI data are output from REDUCE in UVFITS format after they have been Fourier transformed to the frequency domain, flagged for interference and phase and amplitude calibrated. I have developed several useful tools that can be used to manipulate these UVFITS files. In this chapter I focus on the routines that have been developed to concatenate the data, separate multi-source UVFITS files, subtract sources from our maps, simulate sources on maps and to perform jackknife tests on our data. I also include details of additional secondary functionalities of the programs that I have developed.

3.1 Concatenating AMI data

Often there are many separate AMI observations of a specific object or area; each of these observations is run through REDUCE using the standard data reduction pipeline (see Section 2.6) to produce a UVFITS or multi-source UVFITS file and it is useful to have the ability to concatenate UVFITS files. The tool that I have developed for this purpose is the PYTHON program FUSE.

Table 3.1: UVFITS file data table; each multi-channel visibility from each baseline has one entry in this table.

Row name	Information
uu	The u coordinate
vv	The v coordinate
ww	The w coordinate
date	The Julian date of the observation
baseline	The baseline identity
source	The pointing identity (if multi-source UVFITS)
data	The real, imaginary and weight for each frequency channel

3.1.1 FUSE

All UVFITS files output by REDUCE have the same format. Each file begins with a header, this contains the basic information about the observation, such as its frequency, name, date, position and the history of the REDUCE routines that have been applied. The main body of the UVFITS file is split into either 2 or 3 sections: the data table, the AIPS AN table, and for multi-source UVFITS files the AIPS SU table.

The data table contains one row for each multi-channel visibility, the details stored for each of these visibilities is shown in Table 3.1. The AIPS AN table contains one entry for each antenna in the array and describes the antenna information such as its position and name. The AIPS SU table is only required in multi-source UVFITS files, this table is linked to the "source" row in the visibility data table (see Table 3.1) and it specifies the "source" identity, right ascension and declination. For more information on the structure of the AIPS AN and AIPS SU tables the reader is referred to the programmers guide to the AIPS system.

Given a list containing a combination of UVFITS and multi-source UVFITS files, FUSE is able to concatenate the data. This function is performed by copying the data, AIPS AN and AIPS SU tables from the first file in the list and appending or

altering each table accordingly. First, FUSE sorts the data into separate sources (pointings), sources with a J2000 right ascension and declination within 10″ are assumed to be at the same position. We must use this tolerance because AMI observations are observed at the targets current epoch position, i.e. J2011. Hence, an observation of the same object but on different dates will have slightly different J2000 coordinates. The data table from the first file in the list is then appended with the data from all subsequent data tables. If the first file is a single-source UVFITS file then a "source" row is added to the table and all data are relabelled according to which "source" it belongs to. The AIPS SU is appended to contain enough rows to describe all the "source" positions. The AIPS AN table is the same for each observation, so the table from the first file does not require any alterations.

3.1.2 Secondary Functionalities of FUSE

The main purpose of FUSE is to concatenate the UVFITS data, but several other functionalities have been added to the program. FUSE can create AIPS scripts for mapping, flag interference and perform a data reweight.

3.1.2.1 Mapping AMI Data in AIPS

The AIPS script output by FUSE, images either raster or pointed observations from the LA or the SA using the following pipeline:

- `Fitld` – Load the UVFITS data.
- `Imagr` – Fourier transform the UVFITS data to create an image for each channel and pointing. `clean` the image to three times the thermal noise on the map.
- `Flatn` – Combine the images from different positions and perform a primary beam correction, neglecting any data outside the 0.1 power circle. The OPTYPE command is used to create an appropriately weighted noise map from the thermal noise levels on the individual pointings. If the UVFITS file contains only a single pointing then the task `comb` (rather than `flatn`) is used to perform the primary beam correction.

- `Lwpla` and `Fittp` – Export the images in postscript and fits formats.

3.1.2.2 Flagging Interference

During the data concatenation process FUSE runs through all visibilities and ensures that they are linked to the correct "source" in the AIPS SU table. At the same time FUSE calculates the amplitude of each visibility and provides the user with the opportunity to flag any visibilities with an excessive amplitude.

Such flagging is useful because in REDUCE only a single observation is flagged and calibrated at one time. Hence, if there is a problem with the array and this causes consistently high amplitudes for the entirety of a single observation, the flagging routines contained within REDUCE will not identify this bad data. For this reason it is important to combine data from different observations together and scan for interference.

3.1.2.3 Reweighting the Data

When interference is flagged in either FUSE or REDUCE it is not necessarily flagged equally in all channels, resulting in an uneven distribution of weights between channels and pointings. This implies that each observation and each pointing has a slightly different frequency.

For the 10C survey (Davies *et al.* 2010 and **?**) it was important that the central frequency of each pointing was the same. Matthew Davies analysed the 10C data and found that the mean central frequency over the entire survey was 15.7GHz. In FUSE an option was inserted to make the mean frequency for all pointings equal to 15.7GHz. This applies the weights in Table 3.2 to reweight the data according to

$$r_{chan} = \frac{w_{tot} w_{des}}{100 * w_{chan}}, \tag{3.1}$$

where r_{chan} is the reweighting factor, which is multiplied by the weight of each visibility, w_{tot} is the total weight for all channels in the pointing, w_{des} is the reweighting percentage in Table 3.2 and w_{chan} is the total weight in a channel for the pointing. Although this reweighting ensures that every pointing has a central frequency of 15.7GHz it does cause a slight loss of sensitivity.

Table 3.2: The percentage weights that can be applied in FUSE to ensure that the mean frequency is 15.7 GHz.

Channel	Weights (%)	Frequency(GHz)
1	0.0	12.37
2	0.0	13.12
3	7.31	13.87
4	23.03	14.62
5	23.39	15.37
6	20.98	16.12
7	15.26	16.87
8	10.03	17.62

3.2 Separating Multi-source Data

UVSEP is a tool that has been developed to separate multi-source UVFITS files into single-source UVFITS files. This routine is useful to extract individual pointings from an AMI multi-source UVFITS file, allowing the user to thoroughly analyse the data from a given pointing.

As each visibility in a multi-source UVFITS file is linked to a specific pointing (see Table 3.1), the individual pointings can easily be extracted. Once the desired visibilities have been identified they can be copied to a new UVFITS file. The header of the input file is copied to the new file and updated with the correct right ascension and declination from the AIPS SU table of the input file. The AIPS AN table is also copied from the input file to the new file. The AIPS SU table is not required for single-source UVFITS files.

3.3 Source Subtraction and Data Simulation

Sources can significantly contaminate the SZ effect in AMI SA maps. The PYTHON program MUESLI was created to subtract these contaminating sources from AMI UVFITS data. MUESLI is also able to simulate AMI data. $\text{MUESLI}_{\text{sim}}$ was developed to test the completeness of the 10C survey (Davies *et al.* 2010 and

Franzen *et al.* 2010).

3.3.1 MUESLI Source Subtraction

To subtract sources from a UVFITS file we must determine the contribution of each source to each visibility. For this calculation we need to know the phase of the source (ϕ) and its amplitude as a function of frequency ($S(\nu)$). With this knowledge the real and imaginary components of the source signal can be calculated as a function of the baseline u, v and w position. The phase of a source offset from the pointing centre by $\Delta\delta$ and ΔH is:

$$\phi(u,v,w) = 2\pi \begin{pmatrix} u \\ v \\ w \end{pmatrix} . \begin{pmatrix} sin(\Delta H)cos(\Delta\delta) \\ sin(\Delta\delta) \\ cos(\Delta\delta)cos(\Delta H) \end{pmatrix} . \tag{3.2}$$

In the REDUCE `fringe rotation` routine the phase associated with the w coordinate is removed (see Equation 2.1), implying that the data output from REDUCE is the same as those obtained from tracking a source with a baseline perpendicular to the line of sight. Hence, the above equation is simplified to

$$\phi(u,v) = 2\pi(usin(\Delta H)cos(\Delta\delta) + (vsin(\Delta\delta))). \tag{3.3}$$

The Re and Im components of a source with flux $S(\nu)$ are:

$$Re(u,v) = S_{pb}(\nu) * cos(\phi(u,v)) \tag{3.4}$$

$$Im(u,v) = S_{pb}(\nu) * sin(\phi(u,v)), \tag{3.5}$$

where $S_{pb}(\nu)$ is the power primary beam attenuated source flux as a function of frequency.

Given a UVFITS file and a source list that contains the spectral index and flux of a source, MUESLI calculates the contribution of each source to the Re and Im components of each visibility. These calculated values are subtracted from the Re and Im values in the input UVFITS file. Assuming that the input source

parameters accurately describe the source, the output UVFITS file will have the contributions of these sources removed.

MUESLI contains models for both the SA and LA primary beams (see Section 2.5) and can therefore subtract sources from UVFITS data that has been obtained from either array. MUESLI is able to subtract from both UVFITS and multi-source UVFITS files. To increase efficiency when operating on multi-source UVFITS files MUESLI only subtracts sources from pointings within $20'$ on the SA or $5'$ on the LA. At these distances the primary beam attenuation is large enough to ensure that only very bright unsubtracted sources will influence the map.

3.3.1.1 MUESLI Simulation

The MUESLI simulation routine MUESLI$_{\text{SIM}}$ reads in UVFITS (or multi-source UVFITS) data and a source list. The user is given the option to overwrite the Re and Im components of the visibilities and construct a data set that consists only of Gaussian random noise, the level of which is specified by the user. The noise is simulated according to

$$\sigma_{chan} = \frac{\sqrt{\sigma_{Re}^2 + \sigma_{Im}^2}}{\sqrt{2n_{vis} \times n_{chan}}}, \tag{3.6}$$

where σ_{chan} is the channel thermal noise, n_{chan} is the number of channels and n_{vis} is the total number of visibilities. If the user chooses to set the noise at σ_{chan}, MUESLI$_{\text{SIM}}$ draws points from a Gaussian distribution centred on 0 with a standard deviation equal to

$$\sigma_{Re} = \sigma_{Im} = \sigma_{chan}\sqrt{n_{vis} \times n_{chan}}. \tag{3.7}$$

These generated values overwrite the Re and Im components of the input visibility. MUESLI$_{\text{SIM}}$ resets all visibility weighting, hence the noise on the output continuum map (6 channels) is $\sigma_{chan}/\sqrt{6}$.

To add or subtract sources to the simulated Gaussian random noise data we follow the procedure described in Section 3.3.1.

3.4 Jack-knife Tests

Systematic uncertainties can be a problem in astronomical observations; given that the AMI correlator does not operate perfectly (see Section 2.1) such errors must be searched for.

I have written the routine JACK-KNIFE, this performs several different tests on the AMI single-source or multi-source UVFITS data. These tests are:

1. Reverse the Re and Im measurements for all the plus correlator boards. Each baseline has a plus and minus correlator board shifted 180 degrees in phase from each other (see Section 1.2.1).

2. Reverse the Re and Im measurement for the first half of the data.

After JACK-KNIFE has operated on the UVFITS data, the data can then be mapped. The features seen on the maps reveal systematic errors in the observation. The first test checks to see if the lag length errors on the correlator boards result in significant artifacts on the maps. The second check shows the effects of source variability and also longer term instrumental drifts. It should be noted that for the second JACK-KNIFE test the weights in the first half of the data must be kept the same as the weights in the second half. Also, if the weighted uv coverages in each half of the data are not equal then residuals will be expected in regions close to bright sources.

When these two JACK-KNIFE tests are performed on simulated data the resulting image consists of thermal noise. The thermal noise level on the JACK-KNIFED image is as expected equal to the thermal noise of the data before the JACK-KNIFE test. An example of a JACK-KNIFE test on the simulated data is shown in Figure 3.1.

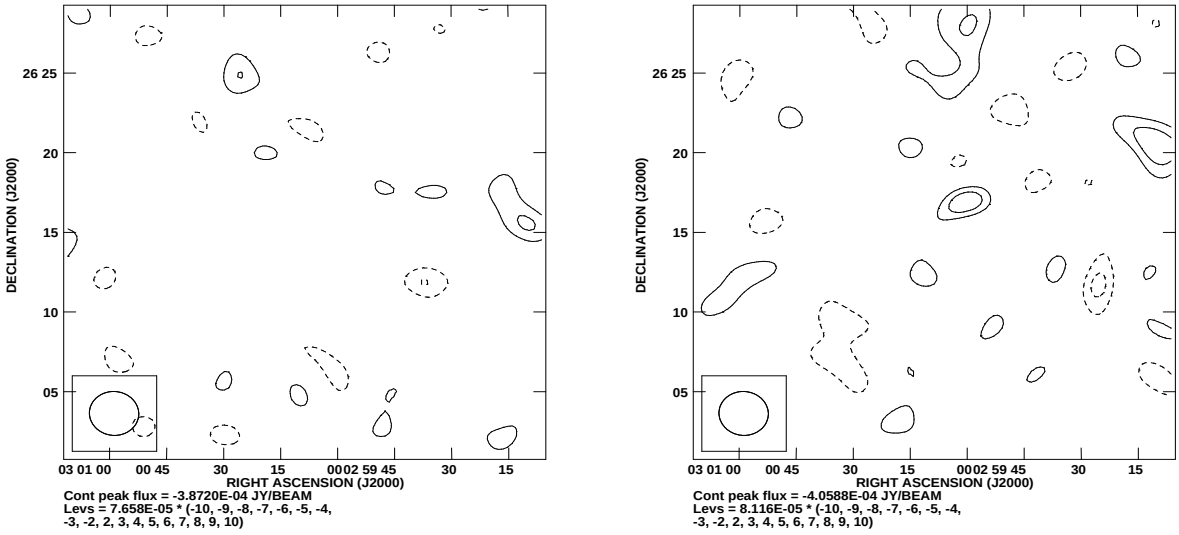

Figure 3.1: JACK-KNIFE tests on the simulated data that is presented in Figure 4.3 on the right. Left: the results from plus correlator boards against minus correlator boards (or odd versus even visibilities). Right: the image from the first half of the data minus the second half.

When JACK-KNIFE tests are performed on real data they highlight the contaminated regions of the map, for example, regions around bright sources are often associated with significant residuals on maps of the jack-knifed data. In Figure 3.2 I present images of the jack-knifed data from a region of the AMI002 survey data (Figure 5.5). From these tests it is apparent that significant residuals are associated with the bright point sources which have fluxes > 10mJy/beam. These errors are larger when the data are split according to date. Both the JACK-KNIFE tests indicate that neither the flux stability nor the phase stability of AMI are good enough to accurately model the contribution of bright sources to our data. However, for the dimmer sources in the field the JACK-KNIFE tests indicate no significant errors associated with these regions. Also, when the JACK-KNIFE test of plus versus minus baselines is performed the thermal noise level on the resulting map is 40% lower than the thermal noise level on the original map. However, when the data is split according to date the thermal noise level is

the same as on the original map. This effect was not seen in JACK-KNIFE tests of simulated data, but can be explained if both the plus and minus baselines are measuring a noise-like signal that is correlated, a possibility could be faint satellite interference.

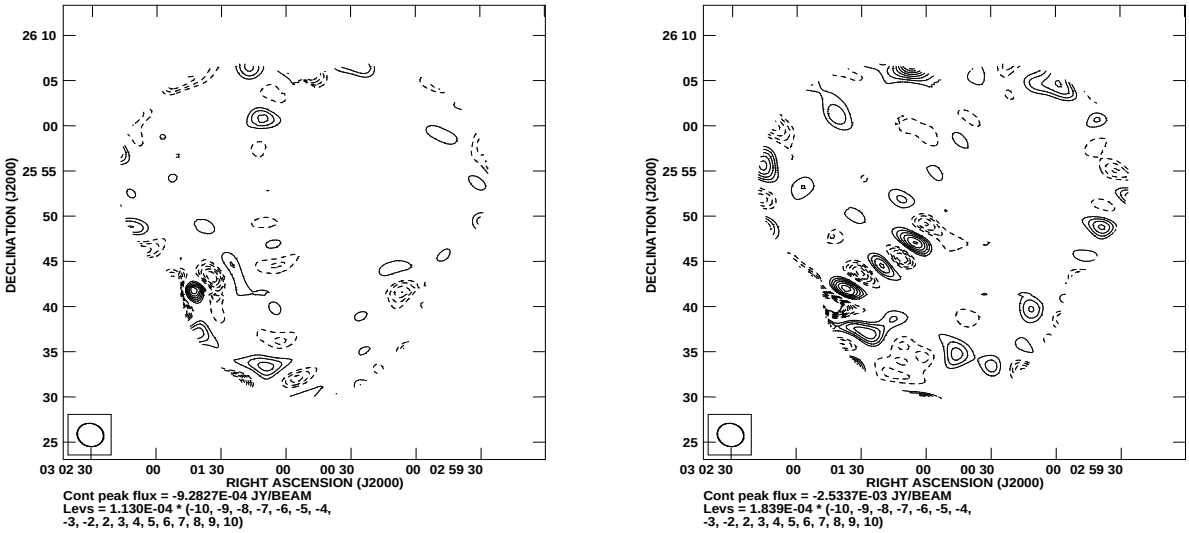

Figure 3.2: JACK-KNIFE tests on the real data presented in a portion of Figure 5.5. The portion was chosen to show the contamination that can be caused by a bright source. Left: the data is split according to baseline. Right: the data is split according the median date.

3.5 Conclusions

I have developed several routines to manipulate AMI data outside of the REDUCE software package. The requirements and achievements of these routines are as follows.

- A routine to concatenate AMI data was needed to simplify our mapping procedure and data storage. The FUSE routine reliably concatenates AMI UVFITS data from either array and produces a standard mapping script for AIPS.

- For detailed analysis of a small area it is often useful to extract single source UVFITS files from multi-source UVFITS files. The script UVSEP performs this task.

- At 15 GHz radio sources are a major contamination for SZ observations. Given source positions, flux-densities and spectral indices the MUESLI software reliably subtracts sources from either the SA or the LA data.

- To understand the completeness of the 10C survey it was necessary to simulate sources in real and simulated AMI survey data. $\text{MUESLI}_{\text{SIM}}$ allows the user to perform these simulations.

- Recognising contaminated data in all AMI observations is important and especially important for the AMI blind cluster survey. The JACK-KNIFE routine provides two tests for identifying contaminated data.

3.6 Further Work

- Presently MUESLI can only subtract point sources from data, it would be useful to add the functionality so that MUESLI can subtract extended sources. A simple elliptical Gaussian could be used to describe extended sources.

Chapter 4

Preparing to analyse the AMI blind survey fields

In this chapter I first describe the Bayesian inference package, McAdam, that is used to analyse AMI observations. I include an introduction to the physical cluster model and a description of a phenomenological model. I describe how these two methods can be used to quantify the significance of cluster detection. Even though McAdam has been used to analyse many SA observations of known clusters (e.g Zwart *et al.* 2010, AMI Consortium: Rodriguez-Gonzalvez *et al.* 2010, AMI Consortium: Rodriguez-Gonzalvez *et al.* 2011 and AMI Consortium: Shimwell *et al.* 2011), only in the work of this thesis has it been applied to search for blind clusters in the SA survey data. Using simulated cluster observations I have investigated the performance of our analyses and the effects of several fundamental priors then address the computational challenges of analysing the entire AMI blind cluster survey.

Hereafter we assume a concordance ΛCDM cosmology, with $\Omega_{\rm m} = 0.3$, $\Omega_\Lambda = 0.7$ and $\mathrm{H}_0 = 70 \mathrm{km\,s^{-1}Mpc^{-1}}$. The dimensionless Hubble parameter h_X is defined as $h_X = \mathrm{H}_0/(\mathrm{X\ km\,s^{-1}Mpc^{-1}})$ and $\sigma_8 = 0.8$.

4.1 McAdam

The McAdam package has been developed by Hobson & Maisinger (2002), Marshall *et al.* (2003) and Feroz *et al.* (2009a). I focus on using it to: search the AMI

survey data for clusters; confirm AMI detections of known clusters; derive cluster parameters; and model the properties of contaminating sources. The operation of McAdam requires the user to input prior knowledge of the parameters that are used to model both sources and clusters. For the analysis of the SA survey data, McAdam is used to calculate the probability that a detected cluster is real without prior knowledge of its existence.

Given a set of AMI data, McAdam can calculate the Bayesian evidence of a model that consists of the parameters (Θ) which describe a galaxy cluster and nearby radio sources. As by-products, the posterior probability distributions for the entire set of parameters are also calculated. In the analysis McAdam can take into account receiver noise, the background flux from undetected radio sources (confusion noise) and the statistics of the primary CMB structures. Bayes' theorem states that

$$\mathrm{P_r}(\Theta|\mathrm{D},\mathrm{H}) = \frac{\mathrm{P_r}(\mathrm{D}|\Theta,\mathrm{H})\mathrm{P_r}(\Theta|\mathrm{H})}{\mathrm{P_r}(\mathrm{D}|\mathrm{H})}, \tag{4.1}$$

where $\mathrm{P_r}(\Theta|\mathrm{D},\mathrm{H})$ is the posterior probability distribution of the parameters given the data D and the hypothesis H, $\mathrm{P_r}(\mathrm{D}|\Theta,\mathrm{H}) \equiv \mathrm{L}(\Theta)$ is the likelihood, $\mathrm{P_r}(\Theta|\mathrm{H}) \equiv \pi(\Theta)$ is the prior probability distribution, and $\mathrm{P_r}(\mathrm{D}|\mathrm{H}) \equiv \mathrm{Z}$ is the Bayesian evidence.

To perform parameter estimation it is not necessary to calculate Z as the value of this is independent of the parameters Θ. The probability distributions for the parameters are found by sampling from the posterior $\mathrm{P_r}(\Theta|\mathrm{D},\mathrm{H})$. To determine individual parameter probability distributions, McAdam marginalises the posterior over the desired parameter.

It is Z that is important for model selection. The higher the value of Z, the better the data support the hypothesis. This implies that for observations towards known clusters we can determine whether AMI has detected the cluster by simply taking the evidence ratio between a run containing a cluster with the position of the cluster (x_c, y_c) and the cluster redshift (if known) set as priors and another run on the same data but without a cluster – this 'null' run is achieved by placing a delta-function prior of value zero on the cluster gas fraction.

For the AMI blind cluster survey, we can also use the Bayesian evidence to determine the probability of cluster detection. However, we are faced with the

additional problem that our fields have been chosen to contain no known clusters and therefore we do not have a priori evidence for a cluster at a particular position (or redshift). In analysing a survey field, the marginalised posterior distribution in the (x_c, y_c)-plane will typically contain a number of local peaks; some of these may correspond to the presence of a real cluster, whereas others may result from chance statistical fluctuations in the primordial CMB, instrument noise and/or source artifacts. I stress that local peaks may also arise from systematics, but I note that, given that the blind survey fields have been chosen to exclude very bright sources and that we are wary of apparent peaks near bright sources (the AMI synthesized beam is shown in Figure 5.2), we have not come up with significant ways that AMI can 'invent' clusters, although of course a real cluster can be hidden by radio emission which obscures its SZ effect. Each local peak in the posterior is automatically identified by the MultiNest sampler (Feroz & Hobson 2008 and Feroz *et al.* 2009b) that is used in our Bayesian analysis. To determine the significance of each such putative cluster detection, we perform a Bayesian model selection, which makes use of the expected number of clusters per unit sky area:

$$\mu = \int_{z_{\rm min}}^{z_{\rm max}} \int_{M_{T,{\rm lim}}}^{M_{T,{\rm max}}} \frac{d^2 n}{dMdz} dMdz, \tag{4.2}$$

where $z_{\rm max}$ is the maximum cluster redshift, $z_{\rm max}$ is the minimum cluster redshift, $M_{T,{\rm lim}}$ is the limiting cluster mass that can be detected, $M_{T,{\rm max}}$ is the maximum mass of a cluster and $n(z, M)$ is the comoving number density of clusters as a function of redshift and mass. We use cluster number counts from analytical theory (e.g. the Evrard *et al.* 2002 approximation to Press & Schechter 1974 which is tied to cluster counts at redshift zero) or numerical modelling (e.g. Jenkins *et al.* 2001) together with measurements of the rms mass fluctuation amplitude on scales of size 8 h_{100}^{-1}Mpc at the current epoch, σ_8 (see e.g. Lahav *et al.* 2002, Seljak *et al.* 2005 and Vikhlinin & et al 2009). Although there are many more recent attempts to estimate the cluster number counts (e.g. Sheth & Tormen 2002, White 2002, Reed *et al.* 2003, Heitmann *et al.* 2006, Warren *et al.* 2006, Reed *et al.* 2007, Lukić *et al.* 2007, Tinker *et al.* 2008, Boylan-Kolchin *et al.* 2009, Crocce *et al.* 2010 and Bhattacharya *et al.* 2011), the $n(z, M)$ predicted by these more recent estimates is similar to that which I have used. It must be borne in

mind that the actual values of the number density of clusters, particularly at high redshift, are uncertain and hence the degree of applicability of these as priors is unclear.

We calculate the probability of two hypotheses: the first, $\Pr(H_{\geq 1}|D)$, assumes at least one cluster with $M_{T,\mathrm{lim}} < M_T < M_{T,\mathrm{max}}$ is associated with the local peak in the posterior distribution under consideration; the second, $\Pr(H_0|D)$, assumes no such cluster is present. Throughout these calculations we define $M_{T,\mathrm{lim}}$, M_T and $M_{T,\mathrm{max}}$ to be total masses within r_{200}, which is defined as the radius inside which the mean total density is 200 times the critical density ρ_{crit} at the cluster redshift. In particular, we consider the ratio R of these two probabilities

$$R \equiv \frac{\Pr(H_{\geq 1}|D)}{\Pr(H_0|D)}. \tag{4.3}$$

To evaluate this ratio, let us first denote by S the area in the (x_c, y_c)-plane of the 'footprint' of the local posterior peak under consideration (we will see below that a precise value for S is not required). This footprint represents the angular extent of the cluster. Also, we denote by H_n the hypothesis that there are n clusters with $M_{T,\mathrm{lim}} < M_T < M_{T,\mathrm{max}}$ with centres lying in the footprint S, so that

$$\Pr(H_{\geq 1}) = \sum_{n=1}^{\infty} \Pr(H_n). \tag{4.4}$$

Thus equation (4.3) can be written as

$$R = \frac{\sum_{n=1}^{\infty} \Pr(H_n|D)}{\Pr(H_0|D)} = \frac{\sum_{n=1}^{\infty} \Pr(D|H_n)\Pr(H_n)}{\Pr(D|H_0)\Pr(H_0)}, \tag{4.5}$$

where we have used Bayes' theorem in the second equality. Assuming that objects are randomly distributed over the sky, then

$$\Pr(H_n) = \frac{e^{-\mu_S}\mu_S^n}{n!}, \tag{4.6}$$

where μ_S is the expected number of clusters with $M_{T,\mathrm{lim}} < M_T < M_{T,\mathrm{max}}$ in the footprint S and is given by $\mu_S = S\mu$. A typical footprint is small ($S < 60'' \times 60''$) and there is a very low probability of two or more clusters having their centres

within this region ($\mu_S \ll 1$). Hence, we neglect μ_S^2 and larger powers of μ_S, so that equation (4.5) can be approximated simply by

$$R \approx \frac{Z_1(S)\mu_S}{Z_0}, \tag{4.7}$$

where the $Z_1(S) = \Pr(D|H_1)$ is the 'local evidence' (see Feroz et al. 2009) associated with the posterior peak under consideration in the single-cluster model, and $Z_0 = \Pr(D|H_0)$ is the 'null' evidence (which does not depend on S).

Our Bayesian analysis uses MultiNest to calculate the Bayesian evidence for the different hypotheses. When searching for clusters in some survey area A, a uniform prior $\pi(x_c, y_c) = 1/A$ is assumed on the position of any cluster, rather than assuming a uniform prior over the footprint S. Thus, MultiNest returns a local evidence associated with the posterior peak that is given by

$$\tilde{Z}_1(S) = \frac{S}{A} Z_1(S), \tag{4.8}$$

and the 'null' evidence $\tilde{Z}_0 = Z_0$ remains unchanged. Thus, if we denote the expected number of clusters in the survey area by $\mu_A = (A/S)\mu_S$, then Equation 4.7 becomes

$$R \approx \frac{\tilde{Z}_1(S)\mu_A}{\tilde{Z}_0} \tag{4.9}$$

Here $\tilde{Z}_1(S)$ and $\tilde{Z}_0$ are outputs of MultiNest and μ_A is easily calculated from Equation 4.2 (using a Fortran algorithm written by Carmen Rodriguez-Gonzalvez) given some assumed cluster mass function, and so R may then be calculated without exact knowledge of S. Moreover, the R value in Equation 4.9 can be turned into a probability p that the putative detection is indeed due to a cluster with mass $M_{T,\mathrm{lim}} < M_T < M_{T,\mathrm{max}}$ and centre lying in S, which is given by

$$p = \frac{R}{1+R}. \tag{4.10}$$

We run McAdam with two models: the first, a physical model, fits a parameterisation based on physical variables such as cluster mass and temperature; the second, a phenomenological model, fits a parameterisation based on observable quantities such as angular size and temperature decrement. For both cluster models we use the same source model, which is discussed in Section 5.8.

4.1.1 Physical Cluster Model

The SA observations of our survey data are analysed using a model characterised by the sampling parameters $\Theta = (\Theta_c, \Psi)$, where $\Theta_c = (x_c, y_c, \phi, f, \beta, r_c, f_g, M_{T,200}, z)$ are physical cluster parameters and $\Psi = (x_s, y_s, S_0, \alpha)$ are source parameters. Here x_c and y_c give the cluster position, ϕ is the orientation angle measured from N through E, f is the ratio of the lengths of the semi-minor (a) to semi-major (b) axes of the best fitting ellipse, β describes the shape of the cluster gas density ρ_g according to Cavaliere & Fusco-Femiano (1976) and Cavaliere & Fusco-Femiano (1978), where the gas density decreases with radius r

$$\rho_g(r) = \frac{\rho_g(0)}{[1 + (r/r_c)^2]^{\frac{3\beta}{2}}}, \tag{4.11}$$

r_c is the core radius, f_g is the baryonic mass fraction, $M_{T,200}$ is the cluster total mass within a radius r_{200} and z is the cluster redshift.

From the sampling parameters we are able to derive other cluster parameters such as the cluster gas mass ($M_{g,200}$), radius (r_{200}) and the cluster electron temperature (T). It should be noted that the physical β model that I have described is not the only cluster profile that McAdam can fit; for example, we are also able use the Navarro *et al.* (1995) (NFW) profile and Generalised NFW (GNFW) models (see e.g. AMI Consortium: Olamaie *et al.* 2010).

4.1.1.1 Priors

It is essential that we understand the effects of our priors in the calculation of Bayesian evidence values (Equation 4.9 and 4.10). Several of the priors, namely those on β, r_c, ϕ and f have been used extensively on simulations and observations of known clusters (see Feroz *et al.* 2009a, Zwart *et al.* 2010, AMI Consortium: Rodriguez-Gonzalvez *et al.* 2010 and AMI Consortium: Olamaie *et al.* 2010). For the f_g prior we have chosen to use a delta function on $0.154h_{70}^{-1}$; this value is derived from the results of Komatsu *et al.* (2010), who found that the universal baryonic mass fraction $f_b = 0.169 \pm 0.029h_{72}^{-1}$, taking into account our value for h and that the baryonic fraction in galaxy clusters is $\sim$0.9 (see e.g. McCarthy *et al.* 2007)of the universal baryonic mass fraction. For the analysis of known

clusters we (e.g. AMI Consortium: Rodriguez-Gonzalvez *et al.* 2011 and AMI Consortium: Shimwell *et al.* 2011) have used a Gaussian prior on f_g but for blind observations we have decided not to do this. This is because SZ data alone can not constrain f_g and there is a large degeneracy between $M_{T,200}$ and f_g. Such a degeneracy will produce a difficulty in determining whether the cluster mass is above a specified $M_{T,lim}$ and hence will complicate our R and p calculations. The effects of $x_c, y_c, M_{T,200}$ and z on R are less clear. To understand the effects of such priors I simulated AMI SA data according to Grainge *et al.* (2002). The search area prior must be uniform as we have not prior knowledge of cluster positions and I test the effects of varying the search area in Section 4.2.6. The options for $M_{T,200}$ and z priors are limited because our analysis technique requires that we use a prior on the cluster number counts as a function of redshift (Evrard *et al.* (2002) or Jenkins *et al.* (2001)), but we are able to alter the mass range of the prior – this is explored in Section 4.2.5. The standard priors for the physical cluster model are presented in Table 4.1. The Evrard *et al.* (2002) and Jenkins *et al.* (2001) joint $M_{T,200}$ and z prior is plotted in Figure 4.1 for several cluster masses.

Table 4.1: Priors used for the Bayesian analysis assuming a physical cluster model.

Parameter	Prior
Redshift (z)	0.2-2.0
	(Jenkins *et al.* 2001 or Evrard *et al.* 2002)
Core radius (r_c/h_{70}^{-1}kpc)	Uniform between 10 and 1000
Beta (β)	Uniform between 0.3 and 2.5
Mass ($M_{T,200}/h_{70}^{-1}M_{\odot}$)	$M_{T,lim}$ – 5 $\times 10^{15}$
	(Jenkins *et al.* 2001 or Evrard *et al.* 2002)
Gas fraction (f_g/h_{70}^{-1})	Set to 0.154
Cluster Position ($\mathbf{x_c}$)	Uniform search box
Orientation angle (ϕ/ deg)	Uniform between 0 and 180
Ratio of the length of semi-minor to semi-major axes (f)	Uniform between 0.5 and 1.0

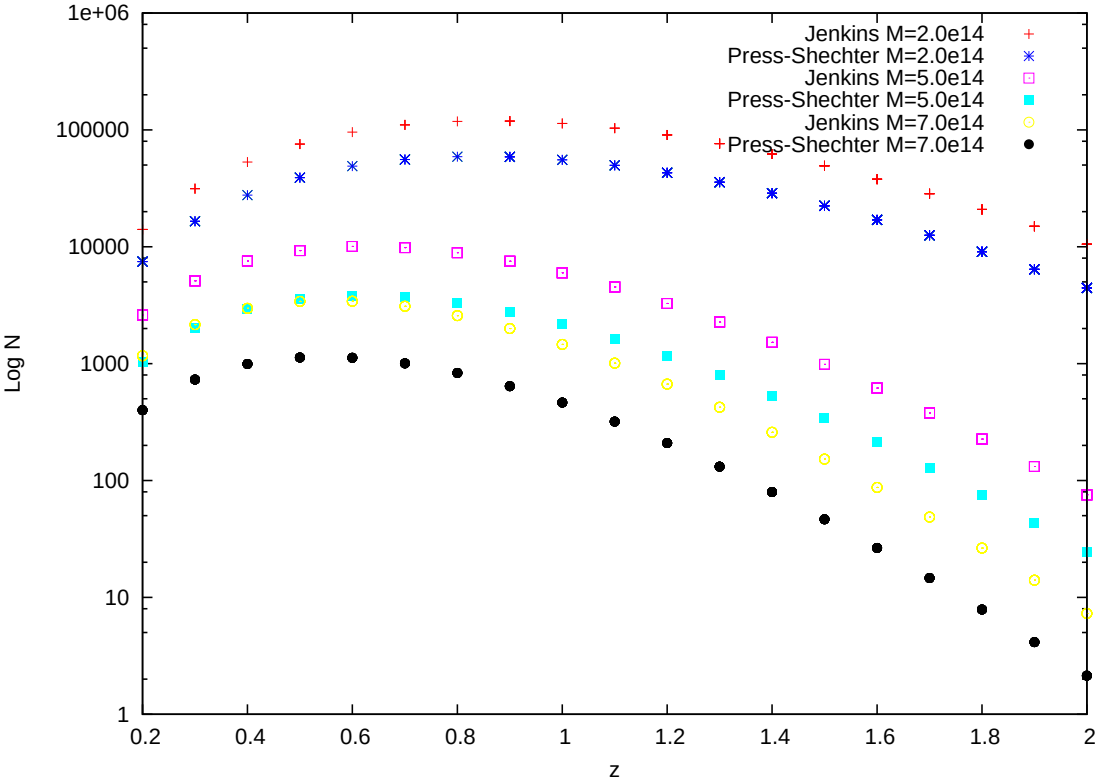

Figure 4.1: The (log) number of clusters (N) as a function of cluster redshift (z) predicted by Evrard *et al.* (2002) and Jenkins *et al.* (2001). I have included clusters of mass $M_{T,200} = 2.0 \times 10^{14}$, 5.0×10^{14} and 7.0×10^{14}.

4.1.2 Phenomenological Model

In this case, at the location of each putative cluster detection identified using the physical cluster model, we simply fit a β profile to the SZ temperature decrement using the parameters θ_c, β and $\Delta\mathrm{T}_0$ to characterise shape and magnitude of the decrement according to

$$\Delta T_{SZ} = \Delta T_0 \left(1 + \frac{\theta^2}{\theta_c^2}\right)^{(1-\frac{3\beta}{2})} . \tag{4.12}$$

4.1.2.1 Priors

We use non informative priors – the priors are wide enough to comfortably fit the probability distributions of the parameters derived from expected cluster observations. The derived temperature posterior distribution allows for the significance of an SZ temperature decrement to be assessed whilst taking into account the CMB anisotropies, radio sources and thermal noise.

The assumed priors on the phenomenological model parameters are summarised in Table 4.2.

Table 4.2: Priors used for the Bayesian analysis of the observational properties of the temperature decrement (equation 4.12).

Parameter	Prior
Cluster Position ($\mathbf{x_c}$)	Gaussian prior centred on candidate ($\sigma = 60''$)
ΔT_0	Uniform between -3000μK and -10μK
θ_c	Uniform between $20''$ and $500''$
β	Uniform between 0.3 and 2.5
Orientation angle (ϕ/ deg)	Uniform between 0 and 180
Ratio of the length of semi-minor to semi-major axes (f)	Uniform between 0.5 and 1.0

4.2 SZ Simulations

Simulations of SA observations were created in the PROFILE package (see Grainge *et al.* (2002)). In this package a two-dimensional image of a β profile cluster was created together with Gaussian random noise and primordial CMB (Lewis *et al.* 2000). The SA baselines and typical *uv* coverage were stated and the maps were convolved with the synthesized beam before being Fourier transformed to create simulated visibilities for the six SA channels. These realistic AMI simulations have been used to: estimate the mass limit ($M_{T,lim}$) of the AMI blind survey; demonstrate the robustness of the probability of detection calculation (Equation

4.9 and 4.10); and determine whether we can retrieve the simulated cluster parameters in our analysis of the data. In addition, I have used the simulations to understand the effects of changing $M_{T,lim}$ and the search area prior.

4.2.1 Simulation Properties

To perform simulations in PROFILE we input the cluster parameters z, T, β, r_c and the central electron number density n_{e0}. The simulations are performed with values $x_c, y_c, \phi, f, \beta, r_c, f_g$ and z that lie comfortably within our priors in Table 4.1. However, the lower end of the range of $M_{T,200}$ values in the simulations falls below the lower end of the range of the prior on this parameter – this is to understand how MCADAM interprets the signals from clusters whose true mass lies below $M_{T,lim}$.

To simulate clusters of different masses we note that if we assume that cluster gas is ideal and virialized, and that clusters are singular isothermal spheres whose kinetic energy is all in gas internal energy then the total cluster mass, $M_{T,200}$, can be calculated using

$$\mathrm{k_B T} = \frac{\mathrm{G}\mu\mathrm{M_{T,200}}}{2\mathrm{r_{200}}}, \tag{4.13}$$

where $\mathrm{k_B}$ is the Boltzmann constant, G is the gravitational constant and μ is the mass per particle. Assuming spherical symmetry we also have

$$M_{T,200} = \frac{4\pi}{3} r_{200}^3 200 \rho_{crit}(z). \tag{4.14}$$

By combining Equations 4.13 and 4.14 and using $\rho_{crit}(z) = \frac{3H(z)^2}{8\pi G}$ we find that

$$\frac{M_{T,200}}{10^{15} h^{-1} M_\odot} = \left(\frac{k_B T}{8.2\mathrm{keV}}\right)^{3/2} \left(\frac{H_0}{H(z)}\right). \tag{4.15}$$

Here H is the Hubble parameter and $H(z)$ is given by

$$H^2(z) = H_0^2(\Omega_M(1+z)^3 + \Omega_\Lambda), \tag{4.16}$$

where Ω_M is the matter density ($\Omega_M = \frac{\rho_{m0}}{\rho_{crit}(0)} = \frac{8\pi G}{3H_0^2}\rho_{m0}$, where ρ_{m0} is the present matter density) and Ω_Λ is the energy density of the vacuum ($\Omega_\Lambda = \frac{\Lambda c^2}{3H_0^2}$ where Λ is the cosmological constant). Here we have assumed that the universe has zero

curvature. Thus, Equation 4.15 implies that $M_{T,200}$ is dependent only on T, z, Ω_M and Ω_Λ. The cluster gas mass ($M_{g,200}$) is given by

$$M_{g,200} = 4\pi \int_0^{r_{200}} r^2 \rho_g(r) dr, \tag{4.17}$$

where $\rho_g(r)$ is described by the β profile (Equation 4.11).

I have simulated two types of cluster:

- Group A – $\rho_{crit}(0.2) = \frac{3H(0.2)^2}{8\pi G}$.
- Group B – $\rho_{crit}(z) = \frac{3H(z)^2}{8\pi G}$

For all the simulations I set $f_{g,200} = \frac{M_{g,200}}{M_{T,200}} = 0.154 h_{70}^{-1}$ to match the McAdam prior (Table 4.1) but the mass and redshift of the simulated cluster are varied. For simulations in group A, $\rho_{crit}(z)$ is calculated at $z = 0.2$ for all simulations. Hence, group A simulations take the same physical object (i.e. of particular fixed temperature and radius) and move it to a different z. For group A simulations I vary $M_{T,200}$ by altering T and to obtain the desired $f_{g,200}$ I tweak $M_{g,200}$ via its dependence on r_c. For the simulations in group B the $\rho_{crit}(z)$ value varies with z, so to take a cluster of a specific $M_{T,200}$ to a different z (keeping $f_{g,200} = 0.154 h_{70}^{-1}$), both T and r_c must be altered. For group B simulations physical properties of the cluster change with z. Hence, group A and group B simulations are effectively non-evolving and evolving cluster models.

I have simulated clusters with masses in the range $1 - 10 \times 10^{14} M_\odot h_{70}^{-1}$ and redshifts in the range 0.2-2.0. The iteration in total mass between simulations is $0.2 \times 10^{14} M_\odot h_{70}^{-1}$ and the redshift iteration is 0.1. Each simulation of a particular $M_{T,200}$ and z is simulated with 10 random realisations of the primary CMB. Therefore, in total we have 8740 unique simulations in each group A and B. For all simulations the CMB contribution is calculated using a power spectrum of primary anisotropy that has been generated for $l < 8000$ using CAMB (Lewis *et al.* 2000) with a ΛCDM cosmology ($\Omega_m = 0.3$, $\Omega_\Lambda = 0.7$, $\sigma_8 = 0.8$ and $h = 0.7$) assumed. Each simulation consisted of four observations each lasting a duration of eight hours. A rms noise of 0.6Jy per baseline in one second was included to provide to a total Gaussian random noise level with an rms of 110μJy/beam (no uv taper) on each set of four concatenated observations – this is a good match

to the thermal noise level in our concatenated SA survey field observations. The simulated data were smoothed by 200. The parameters used for both groups of simulated clusters are summarised in Table 4.3.

Table 4.3: Parameters of simulated clusters.

Parameter	
Cluster position (J2000)	03 00 08.66 +26 15 16.1
Mass ($M_{T,200}/h_{70}^{-1}M_{\odot}$)	1 $\times 10^{14}$ - 10 $\times 10^{14}$
Redshift (z)	0.2-2.0
Gas fraction (f_g/h_{70}^{-1})	0.154
Beta (β)	0.8
Core radius (r_c/h_{70}^{-1}kpc)	100 – 220 (A) 100 – 310 (B)
Temperature (T/keV)	1.49 - 6.90 (A) 1.49 - 13.35 (B)
Central electron number density ($n_{e0}/m^{-3}h_{70}^{-1}$)	0.01 $\times 10^{-6}$
Orientation angle (ϕ/ deg)	0
Ratio of the length of semi-minor to semi-major axes (f)	1.0

4.2.2 The Mass Limit of the AMI Survey

The AMI blind cluster survey has a well defined $M_{T,lim}$ only if for a specific value of $M_{T,200}$ the magnitude of the SZ decrement is independent of the cluster redshift. Previously there have been several attempts to find the mass limit of the AMI survey. In Culverhouse (2006), the AMI selection was explored and 25,000 clusters were simulated with masses in the range $4\times10^{12}h_{70}^{-1}M_{\odot} < M_{T,200} < 1\times10^{15}h_{70}^{-1}M_{\odot}$ at redshifts $0 < z < 4$ according to Evrard *et al.* (2002) and Jenkins *et al.* (2001). The simulated clusters were inserted into simulated AMI observations with a realistic thermal noise (100μJy/beam), CMB and point source contamination. The signal to noise for each simulated cluster was calculated and a plot of the limiting mass function verses redshift was presented – this is shown in Figure 4.2. In Culverhouse (2006) the selection function has a significant redshift dependence and shows that AMI is expected to be able to detect less massive clusters at

higher z; the selection function is steepest at $z < 0.6$. For $z > 0.6$ AMI is expected to detect clusters with $M_{T,200} \geq 3.0 \times 10^{14} M_{\odot} h_{70}^{-1}$. In Culverhouse (2006) the effects of varying the thermal noise level, cluster density profile and cosmology on the selection function are explored. In Hurley-Walker (2009) the mass limit of the survey was estimated using SA observations of the relaxed, small, low-temperature cluster Abell 2259. Hurley-Walker (2009) derived $M_{T,lim}$ by assuming $S \propto M^{5/3}$, where S is the SZ flux from a cluster. Using an estimate of the mass of Abell 2259 together with the noise on the Abell 2259 observations and an estimate of the survey noise (σ_{sur}) Hurley-Walker (2009) derived that at $4\sigma_{sur}$ it should be possible to detect Abell 2259 like clusters with a mass higher than $M_{T,lim} = 2.0 \times 10^{14} M_{\odot} h_{100}^{-1}$ ($M_{T,lim} = 2.9 \times 10^{14} M_{\odot} h_{70}^{-1}$).

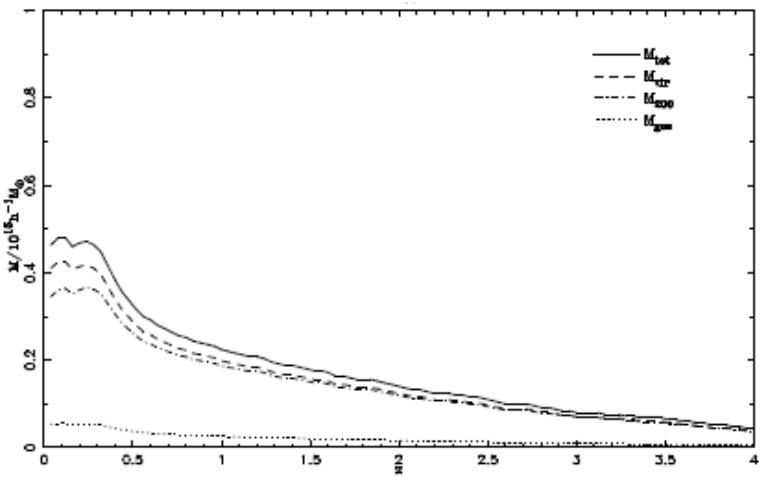

Figure 4.2: A simulated AMI blind survey selection function from Culverhouse (2006) for a thermal noise of 100μJy/beam with realistic CMB and radio source contamination. Here the lowest detectable (limiting) mass is plotted against redshift. The limiting mass decreases with redshift due to the electron density and temperature increasing with redshift and also because the angular size of the clusters is better match to the AMI synthesized beam at higher redshift. The results are presented for M_{tot}, M_{vir}, M_{200} and M_{gas}. Here $h = h_{70}$.

I have calculated $M_{T,lim}$ by evaluating how the flux of the SZ decrement

varies as a function of simulated $M_{T,200}$ and z. Each simulation (in both groups A and B) was mapped using AIPS (example maps are presented in Figure 4.3) and the resulting map was searched for decrements within 60″ of the simulated cluster position and of a peak flux greater than three times the thermal noise of the simulation (σ_{sim}). Figure 4.4 shows the magnitude of these decrements as a function of the simulated $M_{T,200}$ and z for both groups A and B. Figure 4.5 shows the variation of decrement with z and CMB realisation for the most massive cluster simulated ($M_{T,200} = 1.0 \times 10^{15} M_{\odot} h_{70}^{-1}$).

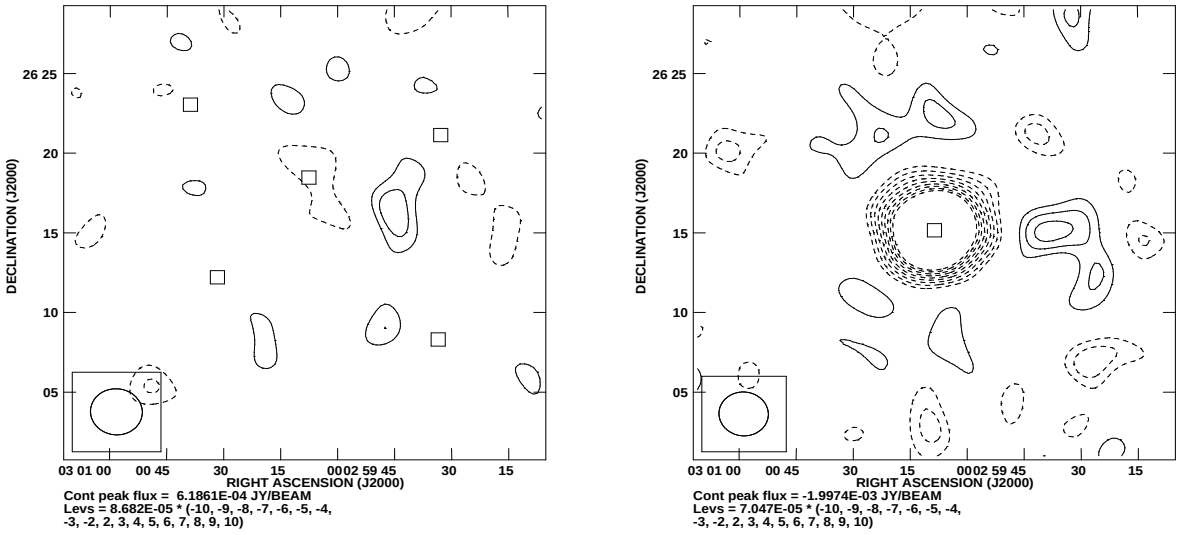

Figure 4.3: Simulated group B cluster maps. The cluster on the left is simulated with $M_{T,200} = 1 \times 10^{14} M_{\odot} h_{70}^{-1}$ and the simulation on the right is of a cluster with$M_{T,200} = 1 \times 10^{15} M_{\odot} h_{70}^{-1}$. Both simulations are at redshift 1.0. Each map uses a different CMB realisation and there are no simulated point sources. Therefore, all features on these maps arise from a cluster signal, CMB and thermal noise. The boxes represent the positions of the modes detected by McADAM, note that the$M_{T,200} = 1 \times 10^{14} M_{\odot} h_{70}^{-1}$ is not a significant detection. These maps have not been primary beam corrected.

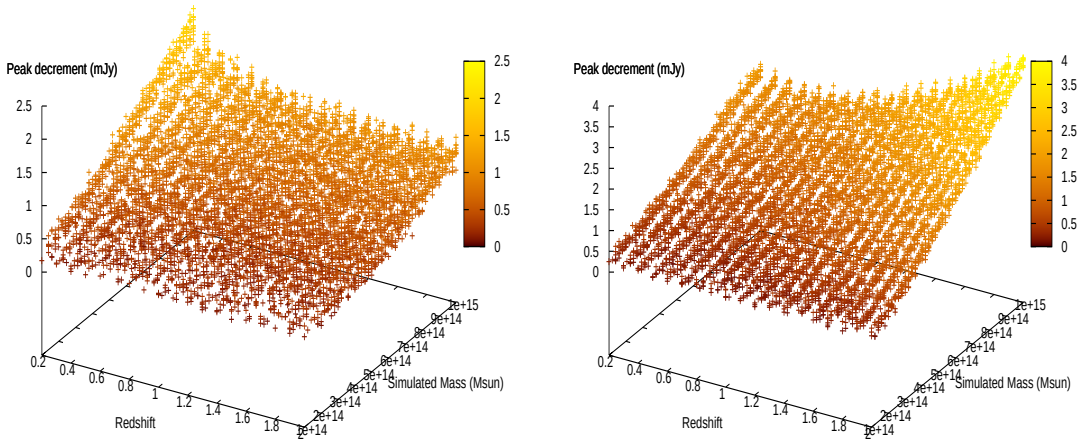

Figure 4.4: The magnitude of the peak decrement of the simulated SZ effect against the simulated cluster mass and redshift. On the left $\rho_{crit}(z)$ is fixed at redshift 0.2 for all simulations (group A) whereas on the right $\rho_{crit}(z)$ is redshift dependent (group B).

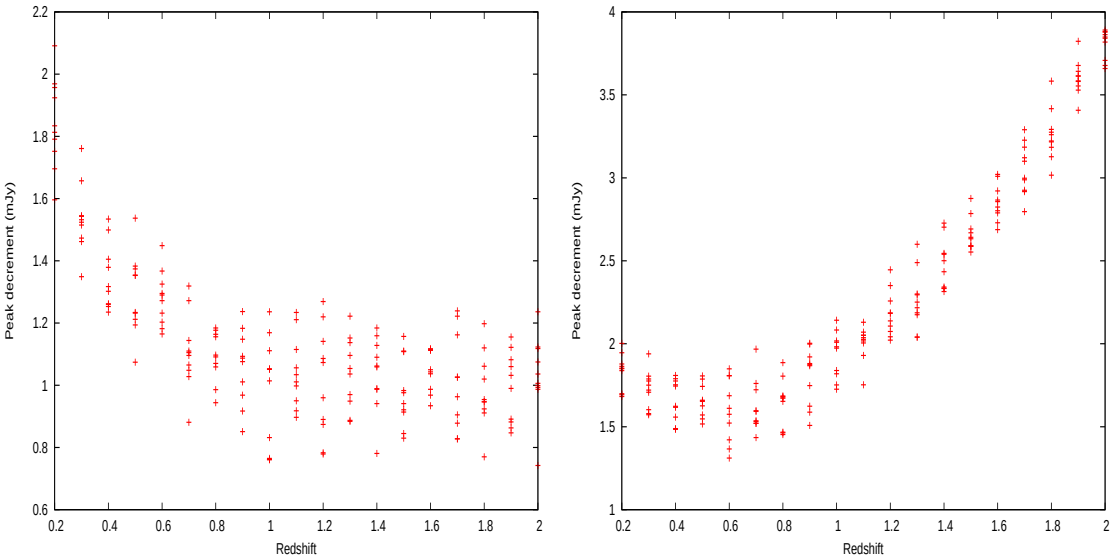

Figure 4.5: A slice taken through the above plots at a simulated cluster mass of $M_{T,200} = 1.0 \times 10^{15} M_{\odot}$. Group A results are on the left and group B results are on the right. The 10 different peak decrements at each z correspond to the 10 random CMB realisations.

All group A simulations of a specific mass have an equal central y-parameter (Equation 1.26); however, due to synthesized beam dilution we find that the recorded peak decrement of a group A cluster of specific mass (Figures 4.4 and 4.5) is redshift dependent – the steepest dependence occurs at $z < 0.6$. The magnitude of the effects of beam dilution is related to both the cluster y-parameter profile and the angular diameter distance to the cluster (Figure 1.8). For example, consider a group A simulated cluster of mass $M_{T,200} = 1.0 \times 10^{15} M_{\odot} h_{70}^{-1}$ at either $z = 0.2$ or $z = 1.0$. For the cluster simulated at $z = 0.2$ the y-parameter drops significantly slower with angular distance from the cluster centre than for the same cluster simulated at $z = 1.0$ (see Figure 4.6). Hence, even though group A clusters of the same mass all have equal central y-parameters, the y-parameter within the AMI synthesized beam ($3'$) is substantially different, and we expect the peak decrement on the map to vary with z. However, the peak decrement would not vary with z for an instrument with infinite resolution.

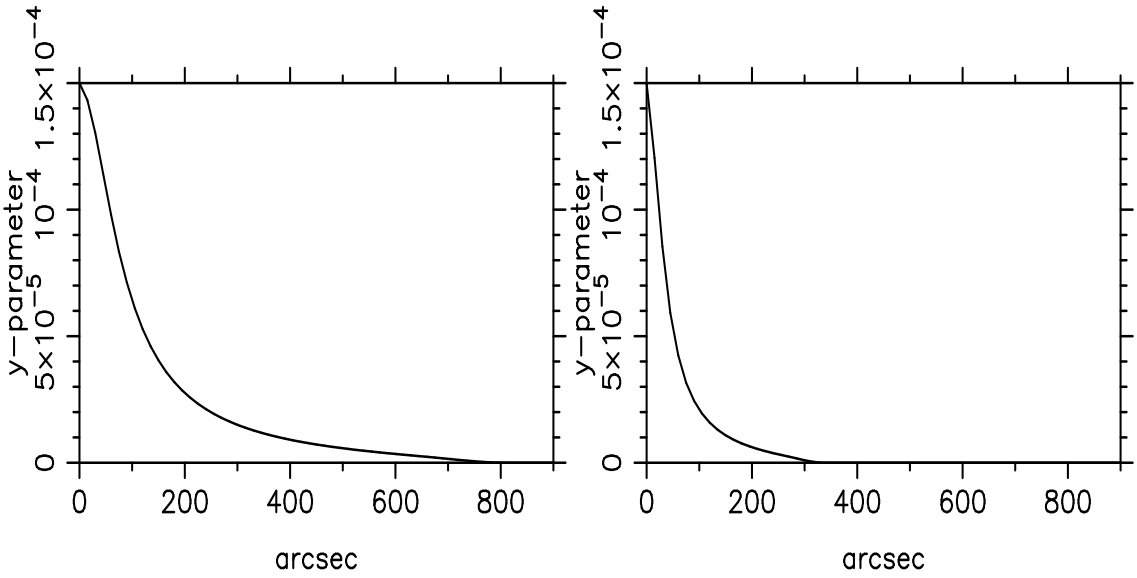

Figure 4.6: The y-parameter for a $M_{T,200} = 1 \times 10^{15} M_{\odot} h_{70}^{-1}$ mass cluster (group A) as a function of angular distance from the cluster centre. On the left the redshift of the cluster is 0.2 and on the right it is 1.0.

For roup B simulations the central y-parameter for a specific mass cluster

is dependent on redshift because the temperature as well as the core radius is redshift dependent (see Equation 4.15). For example, a simulated cluster of mass $M_{T,200} = 1 \times 10^{15} M_{\odot} h_{70}^{-1}$ at $z = 0.2$ has $T = 6.90$keV, whereas a cluster at $z = 2.0$ has $T = 13.35$keV. Hence, a cluster of $M_{T,200} = 1 \times 10^{15} M_{\odot} h_{70}^{-1}$ at $z = 2.0$ has a significantly larger y-parameter than a cluster of the same mass at $z = 0.2$. The curvature of the peak signal with redshift (Figures 4.4 and 4.5) is due to a combination of the y-parameter changing and beam dilution. Figure 4.7 shows the y-parameter as a function of angular distance for a group B simulated cluster of mass $M_{T,200} = 1.0 \times 10^{15} M_{\odot} h_{70}^{-1}$ at $z = 0.2$ and $z = 1.0$.

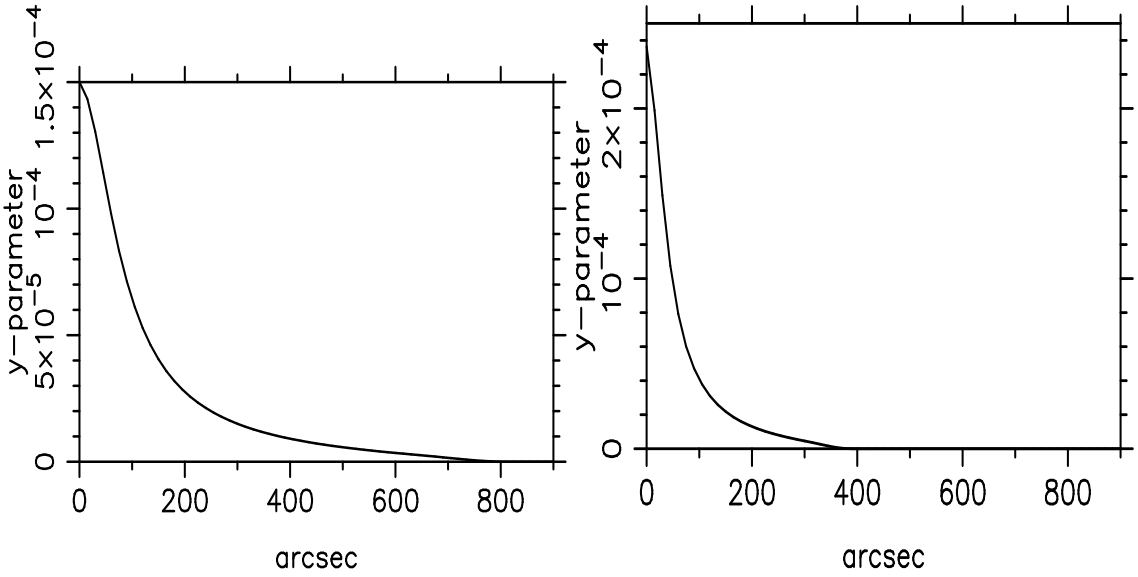

Figure 4.7: The y-parameter for a $M_{T,200} = 1 \times 10^{15} M_{\odot} h_{70}^{-1}$ mass cluster (group B) as a function of angular distance from the cluster centre. On the left the redshift of the cluster is 0.2 and on the right it is 1.0. Note that the Figure on the left is identical to the group A simulated cluster of this mass and redshift (Figure 4.6), this is because group A simulations use $\rho_{crit}(0.2)$. However, the Figure on the right is for a group B cluster simulated $z = 1.0$, this has a slightly smaller angular extent and significantly higher central y-parameter than the equivalent group A simulation, the reason for this is that both T and r_c are different.

To determine the probability that a cluster of a certain $M_{T,200}$ will produce

a signal greater than 3 times the thermal noise, I have chosen to calculate the weighted (over z) proportion of clusters that are detected at each value of $M_{T,200}$. I use the Evrard *et al.* (2002) approximation to Press & Schechter (1974) or Jenkins *et al.* (2001) cluster number counts to weight each simulation. Given the model number count, $C(M_{T,200}, z)$ at a specific $M_{T,200}$ and z, I weight each simulation according to

$$W(M_{T,200}, z) = \frac{C(M_{T,200}, z)}{\sum_{z=0.2}^{2.0} C(M_{T,200}, z)}. \tag{4.18}$$

The weighted probability of the decrement being $>3\sigma_{sim}$ versus $M_{T,200}$ is shown for both simulation groups A and B in Figure 4.8.

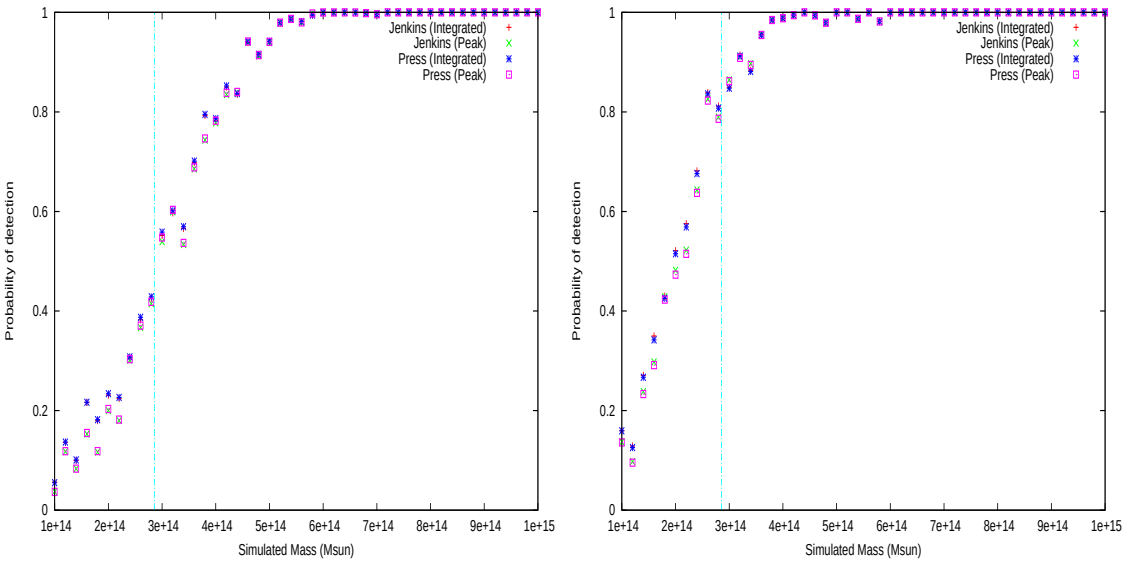

Figure 4.8: The proportion of clusters detected at $S > 3\sigma_{sim}$ as a function of mass. The Evrard *et al.* (2002) approximation to Press & Schechter (1974) and the Jenkins *et al.* (2001) cluster number counts were used for the weighted averaging over the simulated z range. The results are shown for both peak and integrated fluxes. On the left $\rho_{crit}(z)$ is fixed at redshift 0.2 for all simulations (group A) whereas on the right $\rho_{crit}(z)$ is redshift dependent (group B). The value $M_{T,lim} = 2.9 \times 10^{14} M_{\odot} h_{70}^{-1}$ is marked with a vertical line and corresponds to the $M_{T,lim}$ value that was derived in Hurley-Walker (2009).

The simulations have revealed the magnitude with which the signal from a cluster of specific mass (either group A or B) is redshift dependent. There are also other effects that make deciding upon a value for $M_{T,lim}$ difficult, such as: the true CMB contamination at a specific position rather than a statistical CMB contribution; accounting for different cluster morphologies and density profiles; point source contamination; the variation of f_g with redshift and systematics in the SA data. However, group A simulations have a much better defined $M_{T,lim}$ than those from group B. Unfortunately, our prior on $n(z, M)$ is obtained from simulations that have used a redshift-dependent ρ_{crit}. Hence, until $n(z, M)$ is derived for a redshift independent ρ_{crit} our analysis is restricted to group B type simulations only.

The $M_{T,lim} = 2.9 \times 10^{14} M_{\odot} h_{70}^{-1}$ value that was derived in Hurley-Walker (2009) is similar to the results presented in Culverhouse (2006) for clusters at $z > 0.6$ and agrees well with my simulations. In Figure 4.8 I find that 80% of the group B simulated clusters are detected above this mass.

4.2.3 Probability of Cluster Detection

The group B simulations described in the previous section were run through McAdam using the priors shown in Table 4.1, $M_{T,lim} = 2.9 \times 10^{14}\ h_{70}^{-1} M_{\odot}$ and a uniform search box centred on the pointing centre with sides of $1000''$. The Bayesian evidences $\tilde{Z}_1$ and $\tilde{Z}_0$ were calculated and used together with the cluster number counts (μ_A) to calculate the p and R values, which are related simply by Equation 4.10, of all putative cluster detections.

In most simulations, McAdam detected multiple modes – in the 8740 simulations a total of 27233 modes were detected, many of which do not correspond to the simulated cluster (I deal with these later in this Section). In Figures 4.9 and 4.10 I plot the mean p and R values for each mode that corresponds to a simulated cluster. These modes are identified as those with a mean position within $2.5'$ of the simulation cluster position. The lowest probability of detection occurs for the $M_{T,200} = 1 \times 10^{14} M_{\odot} h_{70}^{-1}$ simulations and the largest for the $M_{T,200} = 1 \times 10^{15} M_{\odot} h_{70}^{-1}$ simulations; however, for a cluster of given mass there is a significant redshift dependence in the p and R values.

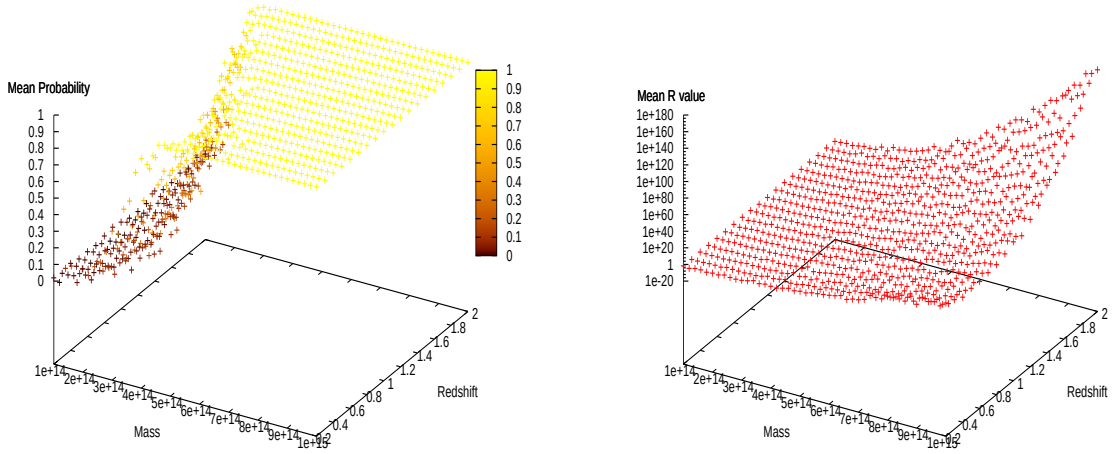

Figure 4.9: The p and R values for clusters of different simulated masses. On the left I present the p values and on the right are the corresponding R values. For these calculations I have used the priors listed in Table 4.1, $M_{T,lim} = 2.9 \times 10^{14}$ $h_{70}^{-1} M_{\odot}$ and a uniform search box of size $1000'' \times 1000''$.

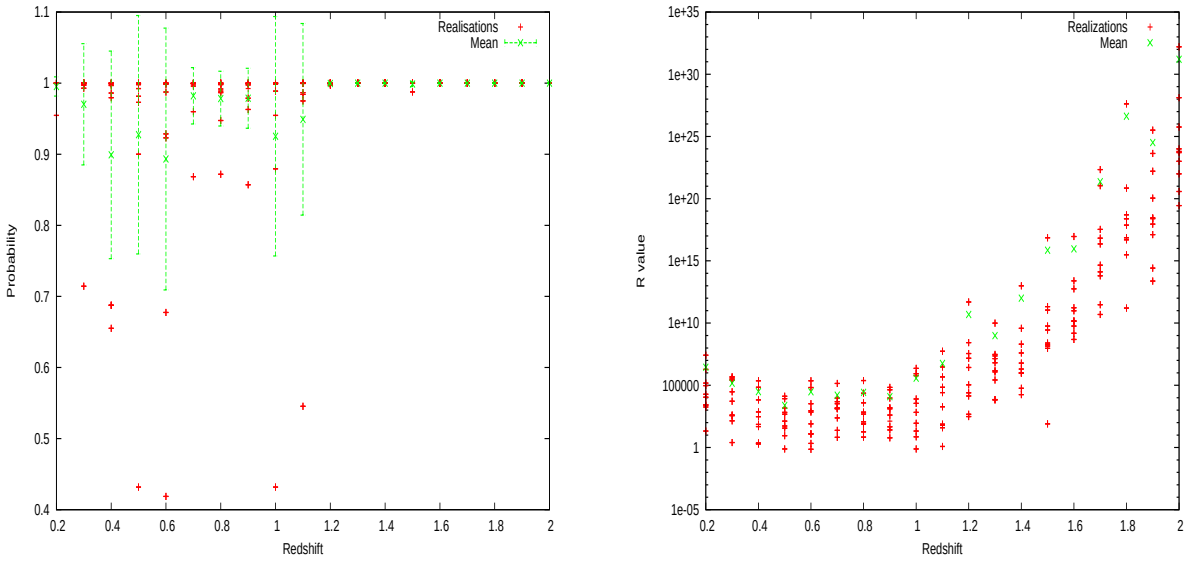

Figure 4.10: The p and R values of the $M_{T,200} = 5 \times 10^{14} M_{\odot} h_{70}^{-1}$ simulations, taken from the above plots. I show the derived values for each of the 10 CMB realisations at each redshift, I also plot the mean value with error bars that correspond to the rms of the values obtained from the 10 CMB realisations.

The p and R value curves in Figure 4.9 indicate that in a manner reminiscent to the peak decrement probability of detection graph (Figure 4.4 right), the McAdam derived probability of detection is not just function of $M_{T,200}$ but has a significant z dependence. Figure 4.10 shows that for the $M_{T,200} = 5 \times 10^{14} M_{\odot} h_{70}^{-1}$ simulation the R value varies from as low 1 at $z = 0.3$ up to 1×10^{30} at $z = 2.0$, the corresponding p values are ≈ 0.4 to 1.0 respectively. The redshift that has a dramatic effect on the derived R value. However, the CMB realisation also has a significant impact, unfavourable CMB realisations may have an R value $\sim \times 10^5$ lower than favourable CMB realisations. All but 9 of the 190 simulations at $M_{T,200} = 5 \times 10^{14} M_{\odot} h_{70}^{-1}$ are detected with probability of detection, p, of greater than 0.8.

In Figure 4.11 I present the weighted mean for the p and R values as a function of mass. Jenkins *et al.* 2001 and Evrard *et al.* 2002 number counts have been used for the weighting. The weighting seems to have an insignificant effect on our results.

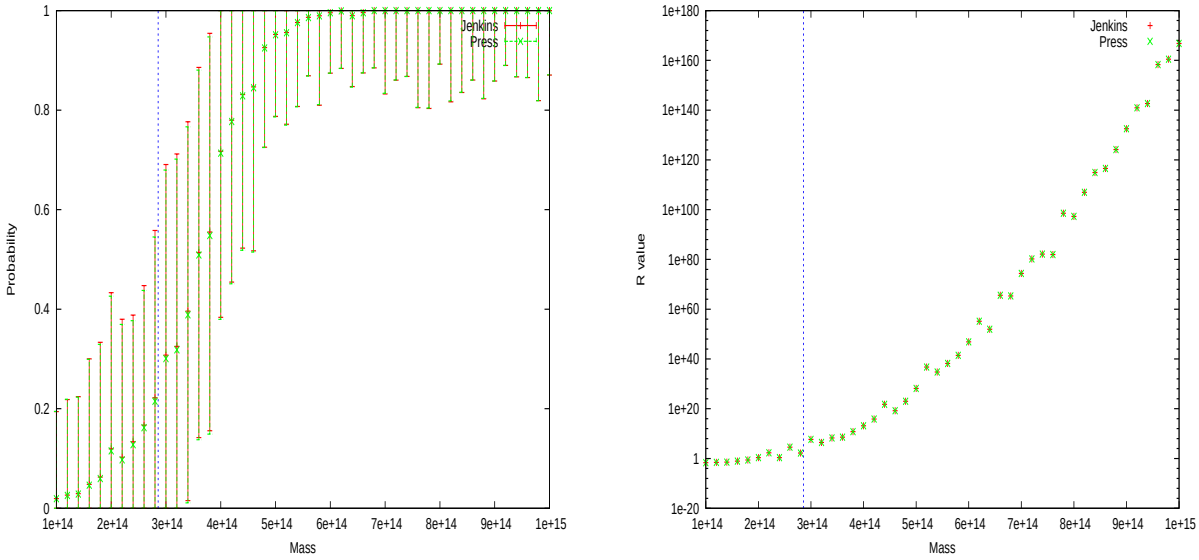

Figure 4.11: The weighted mean p and R values as a function of mass. The weighting used either the Jenkins *et al.* 2001 and Evrard *et al.* 2002 number counts. The error bars on the p values are large because for a cluster of a particular mass there is a significant redshift dependence on the derived p value (see Figure 4.9).

The weighted mean of the p value versus redshift bears a significant resemblance to the probability of detection curves calculated from the measured decrements on the maps (Figure 4.8 right). The shape of the curve is the same, although in the McAdam derived probabilities the entire curve is shifted to higher $M_{T,200}$. Rather than $2.9 \times 10^{14} M_{\odot} h_{70}^{-1}$ corresponding to ≈80% of clusters being detected (above $3\sigma_{sim}$), we find that this mass corresponds to a weighted mean probability of detection of ≈30%. It is not until the clusters are simulated with a mass $> 4 \times 10^{14} M_{\odot} h_{70}^{-1}$ that we obtain a mean probability of detection of ≈80%. This shift is expected because McAdam uses estimated cluster number counts to account for the probability that the decrement is caused by a noise feature.

In Figure 4.12 I present a plot showing all the false detections as a function of the simulated mass and redshift. These false detections are defined as being those which are more than $2.5'$ away from the simulated cluster position.

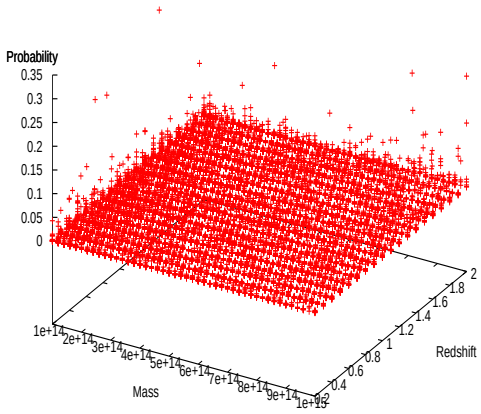

Figure 4.12: A plot showing the derived p values for false-positive detections that McAdam has identified; these do not correspond to significant decrements in the map plane. For these low p values the R value of a mode is almost equal to its P value. For these calculations I have used the priors given in Table 4.1 and $M_{T,lim} = 2.9 \times 10^{14}\ h_{70}^{-1} M_{\odot}$. The highest probability of detection for an false-positive identifications is 0.3.

The highest probability of a false detection is 0.3. On Figure 4.11 this value would correspond to $M_{T,200} = 3.0 \times 10^{14} M_{\odot} h_{70}^{-1}$, but the error bars indicate that we would also be likely to find many higher and lower mass clusters that produce a feature from which McAdam derives this probability. For the vast majority of the false detections we obtain probability of detection values at $< 5\%$. For candidates detected with $30 < p < 90\%$ I would recommend that further independent AMI observations be used to confirm the cluster candidates existence or non existence.

4.2.4 A Comparison Between Simulated and Derived Mass

For simulated clusters that are detected by McAdam, it is important to determine whether the simulated cluster parameters are recovered accurately and of primary importance is the mass parameter. Clusters from simulation group B

have been run through McAdam twice: firstly, with a log uniform prior on the mass ($1 - 10 \times 10^{14}\ h_{70}^{-1} M_{\odot}$) and a delta prior on the redshift (B1), secondly, with the Jenkins *et al.* (2001) number count as a joint prior on mass and redshift (B2). For the other priors both runs use those given in Table 4.1 and a uniform search box of $1000'' \times 1000''$.

In Figure 4.13 I present the mean derived McAdam mass (averaged over 10 CMB realisations) as a function of simulated mass and redshift for both runs B1 and B2. Figure 4.14 shows the mean mass and the mass derived from each realisation for the clusters simulated with $M_{T,200} = 1.0 \times 10^{15}\ h_{70}^{-1} M_{\odot}$.

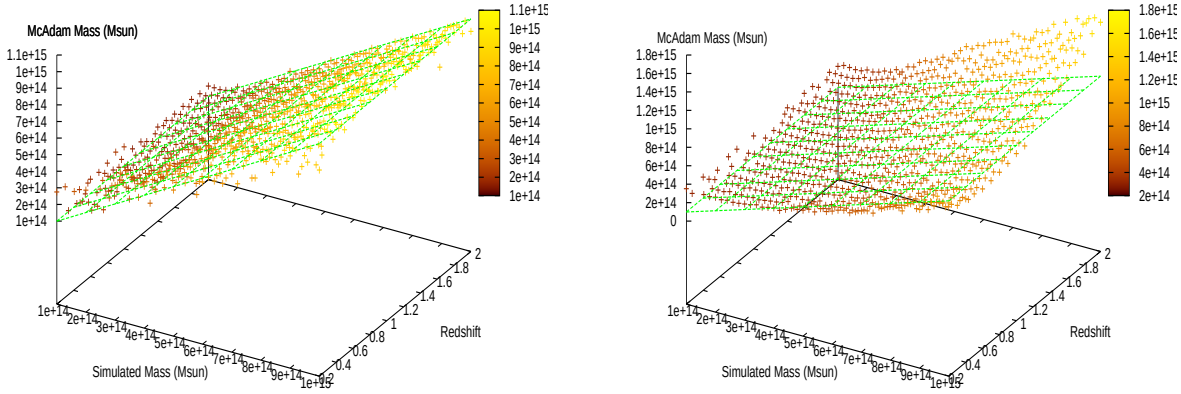

Figure 4.13: The variation in the McAdam derived mass as a function of simulated cluster mass and redshift. The plot on the left shows the results when McAdam is run with a log uniform prior on the mass and a delta prior on the redshift (B1) and on the right McAdam has been run with the Jenkins *et al.* (2001) number count as a joint prior on mass and redshift (B2). The lower limit on the mass prior is $1 \times 10^{14}\ h_{70}^{-1} M_{\odot}$ for B1 runs; for B2 runs the lower limit is $2.9 \times 10^{14}\ h_{70}^{-1} M_{\odot}$. Every McAdam derived mass value must be above the lower limit and this introduces the curvature at low masses that we see in both plots.

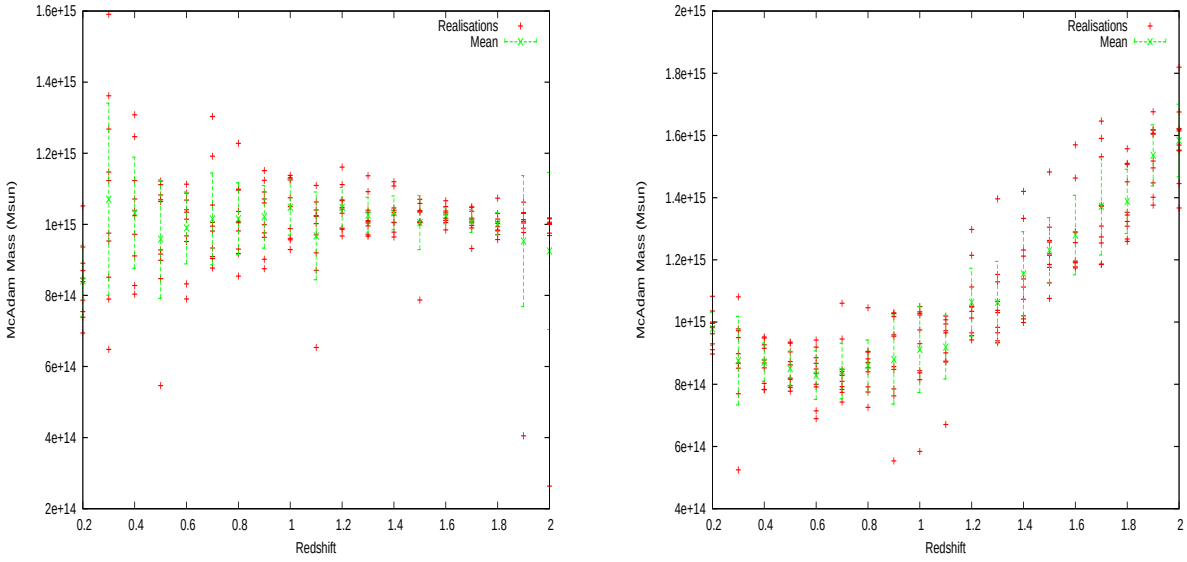

Figure 4.14: A slice taken from the above plots along simulated mass $M_{T,200} = 1.0 \times 10^{15}\ h_{70}^{-1} M_{\odot}$, including the independent results from all the different CMB realisations. Left – B1 runs. Right – B2 runs.

Figures 4.13 and 4.14 demonstrate that McAdam is able to derive the correct cluster mass when it is given the cluster redshift (B1). For blind clusters McAdam is run with only prior knowledge of the cluster number counts as a function of mass and redshift (Jenkins *et al.* (2001) prior, run B2) we are unable to accurately recover the simulated mass of the cluster. Instead, the apparent curve in the derived mass for a cluster of a specific mass has a significant redshift dependence, this behaviour is similar to the peak decrement on the map as a function of redshift (group B in Figures 4.4 and 4.5).

In Figure 4.15 I present the weighted mean derived McAdam mass as a function of input simulated mass. Here I have used the Jenkins *et al.* (2001) number counts for the weighting.

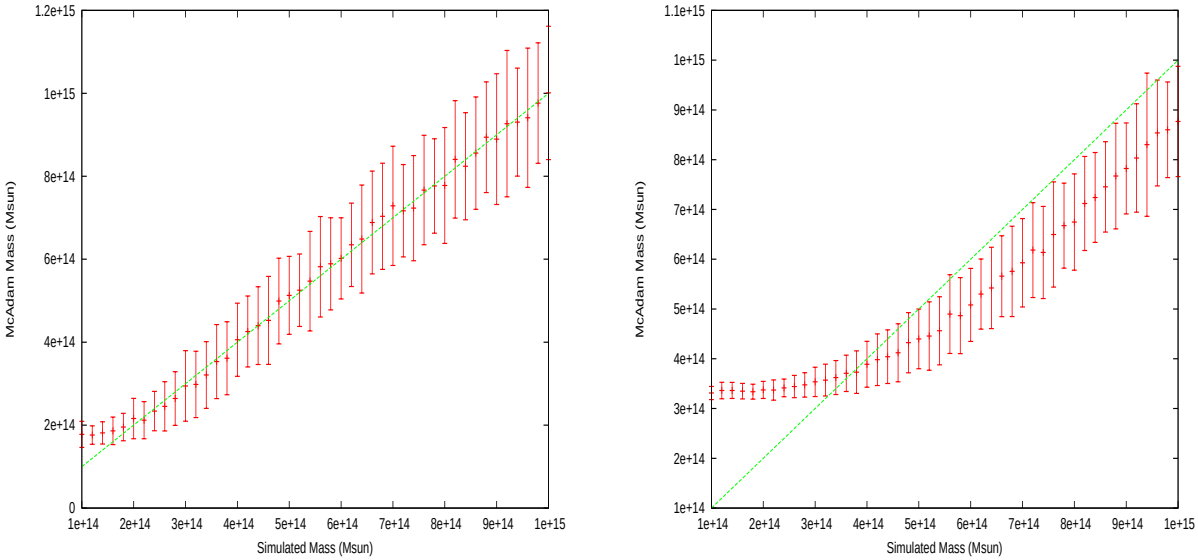

Figure 4.15: The McAdam derived mass as a function of simulated mass, averaged over redshift and different CMB realisations. The plot on the left is for runs B1 (log uniform prior on the mass and a delta prior on the redshift) and on the right are the B2 results from runs with the Jenkins *et al.* (2001) joint prior on mass and redshift. For both B1 and B2 McAdam always outputs a mean mass higher than the lower limiting prior ($1 \times 10^{14} M_{\odot} h_{70}^{-1}$ for B1 and $2.8 \times 10^{14} M_{\odot} h_{70}^{-1}$ for B2). This explains the McAdam overestimates for the mass of low-mass clusters.

It is very important that the results presented in Figure 4.15 are clarified. When McAdam is run with B1 priors we obtain a good mass estimate, but when run with the B2 priors the mass estimate is significantly discrepant from the real cluster mass. Initially, this seemed like a problem with the analysis, but it can be explained by the degeneracy between redshift and mass (see Figure 4.16). The Jenkins *et al.* (2001) prior follows hierarchical structure formation and as such predicts that there are fewer high mass clusters than low mass clusters and that these high mass clusters lie at low redshift. However, for our simulations we have sampled uniformly in both z and $M_{T,200}$. As a consequence of our $n(z, M)$ priors it may be expected that McAdam typically underpredicts the cluster mass. Additionally because of the degeneracy between mass and redshift we have a large degree of uncertainty in the derived parameters (Figure 4.16 shows the parameters derived from B2 runs of a cluster simulated with $M_{T,200} = 1 \times 10^{14} M_{\odot} h_{70}^{-1}$ and from a cluster simulated with $M_{T,200} = 1 \times 10^{15} M_{\odot} h_{70}^{-1}$ – corresponding maps for these simulations are shown in Figure 4.3).

Figure 4.15 should not be interpreted as evidence that analyses with a Jenkins *et al.* (2001) prior overestimate the mass of the low mass clusters. This is not the case as long as one looks at the corresponding detection probability. The reason for this apparent overestimation is that the mass prior range begins at $M_{T,lim} = 2.9 \times 10^{14}\ h_{70}^{-1} M_{\odot}$, hence any object that McAdam detects must be given a mass greater than this. This behaviour also occurs in B1 simulations, but in that case the lower mass limit is $M_{T,200} = 1 \times 10^{14} M_{\odot} h_{70}^{-1}$. It is clear from the probability of detection calculation that McAdam does not conclude that these low mass cluster exists. It is also apparent from the $M_{T,200}$ probability distribution of the $M_{T,200} = 1 \times 10^{14} M_{\odot} h_{70}^{-1}$ presented in Figure 4.16 which shows that the probability distribution is pressed towards the lower limit of the prior.

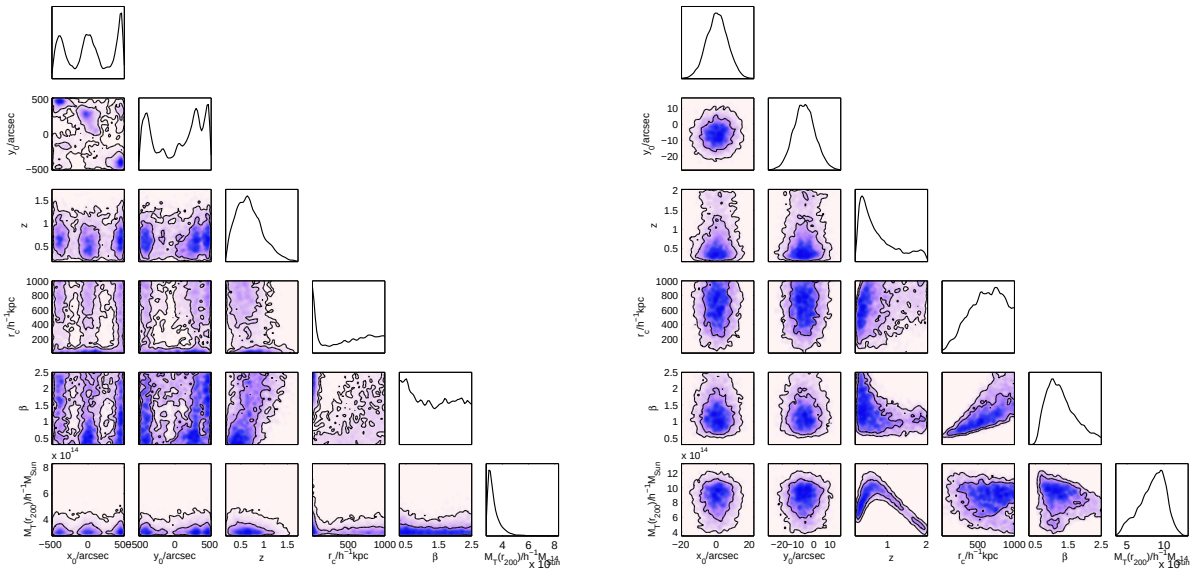

Figure 4.16: McAdam derived parameters from cluster simulations. On the left are the derived parameters from a cluster simulated $M_{T,200} = 1 \times 10^{14} M_{\odot} h_{70}^{-1}$ ($p = 0.0$) and on the right is the parameters for a cluster simulated with $M_{T,200} = 1 \times 10^{15} M_{\odot} h_{70}^{-1}$. The lower mass cluster is a non-detection ($p = 0.0$) whereas the higher mass cluster is detected with $p = 1.0$. Both simulations are at redshift 1.0.

In conclusion to this subsection I emphasise that although the Jenkins *et al.* (2001) prior can be used to calculate the probability of detection it does not produce a mass estimate that is necessarily indicative of the real cluster mass. However, if we obtain redshift information we are able to accurately recover the true mass.

4.2.5 Testing the Influence of the Mass Limit on the Probability of Detection

The concept of a limiting cluster mass ($M_{T,lim}$) is fundamental to the extraction of probabilities from the Bayesian evidences. Without an $M_{T,lim}$ value neither the numerator or the denominator in Equation 4.9 can be determined nor can

we estimate the expected number of clusters within a region. In this subsection I demonstrate how the value of μ_S, the evidences and the probability of cluster detection vary as a function $M_{T,lim}$.

A group B cluster simulated with a mass of $M_T = 5 \times 10^{14} h_{70}^{-1} M_\odot$ at a redshift of 1.0 was run through McAdam with $1 \times 10^{14}\ h_{70}^{-1} M_\odot < M_{T,lim} < 9 \times 10^{14}\ h_{70}^{-1} M_\odot$. In total the data were passed through McAdam 40 times – each time $M_{T,lim}$ is increased by $0.2 \times 10^{14}\ h_{70}^{-1} M_\odot$. The rest of the priors given to these runs are those listed in Table 4.1.

In Figure 4.17 I show the variation of the p and R values with $M_{T,lim}$. In Figure 4.18 I present the $\frac{\tilde{Z}_1}{\tilde{Z}_0}$ and μ dependence on $M_{T,lim}$, which are of interest because $R \approx \frac{\tilde{Z}_1(S)\mu_A}{\tilde{Z}_0}$ and $p = \frac{R}{1+R}$.

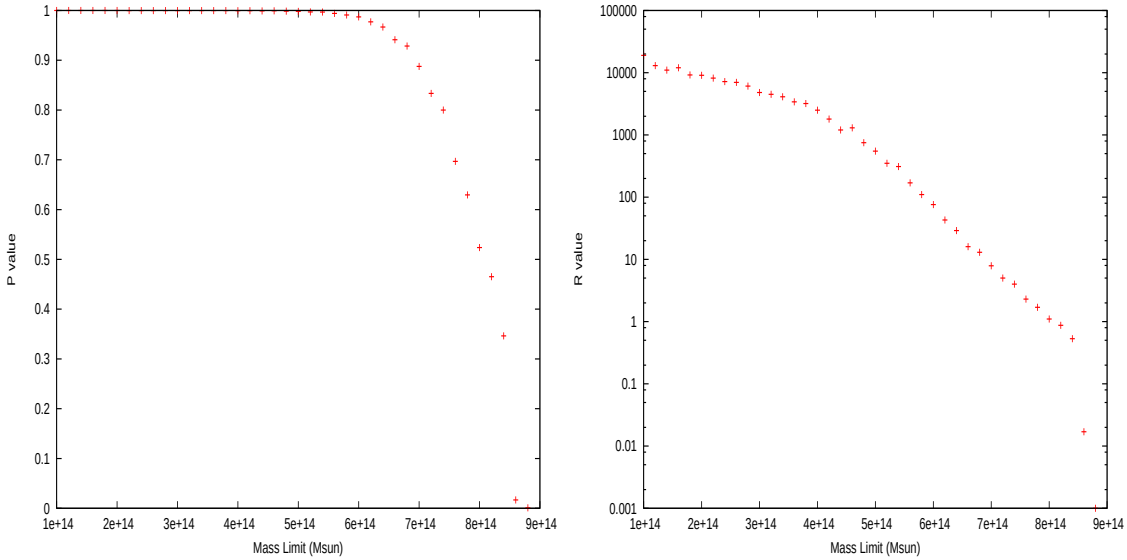

Figure 4.17: The p (left) and R (right) values for a simulation with mass $M_T = 5 \times 10^{14} h_{70}^{-1} M_\odot$ at redshift 1.0 as the limiting mass is varied between $M_{T,lim} = 1 - 9 \times 10^{14} h_{70}^{-1} M_\odot$

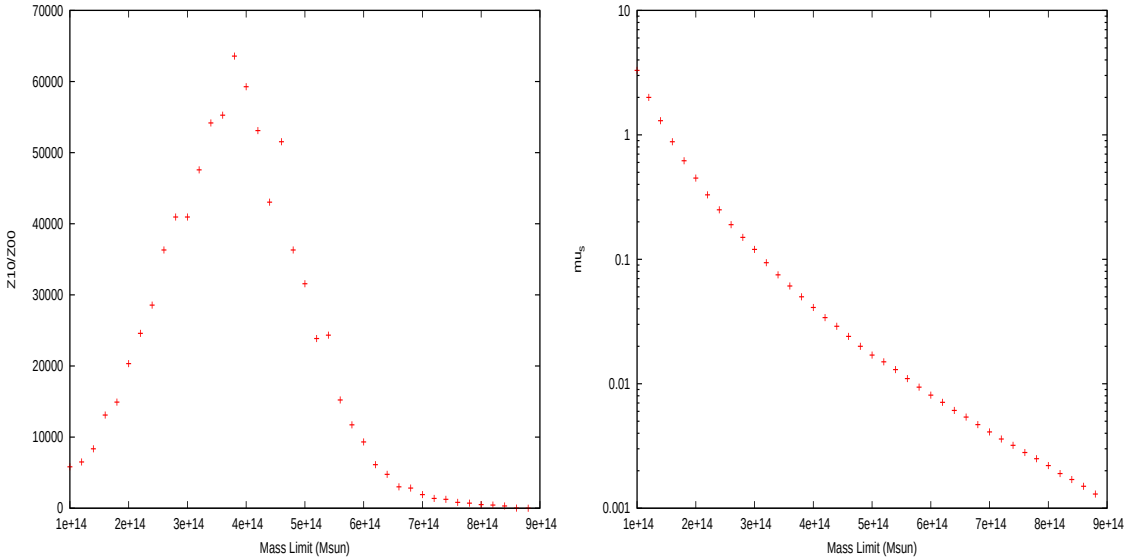

Figure 4.18: The $\frac{\tilde{Z}_1}{\tilde{Z}_0}$ (left) and $\mu_{jenkins}$ (right) values which are multiplied to give the R value for a simulation of a cluster with mass $M_T = 5 \times 10^{14} h^{-1} M_\odot$ at redshift 1.0 as the limiting mass is varied between $M_{T,lim} = 1 - 9 \times 10^{14} h^{-1} M_\odot$

Figure 4.17 demonstrates that until $M_{T,lim} \approx 7.5 \times 10^{14} h^{-1} M_{\odot}$ we derive a probability of detection of greater than 80% for a simulation with mass of $M_{T,200} = 5.0 \times 10^{14} h^{-1} M_{\odot}$. Additionally the R values presented in Figure 4.17 indicate that as $M_{T,lim}$ changes from $M_{T,lim} = 1 - 4 \times 10^{14} h^{-1} M_{\odot}$ the R value decreases gently; however, for $M_{T,lim} > 4 \times 10^{14} h^{-1} M_{\odot}$ the variation in R value is much greater. This gradient change is associated with the turnover in the $\frac{\tilde{Z}_1}{\tilde{Z}_0}$ ratio (Figure 4.18). The curvature in Figure 4.18 occurs because $\tilde{Z}_0$ is constant (regardless of $M_{T,lim}$), whereas when $M_{T,lim}$ is increased in the region $M_{T,lim} < 4 \times 10^{14} h^{-1} M_{\odot}$ the corresponding parameter space of the priors decreases, which therefore results in a better model and hence $\tilde{Z}_1$ increases. However, at a certain $M_{T,lim}$ ($\approx 4.0 \times 10^{14} h^{-1} M_{\odot}$) the model will stop improving because the derived mass probability distribution will be driven too much by the $M_{T,lim}$ prior and at this point the model becomes worse as $M_{T,lim}$ increases and $\tilde{Z}_1$ decreases. This effect is shown in Figure 4.19 which shows that for $M_{T,lim} \gtrapprox 4 \times 10^{14} h^{-1} M_{\odot}$ the derived mass increases at the same rate as $M_{T,lim}$, indicating that the prior is driving the mass estimate. For lower values of $M_{T,lim}$ the derived mass does not rise so rapidly indicating that the effect of raising $M_{T,lim}$ in this region is excluding an area in the parameter space with a low likelihood.

For a simulation of a different mass (e.g. $M_{T,lim} = 6 \times 10^{14} h^{-1} M_{\odot}$) we would expect a similar shape to the plots, although there would be a shift on the mass axis. As $M_{T,lim}$ is increased but remains in the mass range below the simulated cluster mass we expect that $\tilde{Z}_1$ will increase but p and R will slowly decrease; however, as soon as the prior starts to drive our results then $\tilde{Z}_1$ will begin to decrease and p and R will begin to decrease more rapidly.

Overall, the effect of $M_{T,lim}$ on the p and R values for this cluster is very dramatic. But $M_{T,lim}$ is not a completely unknown quantity. If for example, the limit $M_{T,lim} = 3 \times 10^{14} h^{-1} M_{\odot}$ was used to analyse a survey that was sensitive to $M_{T,lim} = 2 \times 10^{14} h^{-1} M_{\odot}$, the derived R values would be a factor five lower than if the correct $M_{T,lim}$ were used. The corresponding p value will remain substantial until $M_{T,lim}$ is larger than the derived mass of the cluster. In previous sections it was concluded that $M_{T,lim}$ cannot be exactly defined but a value of $M_{T,lim} = 2.9 \times 10^{14} h^{-1} M_{\odot}$ was thought to be suitable. Although the work of this

section highlights the importance of $M_{T,lim}$ there is no indication that $M_{T,lim} = 2.9 \times 10^{14} h^{-1} M_{\odot}$ is inappropriate.

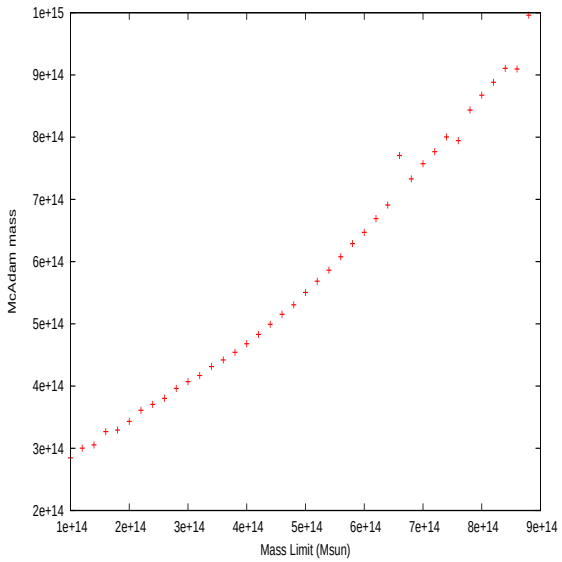

Figure 4.19: The variation in the mean derived $M_{T,200}$ as a function of $M_{T,lim}$.

4.2.6 Testing the Influence of the Cluster Search Area on the Probability of Cluster Detection

The search area is another potentially important parameter in the calculation of the R value (Equation 4.9), since both the evidence and the μ_S parameter are dependent on the area.

For the group B simulation of a cluster with mass $M_{T,200} = 5 \times 10^{14} h^{-1} M_{\odot}$, the R value has been calculated for McAdam runs with search boxes of various sizes. The length of the box sides are changed from 5″ to 500″ in iterations of 5″. In Figure 4.20 I present the R values calculated from these runs. These results demonstrate that the area is not particularly important as the evidence change and the change in the value of μ cancel each other out. However, the R value drops dramatically as the cluster comes to the edge of the search box and it is therefore important that the search boxes of adjacent areas in the blind survey overlap so that no cluster candidates are consistently at the edge of a search box.

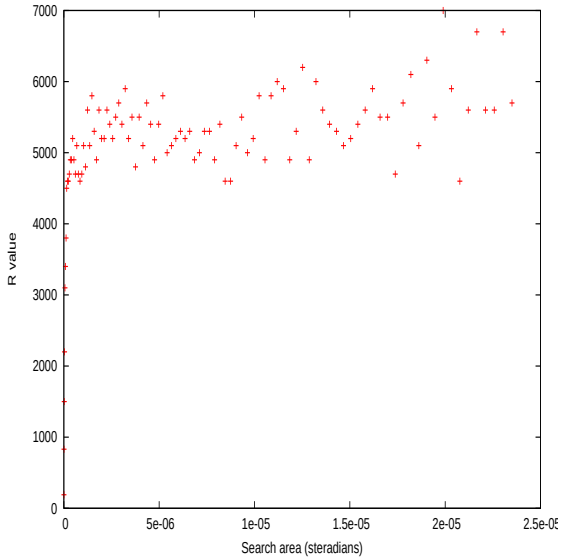

Figure 4.20: The dependence of the R value of cluster detection for the cluster simulated with mass $M_{T,200} = 5 \times 10^{14} h^{-1} M_{\odot}$ with search area.

4.3 Computational Challenges

The reduced AMI blind visibilities have been analysed on both the COSMOS and HPC supercomputers in Cambridge. The specifications of these two machines are summarised in Table 4.4.

Table 4.4: Specification of the COSMOS and HPC supercomputers.

Component	COSMOS	HPC
CPU	Intel NehalemEX 2.67GHz	Intel Westmere 2.67 GHz
Cores	768 (6 per CPU)	1536 (6 per CPU)
RAM	2048GB (16GB per CPU)	4608GB (18GB per CPU)

To reduce the size and hence the computational requirements of the analyses we bin the data from each pointing into three files, each containing all the data from two frequency channels. Note that binning channels together reduces the information content of the data because it decreases our spectral resolution, but

the effect of such binning is small and I have tested that when data are run with two frequency channel binning the derived cluster parameter values, the probability of cluster detection and source parameters are very similar to those derived from the same analysis but with individual channels rather than the two channel bin. We then bin the visibilities from each of these files according to their position on the uv-plane, with a bin size of 40λ – this typically leaves 1000 visibilities per pointing for each two channel file. A value of 40λ is used because the dish diameter is 180λ so a 40λ binning should not result in a significant smearing on the uv plane. Our SA survey fields contain between 24 and 48 different pointing centres. A single Bayesian analysis of the entire field is prohibitively computationally expensive because of the large volume of data and the high dimensionality of the parameter space. Instead, three pointings are analysed at a time. Each set of three pointing centres form a triangle, an example of which is shown in Figure 4.21.

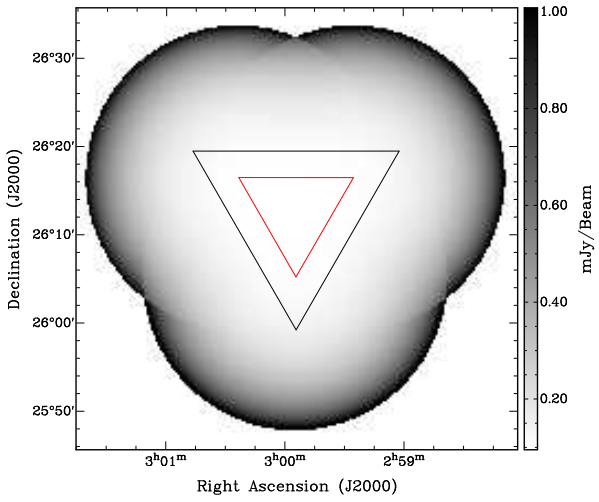

Figure 4.21: Noise map for a SA triangle of observations out to the 0.1 contour of the power primary beam. The inner triangle is between the pointing centres; the outer triangle is the area that is searched for clusters with our Bayesian analysis.

4.4 Conclusions

I have performed a large number of realistic simulations of clusters with various masses and redshifts. All simulations were analysed in the map plane and in McAdam. From these simulations I found that:

- Simulating clusters with a ρ_{crit} that does not vary with redshift have much less variation of SZ signal with redshift than those simulated with ρ_{crit} that is redshift dependent.
- The AMI cluster survey should be able to detect clusters with $M_{T,200} > 2.9 \times 10^{14} h^{-1} M_{\odot}$.
- The Bayesian probability of detection values derived from simulated observations do accurately represent the significance with which an object is detected. The highest false positive detection that is obtained from 8740 McAdam analyses is $p = 0.3$.
- Our analysis will typically underestimate the mass of the cluster, because of the redshift dependence in the observed SZ signal; the problem disappears if the redshift is included.
- The derived p values are sensitive to the $M_{T,lim}$ data that we use to analyse our data.
- The derived p value is insensitive to the search area but due to the computational challenge we are limited to analysing SA survey data three pointings are a time.
- Important to overlap AMI search triangles because the results from candidates at the edge of the search area are unreliable.
- The final priors that are to be used for the analysis of SA survey are summarised in Table 4.1. We have chosen to set $M_{T,lim} = 2.9 \times 10^{14} h^{-1} M_{\odot}$ and the search area as an uniform triangle encompassing the pointing centres between the three triangles.

4.5 Further Work

The simulations that were created for these tests contained realistic CMB and thermal noise contributions. However, it is known that AMI observations are significantly contaminated with point sources. A good understanding of the number of point sources as a function of area and flux density was gained from the 10C survey (Davies *et al.* 2010). An analysis of simulations that contain contributions from a realistic distribution of sources would be insightful.

Chapter 5

The AMI blind survey

In this chapter I describe the two AMI blind deg^2 survey fields that I have analysed, AMI002 and AMI005, as well as the source finding procedure and the McAdam priors. I note the existence of known clusters within the AMI fields before identifying the candidates that have been discovered in my analysis. For each cluster candidate I perform a follow-up investigation with pointed SA observations. The follow-up pointed SA observations have been carefully manually flagged in addition to applying the automatic flagging routines described in Section 2.6. For the survey data such manual flagging was not possible due to the large quantity of data.

As a by-product of the McAdam analysis of these two AMI fields, I have compared the SA and LA source fluxes and investigated the accuracy of the SA-LA calibration.

5.1 Survey Observations

Each survey field has been observed by the LA and the SA. The key points are summarised in Table 5.1.

Table 5.1: Observations of the AMI survey fields.

Field	SA AMI002	LA AMI002	SA AMI005	LA AMI005
Right ascension	02:59:30		09:39:20	
Declination	+26:16:30		+31:17:30	
Start date	2008 Jul 19	2008 Aug 8	2008 Sep 1	2008 Aug 24
End date	2010 Mar 3	2011 Jan 20	2009 Sep 23	2011 Jan 1
Total observing time (hours)	1100	710	760	490
Number of observations	255	65	106	58
Noise level (μJy/beam)	100	50 (inner) 100 (outer)	110	50 (inner) 100 (outer)
Number of pointings	24	600	24	600
Phase calibrator	J0237+2848		+J1018+357 or +J0940+2603	

A rastering technique was used for both the LA and the SA survey observations, where the pointing centres lie on a 2-D hexagonally-gridded lattice. The LA observations form a part of the 10C survey data, which are described in detail in Franzen *et al.* (2010). Additional dedicated pointings towards the cluster candidates are included to ensure that maximum sensitivity was obtained in the LA maps. For the 10C survey observations, the pointing centres are separated by $4'$, which allows us to obtain close to uniform sensitivity over the field while minimising the observing time lost to slewing. In order to detect all important sources within the SA field, the LA field is slightly larger and the thermal noise is typically a factor of two lower than the SA thermal noise. To account for the SA map noise ($\sigma_{\mathrm{SA,SUR}}$) increasing towards the edge of the field, the LA map consists of two distinct regions, the inner and the outer. The inner area of the LA field was observed to an noise level of $\approx 50\mu$Jy/beam, whereas the noise in the outer area was approximately twice as high. The outer region of the LA map is also used to detect bright sources lying just outside the SA field. An example LA noise map is shown in Figure 5.1. For the SA survey observations the pointing centres are separated by $13'$ giving a close-to-uniform noise level of $\approx 100\mu$Jy/beam over the map. The SA noise map is shown in Figure 5.1.

The phase calibrator was observed for two minutes every hour with the SA and for two minutes every ten minutes with the LA. The amplitude calibration for the SA uses 3C286 and 3C48; the assumed flux densities are shown in Table 5.2 and are consistent with the Rudy *et al.* (1987) model of Mars. The LA was flux-density-calibrated from the SA measurements of the LA interleaved calibrator; we adopted this approach to minimise inter-array flux density calibration errors.

Typically our individual observations were 8 hours; this often comprised two separate observations each of 4 hours, interleaved with an observation of a flux density calibrator. Observations were started at different positions in the field to improve the *uv* coverage.

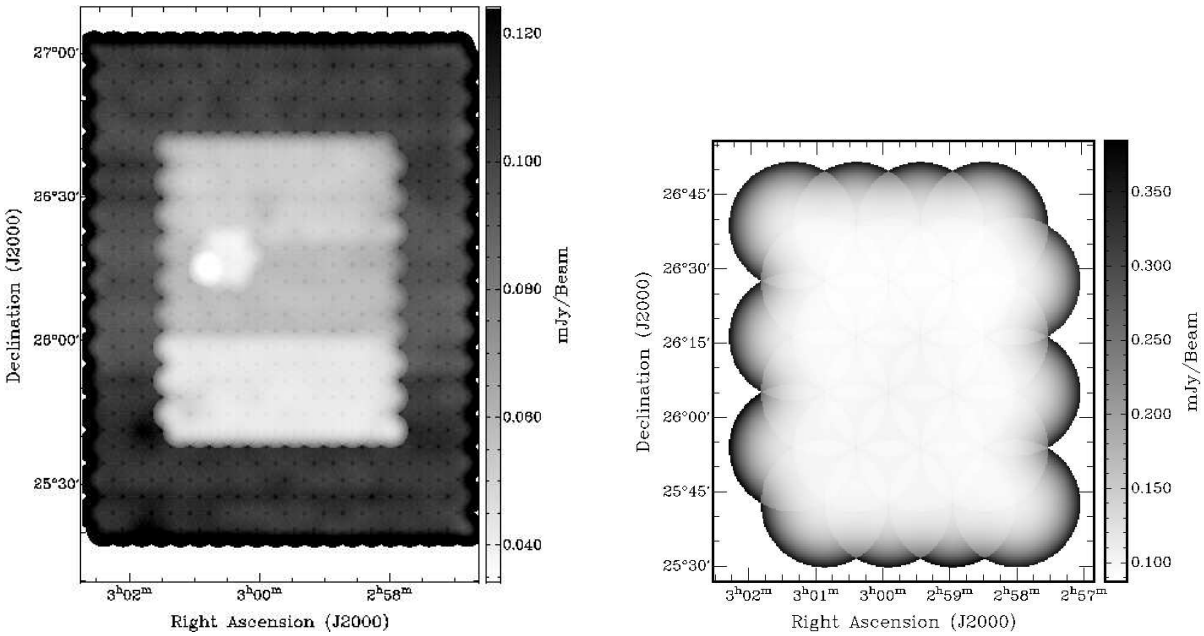

Figure 5.1: On the left is the noise map for the LA AMI002 survey field. The inner region noise is $\approx 50\mu$Jy/beam, while the noise on the outer region is $\approx 100\mu$Jy/beam. The hexagonal region around 03:00:10 +26:15:00 is next to a cluster candidate and was observed to $\approx 30\mu$Jy/beam. The inner region of the LA noise map consists of three subregions; these have slightly different sensitivities due to varying weather conditions and slight differences in observing time. On the right is the noise map for the SA AMI002 field. The noise at the edge of the map increases due to the primary beam of the SA. In the central region the map noise is $\approx 100\mu$Jy/beam.

Table 5.2: Assumed flux densities for the SA flux density calibrators.

Channel	$\bar{\nu}$/GHz	S_{I+Q}/Jy	
		3C286	3C48
1	14.2	3.663	1.850
2	15.0	3.535	1.749
3	15.7	3.414	1.658
4	16.4	3.308	1.575
5	17.1	3.206	1.500
6	17.9	3.111	1.431

Each observation is passed through REDUCE using the standard data reduction pipeline which is detailed in Section 2.6. All imaging is done using AIPS by applying the procedure summarised in Section 3.1.2.1.

5.2 Source Finding

Source finding is carried out on the LA continuum map using the AMI SOURCEFIND software. In this software all pixels on the map with a flux density greater than $0.6 \times 4 \times \sigma_{LA,SUR}$, where $\sigma_{LA,SUR}$ is the LA noise map value for that pixel, are identified as peaks i.e. candidate sources. The flux densities and positions of the peaks are determined using a tabulated Gaussian sinc degridding function to interpolate between the pixels. Only peaks where the interpolated flux density is greater than $4 \times \sigma_{LA,SUR}$ are identified as sources.

For each source we use SOURCEFIND to find the flux densities in the individual AMI-LA channel maps at the positions of the detected sources. Assuming a power-law relationship between flux density and frequency ($S \propto \nu^{-\alpha}$), we use the channel flux densities to determine the spectral index α for each source. The spectral index is calculated using an MCMC method based on that of Hobson & Baldwin (2004) – the prior on the spectral index has a Gaussian distribution with a mean of 0.5 and σ of 2.0, truncated at ± 5.0. The map noise in each channel map in the vicinity of the sources was used to calculate the weighted mean of the channel frequencies and determine the effective central frequency ν_0 of the source

flux measurement. The effective central frequency varies between pointings due to flagging applied in REDUCE. Unlike the work for the 10C survey, the data are not reweighted to the same frequency because this leads to a small loss of sensitivity.

The AIPS routine JMFIT fits a two-dimensional Gaussian to each source identified by SOURCEFIND and gives the angular size and the integrated flux density for the source. These fitted values are compared to the point-source response function of the observation to determine whether the source is extended on the LA map. We find that $\sim$5% of sources are extended on our LA observations; this is in agreement with the 10C survey. However, as the SA synthesized beam is significantly larger we expect far fewer extended sources in the SA maps. It is important that we recognise when a source is extended since currently we have no mechanism for dealing with extended sources in McAdam. If many SZ candidates are discovered close to extended sources then we must add this functionality to McAdam.

For each source we catalogue the right-ascension x_s, declination y_s, flux density at the central frequency S_0, spectral index and the central frequency. If a source is extended on the LA maps we use the centroid of the fitted Gaussian for the position and the integrated flux density instead of the peak flux density.

5.3 McAdam Priors

McAdam was run with both the physical cluster model and the phenomenological model, the priors for these models are given in Table 4.1 and Table 4.2 respectively. This analysis of the survey data has been performed with $M_{T,lim} = 3 \times 10^{14} M_{\odot} h_{70}^{-1}$. I have used a triangular search area which is an enlarged version of the triangle formed between the pointing centres – the radius of the inscribed circle is $3'$ larger to give overlap between adjacent search triangles (see Figure 4.21). For a typical survey field the minimum rms noise within a search triangle is $\approx 100\mu$Jy and the maximum is $\approx 140\mu$Jy.

Given the large number of sources detected by the LA in each of the AMI survey fields the source priors in McAdam are very important. For each source there are four possible priors: x_s, y_s, S_0 and α. Modelling all four for all sources in

the McAdam analysis of each survey triangle would be far too computationally expensive. Instead, we only model sources that have a LA measured flux density which exceeds $4\sigma_{\mathrm{SA,SUR}}$. For the rest of the sources we use the LA values as delta-function priors – this will not increase the parameter space but will inform McAdam of their presence. Sources that are modelled in the survey data are given Gaussian priors on spectral indices and flux densities but delta-function priors on their positions. For the standard deviation of the Gaussian prior on spectral index we use the LA estimated error, whereas on the flux density we use 40% of the measured LA flux density. A wide prior on flux density is used because if the SA flux density is discrepant from the LA value and McAdam is pushed towards the edge of its given prior, then the McAdam run time is significantly increased. A wider prior on the source flux often prevents this from happening so frequently. The SA-measured flux density may be different from that of the LA because of source variability, calibration errors and thermal noise levels. For sources that are not modelled, we use delta-function priors on source positions, spectral indices and flux densities.

All of the cluster candidates have been followed up with SA pointed observations. For the analysis of these follow-up observations the prior on position is a box of $1000'' \times 1000''$ centred on the cluster position. The priors on the cluster are the same as those used to analyse the survey observations and again sources with flux densities exceeding $4\sigma_{SA,POI}$ (where $4\sigma_{SA,POI}$ is the thermal noise on the pointed observation) are modelled. Sources that are modelled in a pointed observation are different to those modelled in the survey observation of that candidate because $\sigma_{SA,POI} \neq \sigma_{SA,SUR}$. Often there are fewer sources modelled in a pointed observation than in a survey triangle and as a consequence the dimensionality of the pointed McAdam run is lower. We can thus increase the number of source parameters that are modelled in pointed observations. For pointed observations we have chosen to allow McAdam to fit for the positions of the sources by using a Gaussian prior centred on the LA derived position of the source with a $5''$ standard deviation. By fitting for the source positions we obtain a cleaner source subtraction and as a result there are fewer residuals on the source-subtracted pointed SA maps.

We are cautious about cluster candidates located at the position of a faint source that has been assigned delta-function priors. For candidates with faint sources that may affect the decrement, I ensure that these sources are modelled in McAdam regardless of their flux density. This approach is particularly cautious, because for a source situated on top of a cluster you may expect the source flux to be underestimated by McAdam, especially if the cluster is at high redshift and not well resolved. Due to the limited dynamic range of the SA, I have been cautious of candidates close to bright sources: all candidates lying $< 5'$ from a source $\geq$ 5mJy/beam are discarded.

We only set priors on sources that have been detected by the LA but McAdam is given knowledge of the statistics of sources that are below our LA detection threshold. This background of sources is referred to as confusion noise and was originally calculated by Scheuer (1957);

$$\sigma^2_{conf} = \Omega_{synth} \int_0^{S_{lim}} \frac{dN}{dS} S^2 dS, \tag{5.1}$$

where $\frac{dN}{dS}$ is the differential source count, Ω_{synth} is the synthesized beam and S_{lim} is the limiting flux density. As a standard we set S_{lim} to four times the LA thermal noise of the source that is closest to the pointing centre of the SA data. For confusion noise we are currently using the combined 10C and 9C 15GHz source counts that were derived in Davies *et al.* (2010):

$$\frac{dN}{dS} = \begin{cases} 48 \left(\frac{S}{\mathrm{Jy}}\right)^{-2.13} (\mathrm{Jy}^{-1}\mathrm{sr}^{-1}) & \text{for 2.2mJy} \leq \mathrm{S} \leq \text{1Jy}, \\ 340 \left(\frac{S}{\mathrm{Jy}}\right)^{-1.81} (\mathrm{Jy}^{-1}\mathrm{sr}^{-1}) & \text{for 0.50mJy} \leq \mathrm{S} \leq \text{2.2mJy}. \end{cases}$$

The 10C source counts were obtained from the LA data that are used in the AMI blind cluster survey, although as previously described the reduction was slightly different. The 9C counts were taken from Waldram *et al.* (2003).

5.4 Cluster Identification

The AMI survey fields were chosen to avoid:

- Objects in the nearby galaxies atlas (Tully *et al.* 1989).

- Nearby superclusters.
- Abell *et al.* (1994) – this all-sky catalogue contains 4073 rich galaxy clusters at redshifts ≤ 0.2
- Abell (1995) catalogue which contains 9134 Zwicky galaxy clusters (as well as 2712 Abell clusters)
- ROSAT All Sky Survey (NORAS, REFLEX, BCS, SGP, NEP, MACS and CIZA) catalogues.

These searches were performed by Richard Saunders before the blind cluster survey began. The fields were also carefully selected so that they did not contain objects bright than magnitude 14 (AB system) in the R or z′ bands.

I have checked the literature again to ensure that there are no known clusters additionally I have searched the Sloan Digital Sky Survey (SDSS) cluster catalogues compiled by Koester *et al.* 2007 and Wen *et al.* 2010, which contain 13823 and 39716 clusters respectively.

The search revealed that the AMI002 field contains no known clusters but that the AMI005 field contains 11 known galaxy clusters. These known clusters were all found in the SDSS optical cluster catalogues. For each of these clusters I have used the mass-richness scaling relationship from Rozo *et al.* (2009) to obtain mean mass estimates. The mass-richness scaling relationship which relates the richness at r_{200} to the mass at that radius is

$$\frac{< M|N >}{10^{14} M_{\odot}} = e^{B_{M|N}} \left(\frac{N}{40}\right)^{\alpha_{M|N}} . \tag{5.2}$$

The constants $B_{M|N}$ and $\alpha_{M|N}$ are 0.95 and 1.06 respectively. The maximum derived mass of the 11 known clusters is $1.07 \times 10^{14} M_{\odot}$ which is significantly lower than the $M_{T,lim}$ of the AMI survey.

In Table 5.3 I present the coordinates, redshift, richness and estimated mass for these known clusters.

Table 5.3: The known galaxy clusters in the AMI005 survey field. For entries that exist in both Koester *et al.* (2007) and Wen *et al.* (2010) I have quoted the values given in the later publication. The stated redshift is the cluster photometric redshift. The masses were obtained from the mass-richness relation presented in Rozo *et al.* (2009). All the derived cluster masses are well below the AMI detection limit.

Right ascension	Declination	Redshift	Richness	Mass $\times 10^{14} M_{\odot}$	Source
09:40:03.2	+30:39:53	0.29	9.2	0.54	Wen *et al.* (2010)
09:37:21.7	+30:42.13	0.34	11.4	0.68	Wen *et al.* (2010)
09:42:09.5	+30:57:17	0.31	12.1	0.73	Wen *et al.* (2010)
09:37:38.3	+30:59:36	0.23	12.0	0.72	Koester *et al.* (2007) and Wen *et al.* (2010)
09:38:39.1	+31:03:59	0.12	12.0	0.72	Koester *et al.* (2007)
09:40:00.7	+31:27:57	0.52	12.8	0.77	Wen *et al.* (2010)
09:37:38.5	+31:23:57	0.37	14.2	0.86	Wen *et al.* (2010)
09:37:41.8	+31:31:18	0.38	9.1	0.54	Wen *et al.* (2010)
09:38:12.6	+31:33:53	0.35	17.4	1.07	Wen *et al.* (2010)
09:40:38.2	+31:52:33	0.38	12.7	0.77	Wen *et al.* (2010)
09:38:22.7	+31:53:38	0.36	10.4	0.62	Wen *et al.* (2010)

5.5 The Analysis of Survey Fields

For the analysis of each field I present maps of the entire field, individual candidates in the field and pointed follow-up observations towards these candidates. For each candidate I present McAdam derived p values and the parameter probability distributions for both the physical cluster model and the SZ cluster model.

As previously described, the McAdam analysis of the survey data properly accounts for the contribution of sources (LA and confusion), the statistics of the CMB primary anisotropies and the thermal noise level; hence the derived probability distributions accurately depict the errors as long as no other random

or systematic error is present. I have presented maps because in these it is easy to spot contamination and also to judge the apparent significance of candidate decrements. However, the interpretation of these maps is non-trivial:

- The CLEAN algorithm is used to deconvolve the synthesized beam (see Figure 5.2 for an example synthesized beam) from the maps because it reduces the sidelobes from objects. However, the CLEAN procedure is not entirely robust: differently CLEANed data, for example to different depths or with different CLEAN boxes, can produce significantly different maps.
- The primordial CMB anisotropies contribute to the maps (see Figure 5.3).
- The weighted *uv* coverage and therefore the synthesized beam of each dataset is different (see Figure 5.2 for an example beam).

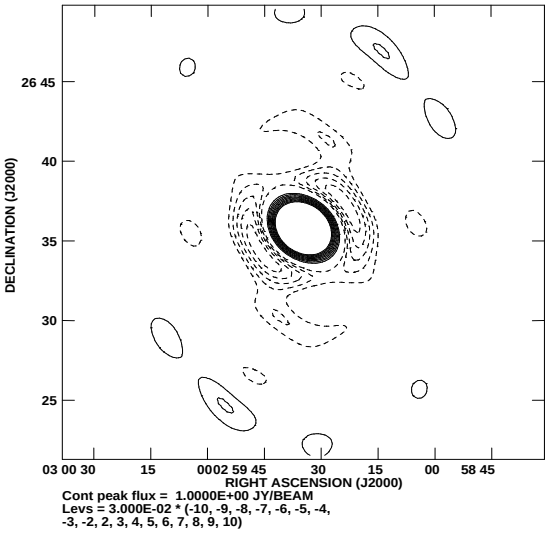

Figure 5.2: A typical AMI synthesized beam for an AMI002 observation. Contours are at $\pm 2\sigma$, $\pm 3\sigma$, $\pm 4\sigma$ etc ., where σ is 3%; negative contours are dashed and positive contours are solid. This beam is for a total of 23 hours of pointed SA observation towards AMI002 candidate 3 at a declination of +25 (Figure 5.16).

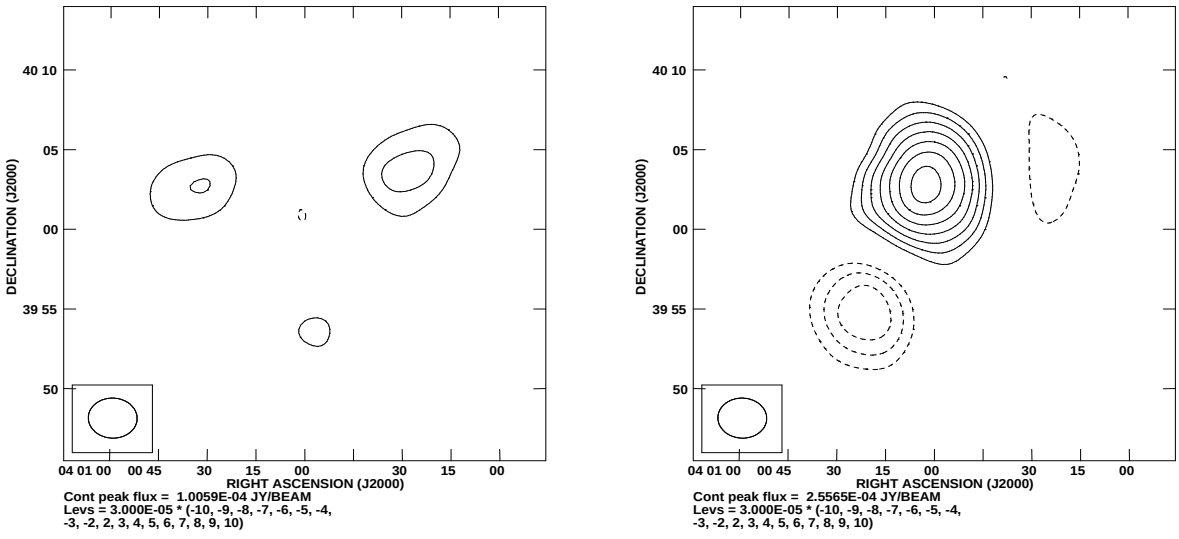

Figure 5.3: The simulated CMB contribution to SA maps assuming the Lewis *et al.* 2000 power spectrum. The contours are at $\pm 2\sigma$, $\pm 3\sigma$, $\pm 4\sigma$ etc ., where σ is 30μJy; negative contours are dashed and positive contours are solid. 20 simulations were run – the map on the left shows the lowest peak CMB flux density obtained and the map on the right shows the highest peak flux density obtained. The mean peak flux density due to the CMB was 150μJy/beam.

Throughout this chapter I refer to survey search triangles via the identities of the pointings that constitute that specific triangle. Note that pointings are numbered from right to left and bottom to top; for example, in Figure 5.5 and 5.1(right) the bottom right pointing centre has ID 1 and on the same row but at the far left the pointing has ID 4. In the maps the pointings can be distinguished by the circular edge effects which are caused by the primary beam corrections.

Maps from the LA and SA survey data (triangles and complete fields) have been primary beam corrected and the noise varies across the image. For these maps I present signal divided by noise maps with contour levels at $\pm 2\sigma$, $\pm 3\sigma$, $\pm 4\sigma$ etc ., where σ is stated in the Figure caption. σ is calculated by measuring the rms on the map outside the primary beam, this is a measure of the thermal noise and is not contaminated by sources. All the SA maps from pointed follow-up observations that are presented here have not been primary beam corrected, i.e. the SA thermal noise is constant across the map. Again the contour levels are $\pm 2\sigma$, $\pm 3\sigma$, $\pm 4\sigma$ etc ., where σ is stated in the caption that is output with the AIPS image and within the text. For all maps negative contours are dashed and positive contours are solid. Unless otherwise stated, all maps are naturally weighted, i.e. have no taper on uv distance. The synthesized-beam FWHM is shown in the bottom left corner of the maps. For all parameter posterior distribution plots the lower limit on the $M_T(r_{200})/h^{-1}M_{Sun}$ axis is $M_{T,lim}$.

Throughout the text I refer to modes that are identified by McAdam. Only modes that have a derived $p \geq 0.3$ in the survey data are referred to as candidates.

5.6 AMI002

The LA and SA AMI002 images of this field are shown in Figures 5.4 and 5.5 respectively. In Figure 5.6 I show maps of the AMI002 SA data subjected to jack-knife tests (Section 3.4); these highlight contaminated regions of the SA maps.

In the LA data a total of 210 sources were detected at $\geq 4\sigma_{LA,SUR}$; 13 of these are extended on the LA maps. The flux densities of the sources range between 0.15mJy/beam and 22mJy/beam. The AMI002 LA source details such as coordinates, flux density and spectral index are given in Appendix Table B.2.

The search for clusters in the 30 data triangles formed within the AMI002 field has produced several cluster candidates. In total 42 modes were detected but many of these have low p values. In Table 5.4 I present the positions and p values for each of the nine putative cluster detections which are detected with $p > 0.3$. I use this limit because in Section 4.2.3 the highest p value for a false positive was 0.3.

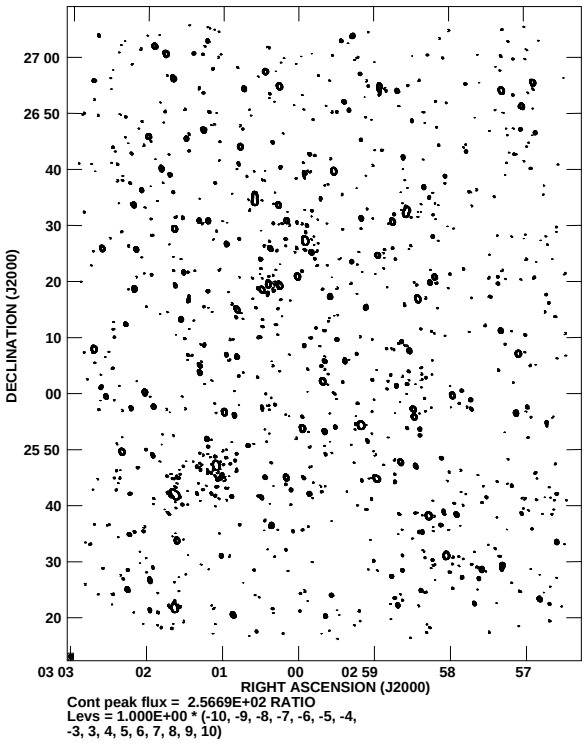

Figure 5.4: The signal-to-noise map for the AMI002 LA field. In the central region the noise is $\approx 50\mu$Jy/beam and in the outer region the noise is $\approx 100\mu$Jy/beam (see Figure 5.1 for the complete noise map). A total of 210 sources were detected with flux densities greater than $4\sigma_{LA,SUR}$, 13 of these are extended.

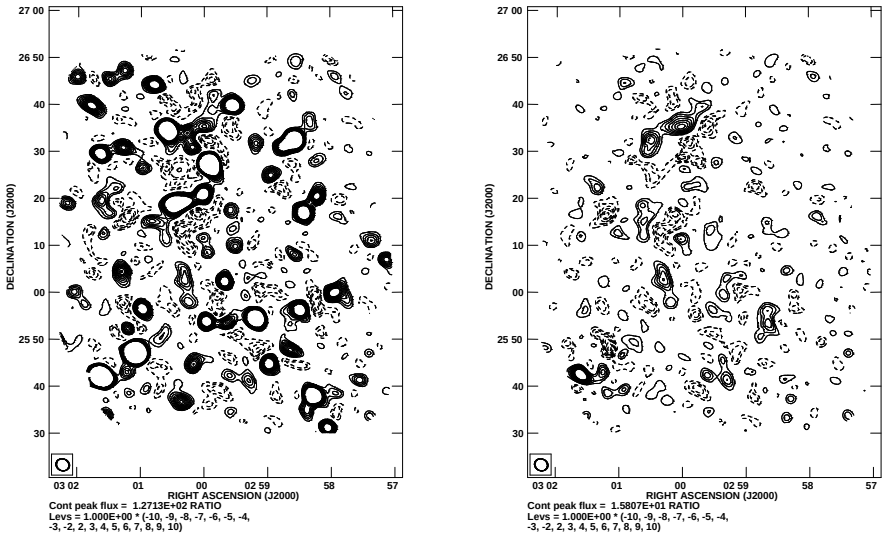

Figure 5.5: The AMI002 SA signal-to-noise map. On the left, sources have not been subtracted; on the right, sources have been subtracted. For sources with flux densities $> 4\sigma_{SA,SUR}$ the McAdam derived values for their flux density and spectral index were used for the subtraction, whereas for fainter sources the LA values were used. The thermal noise is $\sigma_{SA,SUR} \approx 100\mu$Jy/beam.

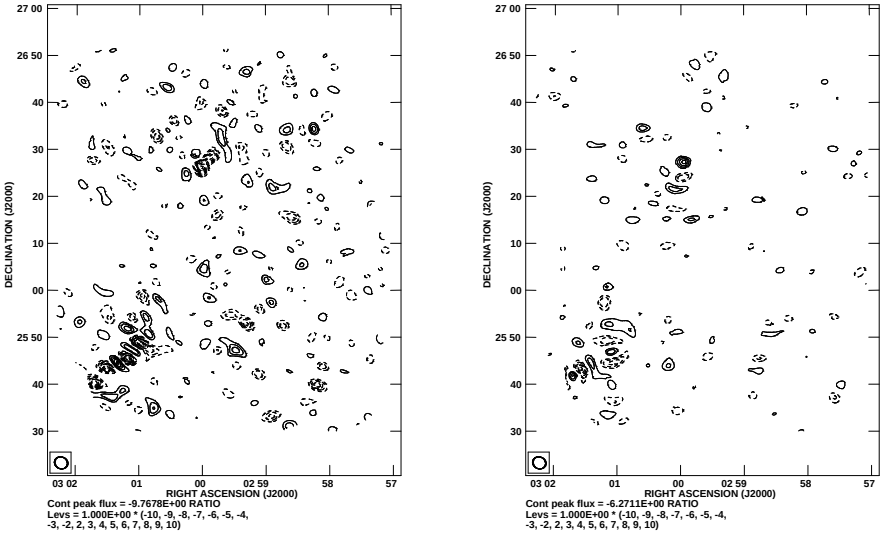

.

Figure 5.6: The signal-to-noise map of the AMI002 jack-knifed SA data set. On the left the data has been split according to the median date and on the right the data has been split into plus and minus baselines. The noise on the map on the left is $\approx 100\mu$Jy/beam and the noise on the map on the right is $\approx 70\mu$Jy/beam. The noise level on the map on the right is lower than 100μJy/beam as expected (see Section 3.4).

Table 5.4: The derived p values for the nine candidates detected in the AMI002 SA data that have $p > 0.3$. Often candidates are detected in multiple triangles, for these I provide the maximum and minimum p and R values. The stated right ascension and declination are obtained from the triangle in which the candidate is detected with highest p value.

Candidate	Pointings	Highest p (R)	Lowest p (R)	Right Ascension	Declination
1	12-15-16, 15-16-20	1.0 (4.4×10^4)	1.0 (3.2×10^2)	03:01:14.7	+26:16:41
2	11-12-15, 11-14-15, 14-15-19, 15-19-20	1.0 (9.5×10^2)	0.5 (1.0)	03:00:15.5	+26:14:02
3	18-19-22	1.0 (2.1×10^2)	1.0 (2.1×10^2)	02:59:34.7	+26:35:48
4	6-7-11, 3-6-7, 6-10-11	0.99 (68)	0.28 (0.4)	02:59:48.1	+25:55:31
5	7-11-12, 7-8-12	0.97 (34)	0.90 (9.5)	03:00:33.5	+25:57:47
6	2-3-6	0.80 (4.1)	0.80 (4.1)	02:59:08.2	+25:48:09
7	5-9-10, 1-2-5	0.80 (4.0)	0.68 (2.1)	02:58:14.8	+25:57:34
8	6-10-11	0.78 (2.5)	0.78 (2.5)	02:59:07.2	+25:59:22
9	13-14-18, 13-17-18	0.37 (0.6)	0.07 (0.0)	02:58:50.7	+26:22:23

In the AMI002 field I have eliminated four cluster candidates at positions 03:00:58.5 +25:46:13, 02:59:57.5 +26:28:12, 03:00:41.8 +26:27:25 and 02:59:03.9 +25:55:08, even though the derived p values are 1.0, 1.0, 0.79 and 0.50 respectively. These candidates are eliminated because they lay close to the brightest

sources in the field; these sources have caused severe contamination that is visible in the jack-knifed SA data set (Figure 5.6).

5.6.1 Candidate 1: 12-15-16 and 15-16-20

This candidate is detected in the search triangles 12-15-16 and 15-16-19, both detections have $p = 1.0$. Given the position of this candidate we would not expect to detect it in any of the other search triangles. The noise in the region of the candidate is lowest in the 15-16-20 triangle and the image of these data is shown in Figure 5.7. We see no bright radio sources in the vicinity of the candidate and after source subtraction most of the source signal is removed. However, a 0.65mJy/beam decrement is clearly visible at the candidate position even before source subtraction. There is also a significant decrement to the west; this is candidate 2 as is described in the Section 5.6.2. In the AMI002 jack-knifed data set (Figure 5.6) there is no significant or unusual contamination in the region of this candidate.

There are two sources subtracted close to the candidate at positions 03:01:06.5 +25:48:53 and 03:01:28.1 +26:16:46. The first lies within the decrement and is not extended on the LA maps and a peak LA flux density of 0.28mJy/beam. The other is slightly west of the candidate, is extended on the LA maps, has a peak flux density of 0.45mJy/beam and an integrated flux density of 0.70mJy/beam. However, even though this source is extended on the LA map it is unlikely to have a significant impact upon the decrement because it is weak and $\approx 3'$ away.

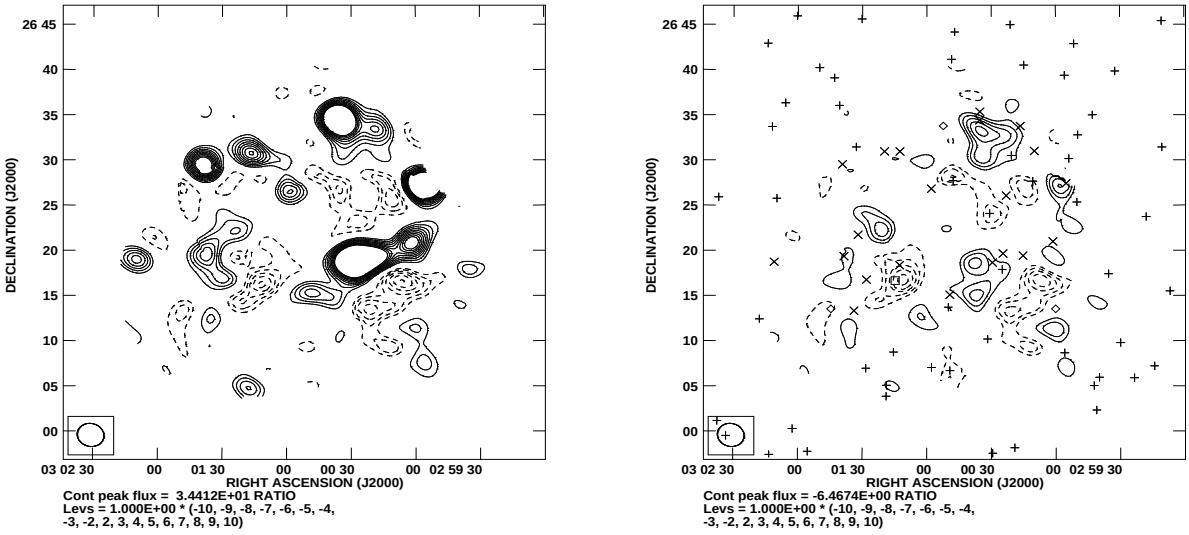

Figure 5.7: Signal-to-noise map for the AMI002 search triangle 15-16-20. On the left is the map before source subtraction and on the right the sources have been subtracted using MUESLI. The thermal noise in the region of the candidate is $\sigma_{A2,SUR,CL1} = 100\mu$Jy/beam. The box symbol represents the cluster candidate, $\times$ symbols show sources with a measured LA flux greater than $4\sigma_{SA,SUR}$, and + symbols show fainter sources.

5.6.1.1 Pointed Follow-up Observation

A total of 22 hours of SA pointed observations towards 03:01:15.4 +26:17:26 were taken between May 2010 and June 2011. The thermal noise on this pointed follow-up observation, $\sigma_{A2,POI,CL1}$, is 100μJy/beam; this is similar to the noise obtained in the survey field observations of this region ($\sigma_{A2,SUR,CL1}$). The data were passed through McAdam and the sources were modelled according to the criteria outlined for pointed observations in Section 5.3; this involves modelling a total of nine sources including the 0.28mJy/beam source (LA flux) within the decrement. The images from the pointed observation are shown in Figure 5.8.

The LA measured 0.28mJy/beam (flux density measurement obtained in an area where $\sigma_{LA,SUR} = 0.051$ mJy) source that is modelled and subtracted from close to the centre of the candidate decrement has a McAdam derived mean flux density of 0.18mJy/beam. It is this derived flux density that is subtracted from

the map. Hence, it appears that even though we underestimate the flux density of this source on the SA map compared with the LA values, we still obtain a 0.60mJy/beam ($5\sigma_{A2,POI,CL1}$) decrement at the position of this candidate. The 0.70mJy/beam extended LA source appears to be correctly subtracted, leaving no artifacts. An incorrect subtraction of this source would mainly affect the morphology of the decrement and not its magnitude.

The follow-up pointed observation has been passed through McAdam using both the physical cluster model and the phenomenological model, the derived parameter probability distribution from each model is shown in Figure 5.9. Tables 5.5 and 5.6 give the mean parameter values. For this pointed observation we use the McAdam evidences to derive a p value of 0.98 (R=44).

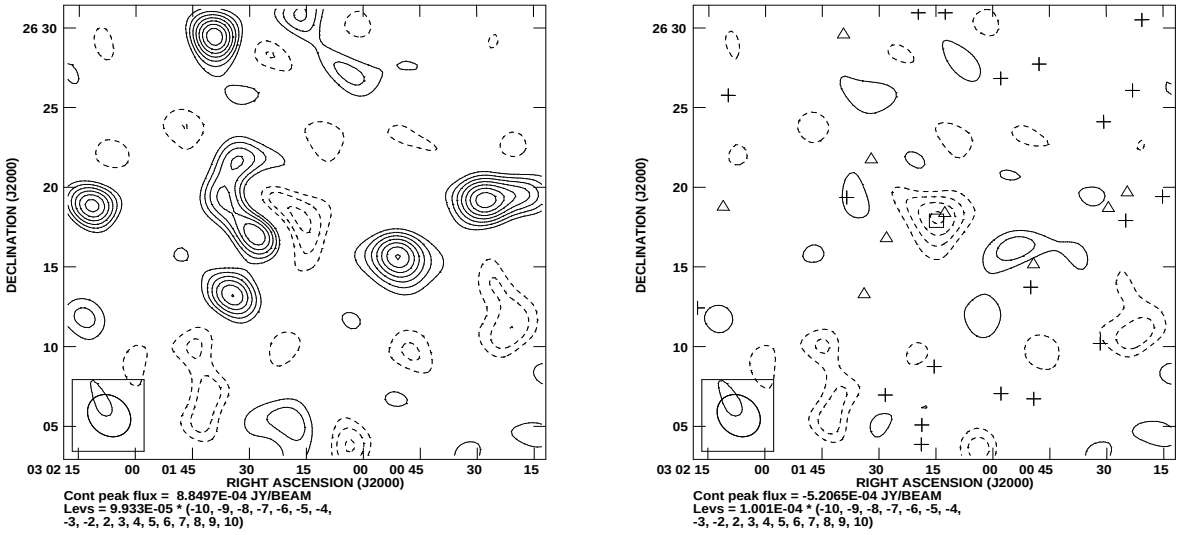

Figure 5.8: Images of the SA follow-up pointed observations towards the AMI002 cluster candidate 1 (03:01:15.4 +26:17:26). These are shown before source subtraction on the left and after sources have been subtracted on the right. The triangle symbols represent sources that have flux densities greater than $4\sigma_{A2,SUR,CL1}$. The position, flux and spectral index of these sources have been modelled and the mean McAdam derived values have been used for the subtraction. The crosses show sources with flux densities below $4\sigma_{A2,SUR,CL1}$; these are subtracted using the LA measured flux densities.

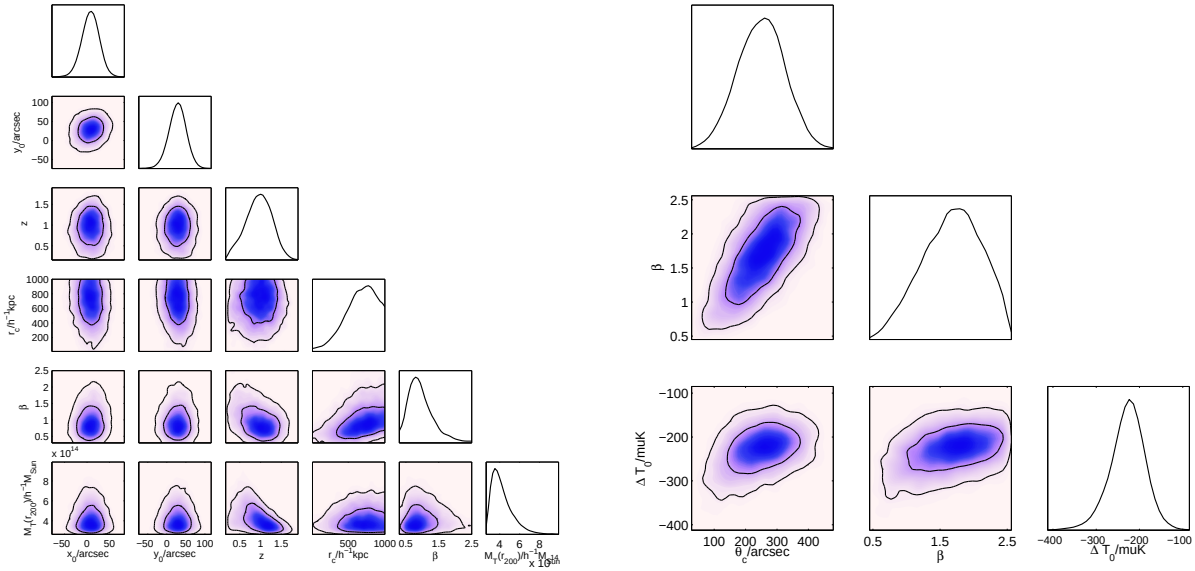

Figure 5.9: The derived parameters for AMI002 cluster candidate 1 at position 03:01:15.4 +26:17:26. On the left are the physical parameters and on the right are the phenomenological model parameters.

Table 5.5: Mean values and 68% confidence limits for the parameters in the physical cluster model for candidate 1.

Parameter	
z	$0.96^{+0.31}_{-0.30}$
$M_T(r_{200})/h^{-1}M_{Sun}$	$4.2^{+1.0}_{-1.0} \times 10^{14}$
$r_c/h^{-1}kpc$	660^{+340}_{-85}
β	$1.0^{+0.1}_{-0.7}$

Table 5.6: Mean values and 68% confidence limits for the parameters in the phenomenological model for candidate 1.

Parameter	
$\Delta T_0/\mu$K	-230^{+37}_{-37}
$\theta_c/arcsec$	250^{+73}_{-75}
β	$1.7^{+0.5}_{-0.5}$

5.6.2 Candidate 2: 11-12-15, 11-14-15, 15-19-20 and 14-15-19

A highly-extended, non-circular negative feature is detected in the McAdam analysis of the search triangles 11-12-15, 11-14-15, 15-19-20 (two modes) and 14-15-19; the derived p values are 1.0, 1.0, 0.5, 0.78 and 0.95 respectively. The noise in the locality of the candidate is lowest for the search triangle 11-12-15 and the map from this triangle is shown in Figure 5.10.

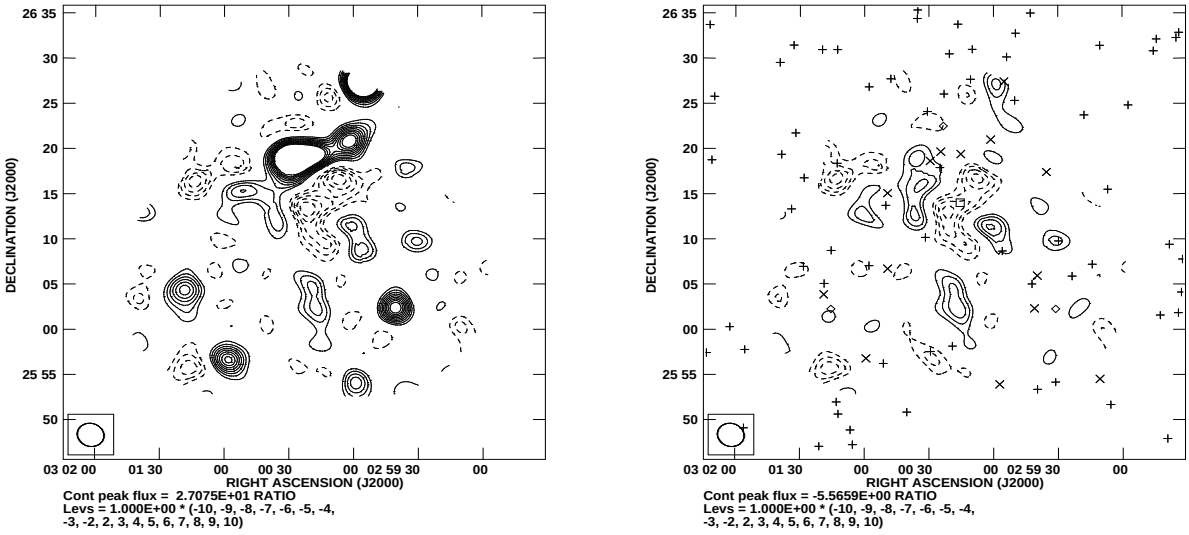

Figure 5.10: Same as for Figure 5.7 but for candidate 2 (found in 11-12-15). The thermal noise in the region of the candidate is $\sigma_{A2,SUR,CL2} \approx 100\mu$Jy/beam.

There are several sources just north of this candidate, the ones most likely to influence the decrement are the sources at 03:00:01.3 +26:21:00, 03:00:29.5 +26:18:40, 03:00:24.6 +26:19:41 and 03:00:15.2 +26:19:25, none of these sources is extended and their LA measured flux densities are 1.8mJy/beam, 1.4mJy/beam, 1.2mJy/beam and 1.1mJy/beam respectively.

The source subtraction leaves little residual flux density on the map. The positive features to the east and west of the candidate may be associated with the sidelobes of the candidate, alternatively they may influence the candidate with their sidelobes. The negative feature at 03:01:14.7 +26:16:41 is candidate 1 and was described in Section 5.6.1. The jack-knife tests (Figure 5.6) reveal only noise-like features in the vicinity of the candidate. After the source subtraction we note that the peak flux density of the cluster decrement is $\approx$ 0.60mJy/beam ($5\sigma_{\rm A2,SUR,CL2}$).

5.6.2.1 Pointed observation

This cluster candidate was followed up with 49 hours of pointed observations, taken in March 2010. The image produced from the pointed-observation data

has a thermal noise level of 65μJy/beam and is shown before and after source subtraction in Figure 5.11. Again we see a highly-extended, non-circular negative feature with a peak flux density decrement of ≈ 0.60mJy/beam ($8\sigma_{\mathrm{A2,POI,CL2}}$). The integrated flux density of the decrement is ≈ 1.2mJy/beam.

The source subtracted map has similar flux density residuals to those seen in the survey data. The positive residuals to the north and west of the candidate may be associated with badly subtracted sources but the majority of the sources subtract well.

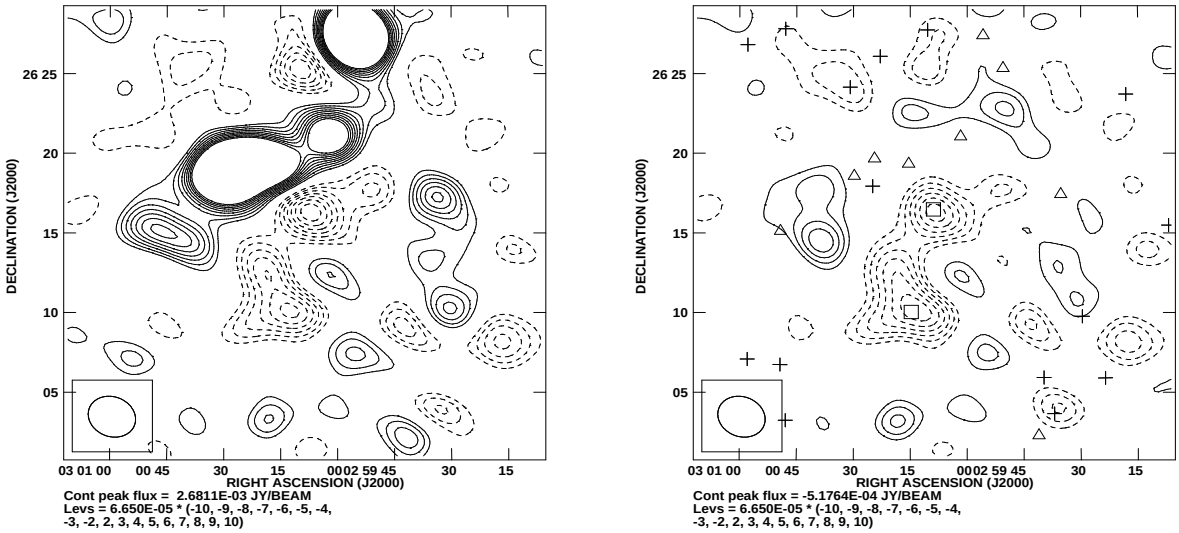

Figure 5.11: Same as Figure 5.8 but for AMI002 candidate 2. We have detected two modes, one at 03:00:14.8 +26:10:02 and another at 03:00:08.9 +26:16:29. When imaging the source subtracted map, CLEAN boxes have been placed around each candidate.

Our Bayesian analysis of the pointed-observation data, which have a higher signal-to-noise ratio than the survey data, finds *two* local peaks in the marginalised posterior distribution in the (x_c, y_c)-plane. These cluster candidates are: candidate 2a at 03:00:14.8 +26:10:02 and candidate 2b at 03:00:08.9 +26:16:29. The significances of the two cluster detections are $p_a = 1.0$ and $p_b = 1.0$ ($R_a = 6.0\times10^5$ and $R_b = 7000$). I also made a direct comparison of the Bayesian evidence for a model containing two clusters and a model containing just a single cluster and

find that the Bayesian evidence is 7.6×10^5 higher for the model containing two clusters.

The 1D and 2D marginal posterior distributions for a selection of the physical parameters of each cluster are shown in Figure 5.12 and the mean values are given in Table 5.7.

Table 5.7: Mean values and 68% confidence limits for the parameters in the physical cluster model for candidate 2 modes a and b.

Parameter	Mode a	Mode b
z	$0.59^{+0.07}_{-0.39}$	$0.71^{+0.09}_{-0.15}$
$M_T(r_{200})/h_{70}^{-1}M_{Sun}$	$5.5^{+1.2}_{-1.3} \times 10^{14}$	$3.5^{+0.9}_{-1.0} \times 10^{14}$
$r_c/h_{70}^{-1}kpc$	640^{+360}_{-84}	340^{+73}_{-330}
β	$1.8^{+0.7}_{-0.2}$	$1.7^{+0.8}_{-0.2}$

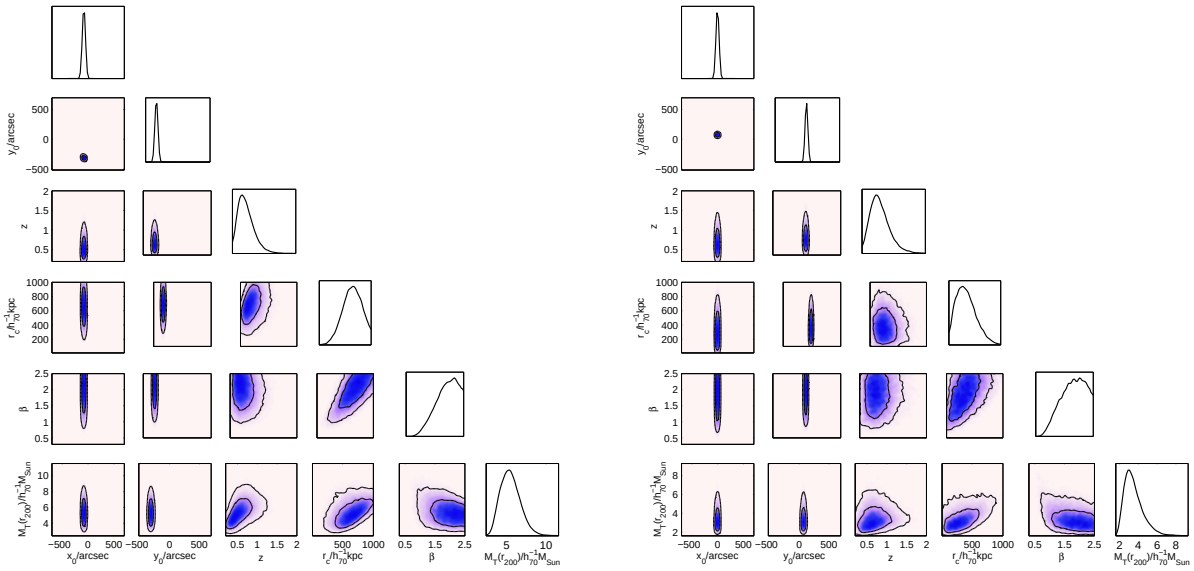

Figure 5.12: 1D and 2D marginal posterior distributions for a selection of the parameters in physical cluster model for candidate 2a (left) and candidate 2b (right). The $M_{T,200}$ values have been divided by 10^{14}.

The 1D and 2D marginal posterior distributions for the phenomenological model parameters θ_c, β and ΔT_0 are shown in Figure 5.13. The mean values and

68% confidence limits for each parameter are given in Table 5.8.

Table 5.8: Mean values and 68% confidence limits for the parameters in the phenomenological model for candidate 2a and candidate 2b.

Parameter	Pointed (candidate 2a)	Pointed (candidate 2b)
$\Delta T_0/\mu$K	-295^{+36}_{-15}	-302^{+70}_{-27}
$\theta_c/arcsec$	156^{+27}_{-25}	121^{+19}_{-100}
β	$1.69^{+0.81}_{-0.24}$	$1.46^{+1.03}_{-1.06}$

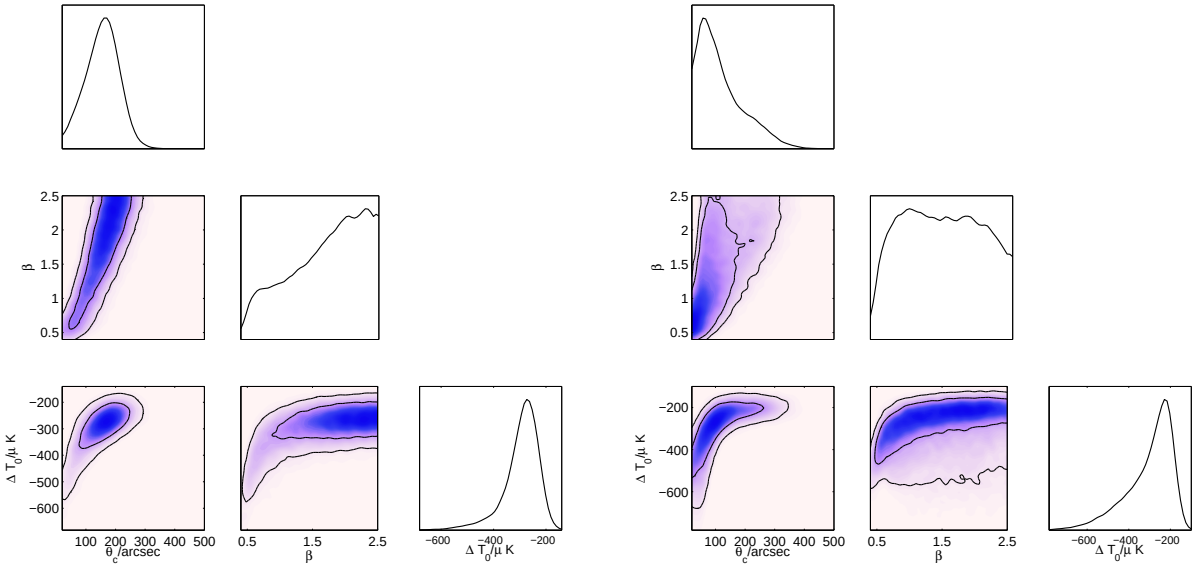

Figure 5.13: 1D and 2D marginal posterior distributions for the parameters in the phenomenological model for candidate 2a (left) and candidate 2b (right).

The jack-knife tests of the pointed observation towards this candidate reveal that when the data are split according to median date, there is a $4\sigma_{A2,POI,CL2}$ decrement centred on the source structure north-east of the cluster candidate (Figure 5.14). This result implies that the flux of this structure is higher in the first half of the data than in the second half. An investigation revealed that the flux of this structure was dependent upon the orientation of the synthesized beam. When the beam was extended in the south-east – north-west axis we found

that the flux density was slightly higher than when the beam was extended in the south-west – north-east axis. The majority of the data taken before the median date had synthesized beams that extended along the south-east – north-west axis. After the median date the majority of the data had a beam extended along the south-west – north-east axis. Hence the decrement that we see after performing a jack-knife test and splitting the data according to median date produces results that we would expect. However, neither jack-knife test reveals any unexpected contamination.

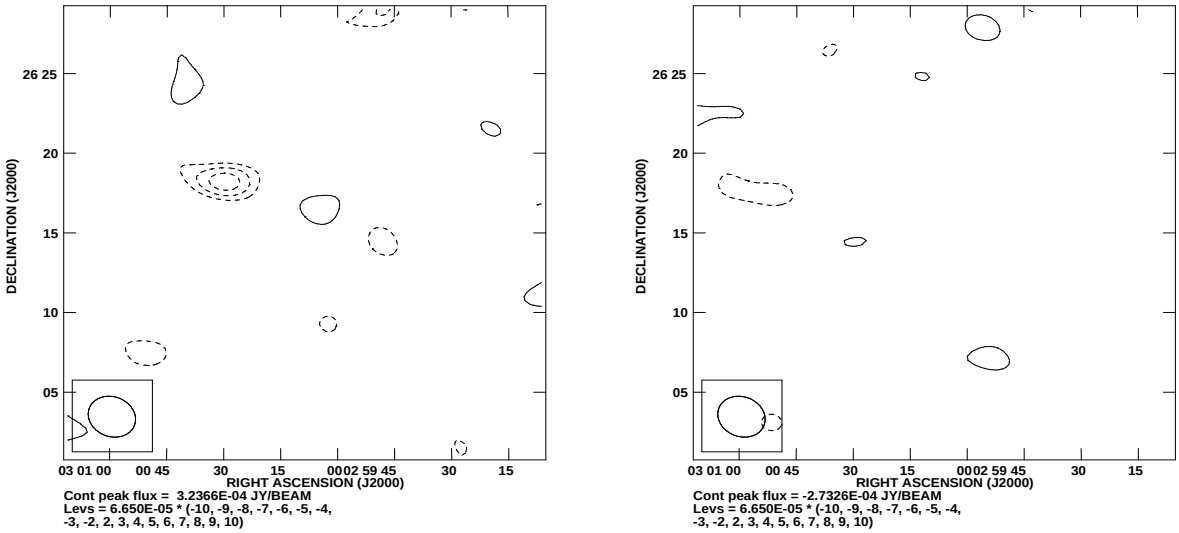

Figure 5.14: The jack-knifed data from Figure 5.11 (left). On the left, data are split according to median date, one the right, data are split into plus and minus baselines. The σ level for contours is 65μJy/beam.

Due to the high p values, high signal-to-noise and the interesting morphology of this decrement I have submitted the results of this detection for publication (AMI Consortium: Shimwell *et al.* 2010) and I have applied for follow-up SZ observations with the Combined Array for Research in Millimetre-wave Astronomy (CARMA; Bock *et al.* 2006).

5.6.3 Candidate 3: 18-19-22

An extended negative structure is detected with $p = 1.0$ in triangle 18-19-20 and $p = 0.52$ in triangle 18-21-22. The candidate was not detected in the search triangle 19-22-23; however, a decrement is clearly visible in that map and the data from that triangle are significantly contaminated by a bright source (see Figure 5.6). The lowest noise in the region of this candidate was obtained in triangle 18-19-22, the image of which is shown in Figure 5.15.

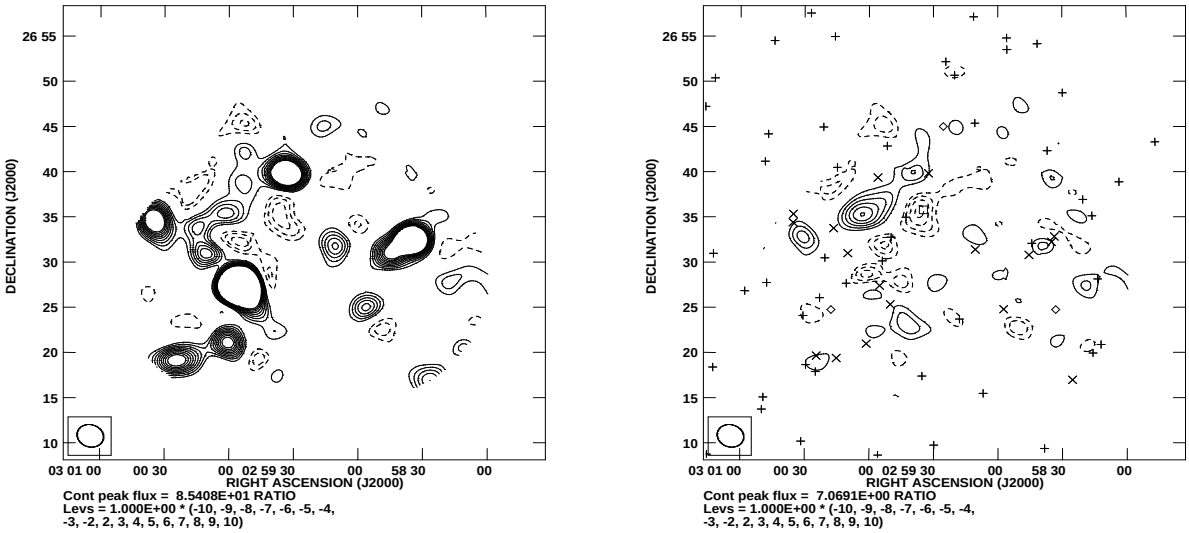

Figure 5.15: Same as for Figure 5.7 but for candidate 3 (found in 18-19-22). The thermal noise in the region of the candidate is $\sigma_{A2,SUR,CL3} = 110\mu$Jy/beam.

Quite large residuals remain on the map after source subtraction, especially in the region of the 8.4mJy/beam (LA measurement) source with coordinates 02:59:55.1 +26:27:26. This contamination is apparent in both the source subtracted pointed observations (Figure 5.15) and the SA survey jack-knifed data set (Figure 5.6). The contamination is not solely confined to the exact position of the source but it is concentrated within a radius of $\approx 5'$. The cluster candidate is separated by $9.5'$ from this source and the apparent contamination at that distance is minimal.

On the map there is positive extended structures to the north and to the east of the candidate – these are not noticeable on the LA maps. There is a possibility

that the extended sources at 02:59:55.9 +26:39:23 (peak flux 0.35mJy/beam, integrated flux 0.50mJy/beam) and 03:00:35.3 +26:35:21 (peak flux 1.3mJy/beam, integrated flux 1.7mJy/beam) are responsible for this structure. To further investigate this I have applied a *uv* cut to the LA data and rejected all data from baselines longer than 2000λ. This cut significantly reduces the resolution of the LA images (the typical *uv* range of the LA is $\approx 1000 - 7000\lambda$), and makes them more comparable to SA images (the SA *uv* range is $\approx 200 - 1200\lambda$). However, even in this *uv* range limited data set the extension that we see on the SA maps is not visible. The NRAO VLA SkySurvey (radio 21cm, NVSS) was searched for extended objects in this region but no evidence of extended emission was found.

5.6.3.1 Pointed Follow-up Observations

The map of 23 hours of follow-up observations ($\sigma_{A2,POI,CL3} = 113\mu$Jy/beam) is shown before and after the sources have been modelled and subtracted in Figure 5.16 – a total of nine sources were modelled.

In the pre-source subtracted map we observe a $4\sigma_{A2,POI,CL3}$ decrement but there are several sources whose sidelobes may artificially influence this decrement. The most likely sources to cause this contamination are the 8.4mJy/beam source and the 2.4mJy/beam source (2:59:32.3 +26:39:51).

After sources are subtracted the shape of the decrement stays the same but the magnitude decreases to $3\sigma_{A2,POI,CL3}$. After subtraction the 8.4mJy/beam source leaves an $8\sigma_{A2,POI,CL3}$ residual, $10'$ from the candidate – the sidelobes of this residual are unlikely to cause contamination at $> 5\%$ of the residual flux density (the synthesized beam for this observation is shown in Figure 5.2). Other sources subtract leaving few residuals.

The data quality of this observation has been carefully checked and the jackknife tests do not reveal contamination. Several unexplained positive and negative features as significant as the candidate are present on the source subtracted map. Some are associated with sources, whilst the $3\sigma_{A2,POI,CL3}$ positive structures to the north and the east of the candidate were also observed in the survey observations. However, the cause the other structures is unclear.

The derived parameters from the McAdam runs are shown in Figures 5.16 and 5.17; the mean parameters are shown in Tables 5.9 and 5.10. Note that the derived position parameters clearly show that two distinct modes were detected. One is the candidate and the second mode corresponds to the $2\sigma_{A2,POI,CL3}$ decrement west of candidate 3. The Bayesian evidence of the second mode is 3.9 lower than that for candidate 3.

For candidate 3 we derive a p value of 0.7 (R=2.3). I find candidate 3 not wholly convincing given that there are unexplained positive and negative residuals with higher or comparable flux densities.

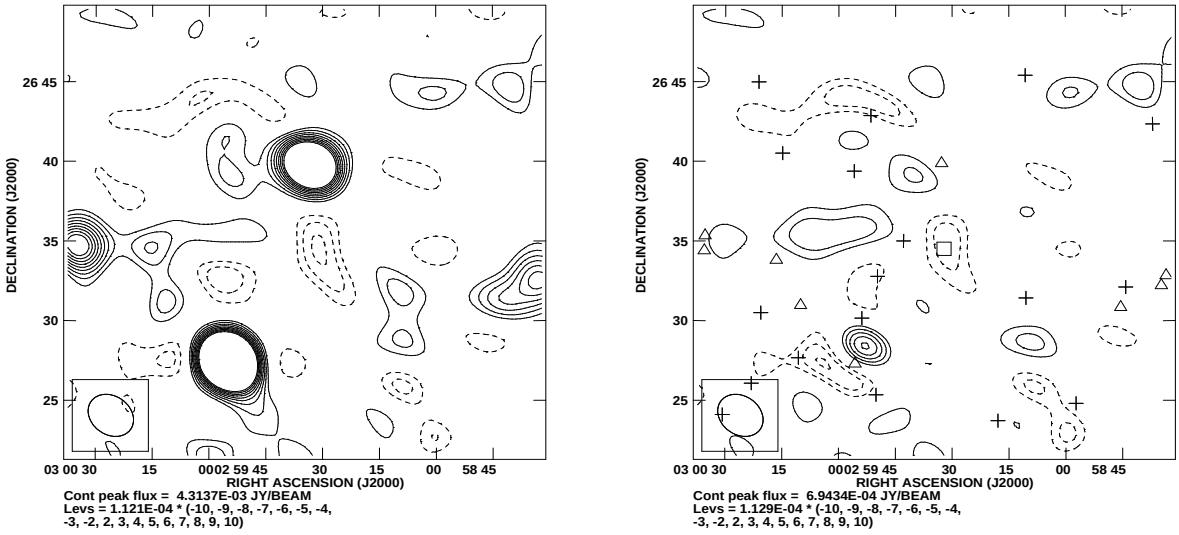

Figure 5.16: Same as Figure 5.8 but for AMI002 candidate 3.

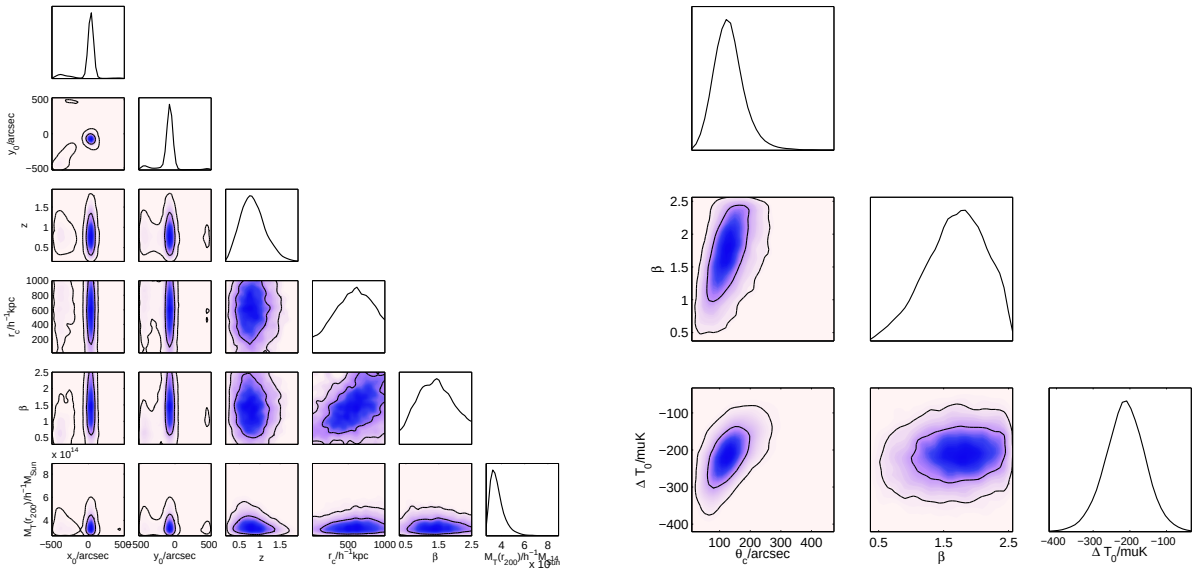

Figure 5.17: The derived parameters for AMI002 cluster candidate 3 . On the left are the physical parameters and on the right are the phenomenological model parameters.

Table 5.9: Mean values and 68% confidence limits for the parameters in the physical cluster model for candidate 3.

Parameter		
z	$0.83^{+0.30}_{-0.30}$	
$M_T(r_{200})/h^{-1}M_{Sun}$	$3.6^{+0.5}_{-0.6} \times 1014\ r_c/h^{-1}kpc$	560^{+440}_{-550}
β	$1.4^{+1.1}_{-1.1}$	

Table 5.10: Mean values and 68% confidence limits for the parameters in the phenomenological model for candidate 3.

Parameter	
$\Delta T_0/\mu$K	-210^{+52}_{-53}
$\theta_c/arcsec$	130^{+43}_{-47}
β	$1.7^{+0.5}_{-0.5}$

5.6.4 Candidate 4: 6-7-11, 3-6-7 and 6-10-11

A $4\sigma_{A2,SUR,CL4}$ decrement with a similar extent to the synthesized beam that may be associated with an extended $2\sigma_{A2,SUR,CL4}$ structure to the north is detected by McAdam in 6-7-11, 3-6-7 and 6-10-11 , with p values of 0.99, 0.55 and 0.28 respectively. This candidate lies outside the search area for all other triangles. The noise is lowest for observation 6-7-11 and an image of these data is shown in Figure 5.18.

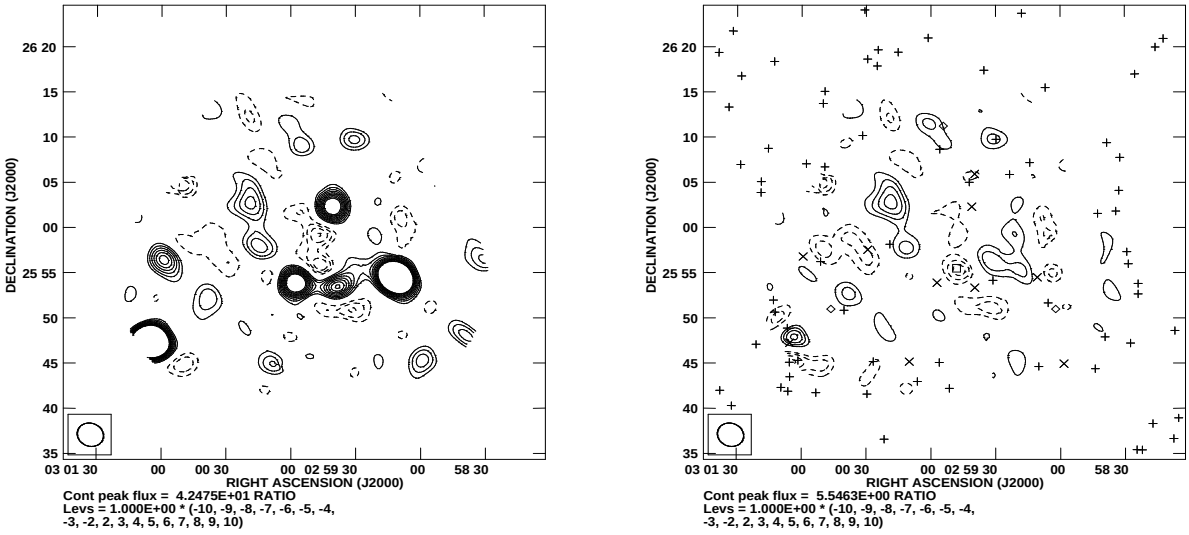

Figure 5.18: Same as for Figure 5.7 but for the candidate 4 (found in 6-7-11). The thermal noise in the region of the candidate is $\sigma_{A2,SUR,CL4} = 100\mu$Jy/beam.

Just to the south of the candidate are two sources that may influence the magnitude of the decrement. These sources lay at positions 02:59:57.2 +25:53:56 (peak flux 1.6mJy/beam) and 02:59:39.7 +25:53:23 (peak flux 0.78mJy/beam); neither of these sources is extended on our LA maps. To the north-east of the candidate there is extended positive structure that is not associated with any LA sources. To search for this structure a map was made from the LA data from baselines shorter than 2000λ but nothing was found. NVSS images of this area also reveal no visible extended structure.

In the 6-7-11 triangle I note that the jack-knifed data (Figure 5.6) does show residuals that are associated with the 3.5mJy/beam source at 02:59:10.7 +25:54:31. These residuals do extend towards this cluster candidate.

5.6.4.1 Pointed Follow-up Observations

A total of 40 hours of SA pointed observations towards this candidate were conducted in June 2011 and a noise level of $\sigma_{A2,POI,CL4} = 130\mu$Jy/beam was reached. The images before and after source subtraction are shown in Figure 5.19. For the analysis of this pointed observation a total of four sources were modelled.

Candidate 4 was identified in the survey data as a peak decrement (02:59:48.1 +25:55:31) which was possibly associated with the $2\sigma_{A2,SUR,CL4}$ negative structure to north. In these follow-up observations the peak decrement of candidate 4 was not detected, but the negative structure to the north was.

The source environment around candidate 4 is not severe. The main contaminating sources are a 1.7mJy/beam source (02:59:41.1 +26:02:20) north of the candidate and the 1.6mJy/beam and 0.78mJy/beam sources that lay south of the candidate. All sources are subtracted from the follow-up data leaving minimal residuals. Before source subtraction the decrement just north of candidate 4 was $5\sigma_{SA,A2CL4}$, but the source sidelobes contribute to the magnitude of the decrement. After source subtraction the decrement is decreased to $3\sigma_{SA,A2CL4}$.

Neither of the jack-knife tests reveal any contamination of the follow-up observations. The derived parameters are shown in Figures 5.19 and 5.20 and Tables 5.11 and 5.12. From the McAdam Bayesian evidences we derive a p value of 0.97 (R=32) for the decrement just north of candidate 4.

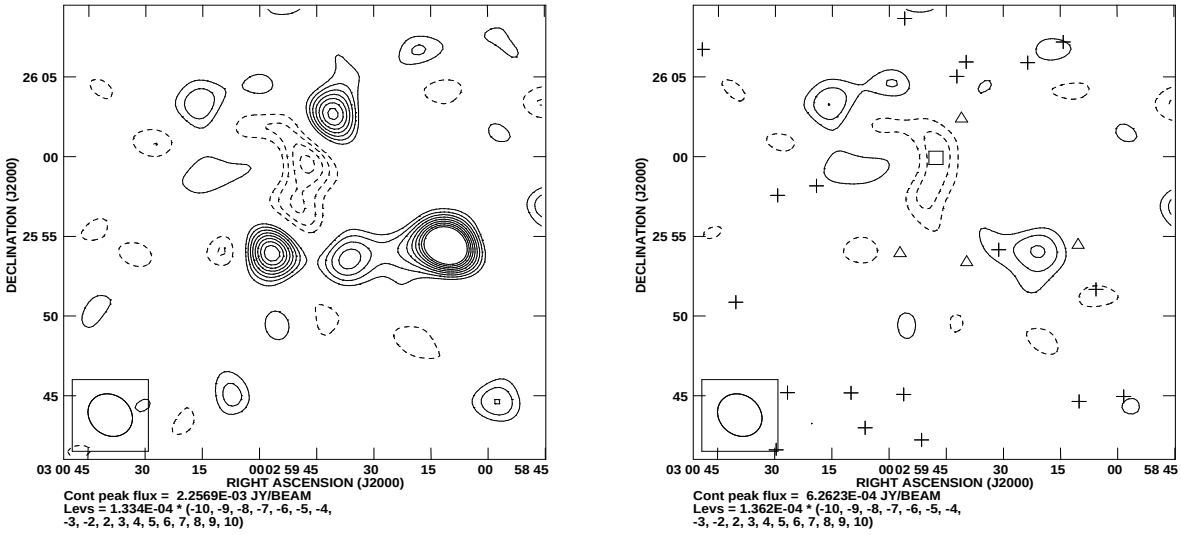

Figure 5.19: Images of the SA pointed observations towards the AMI002 cluster candidate 4.

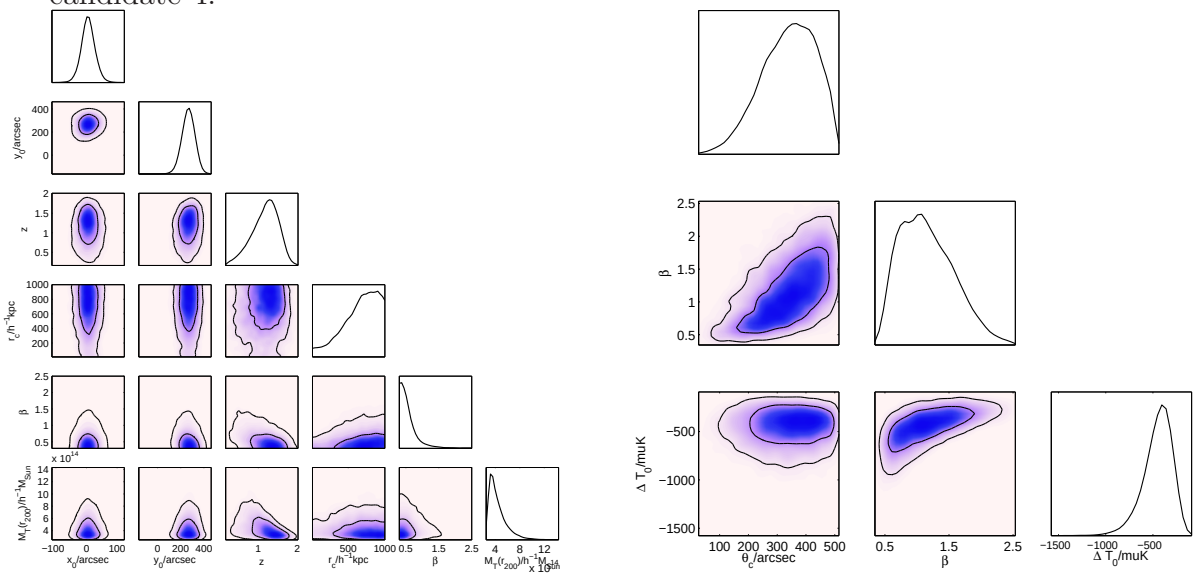

Figure 5.20: The derived parameters for AMI002 cluster candidate 4. On the left are the physical parameters and on the right are the phenomenological model parameters.

Table 5.11: Mean values and 68% confidence limits for the parameters in the physical cluster model for candidate 4.

Parameter	Value
z	$1.2^{+0.3}_{-0.3}$
$M_T(r_{200})/h^{-1}M_{Sun}$	$4.4^{+1.3}_{-1.5} \times 10^{14}$
$r_c/h^{-1}kpc$	660^{+340}_{-84}
β	$0.6^{+0.0}_{-0.3}$

Table 5.12: Mean values and 68% confidence limits for the parameters in the phenomenological model for candidate 4.

Parameter	Value
$\Delta T_0/\mu$K	-450^{+140}_{-140}
$\theta_c/arcsec$	340^{+97}_{-96}
β	$1.2^{+0.4}_{-0.4}$

5.6.5 Candidate 5: 7-11-12 and 7-8-12

An extended $4\sigma_{A2,SUR,CL5}$ decrement is detected in both 7-11-12 and 7-8-12 triangles; the McAdam derived probabilities are 0.97 and 0.90 respectively. This candidate can also be seen in the data from 4-7-8 and 3-4-7 but it is outside those cluster search regions. The map from 7-11-12 is shown in Figure 5.21 – this map is chosen because it has the lowest noise in the vicinity of the candidate.

After source subtraction we find that sources are generally removed well, leaving few residuals (excluding the 14mJy/beam source at 03:01:05.5 +25:47:16 which does leave large residuals but is $> 15'$ from candidate 5). However, there are several $> 4\sigma_{A2,SUR,CL5}$ positive features on the SA map which are not detected by the LA. The most significant of which lies just to the north-west of the candidate and the sidelobes of this structure may have an impact upon the magnitude of the decrement. Another concerning aspect is the existence of a 0.33mJy/beam (03:00:29.4 +25:57:35) extended LA source within the candidate

5 decrement. If this source is extended on the SA then there could be a degeneracy between its flux density and the magnitude of the candidate decrement. In the analysis of the 7-11-12 triangle, McAdam models this source to have a flux density of 0.15mJy/beam. This conservative flux density estimation leads to a lower SZ decrement.

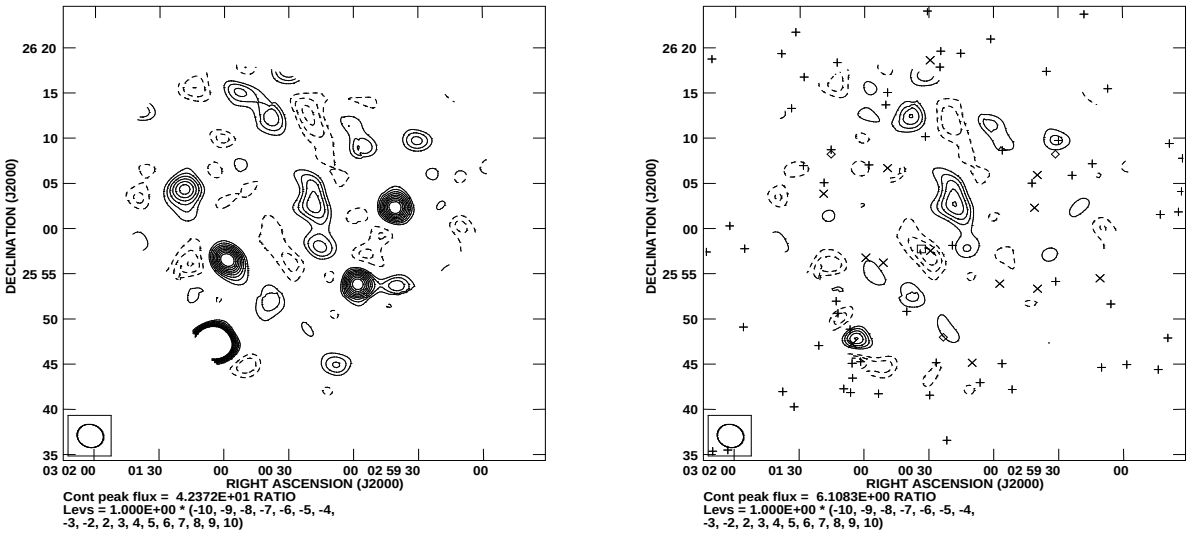

Figure 5.21: Same as for Figure 5.7 but for the candidate 5 (found in 7-11-12). The thermal noise in the region of the candidate is $\sigma_{A2,SUR,CL5} = 105\mu$Jy/beam.

5.6.5.1 Pointed Follow-up Observations

A follow-up program consisting of 31 hours of SA pointed observations was undertaken in June 2011. The thermal noise level achieved was $\sigma_{A2,POI,CL5} = 110\mu$Jy/beam and as a result five sources were modelled in the analysis. The images of these data before and after source subtraction are shown in Figure 5.22. On the source subtracted map there is a $> 3\sigma_{A2,POI,CL5}$ negative feature close to the location of candidate 5, but this is not the brightest negative (or positive) feature on the map.

Excluding the extended 0.33mJy/beam source which is located very close to candidate 5, the main contaminating sources are the 1.4mJy/beam point source at 03:00:59.3 +25:56:49 and the 14mJy/beam source. Before source subtraction the

sidelobes of these sources may contribute significantly to the decrement. However, the 1.4mJy/beam source subtracts leaving no residuals and the 14mJy/beam source leaves only 1.0mJy/beam residuals. The sidelobes of these residuals are unlikely to have more that a 50μJy/beam effect at the location of candidate 5.

The 0.33mJy/beam extended source was modelled to have a flux density of 0.27mJy/beam in the follow-up data (in the survey the derived flux density is 0.15mJy/beam). McAdam can be forced to use the higher flux density LA measurement for this source by putting a delta-function prior of 0.33mJy/beam on its flux. If this is done, then a slightly higher magnitude decrement is obtained at the location of candidate 5. However, the Bayesian evidence drops by 0.2 indicating that McAdam has little preference between the models but does slightly prefer a lower flux density for this source.

McAdam has been able to detect a mode at the position of candidate 5 but the derived parameters are badly constrained and other negative features of higher magnitude are visible. The derived parameters obtained from the follow-up observations of candidate 5 are shown in Figure 5.23 and Tables 5.13 and 5.14. The p value obtained from the analysis of these follow-up observations was 0.33 (R=0.5).

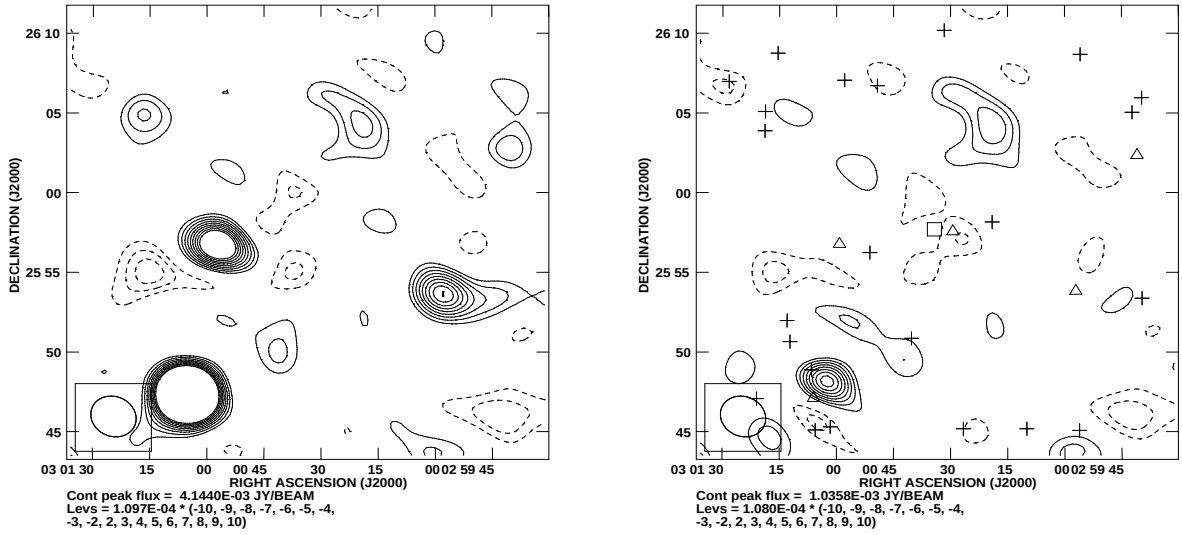

Figure 5.22: Images of the SA pointed observations towards the AMI002 cluster candidate 5.

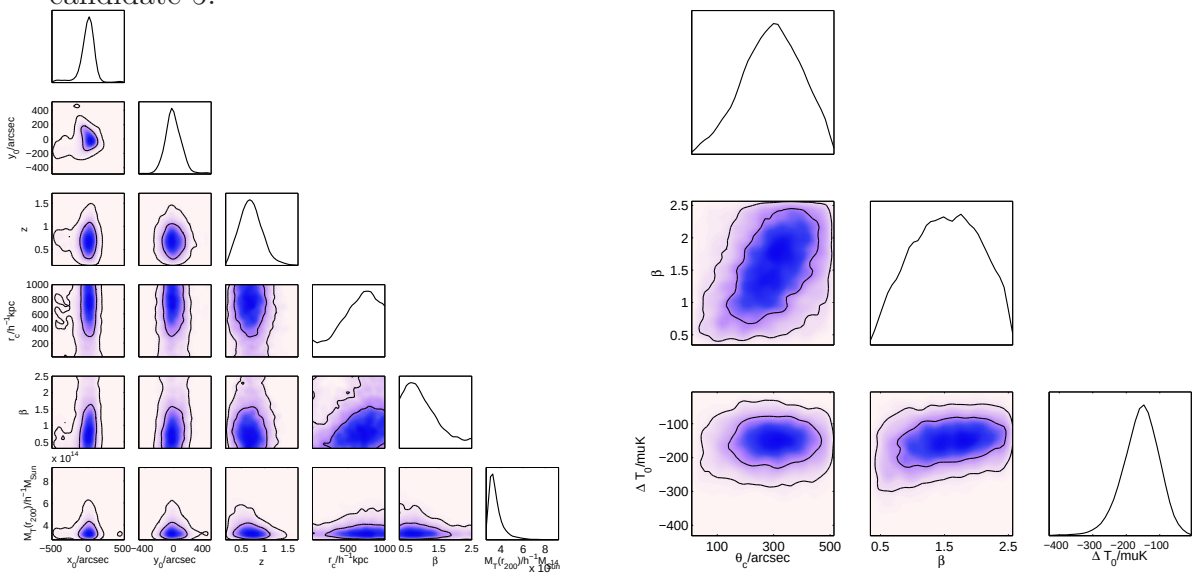

Figure 5.23: The derived parameters for AMI002 cluster candidate 5. On the left are the physical parameters and on the right are the phenomenological model parameters.

Table 5.13: Mean values and 68% confidence limits for the parameters in the physical cluster model for candidate 5.

z	$0.7^{+0.2}_{-0.2}$
$M_T(r_{200})/h^{-1}M_{Sun}$	$3.6^{+0.5}_{-0.7} \times 10^{14}$
$r_c/h^{-1}kpc$	620^{+380}_{-610}
β	$1.0^{+1.5}_{-0.7}$

Table 5.14: Mean values and 68% confidence limits for the parameters in the phenomenological model for candidate 5.

$\Delta T_0/\mu$K	-160^{+53}_{-51}
$\theta_c/arcsec$	290^{+110}_{-100}
β	$1.5^{+0.6}_{-0.6}$

5.6.6 Candidate 6: 2-3-6

A rather peculiar arrangement of $3 > 3\sigma_{A2,SUR,CL6}$ negative features lying along a north-west diagonal are observed in the 2-3-6 triangle. One of these features I identify as candidate 6; its derived p value is 0.8. Another of these decrements corresponds to candidate 4 (see Section 5.6.4). The image of 2-3-6 before and after source subtraction is shown in Figure 5.24. These three decrements were seen in the 2-5-6 triangle map but for that data McAdam was unable to isolate candidate 6 from the surrounding negative flux.

The most significant residual after source subtraction is associated with the 3.4mJy/beam source (02:59:10.7 +25:54:31). South-west of candidate 6 at 02:59:41.1 +26:02:20 lies a resolved LA source, its peak flux is 1.2mJy/beam and its integrated flux is 1.7mJy/beam. This extended source leaves no residuals after subtraction. Other sources also subtract well, and therefore on the source subtracted map I expect little contamination from source residuals at the location of candidate 6.

The jack-knife tests reveal no contamination close to this candidate. However on the SA map, there is a positive feature south of the candidate, which was not

detected on the LA maps. The sidelobes of this positive structure may affect the candidate.

Note that the $4\sigma_{A2,SUR,CL6}$ decrement at 02:59:44.3 +25:39:22 lies outside all the survey search triangles and hence is not detected at all.

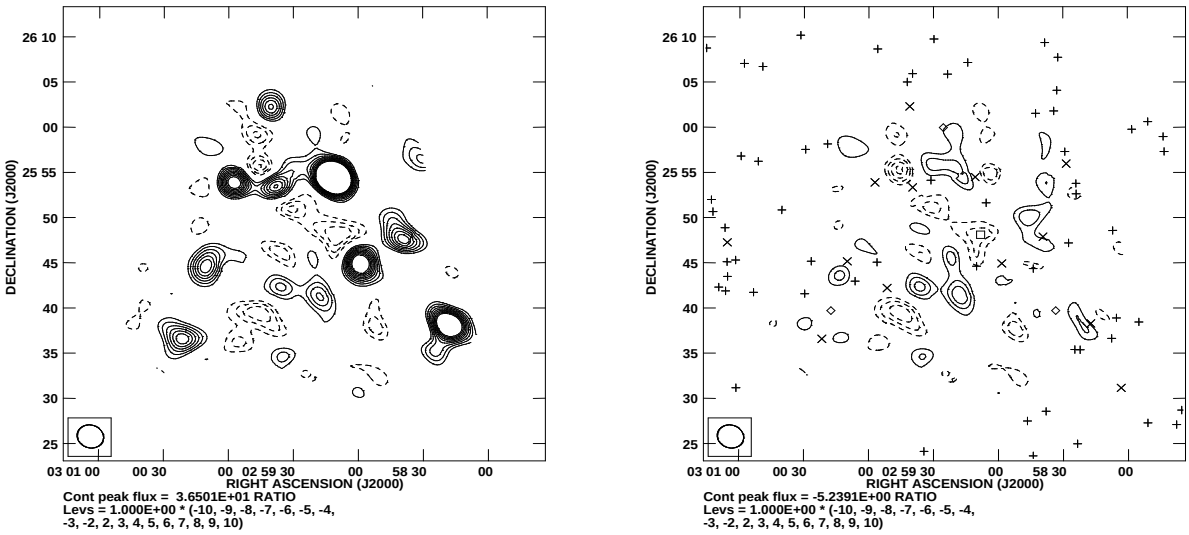

Figure 5.24: Same as for Figure 5.7 but for the candidate 6 (found in 2-3-6). The thermal noise in the region of the candidate is $\sigma_{A2,SUR,CL6} = 100\mu$Jy/beam.

5.6.6.1 Pointed Follow-up Observations

The follow-up of candidate 6 consisted of 28 hours of pointed SA observations. From these data a thermal noise level of $\sigma_{A2,POI,CL6} = 110\mu$Jy/beam was obtained. Above $4\sigma_{A2,POI,CL6}$ there were five LA sources, although another source of LA flux density 0.18mJy/beam (02:59:10.1 +25:44:39) was modelled because it lay at the edge of the candidate decrement. The maps before and after source subtraction are shown in Figure 5.25.

One striking difference between the survey observation and the pointed observation is the absence of candidate 4 but this was discussed in Section 5.6.4. On the pre-source-subtracted map the 3.4mJy/beam point source and 1.7mJy/beam extended source both influence the decrement. Even though the jack-knife tests reveal no contamination in this map I find that both these sources leave $3\sigma_{A2,POI,CL6}$

residuals after subtraction. However, the sidelobes of these residuals will have a negligible impact at the location of candidate 6. The source of flux density 0.18mJy/beam is modelled to have a mean flux density of 0.13mJy/beam and also has negligible impact on the candidate decrement.

Positive residuals are observed to the south and although these are not associated with LA sources they were also present in the SA survey data. These positive structures are unlikely to cause severe contamination to candidate 6 because they have a peak flux density of only $4\sigma_{A2,POI,CL6}$ and are $5'$ from the candidate.

The candidate is the brightest negative feature on the source subtracted map, although there are several positive features of higher magnitude. The McAdam derived parameters from this pointed observation are presented in Figure 5.26 and Tables 5.15 and 5.16 give the mean values of these parameters. For this candidate 6 follow-up observation I use the Bayesian evidences to calculate $p = 0.82$ (R=4.5), which matches the value obtained from the survey field.

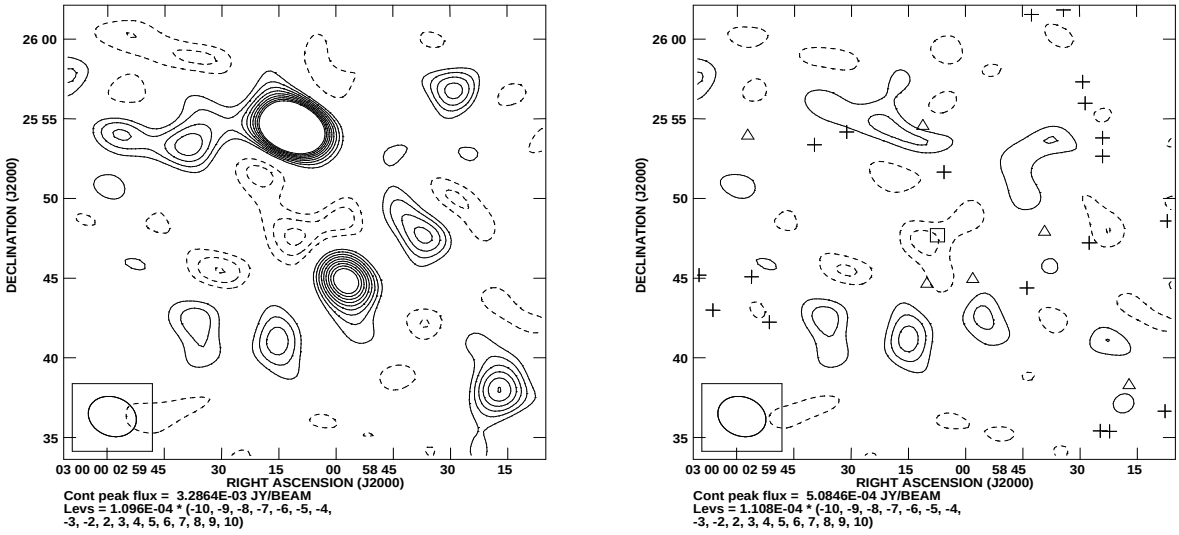

Figure 5.25: Images of the SA pointed observations towards the AMI002 cluster candidate 6.

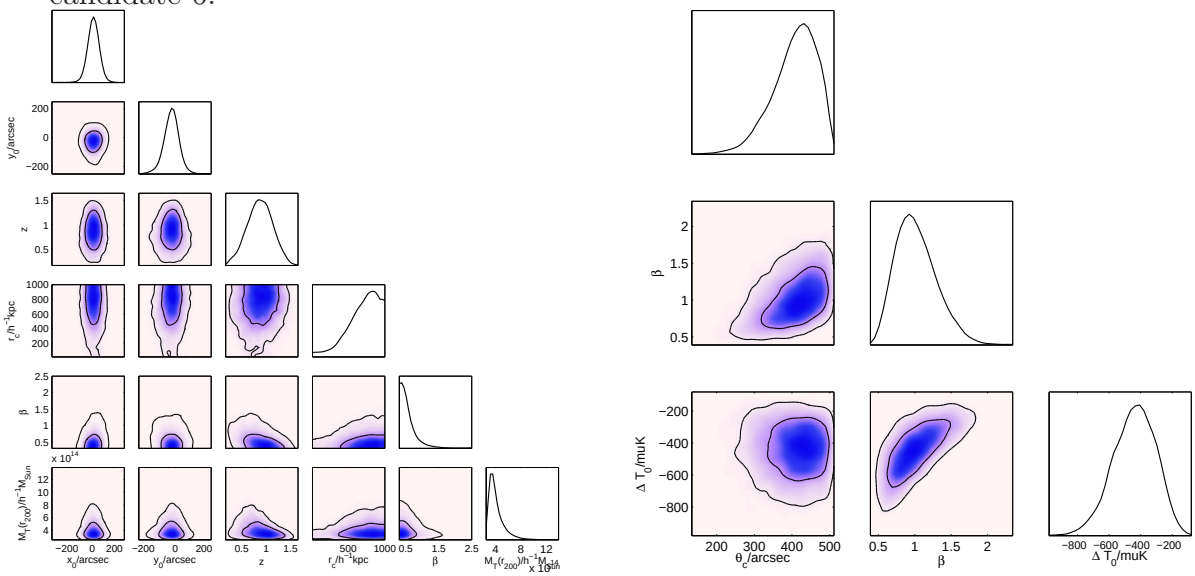

Figure 5.26: The derived parameters for AMI002 cluster candidate 6. On the left are the physical parameters and on the right are the phenomenological model parameters.

Table 5.15: Mean values and 68% confidence limits for the parameters in the physical cluster model for candidate 6.

Parameter	Value
z	$0.9^{+0.3}_{-0.3}$
$M_T(r_{200})/h^{-1}M_{Sun}$	$4.1^{+1.0}_{-1.2} \times 10^{14}$
$r_c/h^{-1}kpc$	700^{+300}_{-73}
β	$0.6^{+0.1}_{-0.3}$

Table 5.16: Mean values and 68% confidence limits for the parameters in the phenomenological model for candidate 6.

Parameter	Value
$\Delta T_0/\mu$K	-440^{+140}_{-130}
$\theta_c/arcsec$	410^{+58}_{-58}
β	$1.0^{+0.3}_{-0.3}$

5.6.7 Candidate 7: 5-9-10 and 1-2-5

A non-circular, double-peaked-decrement is detected between point sources in the 5-9-10 and 1-2-5 search triangles. The derived p values for this candidate are 0.8 and 0.68 from each of these fields respectively. The noise in the region of the candidate is lowest in 5-9-10, the map of which is shown in Figure 5.27. We do not expect to detect this candidate in any other triangles.

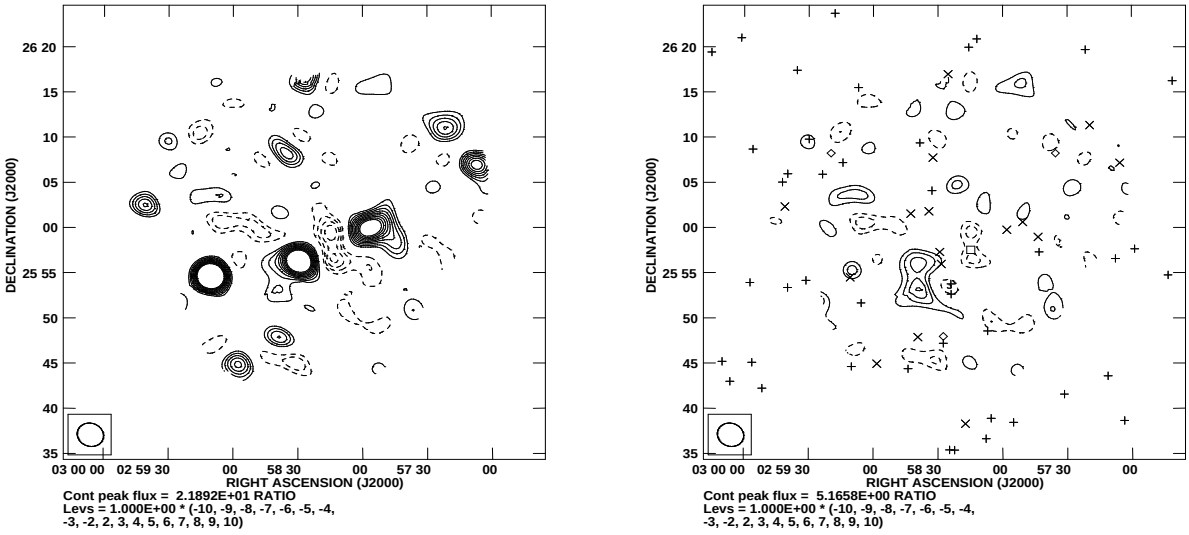

Figure 5.27: Same as for Figure 5.7 but for the candidate 7 (found in 5-9-10). The thermal noise in the region of the candidate is $\sigma_{A2,SUR,CL7} = 110\mu$Jy/beam.

Judging by the unusual morphology of the candidate and the position of the surrounding sources it is apparent that the sources to the east and the west significantly affect the magnitude of the decrement and its shape. The sources to the east that are most likely to influence the decrement lay at 02:58:28.5 +25:55:59 and 02:58:29.2 +25:57:20 and have flux densities of 1.2mJy/beam and 0.96mJy/beam respectively. To the west of the candidate the 1.34mJy/beam source at 02:57:58.1 +25:59:47 is the most likely to influence the decrement. None of these three sources is extended on the LA maps or NVSS images. After source subtraction the only significant residual is the $4\sigma_{A2,SUR,CL7}$ extended positive structure to the west of the candidate.

The jack-knife tests in Figure 5.6 reveal that there is some contamination associated with the 1.34mJy/beam source to the west of the cluster candidate.

5.6.7.1 Pointed Follow-up Observations

A total of 23 hours of SA pointed observations towards candidate 7 were obtained in July 2011. A thermal noise level of $\sigma_{A2,POI,CL7} = 110\mu$ Jy/beam was reached. In McAdam only four sources had a flux density greater than

$4\sigma_{A2,POI,CL7}$ and these were modelled. These were the three sources with flux densities of 1.2mJy/beam, 0.96mJy/beam and 1.34mJy/beam that were previously discussed and one other source at 02:59:10.7 +25:54:31 with a flux density of 3.4mJy/beam. Maps of the data before and after source subtraction are shown in Figure 5.28.

On the source subtracted map we observe a $4\sigma_{A2,POI,CL7}$ decrement at the location of the candidate. We see positive flux density to the east of the candidate, which was also observed in the survey observations. This residual extended structure is likely to be influenced by sidelobes from the decrement and will itself give some influence to the decrement. However, the synthesized beam indicates that this is likely to be less than a 10% effect. Otherwise, the source subtraction of modelled sources shows few residuals.

The largest decrement on the map is a $4\sigma_{A2,POI,CL7}$ decrement at the position of the candidate 7. However, several other 3 and $4\sigma_{A2,POI,CL7}$ decrements are also observed on the map. Often these other decrements are associated with sources being subtracted with delta-function priors. The jack-knife tests of this follow-up data shows no contamination.

The derived parameters for this candidate are given in Figure 5.29 and Tables 5.17 and 5.18. The position parameter has a bimodal distribution but McAdam is able to separate these modes. From the evidences of the mode corresponding to candidate 7 we find that $p = 0.64$ (R=1.8) (for the other mode we find $p = 0.22$ (R=0.28).

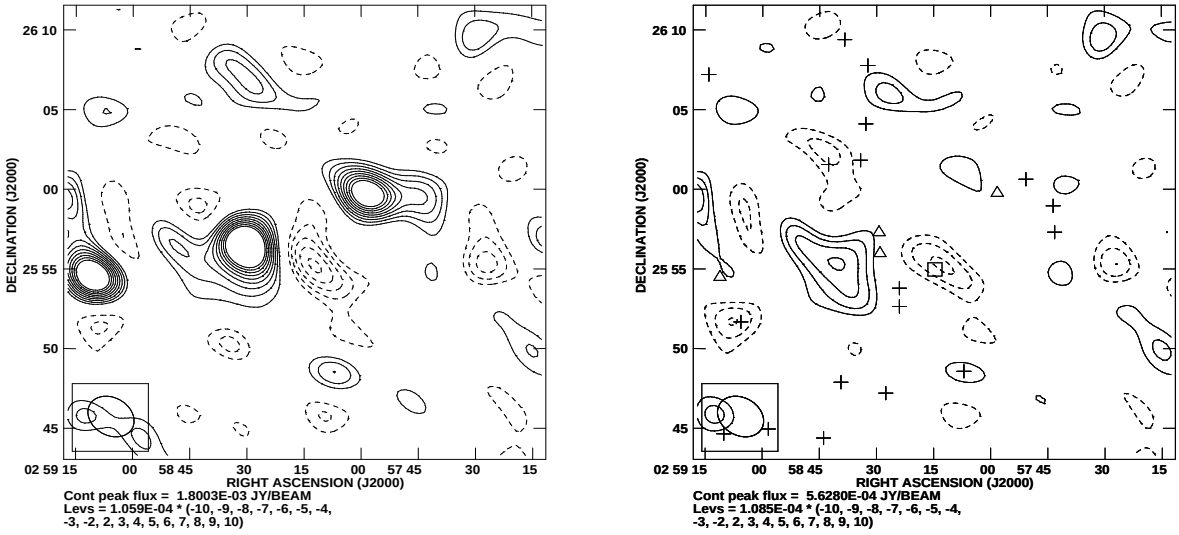

Figure 5.28: Images of the SA pointed observations towards the AMI002 cluster candidate 7.

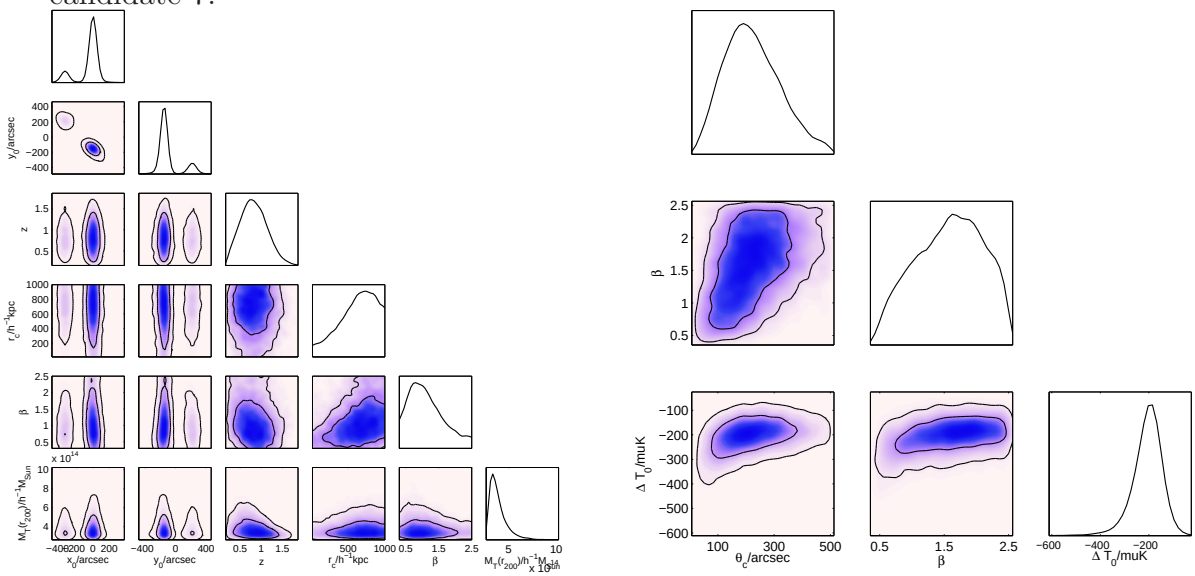

Figure 5.29: The derived parameters for AMI002 cluster candidate 7. On the left are the physical parameters and on the right are the phenomenological model parameters.

Table 5.17: Mean values and 68% confidence limits for the parameters in the physical cluster model for candidate 7.

Parameter	Value
z	$0.8^{+0.3}_{-0.3}$
$M_T(r_{200})/h^{-1}M_{Sun}$	$3.9^{+0.8}_{-1.0} \times 10^{14}$
r_c/h^{-1}kpc	620^{+380}_{-610}
β	$1.1^{+1.4}_{-0.8}$

Table 5.18: Mean values and 68% confidence limits for the parameters in the phenomenological model for candidate 7.

Parameter	Value
$\Delta T_0/\mu$K	-210^{+53}_{-51}
θ_c/arcsec	220^{+100}_{-100}
β	$1.6^{+0.6}_{-0.6}$

5.6.8 Candidate 8: 6-10-11

In the 6-10-11 data candidate 8 was detected with $p = 0.71$ and it shows up as a $3\sigma_{A2,SUR,CL8}$ decrement on the map. The image of this search triangle is shown in Figure 5.30. Given the position of the candidate we would expect it to be detected in the 5-6-10 triangle but it is not (even though a small decrement is visible on that map). At the position of candidate 8 there is no contamination on the image of the jack-knifed SA data.

On the source subtracted map we observe several significant positive and negative features, including candidate 4 (Figure 5.19) and candidate 6 (Figure 5.25). To the south of candidate 8, the positive and negative residuals appear to be associated with the 3.4mJy/beam source at 02:59:10.7 +25:54:31 – this is the only source that is likely to have a significant effect on the candidate. The positive residuals north and east of the candidate do not have LA counterparts.

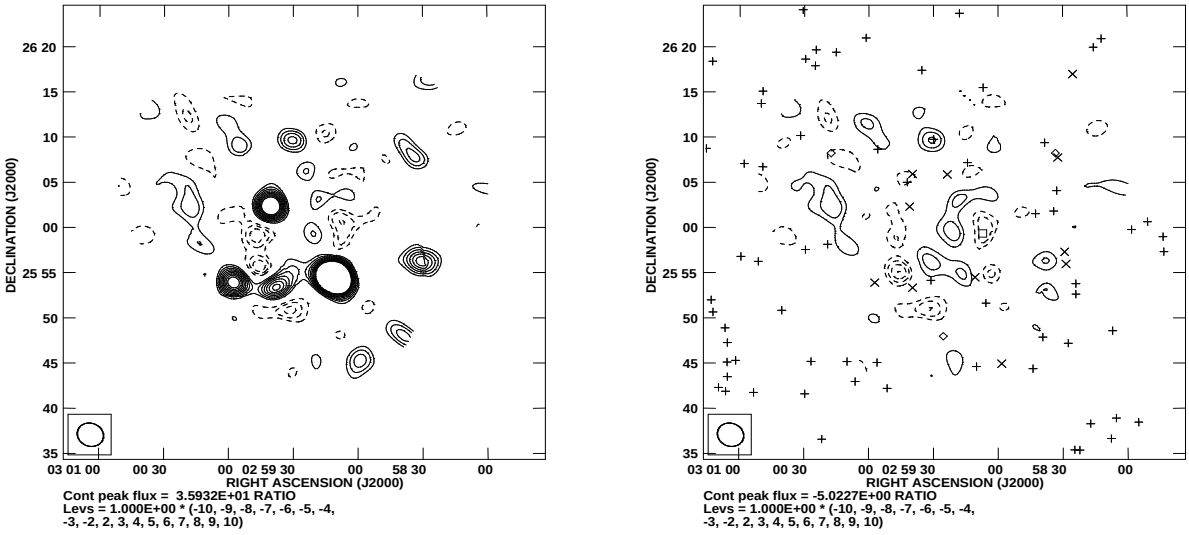

Figure 5.30: Same as for Figure 5.7 but for the candidate 8 (found in 6-10-11). The thermal noise in the region of the candidate is $\sigma_{A2,SUR,CL8} = 110\mu$Jy/beam.

5.6.8.1 Pointed Follow-up Observations

I have obtained 21 hours of SA pointed observations towards this candidate; for this the thermal noise level is $\sigma_{A2,POI,CL8} = 120\mu$Jy/beam. All three sources that are brighter than $4\sigma_{A2,POI,CL8}$ are modelled.

In Figure 5.31 I show images of the data before and after sources have been subtracted. The source subtracted map has few residuals associated with sources, the 3.4mJy/beam source that was previously mentioned subtracts leaving no residual flux density.

At the position of candidate 8 a $4\sigma_{A2,POI,CL8}$ decrement is observed. The candidate is the most significant decrement on the map but there are several other $3\sigma_{A2,POI,CL8}$ decrements. There is also a $4\sigma_{A2,POI,CL8}$ increment to the south east of the map. The $3\sigma_{A2,POI,CL8}$ negative residuals to the west of the map lie close to the positions of candidates 4 and 6.

If a *uv* taper is applied to the SA data to downweight baselines longer than 600kλ then the decrement is again observed a $4\sigma_{A2,POI,CL7}$, however, many of the other features on the map decrease in significance. This *uv* tapered image is shown in Figure 5.33. The brightest feature on the *uv* tapered map is a $5\sigma_{A2,POI,CL7}$

positive residual to the south-east of the map. This positive features also can be seen in the survey data (Figure 5.5) and the data for candidate 7.

The data has been carefully checked for interference and neither of the jack-knife tests reveal contamination. The derived parameters are shown in Figure 5.32 and Tables 5.20 and 5.20. The derived parameters show that McAdam is unable to completely isolate this decrement from surrounding residuals, however, this will have negligible influence on the derived evidences. The p value for this candidate is 0.56 (R=1.3).

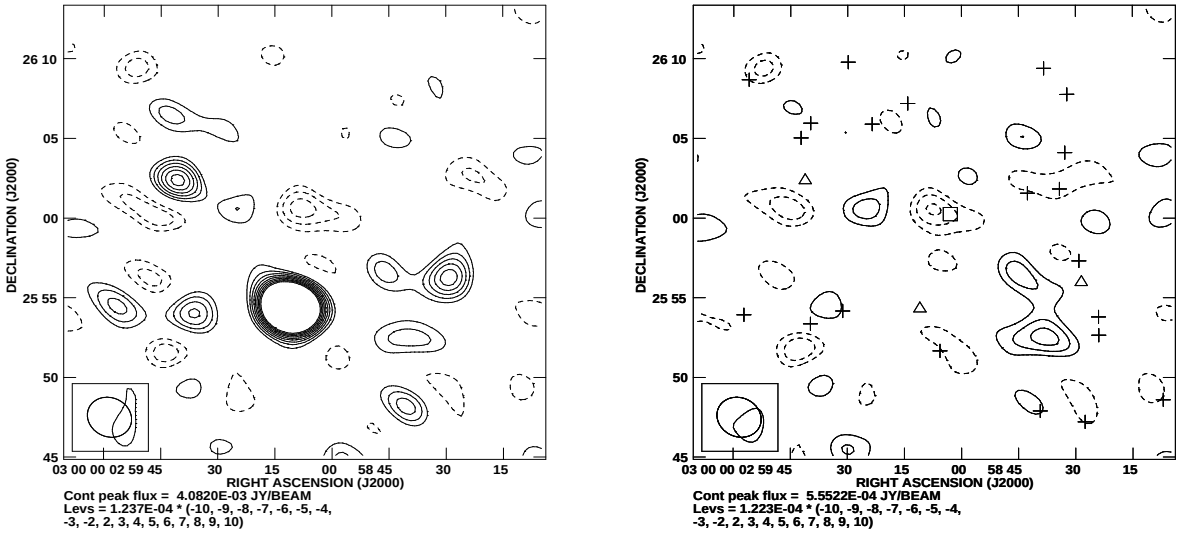

Figure 5.31: Images of the SA pointed observations towards the AMI002 cluster candidate 8.

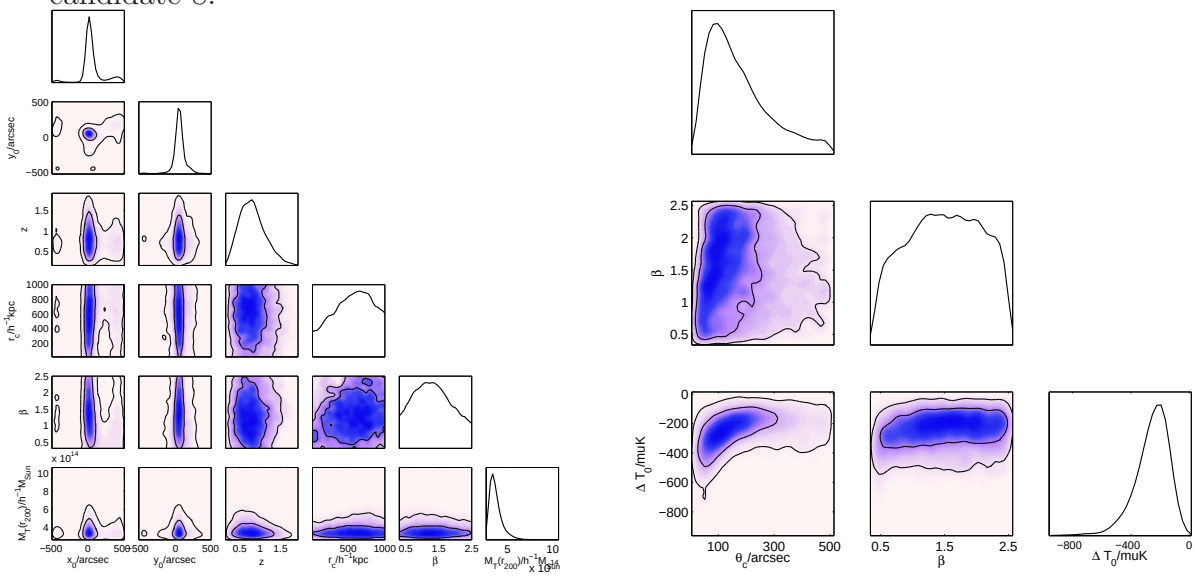

Figure 5.32: The derived parameters for AMI002 cluster candidate 8. On the left are the physical parameters and on the right are the phenomenological parameters.

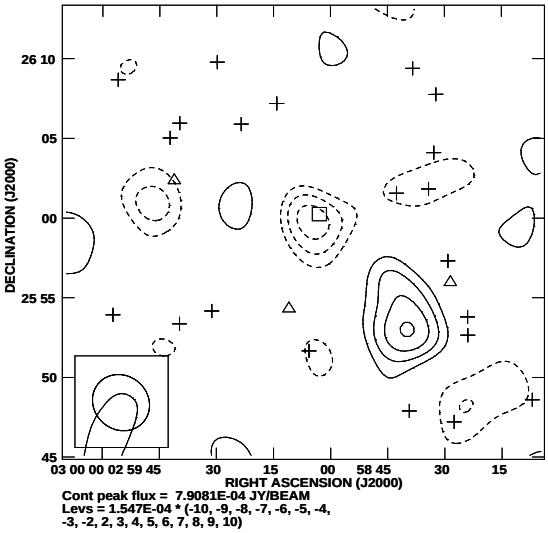

Figure 5.33: A *uv* tapered image of the SA pointed observations towards the AMI002 cluster candidate 8.

Table 5.19: Mean values and 68% confidence limits for the parameters in the physical cluster model for candidate 7.

Parameter	Value
z	$0.8^{+0.3}_{-0.3}$
$M_T(r_{200})/h^{-1}M_{Sun}$	$3.7^{+0.6}_{-0.6} \times 10^{-14}$
r_c/h^{-1}kpc	550^{+450}_{-540}
β	$1.3^{+1.2}_{-1.0e}$

Table 5.20: Mean values and 68% confidence limits for the parameters in the phenomenological model for candidate 7.

Parameter	Value
Δ	-260^{+110}_{-100}
θ_c/arcsec	170^{+110}_{-100}
β	$1.5^{+0.6}_{-0.7}$

5.6.9 Candidate 9: 13-14-18 and 13-17-18

This candidate is detected in 13-14-18 with $p = 0.37$ and in 13-17-18 at $p = 0.07$. Due to the position of this candidate we would not expect to detect it in any of the other survey runs. The data from 13-14-18 is shown in Figure 5.34 before and after the sources have been modelled and subtracted.

The only source likely to significantly influence this decrement is the 0.91mJy/beam point source at 02:58:57.3 +26:24:49. After the sources have been modelled and subtracted there is little residual flux density and jack-knife tests reveal no contamination. The decrement at the position of candidate 9 is the most significant feature on the map. The peak decrement has a flux density of 470μJy/beam, this corresponds to $5\sigma_{A2,SUR,CL9}$.

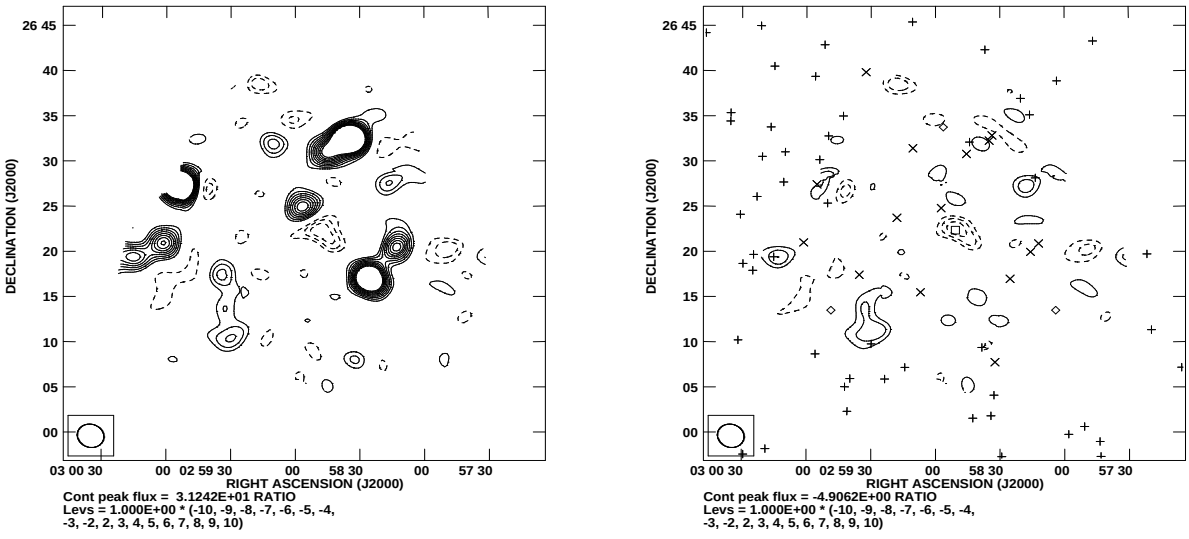

Figure 5.34: Same as for Figure 5.7 but for the candidate 9 (found in 13-14-18). The thermal noise in the region of the candidate is $\sigma_{A2,SUR,CL9} = 100\mu$Jy/beam.

5.6.9.1 Pointed Follow-up Observations

A total of 25 hours of pointed observations towards this candidate were obtained between May 2010 and June 2011. The resulting noise level was $\sigma_{A2,POI,CL9} = 120\mu$Jy/beam. At this noise level there are seven sources with flux densities above $\sigma_{A2,POI,CL9}$. These were modelled by McAdam.

The maps of the pointed follow-up observation before and after source subtraction are shown in Figure 5.35. In our follow-up observation we observe no decrement. I have thoroughly checked the data quality in REDUCE, in total there were five separate observations and each of these was manually flagged for interference. Also the jack-knife tests have revealed no contamination. It seems unlikely that point sources are contributing to this non-detection, the main source that could contribute is the 0.91mJy/beam source that was previously mentioned, but this subtracts leaving no residuals.

I show the McAdam derived parameters for this non detection in Figure 5.36. These show very little constraint on the position, indicating that no strong candidate was found within the search area. Note that some parameters appear constrained, however, this is an effect of our priors. The derived p value is $p = 0.23$ (R=0.31), this reflects the fact that McAdam was unable to find any strong candidates.

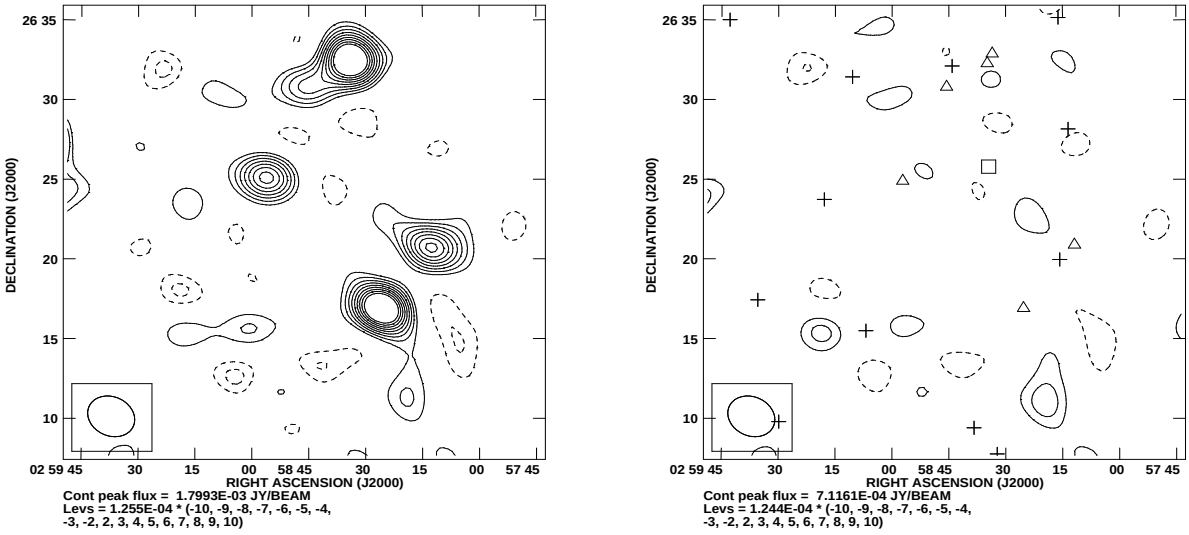

Figure 5.35: Images of the SA pointed observations towards the AMI002 cluster candidate 9.

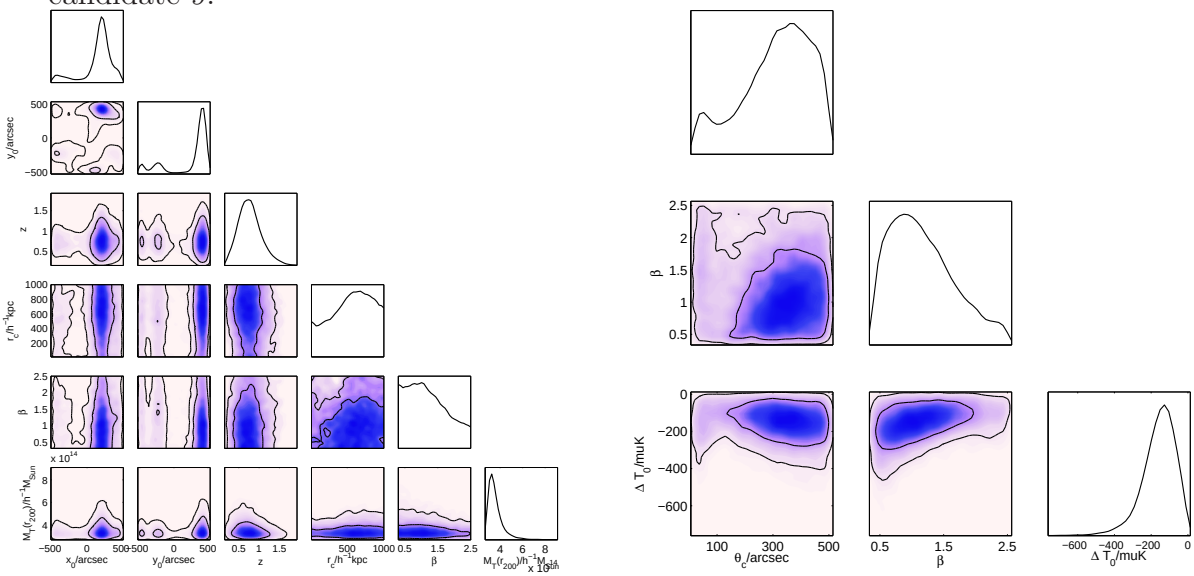

Figure 5.36: The derived parameters for AMI002 cluster candidate 10. On the left are the physical parameters and on the right are the phenomenological model parameters.

5.7 AMI005

The LA and SA images of the AMI005 field are shown in Figures 5.37 and 5.38 accordingly. In Figure 5.39 I show the AMI005 SA maps after jack-knife tests have been performed.

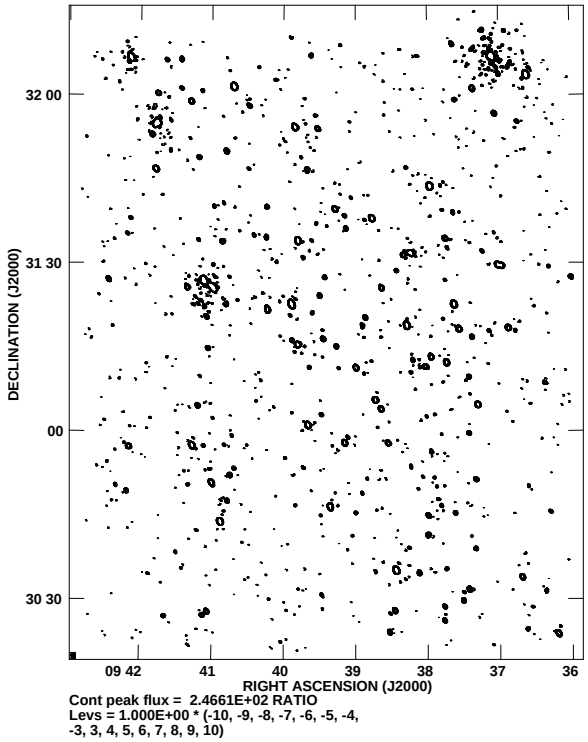

Figure 5.37: The map for the LA AMI005 field. In the central region the map noise is $\approx 50\mu$Jy/beam and in the outer region the noise is $\approx 100\mu$Jy/beam.

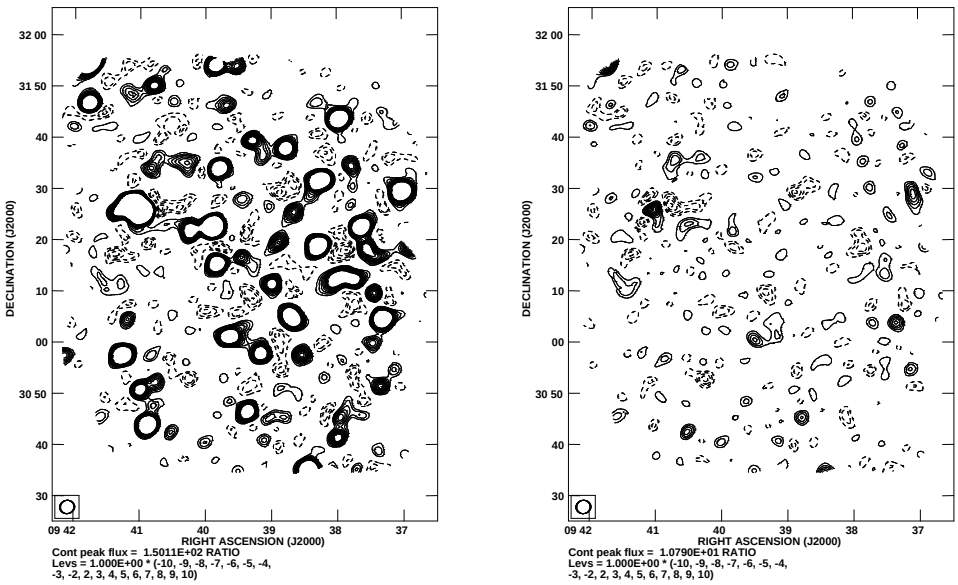

Figure 5.38: The AMI005 SA signal-to-noise map. On the left sources have not been subtracted, on the right sources have been subtracted using the McAdam derived values for their flux and spectral index. The noise level is $\approx 110\mu$Jy/beam.

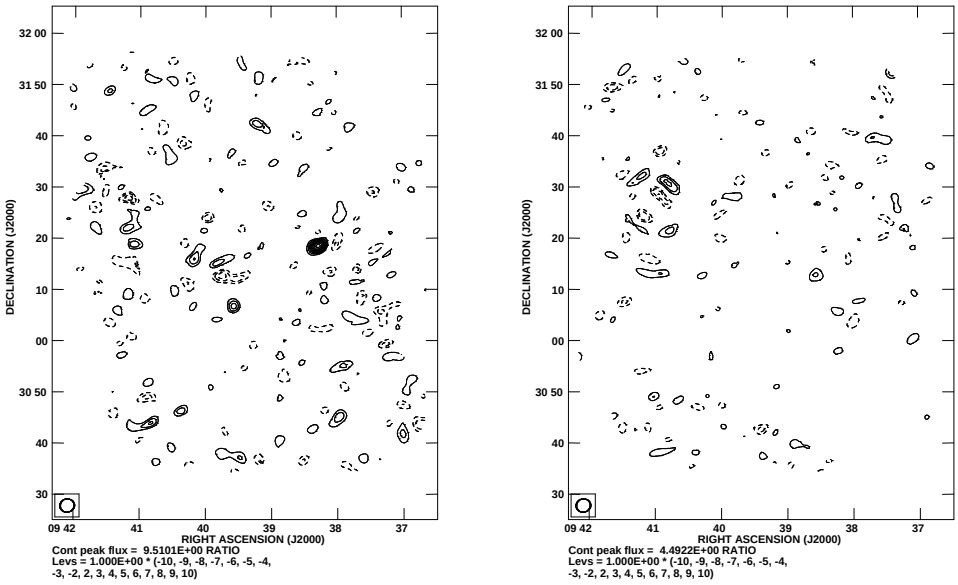

Figure 5.39: The signal-to-noise map of the AMI005 jack-knifed data set. On the left the data has been split according to the median data and on the right the data has been split into plus versus minus baselines. The noise on the map on the left is $\approx 110\mu$Jy/beam and the noise on the map on the right is $\approx 70\mu$Jy/beam.

In the 30 AMI005 search regions a total 43 modes were detected by McAdam. The majority of these modes have a low p value and in this study they are not investigated further. We detect four distinct modes with $p > 0.3$, although one of these modes (15-16-20, $p = 1.0$ at position 09:40:48.1 +31:26:33) is not investigated any further due to the severe contamination in this region (see the jack-knifed SA dataset, Figure 5.39). For the other three candidates I have obtained SA follow-up observations to further investigate the decrements. The search triangles, derived p values and positions of the three AMI005 candidates are given in Table 5.21.

Table 5.21: The derived p values for the three modes detected in the AMI002 SA data that have a highest $p > 0.3$. Often modes are detected in multiple triangles (which contain some of the same data), for these I provide the maximum and minimum derived p and R values. Note that the right ascension and declination are stated for the candidate detected with the highest p value.

Candidate	Fields	Highest p (R)	Lowest p (R)	Right Ascension	Declination
1	3-4-7, 4-7-8	0.93 (13)	0.77 (3.4)	09:40:16.5	+30:53:01
2	13-14-18, 14-18-19 13-17-18, 18-19-22 18-21-22 17-18-21	0.82 (4.7)	0.01 (0.01)	09:38:48.5	+31:29:54
3	9-10-13	0.42 (0.80)	0.42 (0.80)	09:37:51.6	+31:18:15

5.7.1 Candidate 1: 3-4-7 and 4-7-8

A circular decrement of a magnitude of $4\sigma_{A5,SUR,CL1}$ and a similar extent to the SA synthesized beam is detected in the 3-4-7 and 3-4-8 triangles. The derived p values are $p = 0.95$ and $p = 0.77$ respectively. Given the position of the candidate we would not expect to detect it in any other survey fields. The noise in the region

of the candidate is lowest in the 3-4-7 field, the image of these data is shown in Figure 5.7.1.

There are no sources within 3′ of this candidate. The most likely source to influence this decrement is the 6.2mJy/beam point source at 09:40:53.1 +30:43:52. However, this is separated by 12′ from the candidate position and its influence on the pre source subtracted map is likely to be less than 2% of its peak flux. After sources have been subtracted the residual source flux is minimal and hence it is expected that there is negligible contamination from sources at the position of the candidate. Also the jack-knifed data set does not reveal any contamination (Figure 5.39).

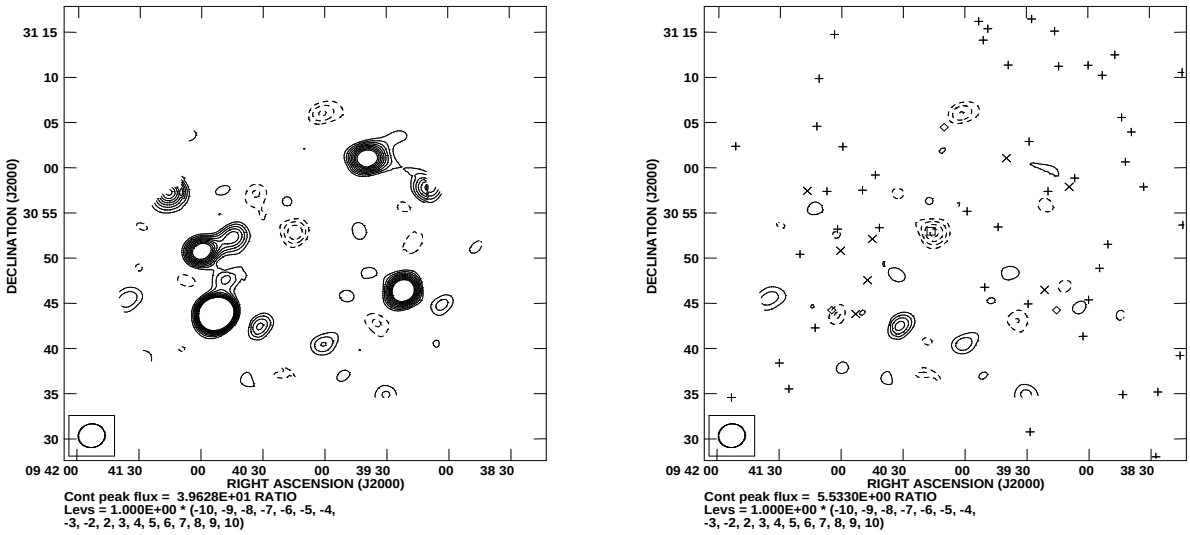

Figure 5.40: AMI005 cluster candidate 1 in the data from 3-4-7. In these data the cluster candidate is detected with $p = 0.95$. The thermal noise in the region of the candidate is $\sigma_{A5,SUR,CL1} = 110\mu$Jy/beam.

5.7.1.1 Pointed Follow-up Observations

We obtained 29 hours of pointed observations towards this candidate between 4th June and 7th June 2011. The resulting map before and after sources have been subtracted is shown in Figure 5.41. For these data we obtained a thermal noise

level of $\sigma_{A5,POI,CL1} = 120\mu$Jy/beam. Five LA sources have flux densities higher than $4\sigma_{A5,POI,CL1}$ and these were modelled by McAdam.

In our follow-up observation we have not detected this candidate. We do not observe a decrement greater than $2\sigma_{A5,POI,CL1}$ in the data before or after source subtraction. We do observe a decrement to the north-west of the pointing centre and this is the McAdam favoured mode, however, it did not appear in the survey data. This mode is made slightly larger by the direct subtraction of the LA source at 09:39:59.0 +30:55:14 with flux density 0.21mJy/beam.

The mild source environment around this candidate means that it is very unlikely that the data are contaminated by sources. Also, due to the discrepancy between the survey observation and this pointed follow-up I have taken special care when manually flagging the data. All interference and bad data that I noticed was removed and neither of the jack-knife tests that were performed on the pointed follow-up observation reveal any contamination.

The McAdam derived parameters for this observation are shown in Figure 5.42. These show that the derived position is not consistent with our survey observation derived position.

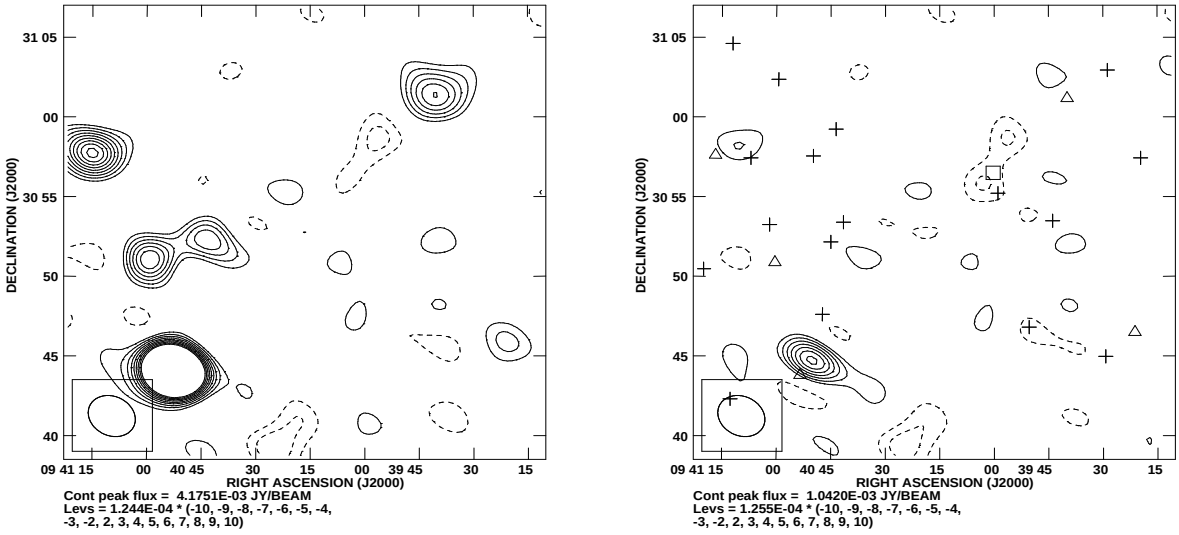

Figure 5.41: Images of the SA pointed observations towards the AMI005 cluster candidate 1.

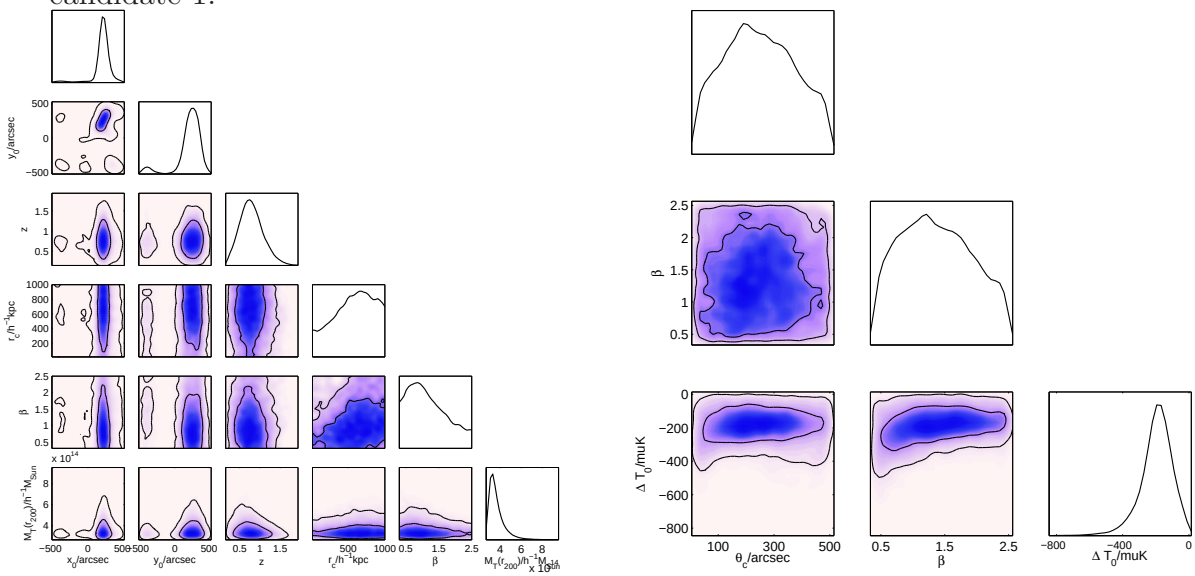

Figure 5.42: The derived parameters for AMI005 cluster candidate 1. On the left are the physical parameters and on the right are the phenomenological model parameters.

5.7.2 Candidate 2: 13-14-18 and 14-18-19

A $5\sigma_{A5,SUR,CL2}$ elliptical cluster candidate is detected in both 13-14-18 and 14-18-19 at values of $p = 0.82$ and $p = 0.5$ respectively. The noise level in this region is lowest in 13-14-18 and I present the maps from that search triangle in Figure 5.7.2.

Before the sources are subtracted those that are closest to the candidate and most likely to influence the decrement have LA measured fluxes of 2.7mJy/beam, 1.0mJy/beam, 1.0mJy/beam and 0.46mJy/beam and lay at 09:38:13.9 +31:31:48, 09:38:20.3 +31:31:28, 09:38:38.6 +31:25:35 and 09:38:26.0 +31:28:40 respectively. None of these sources are extended on the LA maps.

All sources subtract well and the largest residual flux density is $3\sigma_{A5,SUR,CL2}$. The sidelobes of this residual will cause minimal contamination to the observed decrement. The negative feature observed at 09:37:51.6 +31:18:15 is AMI005 candidate 3 and is discussed further in Section 5.7.3.

On the jack-knifed SA map (Figure 5.39) we see no significant contamination with the region of the candidate.

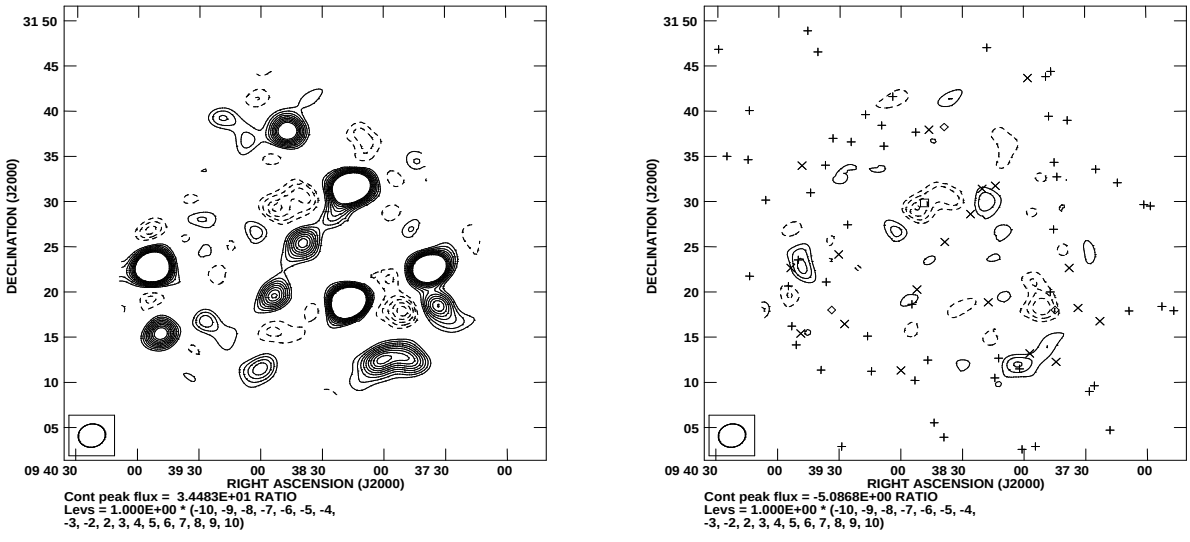

Figure 5.43: The AMI005 search triangle 13-14-18 in which the AMI005 cluster candidate 2 is detected with $p = 0.82$. The thermal noise in the region of the candidate is $\sigma_{A5,SUR,CL2} = 110\mu$Jy/beam.

5.7.2.1 Pointed Follow-up Observations

We gathered 27 hours of pointed observations towards this candidate in June 2011 and obtained a thermal noise of $\sigma_{A5,POI,CL2} = 95\mu$Jy/beam. The resulting map before and after sources have been subtracted is shown in Figure 5.44. A total of 10 LA sources have flux densities greater than $4\sigma_{A5,POI,CL2}$ and were modelled .

Our image of the follow-up data shows that although the sources are subtracted very well there is only a $3\sigma_{A5,POI,CL2}$ decrement at position of candidate 2, but there are several other decrements of similar magnitude. McAdam is unable to constrain the position of the cluster and this is represented in the multi-model distribution of the McAdam derived parameters (Figure 5.45). Because the McAdam derived position is not constrained we are unable to extract any meaningful p value from this observation.

The data has been carefully checked for interference and neither of the jackknife tests that were performed on these observations revealed any contamination in the data.

It should be noted that the synthesized beam for this follow-up observation is highly elliptical. Ideally more observations will be gathered in order to obtain a more circular beam.

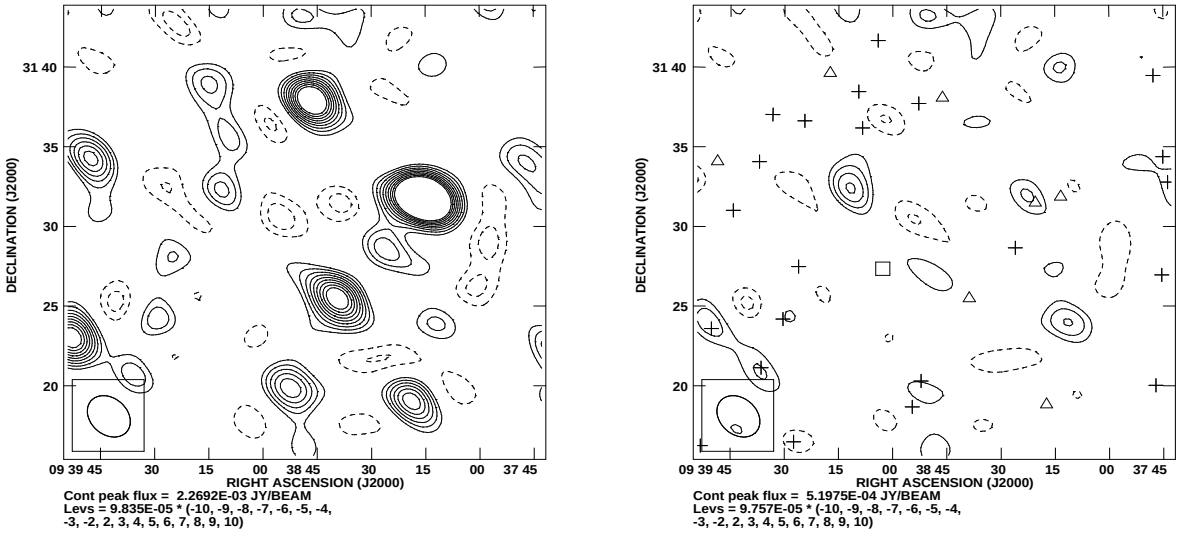

Figure 5.44: Images of the SA pointed observations towards the AMI005 cluster candidate 2.

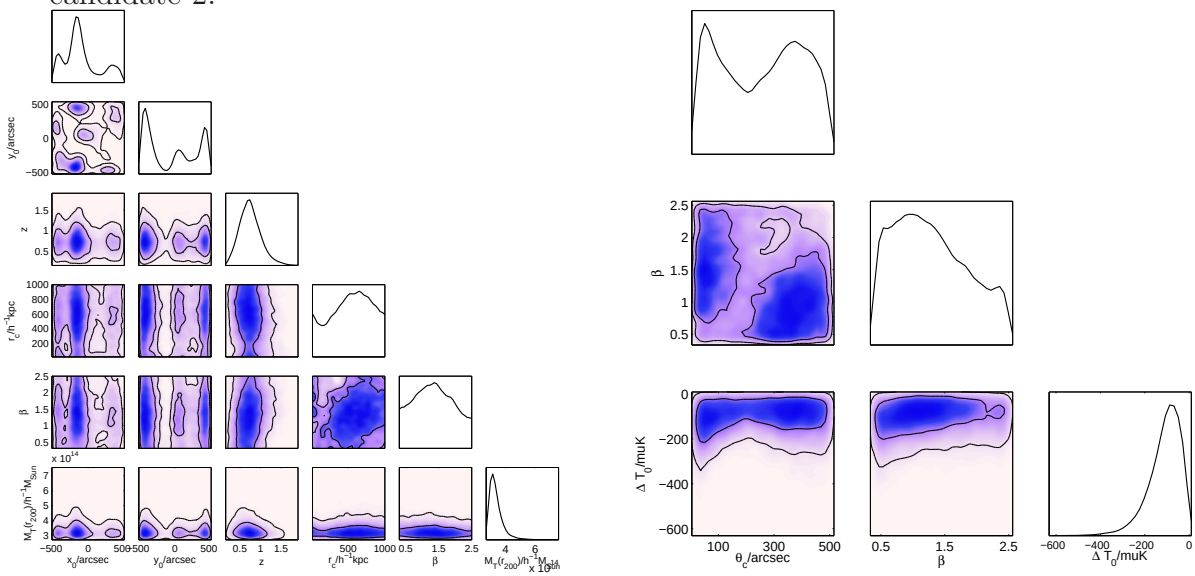

Figure 5.45: The derived parameters for AMI002 cluster candidate 10. On the left are the physical parameters and on the right are the phenomenological model parameters.

5.7.3 Candidate 3: 9-10-13

An elliptical decrement is observed in the 9-10-13 triangle with a significance of $4\sigma_{A5,SUR,CL3}$. This is also detected by McAdam and the Bayesian evidences are used to calculate $p = 0.41$. The image of these data is shown in Figure 5.46.

The source environment around this candidate is complex and there are many sources that are likely to influence the magnitude and shape of the decrement. The two brightest sources that are close to the candidate are the 4.9mJy/beam source at 09:37:37.9 +31:22:41 and the 4.5mJy/beam source at 09:38:17.4 +31:18:54. There are a further eight fainter LA sources within $\approx 10'$ of the cluster candidate, these have fluxes between 2.4mJy/beam and 0.27mJy/beam, none of these are extended. McAdam proficiently models these sources and after subtraction there a few residuals, the largest of which appears to be associated with the 4.9mJy/beam source.

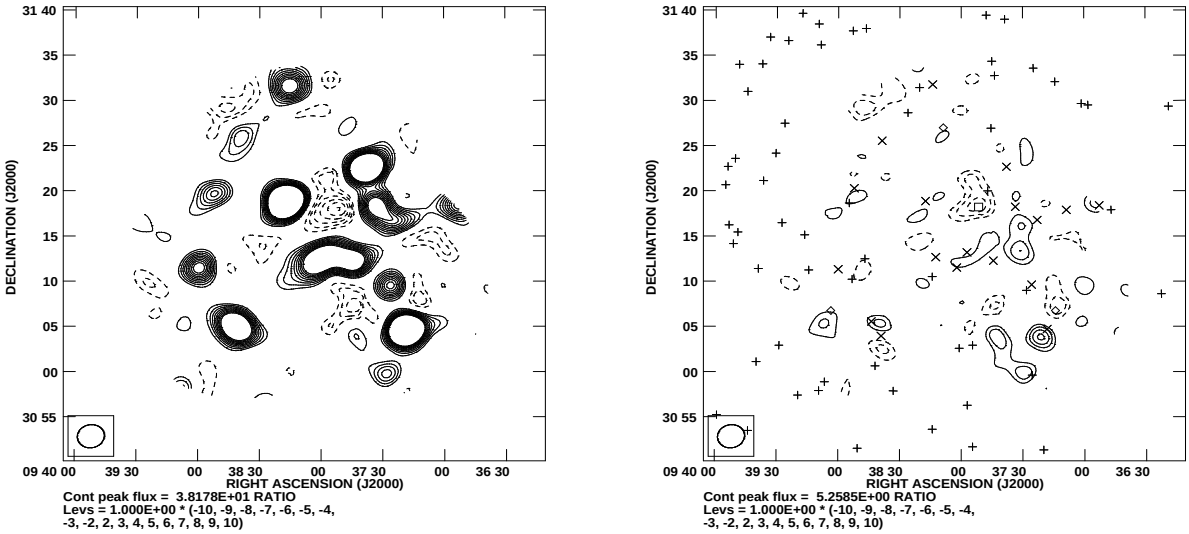

Figure 5.46: AMI005 search triangle 9-10-13. AMI005 candidate 3 is detected with $p = 0.41$. The thermal noise in the region of the candidate is $\sigma_{A5,SUR,CL3} = 120\mu$Jy/beam.

5.7.3.1 Pointed Follow-up Observations

A total of 28 hours SA pointed follow-up observations were conducted between June 13th 2011 and June 16th 2011. From these observations a thermal noise level of $\sigma_{A5,POI,CL3} = 90\mu$Jy/beam was obtained. A map of the data before and after source subtraction is shown in Figure 5.47. With flux densities above $4\sigma_{A5,POI,CL3}$ there are 14 sources. The 0.25mJy/beam source at 09:37:47.1 +31:20:02 is also modelled because it is very close to the candidate.

Unlike all other pointed follow-up observations I have not used Gaussian priors on the source positions and instead I use delta-function priors. The reason for this is that 15 sources are modelled and the dimensionality of the problem would be too large if McAdam was allowed to model four parameters for each source.

McAdam has modelled the sources well and on the source subtracted maps the largest flux density residuals are $3\sigma_{A5,POI,CL3}$. We do observe a $3\sigma_{A5,POI,CL3}$ decrement close to the pointing centre. However, it can be seen from the McAdam derived parameters (Figure 5.48) that the decrement west of the pointing centre is preferred. Neither of these decrements are well constrained by McAdam and it is a possibility that both of these decrements are associated with the 4.9mJy/beam source.

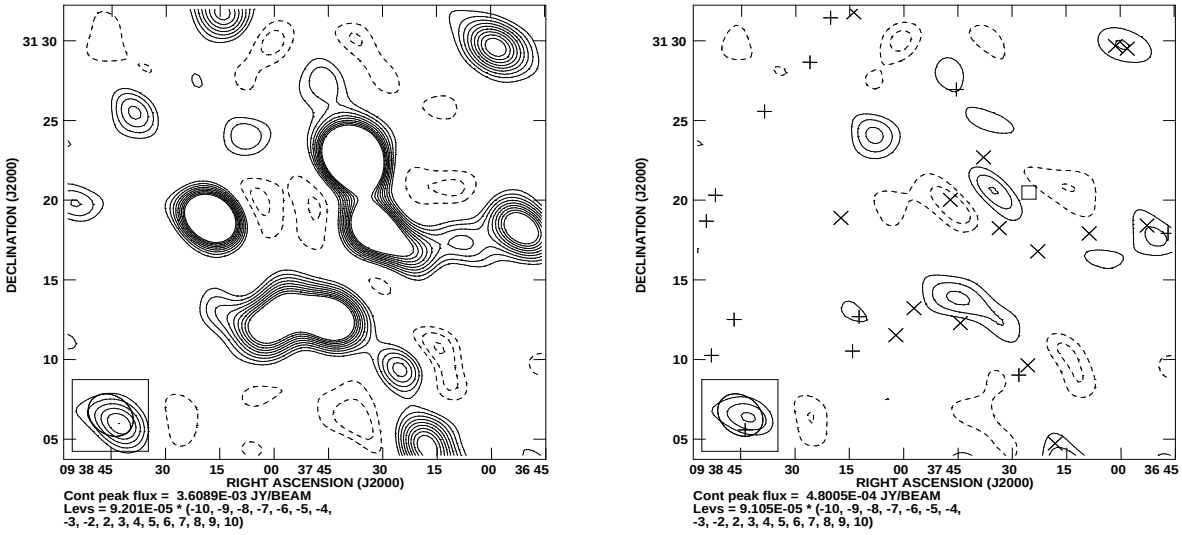

Figure 5.47: Images of the SA pointed observations towards the AMI005 cluster candidate 3.

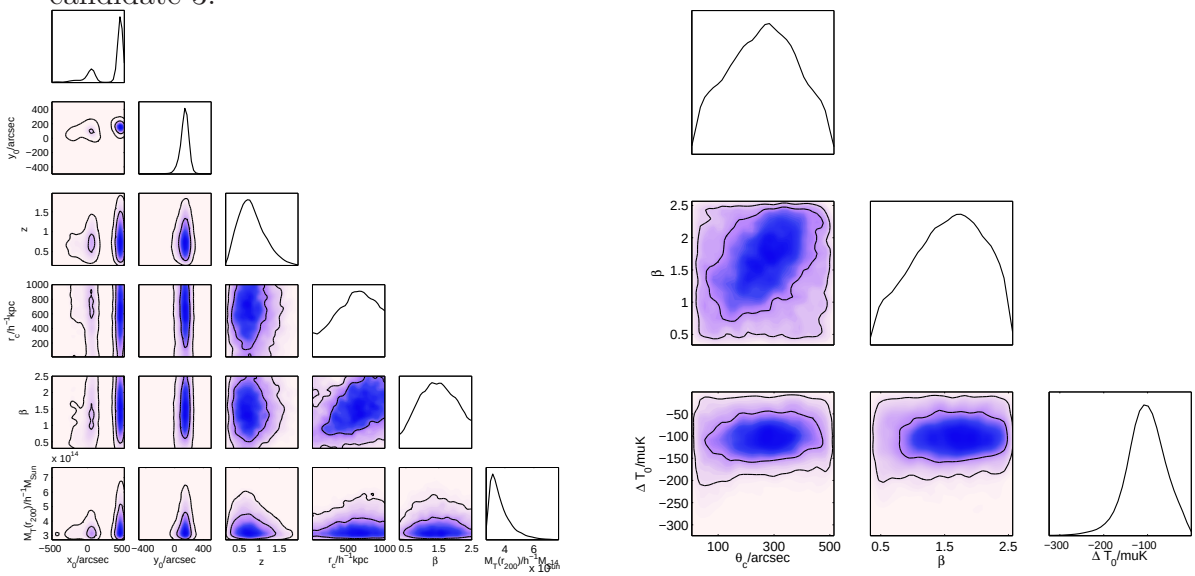

Figure 5.48: The derived parameters for AMI005 cluster candidate 3. On the left are the physical parameters and on the right are the phenomenological model parameters.

5.8 Survey Source Properties

In the AMI002 field we detect a total of 210 sources on the LA maps with flux densities in the range 22mJy/beam to 0.20mJy/beam; 13 of these sources are extended. In the AMI005 field we detect a total of 239 sources on the LA maps with flux densities in the range 41mJy/beam to 0.20mJy/beam, 11 of these sources are extended.

All sources have LA measured flux densities and the majority of the sources have their SA flux density modelled in McAdam. I compare the McAdam flux density to the LA measured flux density. A systematic discrepancy between these two flux values would reveal a systematic difference between the flux estimates of the two arrays. Some sources will be modelled in several search triangles, hence for a single LA measured flux density there are often several McAdam derived flux densities. When several modes have been detected within a search triangle I use the derived source parameters from the mode with the highest evidence.

Figure 5.49 is a histogram of the ratio of the McAdam flux density to the LA flux density for all sources from both AMI002 and AMI005 sources. I find that the best-fit Gaussians have a peak at ≈ 1.0 and a $\sigma \approx 0.2$.

In Figure 5.50 I plot the ratio of McAdam to LA flux density as a function of the LA flux density. Here it can be seen that as the LA flux increases the agreement between the McAdam flux and the LA flux improves. This is especially obvious for the AMI002 sources.

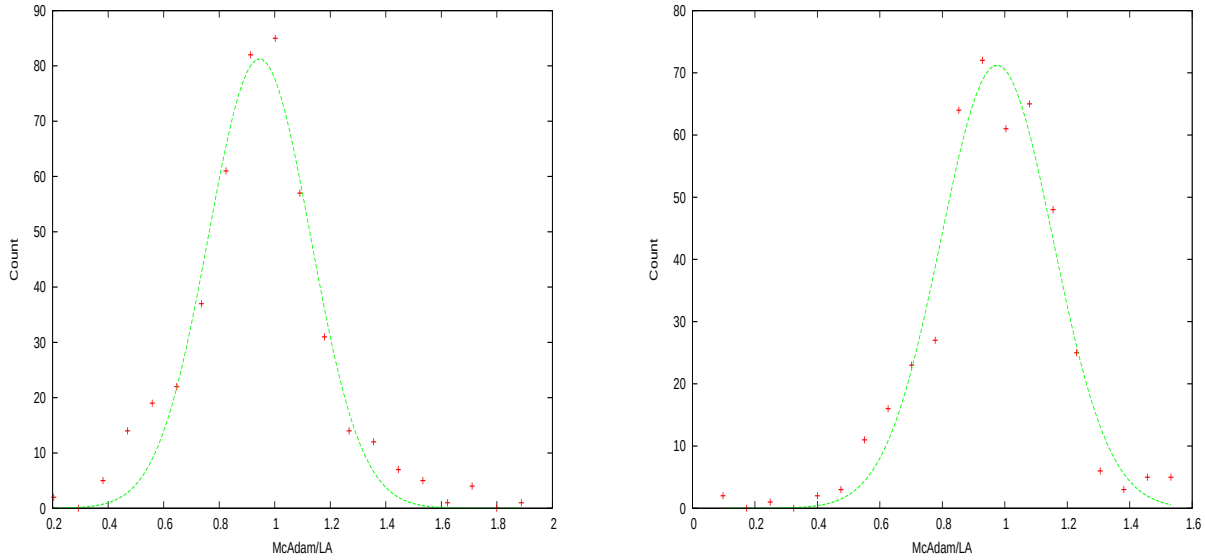

Figure 5.49: A histogram of the McAdam source flux divided by the LA fluxes. The histogram has been fitted with a Gaussian. On the left are the results from the AMI002 field, the amplitude of the Gaussian is 81, the peak is at 0.94 and $\sigma = 0.18$. On the right are the results from the AMI005 field, here the amplitude is 71, the peak is at 0.98 and $\sigma = 0.18$.

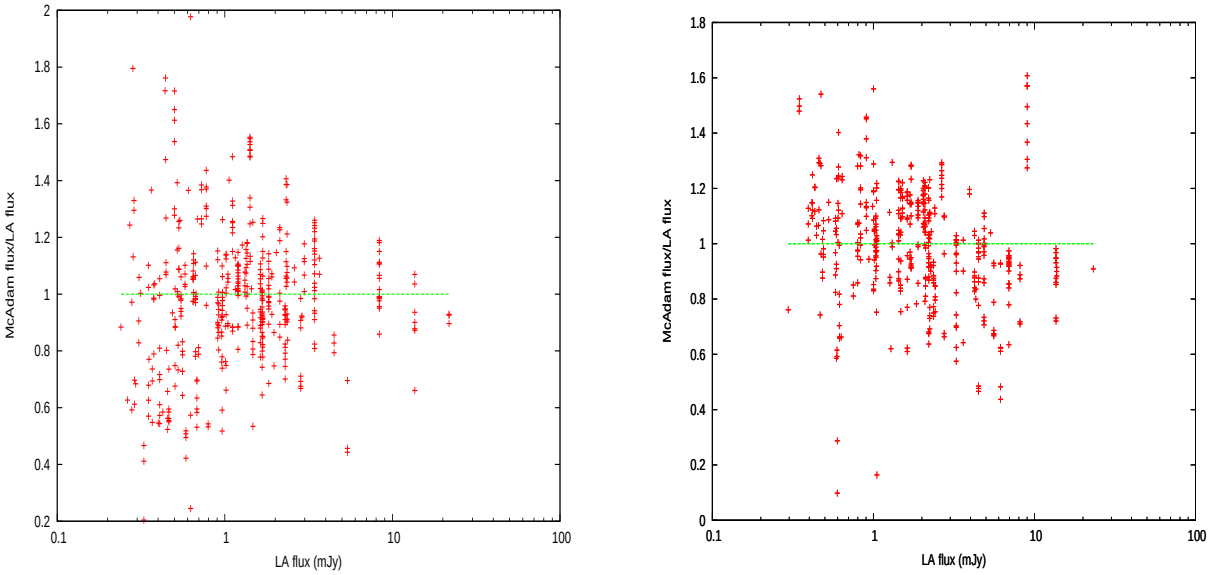

Figure 5.50: The McAdam source flux divided by the LA fluxes as a function of the LA flux. On the left are the AMI002 sources and on the right are the AMI005 sources.

Both Figures 5.49 and 5.50 demonstrate that there is no systematic offset between the LA and SA source fluxes. The histograms plotted in Figure 5.49 are well fit by Gaussians with a standard deviation of 20%. However, these Gaussian fits underestimate the tails of the histograms. These fits show that using a 40% prior on the LA flux density measurement is reasonable but in practice a 20% prior could be used without significant effects on the source fluxes.

5.9 Conclusions

During the course of my investigations I analysed two deg^2 fields of the AMI blind survey data. I have conducted pointed follow-up SA observations for all candidates that were discovered. I found the following:

- In analysis of the AMI002 survey data, nine candidates were discovered with p values greater than 0.3. These have significances on the map of $3\sigma_{SA,SUR}$ to $6\sigma_{SA,SUR}$. Follow-up observations of these candidates revealed that several false positives were detected and that candidates 5 and 9 were

not detected in the follow-up observations. The other seven candidates were again detected with $p > 0.3$ and significances between $3\sigma_{SA}$ and $8\sigma_{SA}$.

- In the AMI005 survey data only three candidates were discovered with derived p values greater than 0.3. In the follow-up observations none of these three candidates were detected by McAdam and no meaningful p values were derived. The most promising is candidate 2, which was detected at $3\sigma_{SA}$ in the follow up observations.

- The follow-up observations have proved vital for checking the candidates in the survey field, especially for clusters originally detected with low p values. All 12 candidates were followed-up; in these pointed observations, five of the candidates disappeared and seven remained. Several of these seven remaining candidates would benefit from deeper observations with the aim of obtaining more definite results.

- Two cluster candidates discovered in the AMI002 field were particularly convincing – candidates 1 and 2. These had the highest derived R values (4.4×10^4 and 9.5×10^2 respectively) of all the clusters detected in the survey and were the highest signal-to-noise detections were in the follow-up observations (5σ and 8σ respectively).

- The McAdam derived source fluxes agree well with the LA measurements. A Gaussian with a standard deviation of 20% of the source flux will be suitable for future analyses of the AMI survey data.

5.10 Future Work

- The analysis of the AMI002 field would be more robust if more pointed observations were obtained towards candidates 3, 4, 7 and 8.

- AMI005 candidate 2 would benefit from additional observations at an hour angle chosen to make the synthesized beam of the concatenated data more circular.

- Follow-up observations with other instruments must be obtained for all candidates. This is not only necessary to confirm the existence of candidates but also to determine their redshifts. I have applied for CARMA observations of the AMI002 candidate 2.
- I have analysed only two fields out of 12. A thorough analysis needs to be performed on the remaining 10 fields.
- Once the AMI survey is complete and we have a firm understanding of the selection function and have obtained redshifts for our candidates, then we can constrain $N(M, z)$.

Chapter 6

SZ Observations of LoCuSS clusters with AMI: High X-ray Luminosity Sample

I present observations from the SA of eight high X-ray luminosity galaxy cluster systems selected from the Local Cluster Substructure Survey (LoCuSS). The SZ effect is detected towards seven of these clusters; for three this is the first published SZ image. For the detected clusters I present posterior probability distributions for large scale (close to the virial radius) cluster parameters such as mass, radius and temperature ($T_{SZ,MT}$). Combining this sample with that of AMI Consortium: Rodríguez-Gonzálvez et al. (2011) provides the first fully Bayesian analysis of a sizeable, mostly L_X limited sample of clusters. By assuming priors on f_g and the cluster redshift I estimate the value of the cluster average temperature, $T_{SZ,MT}$, from the SZ data alone. Where suitable X-ray spectroscopic temperatures, T_X, are available I compare T_X with $T_{SZ,MT}$, an important scaling relation. I find that there is reasonable correspondence between T_X and $T_{SZ,MT}$ values at low T_X, but that for clusters with T_X above around 6keV the correspondence breaks down with T_X exceeding $T_{SZ,MT}$.

In this chapter I first highlight the differences between SZ and X-ray observations, I then describe the cluster sample, the observations and the analysis. I present maps and derived parameters before comparing the $T_{SZ,MT}$ with T_X measurements from the literature.

6.1 X-ray emission and the SZ Effect

The gas within galaxy clusters has a temperature between 10^7K and 10^8K; at this temperature the thermal emission from the cluster gas appears in the X-ray part of the spectrum. The emission is predominately from bremsstrahlung and the X-ray flux density is described by

$$S_X = \frac{1}{4\pi(1+z)^4} \int n_e^2 \Lambda(T_e) dl, \tag{6.1}$$

where $\Lambda(T_e)$ is the electron cooling function and is proportional to the square root of the electron temperature $T_e^{1/2}$ (Sarazin 1986).

The observable signal that arises due to the SZ-effect is a change in the apparent temperature of the CMB and is given by Equation 1.26.

The SZ effect is linear in n_e and T_e, whereas the X-ray emission varies as $n_e^2 T_e^{1/2}$. Hence, from either the properties of the X-ray emission or the SZ effect the parameters n_e, T_e and other cluster properties such as the gas mass M_g can be determined. Due to the differences in the X-ray and SZ effect signals it is useful to compare the SZ effect observed cluster parameters with those derived from X-ray observations.

6.2 The LoCuSS Cluster sample

The Local Cluster Substructure Survey (LoCuSS see Smith et al. 2003, 2005) contains 164 clusters with redshifts between 0.142 and 0.295. The LoCuSS provides a near-snapshot of clusters in z. It aims to measure the relationship between the structure of galaxy clusters and the evolution of the hot gas and galaxies that inhabit them using gravitational lensing data and other observations spanning the electromagnetic spectrum from the radio to X-ray. In this thesis I focus on LoCuSS clusters with a declination greater than 20° and an X-ray luminosity (L_X) greater than 11 $\times 10^{37}$W over the 0.1-2.4 keV band in the cluster rest frame (according to Ebeling et al. 1998, 2000, using $h_{50} = 1$). Radio source contamination can make it difficult to observe the SZ effect at 16 GHz and I have not studied the clusters with sources brighter than 10 mJy/beam within $10'$ of the cluster X-ray centre. Note that our redshifts correspond to those cited in Ebeling

et al. (1998, 2000). I present results from the analysis of eight galaxy cluster systems; Table 6.1 shows the coordinates, redshifts and X-ray luminosities of the selected LoCuSS clusters. In AMI Consortium: Rodriguez-Gonzalvez *et al.* (2011) AMI observations of LoCuSS clusters with an X-ray luminosity in the range 7-11 $\times 10^{37}$W ($h_{50} = 1$) are presented.

Table 6.1: Coordinates, redshifts and X-ray luminosities of the observed LoCuSS clusters. Note that Abell 1758B is included even though it is below our luminosity cut; this is because it is within the field of view of our Abell 1758A observations. Redshifts and X-ray luminosities are taken from Ebeling et al. (1998, 2000).

Cluster	Right ascension (J2000)	Declination (J2000)	Redshift	X-ray luminosity in 10^{37}W ($h_{50} = 1$)
Abell 586	07:32:12	+31:37:30	0.171	11.12
Abell 611	08:00:56	+36:03:40	0.288	13.60
Abell 773 (or RXJ0917.8+5143)	09:17:54	+51:42:58	0.217	13.08
Abell 781	09:20:25	+30:31:32	0.298	17.22
Abell 1413	11:55:18	+23:24:29	0.143	13.28
Abell 1758B	13:32:29	+50:24:42	0.280	07.25
Abell 1758A	13:32:45	+50:32:31	0.280	11.68
Zw1454.8+2233 (or Z7160)	14:57:15	+22:20:34	0.258	13.19
RXJ1720.1+2638	17:20:10	+26:37:31	0.164	16.12

6.3 Observations

SA pointed observations centred at the X-ray cluster position (Table 6.1) for our eight clusters were taken during 2007-2010. The observation lengths were in the range 20-90 hours per cluster before any flagging of the data; the noises on the SA maps reflect the actual observation time used.

With the SA I observed phase calibrators every hour and used bi-daily observations of 3C48 or 3C286 for amplitude calibration. With the LA I typically

conduct 61+19pt hexagonal raster observations centred on the cluster X-ray position. The 61 pointing centres are separated by $4'$; the inner 19 pointings are observed for approximately six times longer than the outer 42 pointings. Phase calibrators were observed every ten minutes. Observations were taken over 2009-2010 and each cluster was observed for 10-25 hours before any flagging of the data.

All our cluster data were passed through the REDUCE pipeline which is detailed in Section 2.6. Thermal noise levels for the SA and the LA maps (σ_{SA} and σ_{LA} respectively), and phase calibrators that have been taken from the Jodrell Bank VLA Survey (Patnaik *et al.* 1992, Browne *et al.* and Wilkinson *et al.*) are summarised in Table 6.2.

Source finding was carried out in exactly the same manner as for the AMI blind cluster survey (see Section 5.8).

Table 6.2: Details of AMI observations of LoCuSS clusters.

Cluster	σ_{SA} (mJy)	σ_{LA} (mJy)	Number of LA $4\sigma_{LA}$ sources	LA phase calibrator
Abell 586	0.172	0.09	23	J0741+3112
Abell 611	0.106	0.07	23	J0808+408
Abell 773	0.133	0.09	09	J0903+468
				or J0905+4850
Abell 781	0.116	0.07	24	J0925+3127
				or J0915+2933
Abell 1413	0.130	0.09	17	J1150+2417
Abell 1758A	0.115	0.08	14	J1349+536
Abell 1758B	0.130	0.08	14	J1349+536
Zw1454.8+2233	0.100	0.10	16	J1513+2338
RXJ1720.1+2638	0.084	0.10	17	J1722+2815

6.4 Bayesian Analysis

The priors that I use in our Bayesian analysis differ from those used to analyse the survey fields. These differences arise because the redshift and the position of

Table 6.3: Priors used in our Bayesian analysis of LoCuSS clusters.

Parameter	Prior
Source position ($\mathbf{x_s}$)	+ or ×: Delta-function using the LA positions.
	△: Gaussian centred on the LA positions with σ=5″.
Source flux densities	× or △: Gaussian centred on the
(S_0/Jy)	LA continuum value with a σ of $0.4S_0$.
	+: Delta-function on the LA value.
Source spectral index (α)	× or △: Gaussian centred on the value calculated
	from the LA channel maps with σ as the LA error.
	+: Delta-function on the LA value.
Redshift (z)	Delta-function on the X-ray value (Table 6.1).
Core radius (r_c/h_{100}^{-1}kpc)	Uniform between 10 and 1000.
Beta (β)	Uniform between 0.3 and 2.5.
Mass ($M_{\rm T,r200}/h_{100}^{-1}M_\odot$)	Uniform in log space over,
	$(0.32-50)\times10^{14}M_\odot h_{100}^{-1}$.
Gas fraction (f_g)	Gaussian prior centred on 0.086, σ=0.02
	(Komatsu *et al.* 2010).
Cluster position ($\mathbf{x_c}$)	Gaussian prior on the X-ray position,
	σ=60″ (Table 6.1).

the LoCuSS clusters are known. The priors that I have used for these pointed observations towards known clusters are shown in Table 6.3.

6.5 Maps and Derived Cluster Parameters

For each cluster I present SA maps before and after source subtraction, and posterior probability distributions of the large-scale cluster parameters obtained from running the SA data through McAdam. The derived cluster parameters are given in Table 6.4. I also present *Chandra* images taken from the *Chandra* Data Archive. In Section 6.6 I compare our derived cluster temperatures with large-radius X-ray temperatures ($r \approx 500$kpc) taken from the literature.

I present the source-subtracted maps with a *uv* taper of 600kλ (a Gaussian taper of value 1.0 at 0kλ falling to 0.3 at 600kλ) since the shorter SA baselines

are more sensitive to the large angular size of the SZ-effect signal. Maps before source subtraction have been CLEANed with a single box over their total extents, whilst source-subtracted maps have been CLEANed with a tight box around the SZ signals. All maps are contoured at $\pm 2\sigma$, $\pm 3\sigma$, $\pm 4\sigma$ etc ., where σ is stated in the caption that is output with the AIPS image. For pre-source subtracted maps σ is also stated in Table 6.2. On all AMI maps negative contours are dashed and positive contours are solid.

6.5.1 Abell 586

Our SA maps and the parameters that have been measured are presented in Figure 6.1. I have overlayed our map on an X-ray *Chandra* image; the cluster centroids match and an extension of the cluster towards the south is observed.

The SZ effect from Abell 586 has previously been observed with OVRA/BIMA by LaRoque *et al.* (2006) and Bonamente *et al.* (2006). LaRoque et al. apply an isothermal β-model to SZ and *Chandra* X-ray observations and find $M_{\rm g}(r_{2500}) = 2.49 \pm 0.32 \times 10^{13} M_{\odot}$ and $M_{\rm g}(r_{2500}) = 2.26^{+0.13}_{-0.11} \times 10^{13} M_{\odot}$ respectively (using $h_{70} = 1$). In addition, they determine an X-ray spectroscopic temperature of the cluster gas of ≈ 6.35keV between a radius of 100kpc and r_{2500}; r_{2500} is the radius at which the average cluster density falls to 2500 times the critical density at that redshift and is determined from *Chandra* observations by Bonamente *et al.* (2006). In comparison, Okabe *et al.* (2010) use *Subaru* to calculate the cluster mass from weak lensing by applying a Navarro, Frenk & White (NFW; Navarro *et al.* 1995) profile. They find $M_{\rm T}(r_{2500}) = 2.41^{+0.45}_{-0.41} \times 10^{14} M_{\odot}$, whilst at large radii they find $M_{\rm T}(r_{500}) = 4.74^{+1.40}_{-1.14} \times 10^{14} M_{\odot}$ (using $h_{70} = 1$).

Abell 586 has been studied extensively in the X-ray e.g. Allen (2000) and White (2000). A recent analysis of the temperature profile (Cypriano *et al.*, 2005) shows how the temperature falls from ≈ 9 keV at the cluster centre to ≈ 5.5keV at a radius $\approx 280''$. Cypriano et al. have used the Gemini Multi-Object Spectrograph together with X-ray data taken from the *Chandra* archive to measure the properties of Abell 586. They compare mass estimates derived from the velocity distribution and from the X-ray temperature profile and find that both give very similar results, $M_{\rm g} \approx 0.46 \times 10^{14} M_{\odot}$ within $1.3 h_{70}^{-1}$Mpc.

Table 6.4: Derived values for cluster parameters.

Cluster name	$M_T(r_{200})$ $\times 10^{14}$ $h_{100}^{-1} M_\odot$	$M_T(r_{500})$ $\times 10^{14}$ $h_{100}^{-1} M_\odot$	$M_g(r_{200})$ $\times 10^{13}$ $h_{100}^{-2} M_\odot$	$M_g(r_{500})$ $\times 10^{13}$ $h_{100}^{-2} M_\odot$	r_{200} h_{100}^{-1}Mpc	r_{500} $\times 10^{-1}$ h_{100}^{-1}Mpc	$f_g(r_{500})$ $\times 10^{-1}$ h_{100}^{-1}	$T_{SZ,MT}(r_{200})$ keV
Abell 586	5.1 ± 2.4	2.1 ± 1.1	4.3 ± 2.0	2.6 ± 0.8	1.2 ± 0.2	6.6 ± 1.1	1.4 ± 0.4	5.2 ± 1.6
Abell 611	4.0 ± 0.8	2.0 ± 0.5	3.5 ± 0.6	2.8 ± 0.3	1.1 ± 0.1	6.3 ± 0.5	1.5 ± 0.4	4.5 ± 0.6
Abell 773	3.6 ± 1.3	1.7 ± 0.7	3.1 ± 1.1	2.1 ± 0.5	1.1 ± 0.1	6.0 ± 0.8	1.4 ± 0.4	4.1 ± 1.0
Abell 781	4.1 ± 0.8	2.0 ± 0.5	3.6 ± 0.6	2.9 ± 0.4	1.1 ± 0.1	6.3 ± 0.5	1.5 ± 0.4	4.5 ± 0.6
Abell 1413	4.0 ± 1.0	1.9 ± 0.6	3.5 ± 0.8	2.7 ± 0.4	1.1 ± 0.1	6.6 ± 0.7	1.5 ± 0.4	4.4 ± 0.8
Abell 1758B	4.4 ± 2.2	2.2 ± 1.2	3.7 ± 1.8	2.2 ± 0.6	1.1 ± 0.2	6.4 ± 1.2	1.2 ± 0.4	4.6 ± 1.5
Abell 1758A	4.1 ± 0.7	2.5 ± 4.4	3.6 ± 0.5	3.4 ± 0.4	1.1 ± 0.1	6.8 ± 0.4	1.4 ± 0.3	4.5 ± 0.5
RXJ1720.1+2638	2.0 ± 0.4	1.2 ± 0.2	1.7 ± 0.3	1.6 ± 0.3	0.9 ± 0.1	5.6 ± 0.4	1.4 ± 0.3	2.8 ± 0.4

They suggest that the cluster is spherical and relaxed with no recent mergers. The elongation of the SZ signal on our map (Figure 6.1) suggests non-sphericity.

6.5.2 Abell 611

The SA maps, large-scale cluster parameters and a *Chandra* image of Abell 611 in Figure 6.2. The Donnarumma & Ettori (2011) analysis of the *Chandra* achieve data shows that the X-ray isophotes are quite circular, the surface brightness profile is smooth and the brightest cluster galaxy lies at the centre of the X-ray emission. These results indicate that the cluster is relaxed. From the X-ray data, the cluster mass was estimated using an NFW profile, spherical symmetry and hydrostatic equilibrium to be $9.32\pm1.39\times10^{14}\mathrm{M}_{\odot}$ (within a radius of 1.8±0.5 Mpc). However, the Donnarumma et al. analysis of strong lensing data indicates that the cluster mass could be closer to $4.68\pm0.31\times10^{14}\mathrm{M}_{\odot}$ (within a radius of 1.5±0.2 Mpc. Note that the values quoted from Donnarumma et al. are an example of their mass estimates; from fitting different models they find that the estimated mass varies significantly (between $9.32–11.11\times10^{14}\mathrm{M}_{\odot}$ for the X-ray mass and between $4.01–6.32\times10^{14}\mathrm{M}_{\odot}$ for the lensing mass). Their mass estimates use $h_{70} = 1$. Several other analyses of *Chandra* data produce comparable mass estimates (e.g. Schmidt & Allen 2007, Morandi *et al.* 2007, Morandi & Ettori 2007 and Sanderson *et al.* 2009).

Romano & et al (2010) perform a weak lensing analysis of Abell 611 using data from the Large Binocular Telescope. With an NFW profile they estimate $M_{\mathrm{T,r200}} = 4–7\times10^{14}\mathrm{M}_{\odot}$ and $r_{200} = 1400 - 1600$kpc, for $h_{70} = 1$. These are in agreement with the values obtained from *Subaru* weak lensing observations by Okabe et al.

Using GMRT observations Venturi *et al.* (2008) concluded that Abell 611 has no radio halo at 610MHz. Abell 611 has also previously been observed in the SZ at 15 GHz by Grainger *et al.* (2002) and Zwart et al. (2010), and at 30 GHz by Bonamente *et al.* (2004), Bonamente *et al.* (2006) and LaRoque et al.

From the analysis of the AMI SA observations of Abell 611 presented in this paper I find that $M_{\mathrm{T,r200}} = 4.0^{+0.3}_{-0.4}\times10^{14}\mathrm{M}_{\odot}$. Note that the mass obtained is significantly smaller than the result given in Zwart et al. (2010); however, their

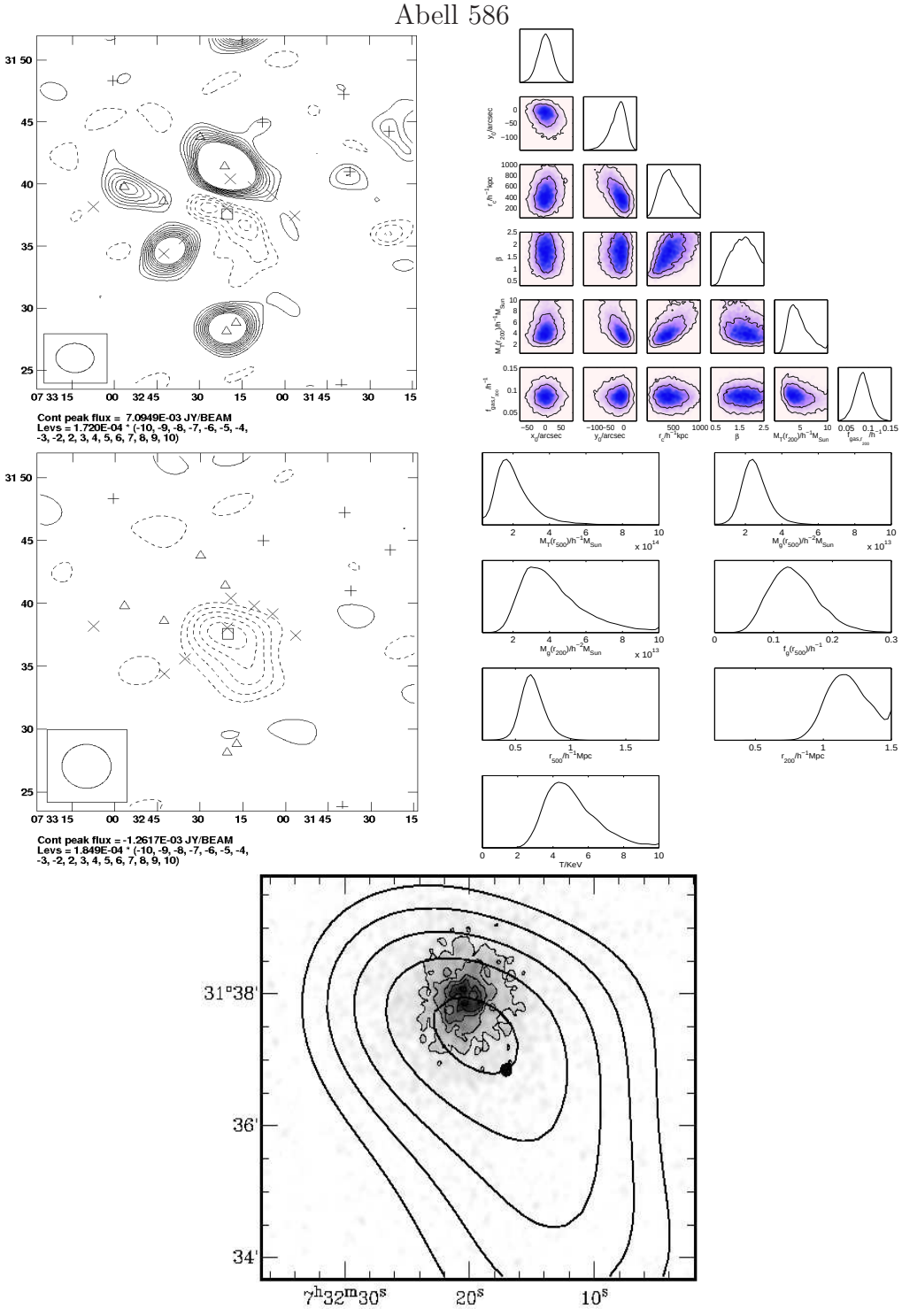

Figure 6.1: The top left image shows the SA map before subtraction, the map in the middle left has had the sources removed, the top right panel shows the cluster parameters that are sampled from in our Bayesian analysis and the middle right plot presents several cluster parameters derived from our sampling parameters. The image at the bottom shows the *Chandra* X-ray map overlayed with SA contours.

$M_{\rm T}$ estimates are biased high. The bias occurs because they used a low-radius X-ray temperature as a constant temperature throughout the cluster, as is explained by them and in Olamaie et al. (2010). The SZ maps presented in this paper are similar to those in Zwart et al. (2010); both sets of observations indicate that the cluster is extended in the NW direction. However, the analysis presented in this paper differs from that by Zwart et al. (2010) who sample from temperature and $M_{g,r200}$ and derive $M_{T,r200}$ under the additional assumption of hydrostatic equilibrium. Instead $M_{\rm T,r200}$ and $f_{g,r200}$ have been sampled from and T has been calculated using the M-T scaling relation given in Rodríguez-Gonzálvez et al. (2010). The differences between these two models are described in detail by Olamaie et al. who demonstrate that the mass estimated using the technique in this paper produces a more reliable value and that the Zwart et al. (2010) analysis underestimates the values for $M_{g,r200}$ and $f_{g,r200}$. The values of β and r_c/h_{100}^{-1}kpc presented here agree with those in the Zwart et al. (2010) analysis.

There is no significant contamination from radio sources and we detect the cluster with a high signal-to-noise ratio. A comparison of the SZ-effect image and the *Chandra* map shows that the centres of the SZ and X-ray emission are coincident.

6.5.3 Abell 773

In Figure 6.3 I show the AMI SA maps of Abell 773, a *Chandra* X-ray map and the cluster parameters derived from our analysis. The SZ effect associated with Abell 773 has been observed several times (Grainge *et al.* 1993, Carlstrom *et al.* 1996, Saunders *et al.* 2003, Bonamente *et al.* 2006, LaRoque et al.). Most recently, Zwart et al. (2010) observed the cluster and found a cluster mass of $M_{\rm T,r200} = 1.9^{+0.3}_{-0.4}\times10^{15}{\rm M}_\odot$ using $h_{70} = 1$; however, their $M_{\rm T}$ estimates are biased high – see Section 6.5.2.

Inspection of a $10'\times10'$ region of the Sloan Digital Sky Survey (SDSS[1]) centred

[1]Funding for the SDSS and SDSS-II has been provided by the Alfred P. Sloan Foundation, the Participating Institutions, the National Science Foundation, the U.S. Department of Energy, the National Aeronautics and Space Administration, the Japanese Monbukagakusho, the Max Planck Society, and the Higher Education Funding Council for England. The SDSS Web Site is http://www.sdss.org/.

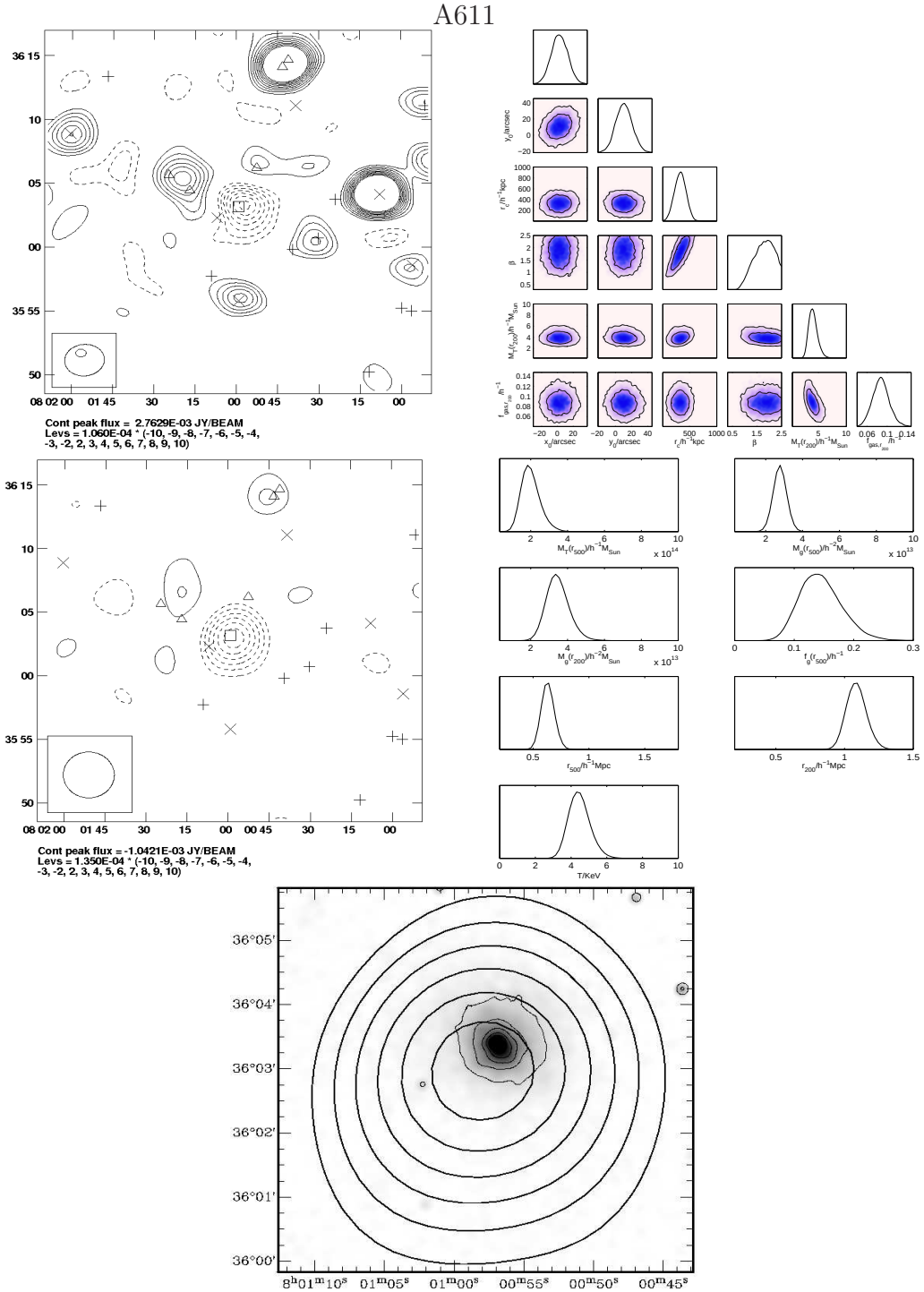

Figure 6.2: The top left image shows the SA map before subtraction, the map in the middle left has had the sources removed, the top right panel shows the cluster parameters that are sampled from in our Bayesian analysis and the middle right plot presents several cluster parameters derived from our sampling parameters. The image at the bottom shows the *Chandra* X-ray map overlayed with SA contours.

on Abell 773 reveals a complex galaxy distribution with some EW extension. Our observations support this extension, but there is no detailed correspondence between the galaxy and gas distributions. The *Chandra* observations appear to show little if any such extension. There is no significant contamination from radio sources and we detect the cluster with a high signal to noise ratio.

For this cluster, Barrena *et al.* (2007) present an intensive study of the optical data from the Telescopio Nazionale Galileo (TNG) telescope and X-ray data from the *Chandra* data archive. They find two peaks in the velocity distribution of the cluster members which are separated by $2'$ along the E-W direction. Two peaks can also be seen in the X-ray, although these are along the NE-SW direction. Barrena et al. estimate the virial mass of the entire system to be M_{vir} = 1.2-2.7$\times10^{15}h_{70}^{-1}$M$_{\odot}$. Giovannini *et al.* (1999) reported the existence of a radio halo in Abell 773. This feature, typical of cluster mergers, was confirmed with 1.4 GHz VLA observations by Govoni *et al.* (2001). Zhang *et al.* (2008) used *XMM-Newton* to study Abell 773 and found $M_{500} = 8.3 \pm 2.5 \times 10^{14}M_{\odot}$, where $r_{500} = 1.33$ Mpc; they assumed isothermality, spherical symmetry and $h_{70} = 1$. Govoni *et al.* (2004) present a *Chandra* temperature map and an X-ray image of Abell 773; they estimate a mean temperature of 7.5$\pm$0.8 keV within a radius of 800 kpc ($h_{70} = 1$).

6.5.4 Abell 781

AMI SA maps, derived parameters and a *Chandra* observation of the Abell 781 cluster are presented in Figure 6.4. From X-ray observations with *Chandra* and *XMM-Newton* (Sehgal *et al.* 2008) it is apparent that Abell 781 is a complex cluster system. The main cluster is surrounded by three smaller clusters, two to the East of the main cluster and one to the West. They estimate the mass of the clusters assuming a NFW matter density profile; the results indicate that the cluster mass of Abell 781 within r_{500} is $5.2^{+0.3}_{-0.7}\times10^{14}M_{\odot}$ from *XMM-Newton* and *Chandra* X-ray observations or $2.7^{+1.0}_{-0.9}\times10^{14}M_{\odot}$ from the Kitt Peak Mayall 4-m telescope lensing observations (where r_{500} is $1.09^{+0.04}_{-0.04}$ and $0.89^{+0.10}_{-0.12}$ respectively). Alternatively, Zhang et al. use XMM Newton observations to estimate

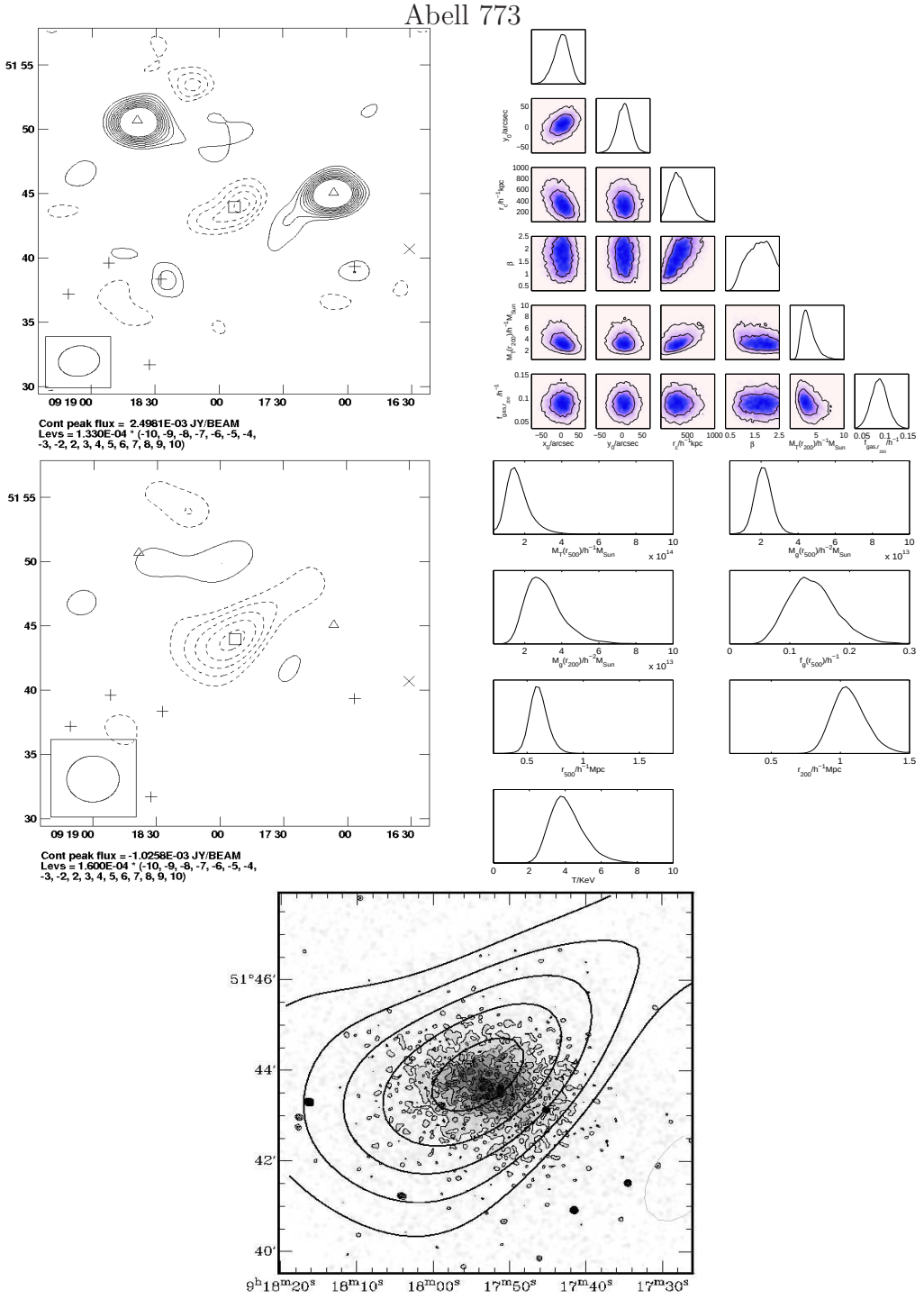

Figure 6.3: The top left image shows the SA map before subtraction, the map in the middle left has had the sources removed, the top right panel shows the cluster parameters that are sampled from in our Bayesian analysis and the middle right plot presents several cluster parameters derived from our sampling parameters. The image at the bottom shows the *Chandra* X-ray map overlayed with SA contours.

$M_{500} = 4.5 \pm 1.3 \times 10^{14} \mathrm{M}_{\odot}$, where $r_{500} = 1.05$Mpc, assuming isothermality and spherical symmetry. Both Zhang et al. and Sehgal et al. use $h_{70} = 1$.

The main cluster of Abell 781 is also known to contain a diffuse peripheral source at 610MHz; this was observed with the GMRT by Venturi *et al.* (2008).

6.5.5 Abell 1413

The SA maps before and after source subtraction are shown in Figure 6.5 together with derived cluster parameters and an overlay of our SZ image on a *Chandra* X-ray map. Abell 1413 has been observed in the X-ray by *XMM-Newton* (e.g. Pratt & Arnaud 2005), *Chandra* (e.g. Vikhlinin *et al.* 2005 and Bonamente *et al.* 2006) and most recently by the low background *Suzaku* satellite (Hoshino *et al.* 2010); SZ images have been made of Abell 1413 with the Ryle Telescope at 15 GHz (Grainge *et al.* 1996) and with OVRO/BIMA at 30 GHz (LaRoque et al. and Bonamente *et al.* 2006). These analyses indicate that Abell 1413 is a relaxed cluster with no evidence of recent merging despite its elliptical morphology. Between the X-ray observations there is good agreement in the temperature and density profiles of the cluster out to half the virial radius. Hoshino et al. measure the variation of the electron temperature with radius, finding a temperature of 7.5keV at the centre and 3.5keV at r_{200}. They assume spherical symmetry, an NFW density profile and hydrostatic equilibrium to calculate $M_{\mathrm{T,r200}} = 6.6 \pm 2.3 \times 10^{14} h_{70}^{-1} \mathrm{M}_{\odot}$; where $r_{200} = 2.24 h_{70}^{-1}$Mpc. Zhang et al. use *XMM-Newton* to study Abell 1413 and find $M_{500} = 5.4 \pm 1.6 \times 10^{14} \mathrm{M}_{\odot}$, where $r_{500} = 1.18$Mpc; they assume isothermality, spherical symmetry and $h_{70} = 1$.

Recent VLA observations (Govoni & Murgia 2009) indicate that there is diffuse 1.4-GHz emission associated with the cluster – this may be due to a mini-halo around the cluster.

In the SA observations the SZ decrement has been detected at high significance. The cluster mass has been determined to be $M_{\mathrm{T,r200}} = 4.0^{+0.3}_{-0.6} \times 10^{14} h_{100}^{-1} \mathrm{M}_{\odot}$ and $r_{200} = 1.14^{+0.4}_{-0.5} h_{100}^{-1}$kpc; both these values are comparable with the Hoshino et al. results.

The source environment around the cluster at 16 GHz is reasonable: the brightest source is 14mJy (11:55:36.63 +23:13:50.1), but this is 700″ from the

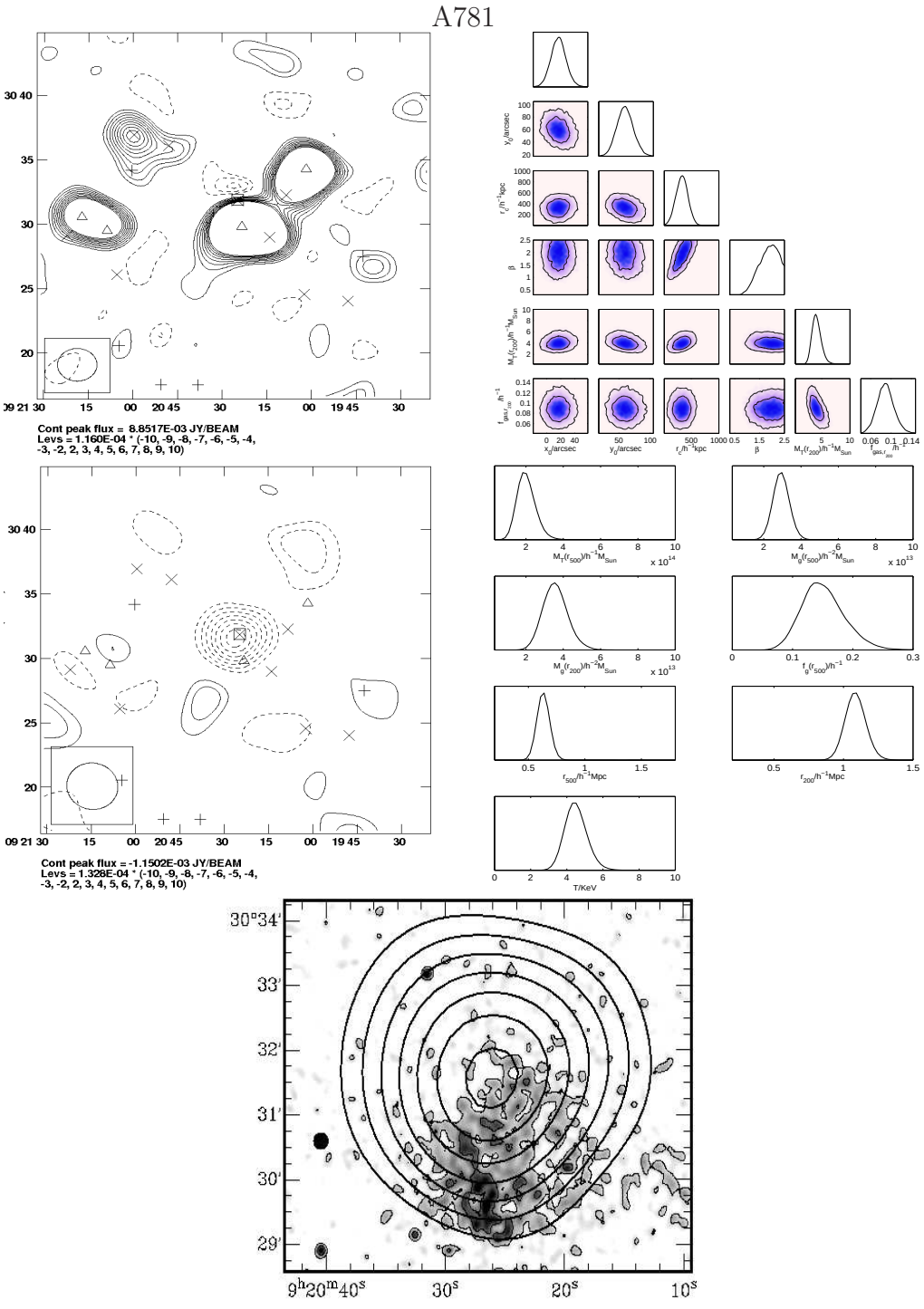

Figure 6.4: The top left image shows the SA map before subtraction, the map in the middle left has had the sources removed, the top right panel shows the cluster parameters that are sampled from in our Bayesian analysis and the middle right plot presents several cluster parameters derived from our sampling parameters. The image at the bottom shows the *Chandra* X-ray map overlayed with SA contours.

cluster X-ray centre. After this bright source is subtracted from our data it is left with a low level of residual flux density on the map; it is unlikely that this residual flux significantly contaminates our cluster detection or parameters. Both the X-ray map and the SZ image indicate that the cluster is elliptical and extended in the N-S direction.

6.5.6 Abell 1758

An analysis of *ROSAT* images clearly shows that this system consists of two interacting clusters, Abell 1758A and Abell 1758B, separated by $8'$ (Rizza *et al.* 1998). In Figure 6.6 I present a single map that contains combined data from observations towards both clusters and the derived parameters for cluster Abell 1758A. I present the derived parameters for cluster Abell 1758A and X-ray maps from both the *Chandra* data archive and *ROSAT*[1]. In Figure 6.7 I show the derived parameters for cluster Abell 1758B.

A detailed analysis of *XMM-Newton* and *Chandra* by David & Kempner (2004) indicates that the clusters Abell 1758A and Abell 1758B are likely to be in an early stage of merging and that both of these clusters are also undergoing major mergers with other smaller systems. A recent analysis of Spitzer/MIPS 24μm data by Haines *et al.* (2009) classifies Abell 1758 as the most active system they have observed at that wavelength. They also identify numerous smaller mass peaks and filamentary structures, which are likely to indicate the presence of infalling galaxy groups, in support of the David & Kempner observations. Zhang et al. use *XMM-Newton* to study Abell 1758A and found $M_{500} = 1.1 \pm 0.3 \times 10^{15} \mathrm{M}_{\odot}$, where $r_{500} = 1.43$Mpc. They assume isothermality, spherical symmetry and $h_{70} = 1$.

6.5.7 Zw1454.8+2233

Several sources are detected close to the cluster centre – a point source with a flux density of 7.97 mJy at 14:56:59.11 +22:18:55.97 and a 4.67 mJy source at 14:57:25.38 +22:37:33.03. No SZ effect is detected from this cluster even though

[1]I acknowledge the use of NASA's SkyView facility (http://skyview.gsfc.nasa.gov) located at NASA Goddard Space Flight Center.

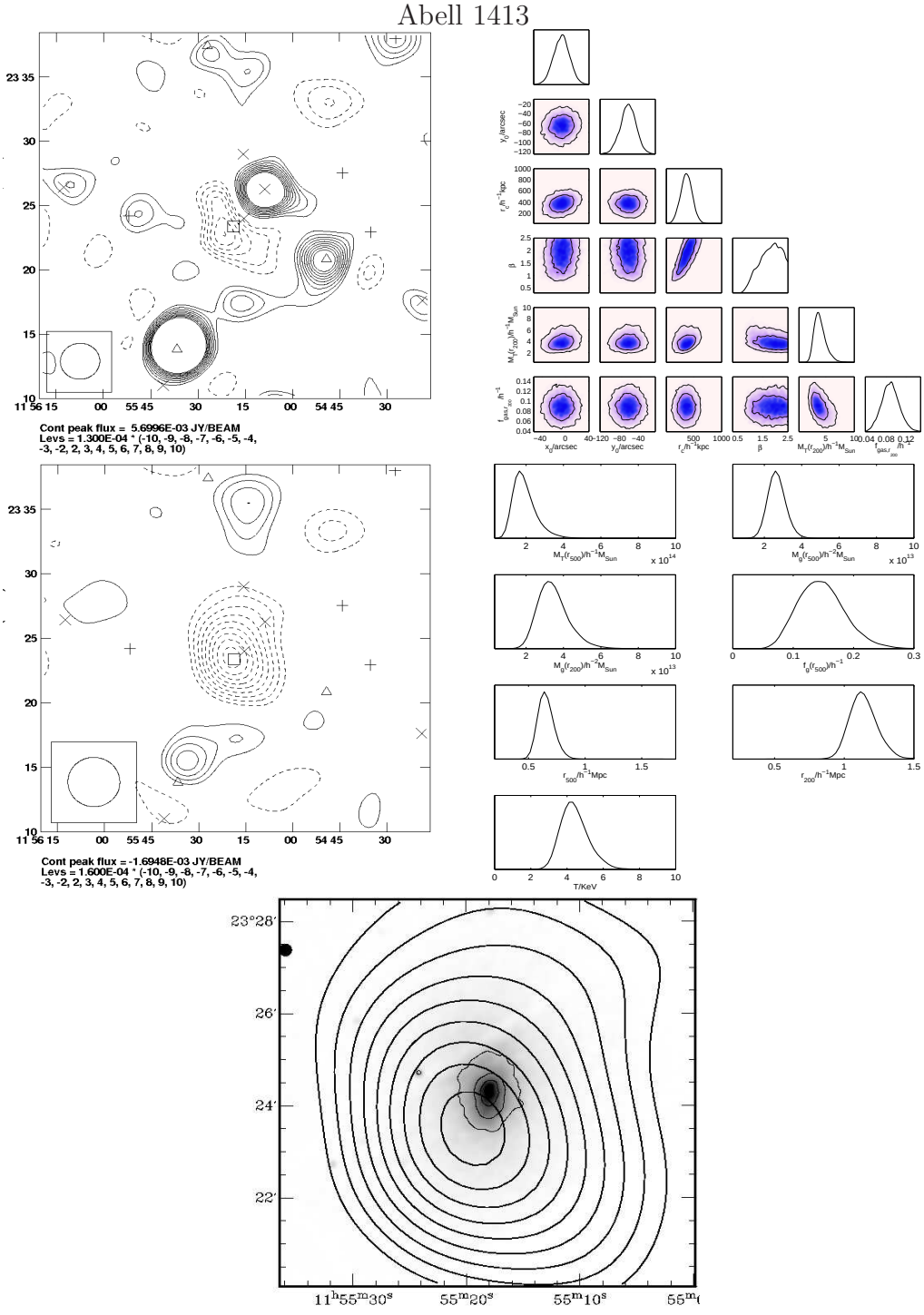

Figure 6.5: The top left image shows the SA map before subtraction, the map in the middle left has had the sources removed, the top right panel shows the cluster parameters that are sampled from in our Bayesian analysis and the middle right plot presents several cluster parameters derived from our sampling parameters. The image at the bottom shows the *Chandra* X-ray map overlayed with SA contours.

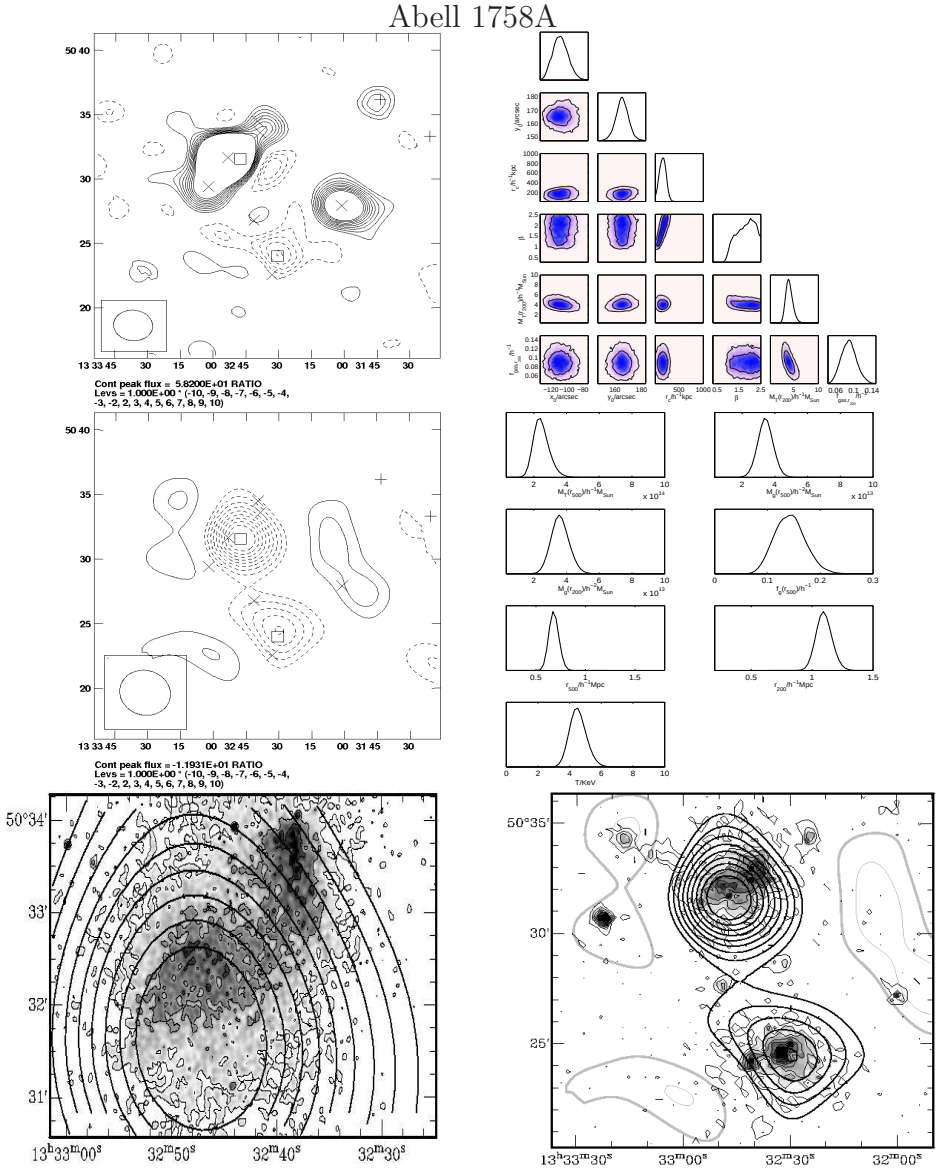

Figure 6.6: The top left image shows the SA map before subtraction, the map in the middle left has had the sources removed. The maps shown here are primary beam corrected signal-to-noise maps cut off at 0.3 of the primary beam. The noise level is $\approx 115\mu$Jy towards the upper cluster (Abell 1758A) and $\approx 130\mu$Jy towards the lower cluster (Abell 1758B). The source subtracted UV tapered map at the middle left has a noise level $\approx 20\%$ higher. The top right panel shows the cluster parameters that are sampled from in our Bayesian analysis and the middle right plot presents several cluster parameters derived from our sampling parameters. The image at the right bottom shows the *ROSAT* PSPC X-ray map overlayed with SA contours, whilst the bottom left shows a *Chandra* image with SA countours.

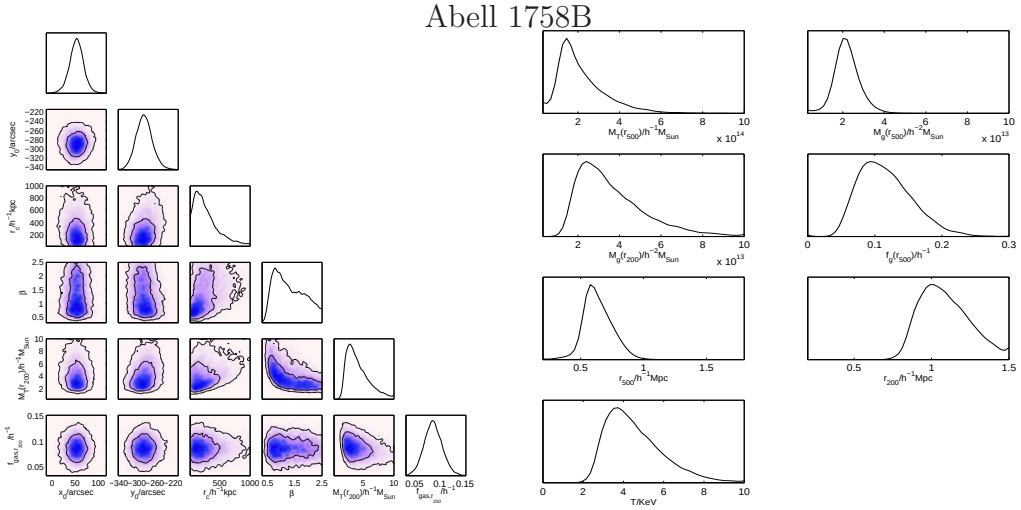

Figure 6.7: On the left I show the cluster parameters that I have sampled from and on the right I present some cluster parameters derived from our sampling parameters.

a detection was expected, given the low noise levels of our SA maps. The SA maps and derived parameters are shown in Figure 6.8. The derived parameters for this non-detection are as expected: it is found that $M_{\mathrm{T,r200}}$ approaches our lower prior limit ($0.32 \times 10^{14} M_{\odot} h_{100}^{-1}$) and that M_g shows simliar behaviour; both r_{200} and $T_{SZ,MT}$ are well constrained because both these parameters are derived from $M_{\mathrm{T,r200}}$ which itself is well constrained at the value of its lower prior limit.

Zhang et al. used XMM Newton to study Zw1454.8+2233 and found $M_{500} = 2.4 \pm 0.7 \times 10^{14} \mathrm{M}_{\odot}$, where $r_{500} = 0.87$Mpc. They assumed isothermality, spherical symmetry and $h_{70} = 1$. Venturi *et al.* (2008) observed the cluster with the GMRT at 610MHz and found that the cluster contains a core-halo source. This is in agreement with the value obtained from *Subaru* weak lensing observations by Okabe et al. The *Chandra* X-ray observations (Bauer *et al.* 2005) also reveal that Zw1454.8+2233 is a cooling core cluster; these are often associated with core-halos.

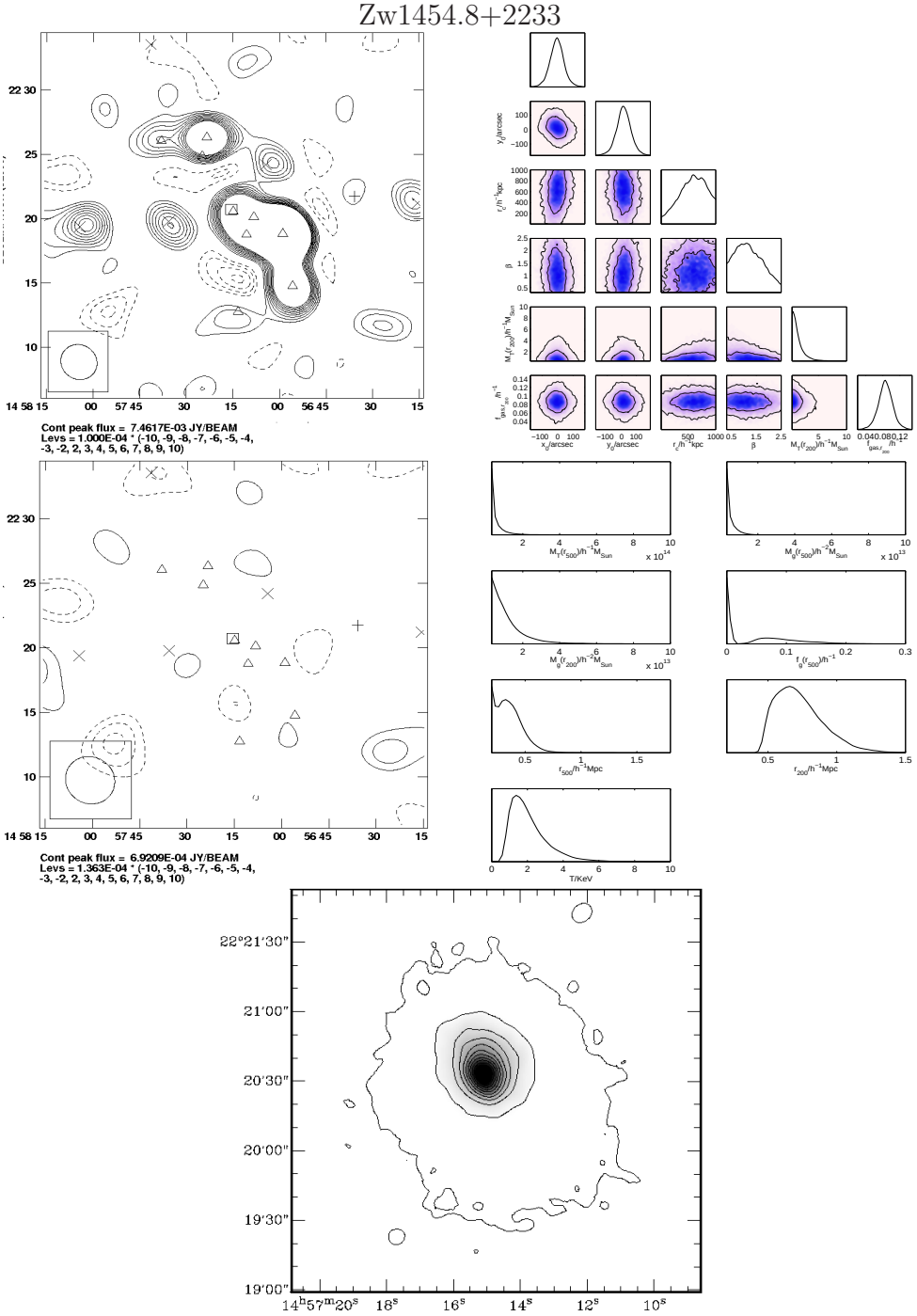

Figure 6.8: The *null detection* of Zw1454.8+2233 in SZ. The top left image is the SA map before subtraction, showing the challenging source environment. the map in the middle left has had the sources removed, however, no decrement is visible. The top panel on the right shows the sampling parameters and on the middle right panel I show the derived cluster parameters, these parameters are what would be expected from a null detection, they indicate mass with a high probability of being 0.0. The image at the bottom shows the *Chandra* X-ray map.

6.5.8 RXJ1720.1+2638

At 16 GHz the source environment around the cluster is challenging: in our LA data there is a 3.9 mJy source at the same position as the cluster, and several other sources with comparable flux densitites $< 500''$ from the cluster centre. However, using our Bayesian analysis to accurately model the positions, flux densities and spectral indices of these sources such that, after they are subtracted from our SA maps, a significant decrement is seen. The AMI SA maps before and after source subtraction are shown in Figure 6.9, as are the derived cluster parameters and a *Chandra* image of the cluster. Our SZ-effect map shows that the cluster may have an irregular shape; there is low signal-to-noise emission to the SE and NW of the cluster X-ray centroid; however, the centre of the SZ emission is coincident with the X-ray centroid.

Chandra observations (Mazzotta *et al.* 2001) indicate that, although the cluster does not have an irregular shape or elongation, it has discontinuities in its density profile; this may indicate it is in the latter stages of merging. The largest discontinuity is observed in the SE sector of the cluster and is noted to have a structure similar to a cold front observed in other merging systems such as Abell 2142 and Abell 3667. Mazzotta et al. determined the mass profile for the cluster assuming hydrostatic equilibrium using two distinct regions (SE and NW) to model the cluster density profile: each region was separately analysed and used to calculate $M_{1000\mathrm{kpc}} = 4 \pm 10 \times 10^{14} h_{50}^{-1} \mathrm{M}_{\odot}$.

6.6 Cluster Temperatures

In Figure 6.10 I compare the AMI SA observed cluster temperatures within r_{200} ($T_{SZ,MT}$) with large-radius X-ray values (T_X) from *Chandra* or *Suzaku* that I have been able to find in the literature. Large radius X-ray temperature values are used as these ignore the complexities of the cluster core and are representative of the average cluster temperature within ≈1Mpc which is measured by AMI. In this plot I have included the derived parameters from the AMI Consortium: Rodriguez-Gonzalvez *et al.* (2011) analysis of 11 medium luminosity LoCuSS clusters. Before comment on these I deal with two technical points. First, for

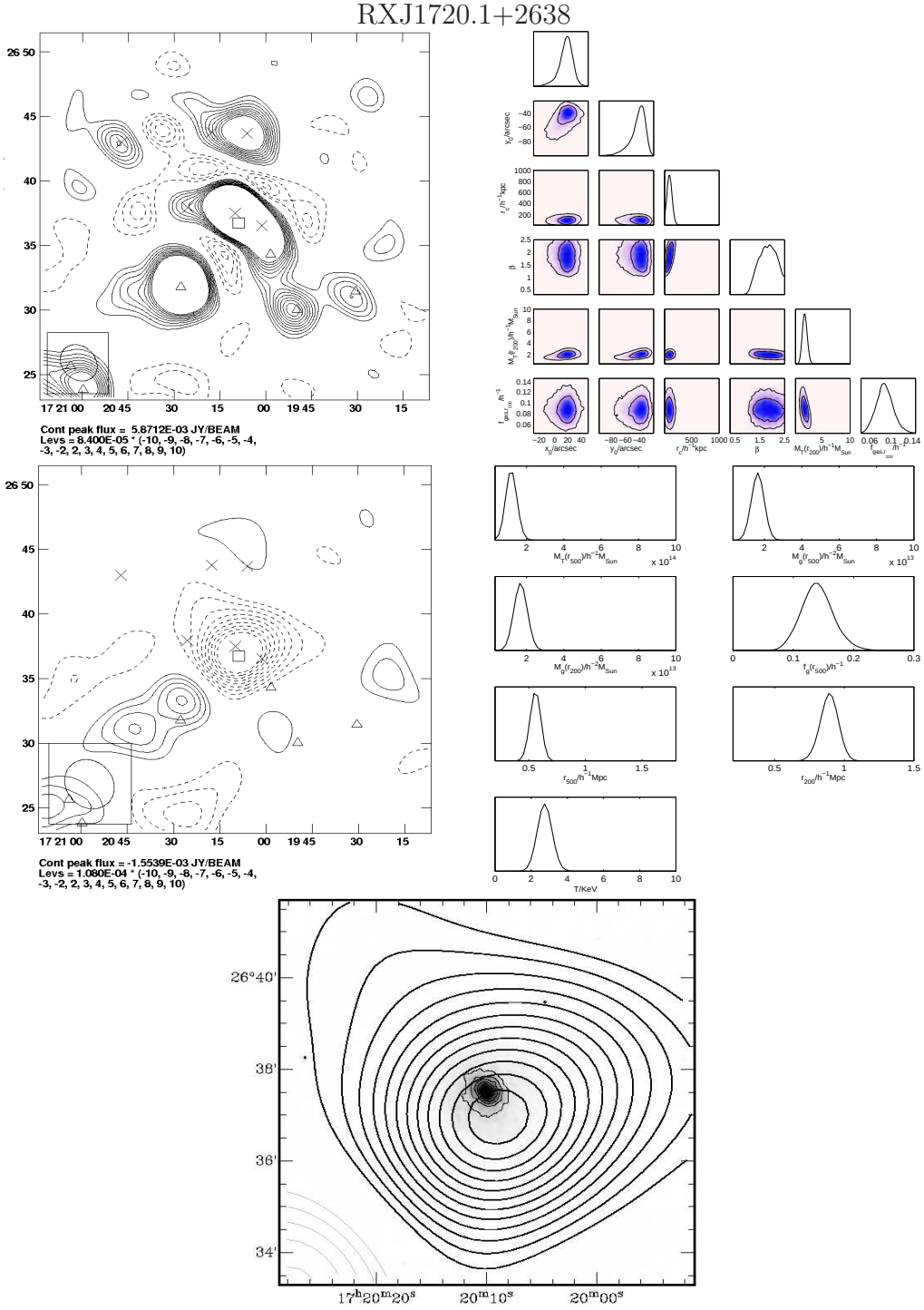

Figure 6.9: The top left image shows the SA map before subtraction, the map in the middle left has had the sources removed, the top right panel shows the cluster parameters that are sampled from in our Bayesian analysis and the middle right plot presents several cluster parameters derived from our sampling parameters. The image at the bottom shows the *Chandra* X-ray map overlayed with SA contours.

Abell 611, I have plotted two X-ray values (from *Chandra* data); one from the ACCEPT archive (Cavagnolo *et al.* 2009) which is higher than our AMI SA measurement, while the second X-ray measurement from *Chandra* (Donnarumma et al.) is consistent with our measurement. Secondly, the ACCEPT archive r= 475-550kpc temperature for Abell 1758A is 16±7keV and for clarity is not included on the plot.

Evidently Abell 586, Abell 611 (with the Donnarumma et al. X-ray temperature) and Abell 1413 have corresponding SZ and X-ray temperatures while Abell 773, Abell 1758A and RXJ1720.1+2638 have X-ray temperatures significantly higher than their SZ temperature. The position is made clearer by combining the values with those in Rodríguez-Gonzálvez et al. (2011). The combined data are shown in Figure 6.11, in which there is reasonable correspondence between SZ and X-ray temperatures at lower X-ray luminosity, with excess (over SZ) X-ray temperatures at higher X-ray luminosity. An exception to this is Abell 1413 which despite its high X-ray luminosity is in good agreement with our SZ value, but for this cluster I have been able to use *Suzuka* measurements over r= 700-1200kpc. It is noteworthy that Abell 773, Abell 1758A and RXJ1720.1+2638 are major mergers.

In Smith *et al.* (2005) *Chandra* temperatures (0.1-2.0 Mpc) are compared with lensing masses within 500 kpc for 10 clusters. The results indicate that disturbed clusters have higher temperatures. However, Marrone *et al.* (2009) compare the SZ $Y_{spherical}$ to lensing masses within 350 kpc for 14 clusters, and find no discrepancy between relaxed and disturbed clusters. Marrone *et al.* (2009) suggests that SZ measurements are less sensitive than T_X to the complexities of the intracluster medium even at low radius. Our analysis has found that major mergers have a larger T_X (500-700 kpc) than $T_{SZ,MT}$ averaged over the whole cluster. This suggests that even at large radius mergers affect n_e^2-weighted T_X measurements more than n_e-weighted $T_{SZ,MT}$ measurements. Such an affect could be due to shocking or clumping.

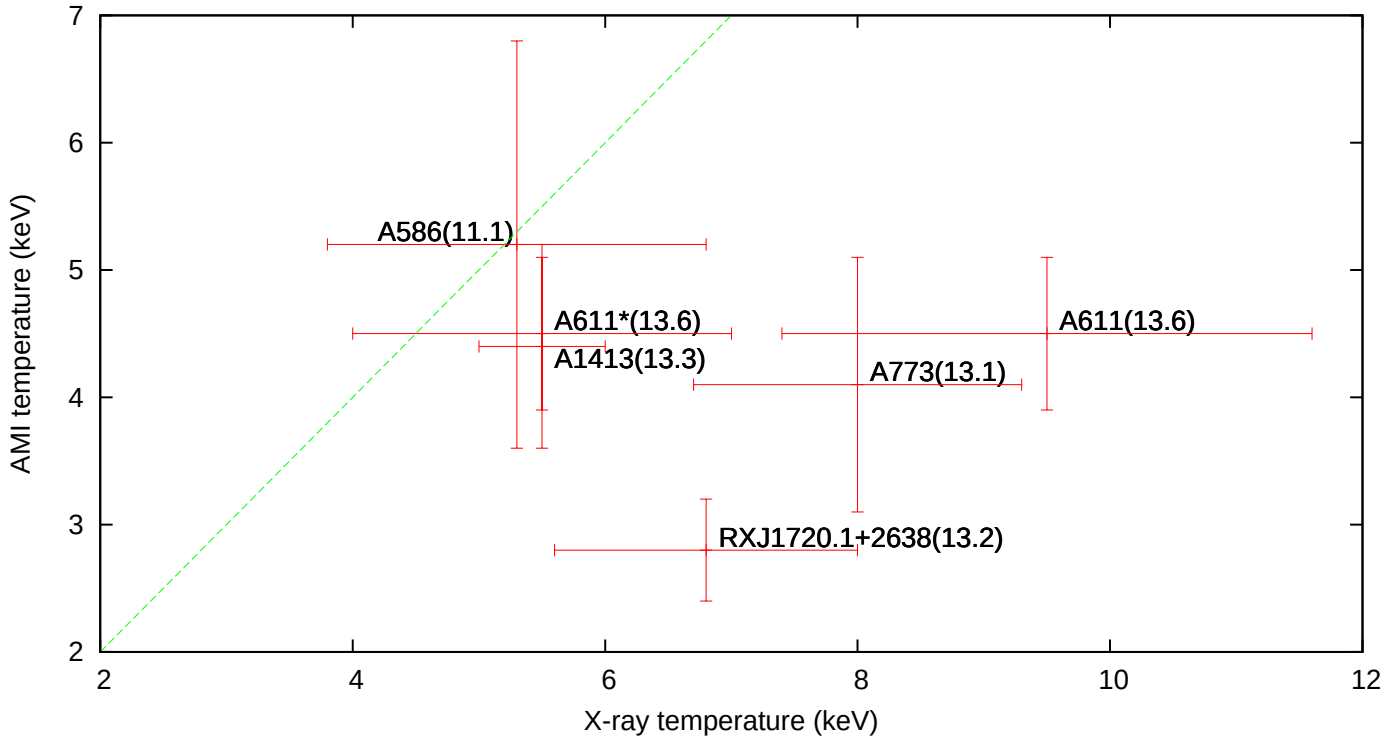

Figure 6.10: The AMI mean temperature within r_{200} versus the X-ray temperature, each point is labelled with the cluster name and X-ray luminosity. Most of the X-ray measurements are large-radius temperatures from the ACCEPT archive (Cavagnolo *et al.* 2009) with 90% confidence bars. The radius of the measurements taken from the ACCEPT archive are 400-600kpc for Abell 586, 300-700kpc for Abell 611, 300-600kpc for Abell 773 and for RXJ1720.1+2638 r = 550-700kpc. The A1413 X-ray temperature is estimated from the 700-1200kpc measurements made with the Suzaku satellite (Hoshino *et al.* 2010), this value is consistant with Vikhlinin *et al.* 2005 and Snowden *et al.* 2008. The Abell 611* temperature is the 450-750kpc value with σ error bars (Donnarumma & Ettori 2011). The ACCEPT archive temperature for Abell 1758A is 16±7keV at r= 475-550kpc with SZ temperature 4.5±0.5, for clarity this has not been included on the plot.

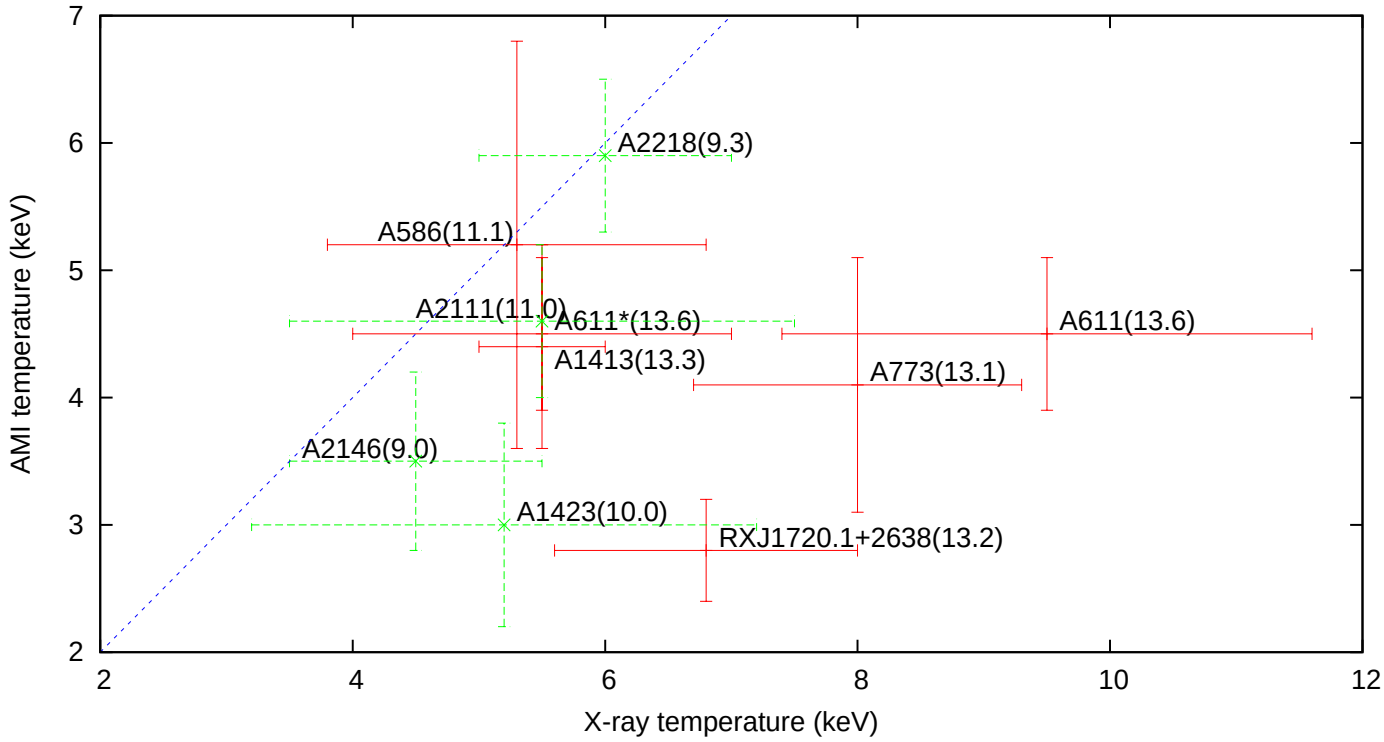

Figure 6.11: The AMI mean temperature within r_{200} versus the X-ray temperature including values from Rodríguez-Gonzálvez et al. (2011). Again Abell 1758A is not shown.

6.7 Conclusions

I have performed a detailed analysis of eight LoCuSS clusters and found the following:

- I have obtained good SZ detections for eight clusters and a non-detection for Zw1454.8+2233. The observed SZ decrements are not spherical but show significant spatial structure.

- For the seven detected clusters with $L_X > 11{\times}10^{37}$W ($h_{50} = 1$), β profiles have been fit to the cluster signals to find $M_{g,r200}$ values of 1.7-4.3$\times10^{13}h_{100}^{-1}M_{\odot}$ and values $M_{T,r200}$ of 2.0-5.1$\times10^{14}h_{100}^{-1}M_{\odot}$.

- For Abell 611 and Abell 773 our values of $M_{g,r200}$ and $M_{T,r200}$ are lower than those in Zwart et al. (2010) which are thought to be biased high, because they use a high value for $T_{SZ,MT}$ (estimated from a low-radius X-ray measurement) and assume this value to be constant throughout the cluster.

- For the six clusters in the work of this paper for which I have found large-radius $r \geq$ 500kpc X-ray spectroscopic temperatures in the literature, it is apparent that the T_X and $T_{SZ,MT}$ values correspond reasonably well for Abell 586, Abell 611 (with the Donnarumma et al. X-ray temperature rather than the ACCEPT archive value) and Abell 1413, but that correspondence falls away for Abell 773, Abell 1758A and RXJ1720.1+2638 which have a high T_X, for these, $T_{SZ,MT}$ is less than T_X.

- The picture seems to become clearer – although all of this work involves only very small numbers – when I add in the data of Rodríguez-Gonzálvez et al. (2011). I find that there is reasonable T_X:$T_{SZ,MT}$ correspondence for the six clusters at lower T_X but that the correspondence breaks down at high T_X. However, two points are evident. The more general one is that

the breakdown of the T_X:$T_{SZ,MT}$ correspondence tends to be associated with high L_X and with major mergers. The more specific one is that Abell 1413 has values of T_X and $T_{SZ,MT}$ that correspond yet has high L_X: but I have used T_X measured by the *Suzaku* at very high radius.

- I suspect this points to agreement between large-radius SZ estimates and larger-radius spectroscopic temperature measurements, but that substantial mergers bias T_X measurements more than $T_{SZ,MT}$; however I stress again that our sample from that and our companion paper is very small.

Chapter 7

Conclusions

In this thesis I have outlined the achievements of my work using AMI. Here I present the conclusions and possible extensions of the work described in previous chapters.

7.1 Commissioning and Calibration

The performance of both the SA and the LA has been improved by characterising the lags on the correlators and refining our measurements of the arrays geometry. Additionally, I have implemented important new routines into the standard data reduction pipeline, these correct for time average smoothing and significantly reduce the interference from geostationary satellites.

Importantly, I have produced what are currently the most accurate measurements of the SA and LA primary beams. Knowledge of these beams is essential in order to obtain accurate flux-density measurements of sources away from the phase centre. Throughout my time in Cambridge I have assisted with testing and automating the present standard data reduction pipeline.

I have developed several very useful routines to concatenate and simulate data, subtract sources and to test for systematics. These routines are regularly used throughout the AMI Consortium.

Improving and monitoring the performance of the interferometers and the data reduction pipeline is an ongoing task. For example, inter-array flux-density calibration is a priority.

7.2 AMI blind survey

I have for the first time applied our Bayesian analysis to search blindly for clusters in the SA survey data. After significant effort testing and characterising the analysis I have been able to obtain the first blind SZ detections with AMI. In two $\deg^2$ regions the two most significant detections that I have found lie at 3:01:14.70 +26:16:40.78 and 03:00:15.50 +26:14:2.25

There are a further 12 fields of AMI survey data to analyse. Using programs and techniques that I have developed for this first analysis I hope to continue to collaborate with the AMI Consortium with the aims of publishing a final cluster catalogue and coordinating follow-up observations with other instruments.

7.3 Pointed SZ observations

The images and derived parameters from the SZ observations of eight high luminosity LoCuSS clusters when combined with those from AMI Consortium: Rodriguez-Gonzalvez *et al.* (2011) provide a significant sample of clusters, which is a luminosity limited near-snapshot in z. Such observations are excellent for constraining cluster scaling relations and I have investigated the scaling between T_x and T_{SZ}. I found an overall agreement in the derived temperatures for relaxed clusters, and larger discrepancies for major mergers.

AMI has observed all observable LoCuSS clusters with luminosities exceeding 7 $\times 10^{37}$W which have insignificant source contamination. There are many LoCuSS clusters at lower luminosities and currently we are in the process of observing these. Additionally, I am in the process of conducting pointed SZ observations towards the hottest ($T > 5$keV) clusters in the XCS cluster sample (Mehrtens *et al.* 2011). The results from this analysis will be compared to those obtained from the LoCuSS sample.

Appendix A

The Friedmann Equation

In this appendix I present a derivation of the Friedmann equation from the Einstein field equation. A similar derivation can be found many standard text books, e.g. Peacock (1999) and Peebles (1993).

The Einstein Field Equation is

$$G_{uv} = R_{uv} - \frac{1}{2} g_{uv} R = 8\pi G T_{uv}, \tag{A.1}$$

where G_{uv} is the Einstein tensor. I shall begin by calculating the Ricci Tensor (R_{uv}) and proceed by calculating the Ricci scalar (R). g_{uv} is described according to the Friedmann-Robertson-Walker metric (Equation 1.7) and the stress energy tensor, T_{uv}, is described in Equation 1.10. Throughout the derivation I set $c = 1$.

The Ricci Tensor (R_{uv}) is given by

$$R_{uv} = \Gamma^{\alpha}_{uv,\alpha} - \Gamma^{\alpha}_{u\alpha,v} + \Gamma^{\alpha}_{\beta\alpha}\Gamma^{\beta}_{uv} - \Gamma^{\alpha}_{\beta v}\Gamma^{\beta}_{u\alpha}, \tag{A.2}$$

where I have used

$$\Gamma^{\alpha}_{uv,\alpha} = \frac{\delta \Gamma^{\alpha}_{uv}}{\delta x^{\alpha}}. \tag{A.3}$$

Computing the Ricci tensor is time consuming and requires calculations of many Christoffel symbols. Not all these calculations shall be presented here however, apart from the the R_{00} and R_{ii} terms all components reduce to zero. I shall demonstrate the calculation of the R_{00} term.

$$R_{00} = \Gamma^{\alpha}_{00,\alpha} - \Gamma^{\alpha}_{0\alpha,0} + \Gamma^{\alpha}_{\beta\alpha}\Gamma^{\beta}_{00} - \Gamma^{\alpha}_{\beta 0}\Gamma^{\beta}_{0\alpha}. \tag{A.4}$$

Because Christoffel symbols are equal to zero if both the bottom indices are 0 this can be simplified to

$$R_{00} = -\Gamma^{\alpha}_{0\alpha,0} - \Gamma^{\alpha}_{\beta 0}\Gamma^{\beta}_{0\alpha}. \tag{A.5}$$

Christoffel symbols are calculated according to

$$\Gamma^{u}_{\alpha\beta} = \frac{g^{uv}}{2}\left(\frac{\delta g_{\alpha v}}{\delta x^{\beta}} + \frac{\delta g_{\beta v}}{\delta x^{\alpha}} + \frac{\delta g_{\alpha\beta}}{\delta x^{v}}\right). \tag{A.6}$$

Therefore,

$$\Gamma^{\alpha}_{0\alpha} = \frac{g^{\alpha v}}{2}\left(\frac{\delta g_{0v}}{\delta x^{\alpha}} + \frac{\delta g_{\alpha v}}{\delta x^{0}} + \frac{\delta g_{0\alpha}}{\delta x^{v}}\right), \tag{A.7}$$

where g^{uv} is the inverse of g_{uv} and we know g_{uv} from the Friedmann-Robertson-Walker metric (Equation 1.7). As g_{uv} is a diagonal matrix then g^{uv} is zero if $u \neq v$, is -1 at $u = v = 0$ and $\frac{1}{a^2(t)}$ at the other points where $u = v$. This implies that in Equation A.7 unless $v = \alpha$, $\Gamma^{\alpha}_{0\alpha} = 0$.

$$\Gamma^{\alpha}_{0\alpha} = \frac{g^{\alpha\alpha}}{2}\left(\frac{\delta g_{0\alpha}}{\delta x^{\alpha}} + \frac{\delta g_{\alpha\alpha}}{\delta x^{0}} + \frac{\delta g_{0\alpha}}{\delta x^{v}}\right) \tag{A.8}$$

The first and last term on the right hand side reduce to derivatives of g_{00} which is a constant (-1) and hence its derivatives are zero. Hence

$$\Gamma^{\alpha}_{0\alpha} = \frac{g^{\alpha\alpha}}{2}\left(\frac{\delta g_{\alpha\alpha}}{\delta x^{0}}\right). \tag{A.9}$$

The derivative in the above equation is not equal to zero for the spatial coordinates ($3 \geq \alpha \geq 1$) but for the time coordinate ($\alpha = 0$) it is zero. The spatial derivatives can be calculated as follows:

$$\Gamma^{1}_{01} = \frac{g^{11}}{2}\left(\frac{\delta g_{11}}{\delta x^{0}}\right) = \frac{1}{2a^2(t)}\frac{\delta a^2(t)}{\delta x^{0}} = \frac{\dot{a}}{a}, \tag{A.10}$$

where $x^0 = t$. The calculation performed above can be use to demonstrate the property that

$$\Gamma^{i}_{0j} = \Gamma^{i}_{j0} = \delta_{ij}\frac{\dot{a}}{a}, \tag{A.11}$$

where here δ_{ij} is a delta-function and is zero if $i \neq j$ and one if $i = j$. It is now possible to substantially simplify Equation A.5 to give

$$R_{00} = -\delta_{ii}\frac{\delta}{\delta t}\left(\frac{\dot{a}}{a}\right) - \delta_{ij}\delta_{ji}\left(\frac{\dot{a}}{a}\right)^2. \tag{A.12}$$

Using the Einstein summation I note that both δ_{ii} and $\delta_{ij}\delta_{ji}$ imply a sum over the three spatial indices. Hence $\delta_{ii} = \delta_{ij}\delta_{ij} = 3$.

$$R_{00} = -3\frac{\delta}{\delta t}\left(\frac{\dot{a}}{a}\right) - 3\left(\frac{\dot{a}}{a}\right)^2 \tag{A.13}$$

Using the quotient rule the time derivation can be determined:

$$\frac{\delta}{\delta t}\frac{\dot{a}}{a} = \frac{\ddot{a}a - \dot{a}\dot{a}}{a^2} = \frac{\ddot{a}}{a} - \frac{\dot{a}^2}{a^2}. \tag{A.14}$$

Therefore, the 00 component of the Ricci Tensor is

$$R_{00} = -3\left(\frac{\ddot{a}}{a} - \frac{\dot{a}^2}{a^2}\right) - 3\left(\frac{\dot{a}}{a}\right)^2 = -3\frac{\ddot{a}}{a}. \tag{A.15}$$

By applying similar working it can also be determined that

$$R_{ij} = \delta_{ij}(2\dot{a}^2 + a\ddot{a}). \tag{A.16}$$

Hence, if $i \neq j$ then $R_{ij} = 0$, otherwise,

$$R_{ii} = 3(2\dot{a}^2 + a\ddot{a}). \tag{A.17}$$

The Ricci scalar can be dervied from R_{uv} according to

$$R = g^{uv}R_{uv}. \tag{A.18}$$

Using an Einstein summation and noting that off diagonal terms in both g_{uv} and R_{uv} are equal to zero we find

$$R = -R_{00} + \frac{1}{a^2}R_{ii}. \tag{A.19}$$

Putting in R_{00} and R_{ii} from Equations A.15 and A.17 respectively gives

$$R = 3\frac{\ddot{a}}{a} + \frac{1}{a^2}3(2\dot{a}^2 + a\ddot{a}) = 6\left(\frac{\ddot{a}}{a} + \frac{\dot{a}^2}{a^2}\right) \tag{A.20}$$

We can now solve the Einstein Field Equation (Equation A.1) for the time component (00) of the Universe.

$$G_{00} = R_{00} - \frac{1}{2}g_{00}R = 8\pi G T_{00} \tag{A.21}$$

$$G_{00} = -3\frac{\ddot{a}}{a} - \frac{1}{2}(-1)6\left(\frac{\ddot{a}}{a} + \frac{\dot{a}^2}{a^2}\right) = 3\left(\frac{\dot{a}}{a}\right)^2 = 8\pi G T_{00} \tag{A.22}$$

Recalling that $T_{00} = \rho$ (Equation 1.10) implies

$$\left(\frac{\dot{a}}{a}\right)^2 = \frac{8\pi G\rho}{3} \tag{A.23}$$

This solution of the Einstein Field Equations is known as the Friedmann equation.

Note that similarly the acceleration equation (1.17) can be derived from the trace of the Einstein Field Equation.

Appendix B

AMI002 LA Source Properties

Table B.1: * extended source, quoting integrated LA flux

Right ascension	Declination	Flux (mJy)	Spectral Index
03:01:37.66	+25:41:58.77	21.78*	0.49
03:01:05.45	+25:47:15.96	13.6	0.4
03:01:38.08	+25:21:48.20	13.55	0.82
02:59:55.14	+26:27:25.95	8.36	0.38
03:02:43.07	+26:07:59.01	8.3	0.65
02:58:03.29	+25:31:10.63	5.39	1.0
02:57:18.26	+26:54:07.93	4.51	0.12
03:00:15.82	+26:54:59.54	4.49	-0.0
03:02:20.25	+25:49:40.57	3.67	0.31
02:59:10.70	+25:54:31.31	3.44	1.21
02:58:17.27	+25:38:18.82	3.43	1.67
03:01:39.31	+26:29:31.87	2.98	0.24
03:01:55.72	+27:02:06.25	2.96	1.11
02:57:05.63	+26:07:10.07	2.88	0.64
02:58:34.96	+26:32:16.11	2.84	1.05
02:59:17.30	+27:04:01.64	2.79	0.4
02:56:52.95	+26:55:30.80	2.78	-0.03
03:01:36.46	+25:33:51.90	2.6	1.69
03:01:46.75	+27:00:46.04	2.44	0.64
02:59:32.31	+26:39:51.24	2.35	0.1
03:00:35.40	+26:34:24.95	2.32	1.29

Table B.1: * extended source, quoting integrated LA flux

Right ascension	Declination	Flux (mJy)	Spectral Index
03:00:27.04	+26:57:34.78	2.31	1.78
02:58:25.30	+26:16:59.79	2.29	1.02
02:57:01.71	+26:51:20.02	2.23	1.14
02:58:33.66	+26:32:51.31	2.13	-0.11
03:02:00.27	+26:45:57.57	2.03	1.11
03:02:36.83	+26:25:54.60	1.99	0.35
03:02:02.42	+26:00:17.81	1.97	0.88
03:00:52.02	+25:20:38.85	1.94	0.72
03:00:46.96	+26:44:11.31	1.91	1.27
02:56:35.91	+25:33:30.01	1.85	0.57
03:00:01.29	+26:21:00.66	1.83	-0.09
03:01:40.53	+26:56:21.42	1.69	1.03
02:59:41.05	+26:02:20.29	1.67	1.13
02:58:55.86	+26:54:49.96	2.37*	1.98
02:57:07.78	+25:56:35.05	1.64	-1.81
02:59:57.18	+25:53:55.96	1.63	2.41
03:02:44.36	+26:55:54.23	1.5	0.95
02:58:45.52	+26:30:48.72	1.47	0.49
03:01:16.32	+26:47:13.02	1.45	1.19
03:02:10.93	+26:18:44.78	1.42	1.46
03:00:29.47	+26:18:39.88	1.41	0.53
02:57:19.14	+25:29:20.26	2.19*	2.74
02:57:35.36	+25:28:41.70	1.39	0.79
03:00:59.25	+25:56:48.61	1.36	0.07
02:57:58.11	+25:59:47.15	1.34	0.01
03:00:21.67	+25:36:36.83	1.32	1.69
02:56:49.80	+25:23:23.17	1.31	1.51
03:02:15.65	+25:25:09.66	1.31	0.38
03:01:49.89	+26:40:13.47	1.27	1.12
03:00:35.26	+26:35:21.31	1.69*	1.46
03:02:12.00	+26:33:42.35	1.27	0.83
03:00:24.55	+26:19:40.64	1.2	1.4
02:58:28.52	+25:55:59.38	1.2	0.17
02:58:58.39	+25:44:57.82	1.68*	1.91
02:57:19.57	+26:11:20.65	1.15	0.91
03:00:33.35	+25:17:36.88	1.15	0.28
03:00:44.06	+26:54:31.04	1.14	0.02

Table B.1: * extended source, quoting integrated LA flux

Right ascension	Declination	Flux (mJy)	Spectral Index
03:00:15.21	+26:19:25.25	1.11	1.87
03:02:33.31	+25:59:31.01	1.07	0.7
03:01:30.19	+26:45:36.81	1.06	1.84
02:58:39.33	+25:47:54.29	1.05	0.35
03:02:09.80	+26:25:46.42	1.03	1.36
03:01:13.43	+27:03:05.56	1.03	0.45
02:59:26.31	+27:03:07.09	1.02	0.54
03:00:09.89	+26:31:00.88	1.02	0.91
03:01:55.47	+25:57:46.89	1.01	0.02
03:01:57.80	+25:26:47.56	0.98	0.18
03:00:16.51	+26:33:46.57	0.97	-0.29
02:58:29.18	+25:57:19.60	0.96	2.01
02:58:12.01	+26:20:54.06	0.96	1.2
02:58:41.82	+25:22:23.95	0.94	-0.09
03:00:09.98	+25:45:11.05	0.92	0.29
02:58:57.32	+26:24:49.28	0.91	1.22
03:02:05.76	+26:36:20.41	0.83	-0.16
02:56:35.67	+25:42:09.01	0.8	1.09
03:01:33.84	+26:13:19.71	0.8	2.45
02:59:24.23	+26:52:12.84	0.78	1.95
02:59:39.69	+25:53:22.67	0.78	-0.52
02:58:46.58	+25:27:31.40	0.75	-0.29
02:57:41.23	+25:22:36.82	0.73	0.15
03:01:19.63	+26:30:57.57	0.73	0.59
02:58:41.62	+26:54:10.96	0.72	-0.86
02:56:41.92	+25:22:30.81	0.72	1.2
03:02:37.36	+26:01:09.45	0.71	-0.05
03:02:14.25	+25:34:55.15	0.69	0.27
03:01:43.00	+26:39:05.99	0.69	0.37
02:58:23.50	+25:24:60.00	0.68	0.39
03:00:49.26	+26:15:05.07	0.68	0.73
02:59:20.14	+26:50:42.80	0.68	-1.16
03:01:55.90	+25:49:06.62	0.68	1.58
02:57:37.70	+25:27:06.24	0.68	0.01
02:59:38.93	+25:20:26.24	0.68	1.95
03:01:57.75	+25:21:19.72	1.24*	0.7
02:57:55.07	+25:38:28.19	0.67	-0.14

Table B.1: * extended source, quoting integrated LA flux

Right ascension	Declination	Flux (mJy)	Spectral Index
02:59:35.41	+26:17:25.68	0.67	0.78
03:01:01.33	+25:31:10.67	0.65	1.77
03:01:18.86	+26:03:52.86	0.65	0.37
02:58:32.31	+26:07:46.34	0.65	-0.2
02:59:34.39	+25:24:10.43	0.63	0.59
02:58:07.69	+25:36:39.55	0.61	-0.4
02:56:51.23	+26:46:33.71	0.6	1.09
03:00:49.22	+26:06:43.78	0.59	1.0
03:01:12.53	+26:30:57.78	0.58	-0.6
02:58:38.02	+25:28:35.49	0.57	1.27
02:57:03.04	+26:47:12.04	0.57	-1.32
02:58:15.74	+26:19:58.02	0.56	1.02
03:02:17.82	+26:12:25.88	0.56	-1.61
02:57:51.01	+25:27:17.41	0.56	0.27
02:57:11.31	+25:43:36.62	0.55	0.84
02:59:10.48	+26:31:25.81	0.55	-0.07
03:02:13.24	+25:57:24.84	0.54	1.17
02:58:22.26	+25:35:23.91	0.54	-1.01
03:00:23.05	+26:26:04.58	0.53	0.63
03:01:31.99	+26:21:44.81	0.53	-1.37
02:58:36.95	+26:42:20.87	0.52	-0.19
03:01:18.72	+26:05:05.60	0.52	1.44
03:01:24.17	+27:00:49.43	0.51	-0.2
02:58:44.02	+25:23:39.99	0.51	0.11
02:57:43.57	+25:58:58.65	0.51	1.06
03:00:21.16	+26:44:58.86	0.51	-0.5
02:58:29.79	+26:48:45.88	0.5	-0.92
02:59:50.12	+26:25:21.21	0.5	1.67
02:57:03.68	+25:38:39.42	0.5	1.1
03:02:13.87	+25:42:12.16	0.5	0.74
02:57:46.66	+26:43:18.39	0.49	-0.08
02:59:11.22	+26:57:10.94	0.49	-0.27
02:57:31.51	+25:41:35.88	0.49	-0.06
02:58:24.68	+25:35:25.67	0.49	1.08
03:01:32.33	+25:40:17.79	0.48	-0.12
03:02:02.99	+25:35:29.91	0.48	0.06
02:56:43.40	+25:54:45.30	0.9*	0.69

Table B.1: * extended source, quoting integrated LA flux

Right ascension	Declination	Flux (mJy)	Spectral Index
02:59:06.91	+26:15:30.41	0.46	0.73
03:02:09.97	+25:35:21.96	0.46	1.47
03:00:51.20	+25:56:15.20	0.46	0.95
03:01:40.66	+26:36:03.18	0.45	0.06
03:01:28.05	+26:16:46.80	0.7*	0.25
03:00:57.87	+26:26:50.43	0.45	-0.2
03:01:12.96	+25:51:59.42	0.44	0.48
03:01:38.54	+26:19:22.17	0.44	1.03
03:01:11.84	+26:50:22.74	0.44	2.26
02:58:55.70	+26:53:32.20	0.43	1.67
02:58:05.39	+25:38:55.44	0.43	-0.07
02:59:10.65	+26:45:24.71	0.42	1.74
03:01:01.61	+25:45:18.49	0.63*	-0.84
02:56:41.13	+26:16:13.95	0.41	-0.53
02:59:39.72	+26:05:57.71	0.41	1.39
02:58:27.53	+25:47:13.44	0.41	1.28
02:56:58.80	+25:57:39.72	0.41	0.67
03:01:32.85	+26:31:27.70	0.4	-1.21
03:02:14.00	+26:42:55.36	0.4	1.08
02:57:21.56	+26:19:42.69	0.39	1.03
02:59:51.51	+26:42:52.91	0.38	0.39
02:59:23.54	+26:05:54.53	0.38	0.59
02:59:51.47	+25:42:14.50	0.37	2.06
02:57:50.69	+26:00:38.22	0.36	0.37
03:00:29.60	+25:41:36.57	0.35	-0.81
02:58:42.66	+26:01:33.80	0.35	-0.53
02:59:55.87	+26:39:23.19	0.51*	2.68
02:58:20.37	+26:36:56.09	0.35	-0.26
02:58:03.49	+26:38:53.78	0.34	-0.8
02:57:43.15	+25:57:19.26	0.33	-0.64
02:58:07.02	+25:48:35.56	0.31	-0.42
02:58:38.38	+26:09:24.04	0.31	0.28
03:00:57.85	+26:07:04.17	0.29	-0.9
02:59:17.90	+26:23:44.17	0.29	0.15
03:01:28.30	+26:06:58.69	0.29	0.64
02:58:24.00	+25:53:48.22	0.29	0.58
02:58:13.53	+26:28:09.74	0.29	0.76

Table B.1: * extended source, quoting integrated LA flux

Right ascension	Declination	Flux (mJy)	Spectral Index
02:59:53.84	+26:30:09.90	0.28	1.61
02:59:29.86	+26:09:47.26	0.28	1.25
03:00:26.67	+25:45:12.14	0.28	0.66
03:01:12.65	+26:18:23.51	0.28	0.86
02:59:31.23	+25:54:10.70	0.28	-0.8
03:00:40.27	+25:50:51.95	0.27	1.84
03:00:30.71	+26:24:06.76	0.26	1.14
03:01:15.44	+26:08:45.35	0.25	-0.77
02:59:42.22	+26:05:02.75	0.25	0.2
03:01:20.99	+25:47:04.94	0.25	0.85
03:00:14.84	+26:40:30.91	0.25	0.68
03:01:05.55	+25:45:06.08	0.32*	0.97
02:59:55.91	+26:08:41.13	0.25	2.13
02:58:34.24	+26:01:50.14	0.24	0.4
03:01:06.53	+25:48:53.38	0.24	0.14
03:00:06.30	+25:42:59.57	0.24	1.4
03:00:48.44	+26:41:09.81	0.23	-1.49
02:59:05.66	+25:51:40.50	0.23	0.39
03:00:53.30	+25:41:45.27	0.23	0.22
03:00:29.35	+25:57:34.53	0.33*	0.54
02:58:16.15	+26:35:08.80	0.22	0.72
03:01:12.19	+25:50:39.41	0.21	1.35
02:59:14.18	+26:07:12.26	0.21	0.34
03:00:31.69	+26:10:12.17	0.21	-0.74
02:58:32.81	+26:04:06.62	0.21	-0.02
03:00:10.64	+26:27:40.91	0.21	0.71
03:00:47.73	+26:27:44.50	0.21	-0.05
02:59:42.85	+26:35:00.46	0.21	-0.65
03:01:09.43	+25:42:18.72	0.21	0.89
02:58:44.16	+26:32:06.94	0.21	1.63
02:59:49.71	+26:32:47.66	0.21	0.41
03:01:05.37	+25:43:29.94	0.21	2.16
03:01:06.22	+25:41:53.57	0.2	0.72
02:58:23.97	+25:52:39.51	0.2	0.51
02:59:56.17	+25:45:05.57	0.19	1.68
03:00:19.09	+25:58:10.07	0.19	-0.28
03:00:20.57	+26:30:30.60	0.19	2.07

Table B.1: * extended source, quoting integrated LA flux

Right ascension	Declination	Flux (mJy)	Spectral Index
03:00:24.93	+26:17:54.64	0.25*	0.92
02:58:43.89	+25:44:24.13	0.18	0.39
02:59:10.10	+25:44:39.30	0.18	0.6
03:00:50.02	+26:13:44.30	0.14	1.25

B.1 AMI005 LA Source Properties

Table B.2: * extended source, quoting integrated LA flux

Right ascension	Declination	Flux (mJy)	Spectral Index
09:37:06.19	+32:06:57.11	46.83	0.46
09:42:08.84	+32:06:42.54	20.7	1.19
09:36:36.87	+32:03:34.35	18.74	1.23
09:35:59.46	+31:27:26.17	16.98	-0.21
09:41:46.66	+31:54:59.88	23.2*	1.08
09:38:26.59	+30:35:12.56	13.74	0.54
09:40:42.10	+32:01:29.03	11.48	1.35
09:41:07.44	+31:26:56.28	9.01	1.53
09:40:59.49	+31:25:36.88	13.61*	1.51
09:39:50.86	+31:54:15.16	8.14	1.46
09:36:11.92	+30:23:49.63	7.9	-0.1
09:40:53.05	+30:43:51.94	6.16	1.71
09:37:58.06	+31:43:43.22	5.59	1.12
09:39:53.78	+31:22:41.34	6.94*	1.74
09:41:47.45	+31:46:48.59	5.34	-0.42
09:37:18.16	+31:04:44.68	4.87	2.81
09:37:37.89	+31:22:41.08	4.86	0.28
09:38:17.39	+31:18:54.03	4.5	0.52
09:37:01.32	+31:29:40.91	4.32	1.06
09:41:16.67	+30:57:28.86	4.24	2.65
09:36:58.06	+31:29:31.31	3.95	0.08

Table B.2: * extended source, quoting integrated LA flux

Right ascension	Declination	Flux (mJy)	Spectral Index
09:37:39.56	+32:09:10.99	3.74	2.45
09:36:41.78	+30:33:55.15	3.73	0.5
09:36:52.68	+31:18:24.46	3.61	1.59
09:39:48.40	+31:34:00.15	3.27	1.55
09:37:22.10	+32:01:08.03	3.03	0.98
09:41:18.05	+31:58:51.31	2.84	0.87
09:39:31.91	+31:54:00.35	2.75	0.13
09:38:27.65	+30:28:01.18	2.7	0.49
09:42:12.23	+32:09:30.49	2.68	1.35
09:38:13.88	+31:31:47.79	2.66	1.14
09:37:13.91	+32:11:32.41	2.58	2.88
09:41:04.10	+30:27:48.15	2.52	2.7
09:37:25.66	+30:31:45.07	2.45	-0.3
09:41:45.83	+32:00:18.91	2.44	0.88
09:37:33.62	+31:18:15.62	2.42	2.16
09:42:09.50	+30:57:18.67	2.4	1.66
09:38:46.38	+31:37:59.78	2.36	1.08
09:41:50.78	+31:52:59.16	2.29	-0.87
09:40:48.10	+31:49:58.86	2.27	-1.05
09:39:21.35	+30:46:31.58	2.24	1.85
09:38:43.76	+31:05:35.30	2.21	1.04
09:37:44.33	+31:12:18.00	2.2	0.8
09:36:44.11	+32:11:28.57	2.17	-0.44
09:37:03.77	+31:56:41.11	2.12	-0.05
09:41:00.40	+30:50:51.51	2.11	2.06
09:39:48.86	+31:15:26.35	2.09	0.09
09:42:26.71	+31:27:07.11	2.09	2.22
09:39:39.83	+31:01:06.82	2.04	0.36
09:40:13.89	+31:21:45.67	1.89	1.33
09:38:07.34	+30:34:40.67	1.85	2.92
09:38:32.11	+30:24:05.80	1.83	1.94
09:38:39.02	+31:03:58.91	1.72	0.32
09:41:21.10	+31:25:42.70	1.69	-0.53
09:40:29.13	+31:58:05.15	1.68	3.49
09:39:09.34	+30:57:56.00	1.62	3.32
09:36:22.48	+31:08:37.12	1.58	2.99
09:37:01.95	+32:06:19.17	1.53	-3.01

Table B.2: * extended source, quoting integrated LA flux

Right ascension	Declination	Flux (mJy)	Spectral Index
09:39:13.06	+32:08:58.60	1.52	0.65
09:37:57.17	+31:13:14.13	1.51	0.01
09:36:55.25	+32:11:28.27	1.49	2.99
09:39:17.42	+31:39:40.39	1.48	1.81
09:37:22.94	+31:16:48.34	1.47	0.36
09:37:37.22	+31:59:08.74	1.45	1.46
09:38:59.96	+31:11:21.81	1.44	0.64
09:37:08.33	+32:08:05.39	1.39	-0.61
09:37:05.78	+30:21:48.59	1.38	-0.74
09:37:30.80	+30:29:46.60	1.37	-0.11
09:37:46.16	+30:28:39.38	1.34	0.09
09:39:37.49	+32:07:01.94	1.31	1.88
09:37:59.96	+30:41:28.14	1.31	4.98
09:37:46.28	+30:26:12.45	1.3	-0.44
09:37:11.82	+32:07:32.01	1.29	0.56
09:37:12.04	+32:10:06.66	1.29	1.84
09:41:26.10	+32:06:23.08	1.29	1.83
09:37:20.27	+30:39:02.75	1.29	1.43
09:37:25.71	+31:09:38.73	1.27	1.69
09:37:19.85	+30:51:22.26	1.26	0.48
09:36:10.42	+30:25:05.36	1.25	0.08
09:37:00.19	+32:03:41.84	1.18	-0.38
09:41:07.94	+30:27:11.66	1.17	-1.33
09:40:02.66	+30:22:21.50	1.16	0.29
09:37:22.10	+32:08:16.07	1.6*	0.16
09:36:18.70	+31:29:21.82	1.14	1.73
09:41:39.82	+30:27:02.46	1.08	-0.09
09:41:38.59	+32:06:17.04	1.05	-0.74
09:38:20.34	+31:31:27.68	1.05	0.02
09:37:59.69	+30:44:58.18	1.05	1.56
09:37:02.36	+32:04:59.42	1.05	1.4
09:38:38.58	+31:25:34.57	1.04	0.72
09:37:45.09	+31:34:22.86	1.03	1.33
09:39:40.84	+31:46:35.86	1.01	-1.67
09:38:33.11	+30:57:54.12	1.0	0.39
09:42:11.00	+30:49:22.20	1.0	0.86
09:41:11.15	+31:48:53.47	0.99	-0.09

Table B.2: * extended source, quoting integrated LA flux

Right ascension	Declination	Flux (mJy)	Spectral Index
09:37:06.04	+32:10:49.20	0.96	0.28
09:37:08.70	+31:17:55.26	0.94	0.49
09:36:44.52	+31:55:14.05	0.94	1.75
09:37:11.24	+32:08:46.95	0.93	1.87
09:36:51.44	+32:05:22.35	2.07*	4.11
09:41:26.14	+32:01:12.39	0.91	1.11
09:38:02.16	+31:11:32.77	0.9	1.88
09:41:12.06	+31:04:36.89	0.9	0.98
09:42:10.51	+32:05:52.44	0.9	0.42
09:36:17.77	+30:45:35.86	0.88	1.11
09:37:01.77	+32:07:37.64	0.88	0.09
09:41:08.64	+32:00:44.11	0.86	2.0
09:42:08.52	+31:38:01.97	0.84	0.36
09:36:37.39	+30:24:35.03	1.45*	1.42
09:37:44.54	+30:35:24.53	0.83	0.9
09:39:27.43	+31:16:29.85	0.83	-0.08
09:36:59.24	+32:08:25.99	0.83	1.09
09:36:34.78	+32:04:49.81	0.83	-0.03
09:37:04.03	+32:05:29.69	0.82	-0.79
09:36:56.33	+32:08:50.35	0.82	-0.14
09:37:25.50	+30:59:38.55	0.81	0.54
09:38:52.16	+31:20:18.70	0.8	0.89
09:42:11.15	+31:35:18.67	0.79	0.78
09:36:21.83	+30:31:27.75	0.79	1.53
09:36:46.89	+31:17:55.20	0.77	-1.73
09:37:08.04	+32:04:32.45	0.76	1.27
09:36:49.84	+32:08:12.73	0.75	0.19
09:37:14.19	+31:32:06.06	0.75	0.22
09:41:35.10	+31:55:30.33	0.69	1.4
09:42:20.25	+30:50:27.52	0.68	1.52
09:37:30.25	+30:31:16.34	0.66	0.96
09:36:36.18	+30:50:09.42	0.66	2.51
09:38:09.11	+32:07:00.54	0.65	0.33
09:40:45.02	+30:52:09.98	0.64	2.0
09:38:15.74	+30:39:13.45	0.63	-0.19
09:39:33.85	+31:56:19.41	0.63	0.97
09:36:40.17	+32:02:50.58	0.62	0.94

Table B.2: * extended source, quoting integrated LA flux

Right ascension	Declination	Flux (mJy)	Spectral Index
09:37:13.05	+32:05:19.62	0.62	-0.31
09:40:48.49	+31:22:39.36	0.62	1.93
09:41:03.53	+31:14:47.56	0.61	0.7
09:39:08.41	+31:36:11.24	0.61	1.52
09:41:29.95	+30:38:25.11	0.6	1.29
09:40:51.61	+31:33:53.06	0.6	0.57
09:42:27.30	+30:54:32.43	0.6	1.83
09:41:04.62	+31:20:24.23	0.59	-0.01
09:39:53.21	+31:16:14.65	0.59	-0.71
09:41:43.96	+31:55:56.09	0.59	0.56
09:42:05.52	+32:04:48.14	0.59	-0.01
09:42:10.27	+32:04:28.83	0.94*	-0.37
09:39:30.41	+31:24:11.60	0.58	1.28
09:41:25.29	+30:35:33.46	0.58	0.82
09:38:31.54	+30:27:28.47	0.57	0.49
09:36:33.37	+30:28:34.94	0.56	1.58
09:39:28.53	+30:30:49.33	0.56	0.63
09:41:53.11	+30:34:35.34	0.56	1.0
09:41:48.99	+31:57:51.22	1.59*	0.26
09:38:43.61	+30:34:55.62	0.55	-0.76
09:40:29.14	+31:59:15.20	0.55	0.54
09:40:21.11	+32:04:58.04	0.54	-0.76
09:41:51.51	+31:02:23.40	0.54	-0.89
09:41:35.27	+31:50:14.53	1.05*	1.5
09:40:07.14	+32:02:43.44	0.54	0.53
09:42:03.35	+31:55:35.44	0.53	-1.03
09:40:47.30	+30:47:36.87	0.53	0.72
09:39:05.28	+31:55:13.44	0.51	-0.19
09:37:10.02	+32:03:32.34	0.5	0.23
09:42:18.69	+32:02:18.86	0.49	1.02
09:39:16.30	+31:15:09.33	0.49	1.53
09:37:37.19	+30:45:23.77	0.49	-0.99
09:40:14.28	+31:40:04.65	0.48	0.62
09:40:14.82	+31:34:38.50	0.47	2.08
09:41:06.74	+31:22:16.70	0.47	1.09
09:38:26.01	+31:28:39.92	0.46	-1.38
09:39:02.74	+30:41:23.01	0.46	2.97

Table B.2: * extended source, quoting integrated LA flux

Right ascension	Declination	Flux (mJy)	Spectral Index
09:39:45.84	+31:48:55.28	0.45	0.67
09:39:26.10	+31:27:29.23	0.44	0.28
09:39:28.75	+31:02:56.64	0.43	0.64
09:39:09.45	+31:38:28.63	0.42	0.91
09:37:48.86	+30:46:41.93	0.42	0.5
09:37:57.10	+30:56:18.69	0.42	0.69
09:41:12.68	+30:42:18.80	0.4	0.95
09:38:12.38	+31:12:42.65	0.39	3.16
09:37:38.70	+31:39:01.65	0.39	0.75
09:37:28.21	+31:09:01.96	0.39	0.38
09:38:17.97	+31:47:04.35	0.39	0.3
09:37:24.77	+31:33:36.35	0.36	0.04
09:38:54.61	+31:18:41.27	0.35	0.84
09:40:29.53	+31:46:50.73	0.35	1.44
09:39:00.07	+30:45:25.34	0.35	0.82
09:41:20.07	+30:50:28.15	0.34	0.85
09:41:11.52	+31:34:08.89	0.32	0.55
09:40:58.51	+31:40:07.97	0.31	-0.08
09:41:16.47	+31:22:35.11	0.6*	2.91
09:40:59.36	+31:29:44.24	0.31	1.52
09:41:07.04	+30:57:26.16	0.3	-0.05
09:41:14.42	+31:24:03.57	0.3	0.38
09:40:41.56	+30:53:24.26	0.3	-0.64
09:39:36.48	+31:21:08.72	0.3	0.59
09:38:14.17	+31:10:32.55	0.29	1.01
09:39:44.21	+31:31:00.81	0.29	1.48
09:40:25.20	+31:35:01.00	0.29	1.86
09:37:51.54	+30:47:51.47	0.28	1.98
09:39:38.90	+31:11:24.29	0.28	-0.16
09:38:14.14	+30:53:40.19	0.28	-0.27
09:38:52.79	+31:37:43.52	0.28	-0.66
09:41:09.41	+31:23:21.18	0.28	0.71
09:37:43.75	+31:32:47.01	0.26	2.06
09:39:54.94	+31:20:40.45	0.26	0.73
09:40:43.57	+30:59:14.70	0.26	0.46
09:37:47.12	+31:20:02.00	0.25	1.26
09:39:29.34	+30:44:58.72	0.25	1.04

Table B.2: * extended source, quoting integrated LA flux

Right ascension	Declination	Flux (mJy)	Spectral Index
09:37:45.46	+31:26:57.71	0.25	0.27
09:41:01.87	+30:53:14.69	0.24	0.84
09:37:49.19	+31:43:52.16	0.24	-0.22
09:39:06.59	+30:58:53.79	0.24	2.15
09:40:49.79	+30:57:33.59	0.24	-0.11
09:39:36.99	+31:34:03.92	0.24	1.12
09:38:01.04	+31:02:37.76	0.23	0.03
09:39:14.33	+31:11:15.84	0.23	0.29
09:40:59.41	+31:02:21.92	0.23	0.83
09:37:47.74	+31:39:28.50	0.23	1.07
09:38:54.67	+30:48:55.00	0.23	-0.01
09:37:46.70	+31:44:26.89	0.23	1.16
09:39:43.88	+30:53:29.08	0.23	-1.98
09:37:52.69	+30:50:06.65	0.23	0.43
09:38:53.14	+31:10:15.90	0.22	0.87
09:39:33.27	+31:37:01.75	0.22	-0.33
09:37:54.56	+30:51:42.55	0.22	-0.45
09:39:51.04	+31:14:10.11	0.22	0.93
09:40:50.50	+31:40:42.61	0.22	1.09
09:39:50.21	+31:23:35.16	0.22	0.05
09:37:54.45	+31:02:57.13	0.21	1.38
09:41:11.05	+31:09:54.18	0.41*	-0.58
09:40:06.17	+31:30:10.68	0.21	-1.18
09:39:04.09	+31:41:40.27	0.21	0.76
09:39:50.39	+30:46:49.31	0.21	-1.0
09:39:58.99	+30:55:13.62	0.21	2.16
09:38:50.60	+30:51:33.58	0.2	0.48
09:38:46.90	+31:12:30.95	0.2	0.21
09:40:45.57	+31:27:32.09	0.2	1.71
09:38:41.95	+31:00:40.54	0.2	0.73
09:38:08.03	+30:49:42.51	0.19	0.06
09:39:19.60	+30:57:25.85	0.19	0.12
09:39:24.38	+31:36:38.49	0.19	0.62

References

Abell, G.O. (1995). Abell and Zwicky Clusters of Galaxies (Abell+ 1974). *VizieR Online Data Catalog*, **7004**, 0–+. 119

Abell, G.O., Corwin, H.G., Jr. & Olowin, R.P. (1994). Rich Clusters of Galaxies (Abell+ 1989). *VizieR Online Data Catalog*, **7110**, 0–+. 119

Allen, S.W. (2000). The properties of cooling flows in X-ray luminous clusters of galaxies. MNRAS, **315**, 269–295. 187

AMI Consortium, Hurley-Walker, N., Brown, M.L., Davies, M.L., Feroz, F., Franzen, T.M.O. & et al. (2011). Further Sunyaev-Zel'dovich observations of two Planck ERCSC clusters with the Arcminute Microkelvin Imager. MNRAS, L258+. 33

AMI Consortium: Olamaie, A., Rodriguez-Gonzalvez, C., Davies, M.L., Feroz, F., Franzen, T.M.O. & et al. (2010). Parameterization Effects in the analysis of Sunyaev-Zel'dovich Observations. *ArXiv e-prints*. 81

AMI Consortium: Rodriguez-Gonzalvez, C., Olamaie, M., Davies, M.L., Fabian, A.C., Feroz, F., Franzen, T.M.O. & et al. (2010). Sunyaev-Zel'dovich observation of the Bullet-like cluster A2146 with the Arcminute Microkelvin Imager. *ArXiv e-prints*. 76, 81

AMI Consortium: Rodriguez-Gonzalvez, C., Shimwell, T.W., Davies, M.L., Feroz, F., Franzen, T.M.O., Grainge, K.J.B. & et al. (2011). Sunyaev-Zel'dovich observations of LoCuSS clusters with the

Arcminute Microkelvin Imager: moderate X-ray luminosity sample. *ArXiv e-prints*. 76, 82, 184, 202, 210

AMI Consortium: Shimwell, A.C.T.W., Barker, R.W., Biddulph, P., Bly, D., Boysen, R.C., Brown, A.R., Brown, M.L. & et al. (2010). A blind detection of a large, complex, Sunyaev–Zel'dovich structure. *ArXiv e-prints*. 31, 136

AMI Consortium: Shimwell, T.A.C.T.W., Rodriguez-Gonzalvez, C., Davies, M.L., Feroz, F., Franzen, T.M.O. & et al. (2011). Sunyaev-Zel'dovich observations of LoCuSS clusters with the Arcminute Microkelvin Imager: high X-ray luminosity sample. *ArXiv e-prints*. 76, 82

AMI Consortium: Zwart, J.T.L., Barker, R.W., Biddulph, P., Bly, D., Boysen, R.C., Brown, A.R., Clementson, C. & et al. (2008). The Arcminute Microkelvin Imager. MNRAS, **391**, 1545–1558. 18

Arnaud, M., Pratt, G.W., Piffaretti, R., Böhringer, H., Croston, J.H. & Pointecouteau, E. (2010). The universal galaxy cluster pressure profile from a representative sample of nearby systems (REXCESS) and the Y_{SZ} - M_{500} relation. A&A, **517**, A92+. 16, 17

Barrena, R., Boschin, W., Girardi, M. & Spolaor, M. (2007). Internal dynamics of the radio halo cluster Abell 773: a multiwavelength analysis. A&A, **467**, 37–48. 193

Bartlett, J.G. & Silk, J. (1994). The Sunyaev-Zel'dovich effect and cluster evolution. ApJ, **423**, 12–18. 15

Bauer, F.E., Fabian, A.C., Sanders, J.S., Allen, S.W. & Johnstone, R.M. (2005). The prevalence of cooling cores in clusters of galaxies at z˜ 0.15-0.4. MNRAS, **359**, 1481–1490. 200

Bhattacharya, S., Heitmann, K., White, M., Lukić, Z., Wagner, C. & Habib, S. (2011). Mass Function Predictions Beyond ΛCDM. ApJ, **732**, 122–+. 78

Birkinshaw, M. (1999). The Sunyaev-Zel'dovich effect. Phys. Rep., **310**, 97–195. 1, 13

Bock, D.C.J., Bolatto, A.D., Hawkins, D.W., Kemball, A.J., Lamb, J.W., Plambeck, R.L., Pound, M.W., Scott, S.L., Woody, D.P. & Wright, M.C.H. (2006). First results from CARMA: the combined array for research in millimeter-wave astronomy. In *Society of Photo-Optical Instrumentation Engineers (SPIE) Conference Series*, vol. 6267 of *Society of Photo-Optical Instrumentation Engineers (SPIE) Conference Series*. 136

Bonamente, M., Joy, M.K., Carlstrom, J.E., Reese, E.D. & LaRoque, S.J. (2004). Markov Chain Monte Carlo Joint Analysis of Chandra X-Ray Imaging Spectroscopy and Sunyaev-Zel'dovich Effect Data. ApJ, **614**, 56–63. 189

Bonamente, M., Joy, M.K., LaRoque, S.J., Carlstrom, J.E., Reese, E.D. & Dawson, K.S. (2006). Determination of the Cosmic Distance Scale from Sunyaev-Zel'dovich Effect and Chandra X-Ray Measurements of High-Redshift Galaxy Clusters. ApJ, **647**, 25–54. 187, 189, 191, 195

Boylan-Kolchin, M., Springel, V., White, S.D.M., Jenkins, A. & Lemson, G. (2009). Resolving cosmic structure formation with the Millennium-II Simulation. MNRAS, **398**, 1150–1164. 78

Bracewell, R.N. (2000). *The Fourier Transform and its Applications, 3rd Edition*. The McGraw-Hill Companies. 26

Browne, I.W.A., Wilkinson, P.N., Patnaik, A.R. & Wrobel, J.M. (????). Interferometer phase calibration sources. II. 185

Carlstrom, J.E., Joy, M. & Grego, L. (1996). Interferometric Imaging of the Sunyaev-Zeldovich Effect at 30 GHz. ApJ, **456**, L75+. 1, 191

Carlstrom, J.E., Holder, G.P. & Reese, E.D. (2002). Cosmology with the Sunyaev-Zel'dovich Effect. ARA&A, **40**, 643–680. 13

Carlstrom, J.E., Ade, P.A.R., Aird, K.A., Benson, B.A., Bleem, L.E., Busetti, S., Chang, C.L. & et al. (2009). The 10 Meter South Pole Telescope. *ArXiv e-prints*. 31

Cavagnolo, K.W., Donahue, M., Voit, G.M. & Sun, M. (2009). Intracluster Medium Entropy Profiles for a Chandra Archival Sample of Galaxy Clusters. ApJS, **182**, 12–32. 204, 205

Cavaliere, A. & Fusco-Femiano, R. (1976). X-rays from hot plasma in clusters of galaxies. A&A, **49**, 137–144. 81

Cavaliere, A. & Fusco-Femiano, R. (1978). The Distribution of Hot Gas in Clusters of Galaxies. A&A, **70**, 677–+. 81

Challinor, A., Lasenby, A., Somaroo, S., Doran, C. & Gull, S. (1997). Tunnelling times of electrons. *Physics Letters A*, **227**, 143–152. 14

Crocce, M., Fosalba, P., Castander, F.J. & Gaztañaga, E. (2010). Simulating the Universe with MICE: the abundance of massive clusters. MNRAS, **403**, 1353–1367. 78

Culverhouse, T.C. (2006). *Science Targets for The Arcminute Microkelvin Imager*. Ph.D. thesis, University of Cambridge. 87, 88, 94

Cypriano, E.S., Lima Neto, G.B., Sodré, L., Jr., Kneib, J.P. & Campusano, L.E. (2005). Gemini and Chandra Observations of Abell 586, A Relaxed Strong-lensing Cluster. ApJ, **630**, 38–49. 187

David, L.P. & Kempner, J. (2004). Chandra and XMM-Newton Observations of the Double Cluster A1758. ApJ, **613**, 831–840. 197

Davies, M.L., Franzen, T.M.O., Waldram, E.M., Grainge, K.J.B., Hobson, M.P., Hurley-Walker, N. & et al. (2010). 10C Survey of Radio Source at 15.7 GHz: II - First Results. *ArXiv e-prints*. 68, 69, 111, 118

Donnarumma, A. & Ettori, S.e.a. (2011). Abell 611. II. X-ray and strong lensing analyses. A&A, **528**, A73+. 189, 205

Evrard, A.E., MacFarland, T.J., Couchman, H.M.P., Colberg, J.M., Yoshida, N., White, S.D.M. & et al. (2002). Galaxy Clusters in Hubble Volume Simulations: Cosmological Constraints from Sky Survey Populations. ApJ, **573**, 7–36. 78, 82, 83, 87, 93, 96, 97

Feroz, F. & Hobson, M.P. (2008). Multimodal nested sampling: an efficient and robust alternative to Markov Chain Monte Carlo methods for astronomical data analyses. MNRAS, **384**, 449–463. 78

Feroz, F., Hobson, M.P. & Bridges, M. (2009a). MULTINEST: an efficient and robust Bayesian inference tool for cosmology and particle physics. MNRAS, **398**, 1601–1614. 76, 81

Feroz, F., Hobson, M.P. & Bridges, M. (2009b). MULTINEST: an efficient and robust Bayesian inference tool for cosmology and particle physics. MNRAS, **398**, 1601–1614. 78

Fowler, J.W. (2004). The Atacama Cosmology Telescope Project. In C. M. Bradford, P. A. R. Ade, J. E. Aguirre, J. J. Bock, M. Dragovan, L. Duband, L. Earle, J. Glenn, H. Matsuhara, B. J. Naylor, H. T. Nguyen, M. Yun, & J. Zmuidzinas, ed., *Society of Photo-Optical Instrumentation Engineers (SPIE) Conference Series*, vol. 5498 of *Presented at the Society of Photo-Optical Instrumentation Engineers (SPIE) Conference*, 1–10. 32

Franzen, T.M.O., Davies, M.L., Waldram, E.M., Grainge, K.J.B., Hobson, M.P., Hurley-Walker, N. & et al. (2010). 10C Survey of Radio Sources at 15.7 GHz: I - Observing, mapping and source extraction. *ArXiv e-prints*. 70, 113

Giovannini, G., Tordi, M. & Feretti, L. (1999). Radio halo and relic candidates from the NRAO VLA Sky Survey. **4**, 141–155. 193

Govoni, F. & Murgia, M.e.a. (2009). A search for diffuse radio emission in the relaxed, cool-core galaxy clusters A1068, A1413, A1650, A1835, A2029, and Ophiuchus. A&A, **499**, 371–383. 195

Govoni, F., Feretti, L., Giovannini, G., Böhringer, H., Reiprich, T.H. & Murgia, M. (2001). Radio and X-ray diffuse emission in six clusters of galaxies. A&A, **376**, 803–819. 193

Govoni, F., Markevitch, M., Vikhlinin, A., van Speybroeck, L., Feretti, L. & Giovannini, G. (2004). Chandra Temperature Maps for Galaxy Clusters with Radio Halos. ApJ, **605**, 695–708. 193

Grainge, K., Jones, M., Pooley, G., Saunders, R. & Edge, A. (1993). Detection of the Sunyaev / Zeldovich Effect in ABELL:773. MNRAS, **265**, L57+. 191

Grainge, K., Jones, M., Pooley, G., Saunders, R., Baker, J., Haynes, T. & Edge, A. (1996). A resolved image of the Sunyaev-Zel'dovich effect in Abell 1413. MNRAS, **278**, L17–L22. 195

Grainge, K., Jones, M.E., Pooley, G., Saunders, R., Edge, A., Grainger, W.F. & Kneissl, R. (2002). Measuring the Hubble constant from Ryle Telescope and X-ray observations, with application to Abell 1413. MNRAS, **333**, 318–326. 82, 84

Grainger, W.F., Das, R., Grainge, K., Jones, M.E., Kneissl, R., Pooley, G.G. & Saunders, R.D.E. (2002). A maximum-likelihood approach to removing radio sources from observations of the Sunyaev-Zel'dovich effect, with application to Abell 611. MNRAS, **337**, 1207–1214. 189

Haines, C.P., Smith, G.P., Egami, E., Okabe, N., Takada, M., Ellis, R.S., Moran, S.M. & Umetsu, K. (2009). LoCuSS: luminous infrared galaxies in the merging cluster Abell1758 at z = 0.28. MNRAS, **396**, 1297–1307. 197

Heitmann, K., Lukić, Z., Habib, S. & Ricker, P.M. (2006). Capturing Halos at High Redshifts. ApJ, **642**, L85–L88. 78

Hincks, A.D., Acquaviva, V., Ade, P.A.R., Aguirre, P., Amiri, M., Appel, J.W., Barrientos, L.F., Battistelli, E.S. & et al (2010). The

Atacama Cosmology Telescope (ACT): Beam Profiles and First SZ Cluster Maps. ApJS, **191**, 423–438. 32

Hobson, M.P. & Baldwin, J.E. (2004). Markov-Chain Monte Carlo Approach to the Design of Multilayer Thin-Film Optical Coatings. Appl.Optics, **43**, 2651–2660. 115

Hobson, M.P. & Maisinger, K. (2002). Maximum-likelihood estimation of the cosmic microwave background power spectrum from interferometer observations. MNRAS, **334**, 569–588. 76

Holler, C. (2003). *Correlator and antenna design for the Arcminute Microkelvin Imager*. Ph.D. thesis, Cambridge University, Department of Physics. 37

Holler, C.M., Kaneko, T., Jones, M.E., Grainge, K. & Scott, P. (2007a). A 6-12 GHz analogue lag-correlator for radio interferometry. A&A, **464**, 795–806. 37

Holler, C.M., Kaneko, T., Jones, M.E., Grainge, K. & Scott, P. (2007b). A 6-12GHz Analogue Lag-Correlator for Radio Interferometry. *A&A*, **464**, 795–806. 27

Hoshino, A., Henry, J.P. & et al. (2010). X-Ray Temperature and Mass Measurements to the Virial Radius of Abell 1413 with Suzaku. PASJ, **62**, 371–389. 195, 205

Hurley-Walker, N. (2009). *Targeted Science Observations with the Arcminute Microkelvin Imager (AMI)*. Ph.D. thesis, University of Cambridge. 47, 56, 88, 93, 94

Itoh, N., Kohyama, Y. & Nozawa, S. (1998). Relativistic Corrections to the Sunyaev-Zeldovich Effect for Clusters of Galaxies. ApJ, **502**, 7–+. 14

Jenkins, A., Frenk, C.S., White, S.D.M., Colberg, J.M., Cole, S., Evrard, A.E., Couchman, H.M.P. & Yoshida, N. (2001). The mass function of dark matter haloes. MNRAS, **321**, 372–384. 78, 82, 83, 87, 93, 96, 97, 99, 100, 101, 102, 103

Kaneko, T. (2005). *The Arcminute Microkelvin Imager (AMI)*. Ph.D. thesis, University of Cambridge. 28, 37

Keisler, R., Reichardt, C.L., Aird, K.A., Benson, B.A., Bleem, L.E., Carlstrom, J.E., Chang, C.L. & et al. (2011). A Measurement of the Damping Tail of the Cosmic Microwave Background Power Spectrum with the South Pole Telescope. *ArXiv e-prints*. 9, 10

Koester, B.P., McKay, T.A., Annis, J., Wechsler, R.H., Evrard, A., Bleem, L., Becker, M., Johnston, D., Sheldon, E., Nichol, R., Miller, C., Scranton, R., Bahcall, N., Barentine, J., Brewington, H., Brinkmann, J., Harvanek, M., Kleinman, S., Krzesinski, J., Long, D., Nitta, A., Schneider, D.P., Sneddin, S., Voges, W. & York, D. (2007). A MaxBCG Catalog of 13,823 Galaxy Clusters from the Sloan Digital Sky Survey. ApJ, **660**, 239–255. 119, 120

Komatsu, E., Smith, K.M., Dunkley, J., Bennett, C.L., Gold, B., Hinshaw, G., Jarosik, N., Larson, D., Nolta, M.R., Page, L., Spergel, D.N., Halpern, M., Hill, R.S., Kogut, A., Limon, M., Meyer, S.S., Odegard, N., Tucker, G.S., Weiland, J.L., Wollack, E. & Wright, E.L. (2010). Seven-Year Wilkinson Microwave Anisotropy Probe (WMAP) Observations: Cosmological Interpretation. *ArXiv e-prints*. 81, 186

Kompaneets, A.S. (1957). The establishment of thermal equilibrium between quanta and electrons. *Soviet Physics*, **4**, 730. 13

Lahav, O., Bridle, S.L., Percival, W.J., Peacock, J.A., Efstathiou, G., Baugh, C.M., Bland-Hawthorn, J. & et al. (2002). The 2dF Galaxy Redshift Survey: the amplitudes of fluctuations in the 2dFGRS and the CMB, and implications for galaxy biasing. MNRAS, **333**, 961–968. 78

LaRoque, S.J., Bonamente, M., Carlstrom, J.E., Joy, M.K., Nagai, D., Reese, E.D. & Dawson, K.S. (2006). X-Ray and Sunyaev-Zel'dovich Effect Measurements of the Gas Mass Fraction in Galaxy Clusters. ApJ, **652**, 917–936. 187

Larson, D., Dunkley, J., Hinshaw, G., Komatsu, E., Nolta, M.R., Bennett, C.L., Gold, B., Halpern, M. & et al. (2011). Seven-year Wilkinson Microwave Anisotropy Probe (WMAP) Observations: Power Spectra and WMAP-derived Parameters. ApJS, **192**, 16–+. 7, 9, 10

Lewis, A., Challinor, A. & Lasenby, A. (2000). Efficient Computation of Cosmic Microwave Background Anisotropies in Closed Friedmann-Robertson-Walker Models. ApJ, **538**, 473–476. 84, 86, 122

Liddle, A. (2003). *An Introduction to Modern Cosmology, 2nd Edition*. West Sussex: Wiley. 11

Longair, M.S. (1996). *Our evolving universe*. 1

Lukić, Z., Heitmann, K., Habib, S., Bashinsky, S. & Ricker, P.M. (2007). The Halo Mass Function: High-Redshift Evolution and Universality. ApJ, **671**, 1160–1181. 78

Marriage, T.A., Acquaviva, V., Ade, P.A.R., Aguirre, P., Amiri, M., Appel, J.W., Barrientos, L.F., Battistelli, E.S. & et al. (2010). The Atacama Cosmology Telescope: Sunyaev Zel'dovich Selected Galaxy Clusters at 148 GHz in the 2008 Survey. *ArXiv e-prints*. 32

Marrone, D.P., Smith, G.P. & et al. (2009). LoCuSS: A Comparison of Sunyaev-Zel'dovich Effect and Gravitational-Lensing Measurements of Galaxy Clusters. ApJ, **701**, L114–L118. 204

Marshall, P.J., Hobson, M.P. & Slosar, A. (2003). Bayesian joint analysis of cluster weak lensing and Sunyaev-Zel'dovich effect data. MNRAS, **346**, 489–500. 76

Mazzotta, P., Markevitch, M., Vikhlinin, A., Forman, W.R., David, L.P. & van Speybroeck, L. (2001). Chandra Observation of RX J1720.1+2638: a Nearly Relaxed Cluster with a Fast-moving Core? ApJ, **555**, 205–214. 202

McCarthy, I.G., Bower, R.G. & Balogh, M.L. (2007). Revisiting the baryon fractions of galaxy clusters: a comparison with WMAP 3-yr results. MNRAS, **377**, 1457–1463. 81

Mehrtens, N., Romer, A.K., Lloyd-Davies, E.J. & et al. (2011). The XMM Cluster Survey: Optical analysis methodology and the first data release. *ArXiv e-prints*. 210

Menanteau, F.e.a. (2010). The Atacama Cosmology Telescope: Physical Properties and Purity of a Galaxy Cluster Sample Selected via the Sunyaev-Zel'dovich Effect. ApJ, **723**, 1523–1541. 35

Morandi, A. & Ettori, S. (2007). Entropy profiles in X-ray luminous galaxy clusters at z $>$ 0.1. MNRAS, **380**, 1521–1532. 189

Morandi, A., Ettori, S. & Moscardini, L. (2007). X-ray and Sunyaev-Zel'dovich scaling relations in galaxy clusters. MNRAS, **379**, 518–534. 189

Muchovej, S., Leitch, E., Carlstrom, J.E. & Culverhouse, T.e.a. (2011). Cosmological Constraints from a 31 GHz Sky Survey with the Sunyaev-Zel'dovich Array. ApJ, **732**, 28–+. 34

Navarro, J.F., Frenk, C.S. & White, S.D.M. (1995). The assembly of galaxies in a hierarchically clustering universe. MNRAS, **275**, 56–66. 81, 187

Okabe, N., Takada, M., Umetsu, K., Futamase, T. & Smith, G.P. (2010). LoCuSS: Subaru Weak Lensing Study of 30 Galaxy Clusters. PASJ, **62**, 811–. 187

Patnaik, A.R., Browne, I.W.A., Wilkinson, P.N. & Wrobel, J.M. (1992). Interferometer phase calibration sources. I - The region 35-75 deg. MNRAS, **254**, 655–676. 185

Peacock, J.A. (1999). *Cosmological Physics*. Cambridge Universe Press. 1, 211

Peebles, P.J.E. (1993). *Principles of Physical Cosmology*. Princeton University Press, 1993, ISBN 0691019339. 1, 211

Penzias, A.A. & Wilson, R.W. (1965). A Measurement of Excess Antenna Temperature at 4080 Mc/s. ApJ, **142**, 419–421. 8

Planck Collaboration, Ade, P.A.R., Aghanim, N., Arnaud, M., Ashdown, M., Aumont, J., Baccigalupi, C., Baker, M., Balbi, A., Banday, A.J. & et al. (2011a). Planck Early Results: The Planck mission. *ArXiv e-prints*. 33

Planck Collaboration, Ade, P.A.R., Aghanim, N., Arnaud, M., Ashdown, M., Aumont, J., Baccigalupi, C., Balbi, A., Banday, A.J., Barreiro, R.B. & et al. (2011b). Planck Early Results: The all-sky Early Sunyaev-Zeldovich cluster sample. *ArXiv e-prints*. 33, 34, 35

Planck Collaboration, Ade, P.A.R., Aghanim, N., Arnaud, M., Ashdown, M., Aumont, J., Baccigalupi, C., Balbi, A., Banday, A.J., Barreiro, R.B. & et al. (2011c). Planck Early Results XI: Calibration of the local galaxy cluster Sunyaev-Zeldovich scaling relations. *ArXiv e-prints*. 15

Planck Collaboration, Aghanim, N., Arnaud, M., Ashdown, M., Atrio-Barandela, F., Aumont, J., Baccigalupi, C., Balbi, A., Banday, A.J., Barreiro, R.B. & et al. (2011d). Planck Early Results XXVI: Detection with Planck and confirmation by XMM-Newton of PLCK G266.6-27.3, an exceptionally X-ray luminous and massive galaxy cluster at z˜1. *ArXiv e-prints*. 33

Planck Collaboration, Aghanim, N., Arnaud, M., Ashdown, M., Aumont, J., Baccigalupi, C., Balbi, A., Banday, A.J., Barreiro, R.B. & et al. (2011e). Planck early results: XMM-Newton follow-up for validation of Planck cluster candidates. *ArXiv e-prints*. 33

Planck HFI Core Team, Ade, P.A.R., Aghanim, N., Ansari, R., Arnaud, M., Ashdown, M., Aumont, J. & et al. (2011). Planck early results: first assessment of the High Frequency Instrument in-flight performance. *ArXiv e-prints*. 33

Pratt, G.W. & Arnaud, M. (2005). XMM-Newton observations of three poor clusters: Similarity in dark matter and entropy profiles down to low mass. A&A, **429**, 791–806. 195

Press, W.H. & Schechter, P. (1974). Formation of Galaxies and Clusters of Galaxies by Self-Similar Gravitational Condensation. ApJ, **187**, 425–438. 78, 93

Reed, D., Gardner, J., Quinn, T., Stadel, J., Fardal, M., Lake, G. & Governato, F. (2003). Evolution of the mass function of dark matter haloes. MNRAS, **346**, 565–572. 78

Reed, D.S., Bower, R., Frenk, C.S., Jenkins, A. & Theuns, T. (2007). The halo mass function from the dark ages through the present day. MNRAS, **374**, 2–15. 78

Riess, A.G., Filippenko, A.V., Challis, P., Clocchiatti, A., Diercks, A., Garnavich, P.M., Gilliland, R.L., Hogan, C.J., Jha, S., Kirshner, R.P., Leibundgut, B., Phillips, M.M., Reiss, D., Schmidt, B.P., Schommer, R.A., Smith, R.C., Spyromilio, J., Stubbs, C., Suntzeff, N.B. & Tonry, J. (1998). Observational Evidence from Supernovae for an Accelerating Universe and a Cosmological Constant. AJ, **116**, 1009–1038. 7

Rizza, E., Burns, J.O., Ledlow, M.J., Owen, F.N., Voges, W. & Bliton, M. (1998). X-ray observations of distant Abell clusters. MNRAS, **301**, 328–342. 197

Romano, A. & et al (2010). Abell 611. I. Weak lensing analysis with LBC. A&A, **514**, A88+. 189

Rozo, E., Rykoff, E.S., Evrard, A., Becker, M., McKay, T., Wechsler, R.H., Koester, B.P., Hao, J., Hansen, S., Sheldon, E., Johnston, D., Annis, J. & Frieman, J. (2009). Constraining the Scatter in the Mass-richness Relation of maxBCG Clusters with Weak Lensing and X-ray Data. ApJ, **699**, 768–781. 119, 120

Rudy, D.J., Muhleman, D.O., Berge, G.L., Jakosky, B.M. & Christensen, P.R. (1987). Mars - VLA observations of the northern hemisphere and the north polar region at wavelengths of 2 and 6 CM. **71**, 159–177. 114

Sanderson, A.J.R., Edge, A.C. & Smith, G.P. (2009). LoCuSS: the connection between brightest cluster galaxy activity, gas cooling and dynamical disturbance of X-ray cluster cores. MNRAS, **398**, 1698–1705. 189

Sarazin, C.L. (1986). X-ray emission from clusters of galaxies. *Reviews of Modern Physics*, **58**, 1–115. 183

Saunders, R., Kneissl, R., Grainge, K. & et al (2003). A measurement of H0 from Ryle Telescope, ASCA and ROSAT observations of Abell 773. MNRAS, **341**, 937–940. 191

Scheuer, P.A.G. (1957). *Proc. Cam. Phil. Soc.*, **53**, 764. 118

Schmidt, R.W. & Allen, S.W. (2007). The dark matter haloes of massive, relaxed galaxy clusters observed with Chandra. MNRAS, **379**, 209–221. 189

Sehgal, N., Hughes, J.P., Wittman, D., Margoniner, V., Tyson, J.A., Gee, P. & dell'Antonio, I. (2008). Probing the Relation Between X-Ray-Derived and Weak-Lensing-Derived Masses for Shear-Selected Galaxy Clusters. I. A781. ApJ, **673**, 163–175. 193

Seljak, U., Makarov, A., McDonald, P., Anderson, S.F., Bahcall, N.A., Brinkmann, J., Burles, S., Cen, R. & et al. (2005). Cosmological parameter analysis including SDSS Lyα forest and galaxy bias: Constraints on the primordial spectrum of fluctuations, neutrino mass, and dark energy. Phys.Rev.D, **71**, 103515–+. 78

Sheth, R.K. & Tormen, G. (2002). An excursion set model of hierarchical clustering: ellipsoidal collapse and the moving barrier. MNRAS, **329**, 61–75. 78

Silk, J. (1968). Cosmic Black-Body Radiation and Galaxy Formation. ApJ, **151**, 459. 10

Smith, G.P., Kneib, J.P., Smail, I., Mazzotta, P., Ebeling, H. & Czoske, O. (2005). A Hubble Space Telescope lensing survey of X-ray luminous galaxy clusters - IV. Mass, structure and thermodynamics of cluster cores at z= 0.2. MNRAS, **359**, 417–446. 204

Smoot, G.F., Bennett, C.L., Kogut, A., Wright, E.L., Aymon, J., Boggess, N.W., Cheng, E.S., de Amici, G. & et al. (1992). Structure in the COBE differential microwave radiometer first-year maps. ApJ, **396**, L1–L5. 9

Snowden, S.L., Mushotzky, R.F., Kuntz, K.D. & Davis, D.S. (2008). A catalog of galaxy clusters observed by XMM-Newton. A&A, **478**, 615–658. 205

Staniszewski, Z., Ade, P.A.R., Aird, K.A., Benson, B.A., Bleem, L.E., Carlstrom, J.E. & et al. (2009). Galaxy Clusters Discovered with a Sunyaev-Zel'dovich Effect Survey. ApJ, **701**, 32–41. 32

Sunyaev, R.A. & Zeldovich, Y.B. (1970). The Spectrum of Primordial Radiation, its Distortions and their Significance. *Comments on Astrophysics and Space Physics*, **2**, 66–+. 1, 13

Sunyaev, R.A. & Zeldovich, Y.B. (1972). The Observations of Relic Radiation as a Test of the Nature of X-Ray Radiation from the Clusters of Galaxies. *Comments on Astrophysics and Space Physics*, **4**, 173–+. 13

Thompson, A.R., Moran, J.M. & Swenson, G.W., Jr. (2001). *Interferometry and Synthesis in Radio Astronomy, 2nd Edition*. New York: Wiley. 1, 44

Tinker, J., Kravtsov, A.V., Klypin, A., Abazajian, K., Warren, M., Yepes, G., Gottlöber, S. & Holz, D.E. (2008). Toward a Halo Mass Function for Precision Cosmology: The Limits of Universality. ApJ, **688**, 709–728. 78

Tully, R.B., van der Kruit, J.R. & Fisher, P.C. (1989). Book-Review - Nearby Galaxies Atlas. Space Sci.Rev., **50**, 388–+. 118

Vanderlinde, K., Crawford, T.M., de Haan, T., Dudley, J.P., Shaw, L., Ade, P.A.R., Aird, K.A. & et al. (2010). Galaxy Clusters Selected with the Sunyaev-Zel'dovich Effect from 2008 South Pole Telescope Observations. ApJ, **722**, 1180–1196. 32, 35

Venturi, T., Giacintucci, S., Dallacasa, D., Cassano, R., Brunetti, G., Bardelli, S. & Setti, G. (2008). GMRT radio halo survey in galaxy clusters at z = 0.2-0.4. II. The eBCS clusters and analysis of the complete sample. A&A, **484**, 327–340. 189, 195, 200

Vikhlinin, A. & et al (2009). Chandra Cluster Cosmology Project III: Cosmological Parameter Constraints. ApJ, **692**, 1060–1074. 78

Vikhlinin, A., Markevitch, M., Murray, S.S., Jones, C., Forman, W. & Van Speybroeck, L. (2005). Chandra Temperature Profiles for a Sample of Nearby Relaxed Galaxy Clusters. ApJ, **628**, 655–672. 195, 205

Waldram, E.M., Pooley, G.G., Grainge, K.J.B., Jones, M.E., Saunders, R.D.E., Scott, P.F. & Taylor, A.C. (2003). 9C: a survey of radio sources at 15 GHz with the Ryle Telescope. *MNRAS*, **342**, 915–925. 118

Warren, M.S., Abazajian, K., Holz, D.E. & Teodoro, L. (2006). Precision Determination of the Mass Function of Dark Matter Halos. ApJ, **646**, 881–885. 78

Wen, Z.L., Han, J.L. & Liu, F.S. (2010). Galaxy clusters identified from the SDSS-DR6 (Wen+, 2009). *VizieR Online Data Catalog*, **218**, 30197–+. 119, 120

White, D.A. (2000). Deconvolution of ASCA X-ray data - II. Radial temperature and metallicity profiles for 106 galaxy clusters. MNRAS, **312**, 663–688. 187

White, M. (2002). The Mass Function. ApJS, **143**, 241–255. 78

Wilkinson, P.N., Browne, I.W.A., Patnaik, A.R., Wrobel, J.M. & Sorathia, B. (????). Interferometer phase calibration sources - III. 185

Williamson, R., Benson, B.A., High, F.W., Vanderlinde, K., Ade, P.A.R., Aird, K.A., Andersson, K., Armstrong, R., Ashby, M.L.N. & et al. (2011). An SZ-selected sample of the most massive galaxy clusters in the 2500-square-degree South Pole Telescope survey. *ArXiv e-prints*. 32

Zhang, Y.Y., Finoguenov, A., Böhringer, H., Kneib, J.P., Smith, G.P., Kneissl, R., Okabe, N. & Dahle, H. (2008). LoCuSS: comparison of observed X-ray and lensing galaxy cluster scaling relations with simulations. A&A, **482**, 451–472. 193

Zwart, J.T.L., Feroz, F., Davies, M.L., Franzen, T.M.O., Grainge, K.J.B., Hobson, M.P., Hurley-Walker, N. & et al. (2010). Sunyaev-Zel'dovich observations of galaxy clusters out to the virial radius with the Arcminute Microkelvin Imager. *ArXiv e-prints*. 76, 81